The Physics of the Coronal and Broad Line Regions for Galaxies in The Sloan Digital Sky Survey's Mapping Nearby Galaxies at Apache Point Observatory Catalog

by

James Negus

B.A., The University of Chicago, 2013

M.S., University of Colorado Boulder, 2019

A thesis submitted to the

Faculty of the Graduate School of the

University of Colorado in partial fulfillment

of the requirements for the degree of

Doctor of Philosophy

Department of Astrophysical and Planetary Science

2023

Committee Members:

Dr. Julia Comerford, Chair

Dr. Francisco Müller Sánchez

Dr. Jeremy Darling

Dr. Adam Kowalski

Dr. Jay McMahon

Negus, James (Ph.D., Astrophysics)

The Physics of the Coronal and Broad Line Regions for Galaxies in The Sloan Digital Sky Survey's Mapping Nearby Galaxies at Apache Point Observatory Catalog

Thesis directed by Dr. Julia Comerford

There is growing evidence that Active Galactic Nucleus (AGN) processes play a vital role in galaxy evolution (e.g., regulating star formation and galactic growth). However, accurate AGN identification is often challenging, as common AGN diagnostics can be confused by contributions from star formation, supernovae, and shocks. However, one promising avenue for identifying the strong ionizing continuum of an AGN are "coronal emission lines" ("CLs"), which are highly ionized species of gas with ionization potentials $\geq$ 100 eV - above the limit of star formation. Here, I present my graduate work that explores the feasibility of using optical CLs to accurately trace AGNs, using the most extensive optical CL catalogs available, which I assembled using the Sloan Digital Sky Survey's Mapping Nearby Galaxies at Apache Point Observatory (MaNGA) catalog. In this work, I detect CL emission from [NeV], [FeVII], and/ or [FeX] with $\geq 5\sigma$ confidence. I focus particularly on the strength and distribution of the CLs; I also provide the fraction of confirmed CL AGNs to showcase the reliability of using CLs to detect AGNs. I then review the physical CL gas properties (e.g., electron temperatures and densities) to deduce the primary mechanism(s) that generate the CLs. Next, I discuss which CLs are ideal for identifying high luminosity AGNs and investigate the role of dust extinction on optical CL detections. I then search for broad Hα and Hβ emission, which trace the high velocity clouds found near the AGN accretion disk, and assemble one of the largest broad line (BL) MaNGA AGN catalogs. I detect 1,042 unique BL galaxies and find that 109 feature BLs from a companion galaxy, not the target MaNGA galaxy (i.e., "offset AGNs"). I conclude by considering how multi-wavelength CL observations (e.g., X-ray and IR) can help to improve AGN identification.

Acknowledgements

I would like to extend my gratitude to my advisor, Dr. Julia Comerford, for providing me with the tools and resources I needed to complete my Ph.D. I also want to thank my mentor, Dr. Jeffrey Bennett, who remains an invaluable source of inspiration, encouragement, and motivation. Throughout the challenging and isolating years during my Ph.D., his belief in me, my vision, and my value to the astronomical community prevented my flames from withering, despite my own doubts. Finally, I would also like to thank my mother and grandmother for their unwavering support; I truly owe everything to them. They remind me of my roots and this accomplishment honors them.

Oh, and of course I would be remiss if I didn't thank Dwight Schrute, the entire cast of The Office, and Star Trek: Deep Space Nine, for getting me through the darkest phases of this degree!

Contents

Chapter

Tables

Table

Figures

Figure

Chapter 1

Introduction

In this section, I provide a brief introduction on galaxy formation, the nature of an Active Galactic Nucleus (AGN), and the importance of AGNs in the context of galaxy evolution. I also overview existing AGN selection techniques, possible improvements to these techniques (e.g., using multi-wavelength spectroscopy), and the importance of AGN identification in large-scale studies of AGNs. Accurately finding AGNs and the impact of AGN processes on their local environments remain topics of astrophysical debate, and my contributions reflect a step forward on the larger quest to uncover hidden populations of AGNs in the Universe, and to comprehend their influence on galactic growth.

1.1 Hierarchical Galactic Evolution

Edwin Hubble was the first to propose the "Tuning Fork Galaxy Classification Scheme" to differentiate varying galaxy types in the Universe ([131]). He posited that three galaxy types exist: spiral (primarily blue and star-forming), elliptical (typically red and non-star forming), and irregular. He devised the model after he observed Cepheid variable stars in the Andromeda galaxy with the 100-inch Hooker Telescope at the Mount Wilson Observatory ([130]). By resolving individual Cepheid stars and measuring their variable luminosities, he deduced that they were significantly further away than the stars in our own Milky Way galaxy. Moreover, he studied many large, distant, clouds of dust and gas that were termed "nebulae" at the time. Eventually, he would discover these to be galaxies, and reasoned that

millions existed in an expanding universe ([132, 133, 129]).

Over the past several decades, subsequent observational studies have peered even deeper into the nature of galaxies and their evolution. The scope of these studies has been wide-ranging and the most impactful have employed a multitude of multi-wavelength observations. For example, the discovery of "Lyman-break" galaxies, which are luminous galaxies undergoing active star-formation between redshifts $z \sim 3$ - 4 (e.g., [267, 269, 268, 2]), measurements of star-formation histories from $z = 4.5$ to present day (e.g., [231, 171, 172, 229]), and estimations of the galaxy luminosity function (e.g., [247, 81, 267]) have served as breakthrough moments in extragalactic astronomy.

Moreover, these observations have been supplemented by extensive theoretical initiatives. For example, N-body simulations have been used to numerically solve the non-linear equations driving galaxy formation, and semi-analytic models have been used to create analytic approximations of physical galaxy processes. Many of these efforts have incorporated an extensive array of parameters to accurately model galactic processes, which include, but are not limited to: disk size, morphology, star-formation and feedback, stellar bursts, chemical evolution, dust extinction, dark matter halo distribution, stellar population synthesis models, bars, metallicity, gas fractions, color, mass-to-light ratios, mergers, emission line modeling, galaxy size, dynamical friction, temperature, density, gravitation, hydrodynamics, radiative transfer/ cooling, and luminosity functions (e.g., [32, 295, 139, 138, 155, 1, 68, 190, 262, 21, 265, 189, 264, 202]).

The tandem of theoretical and observational efforts has led to the widely adopted narrative that galaxies evolve hierarchically, where each galaxy is produced through fundamental density perturbations initialized during inflation and the gravitational influences of cold dark matter (the primary mass component of the Universe). In the process, gas and dust begin to amalgamate with dark matter. Then, when the dark matter halos collapse, visible baryonic matter condenses, as stars form out of the gas that has cooled on the galactic disk (see [22] for a thorough review).

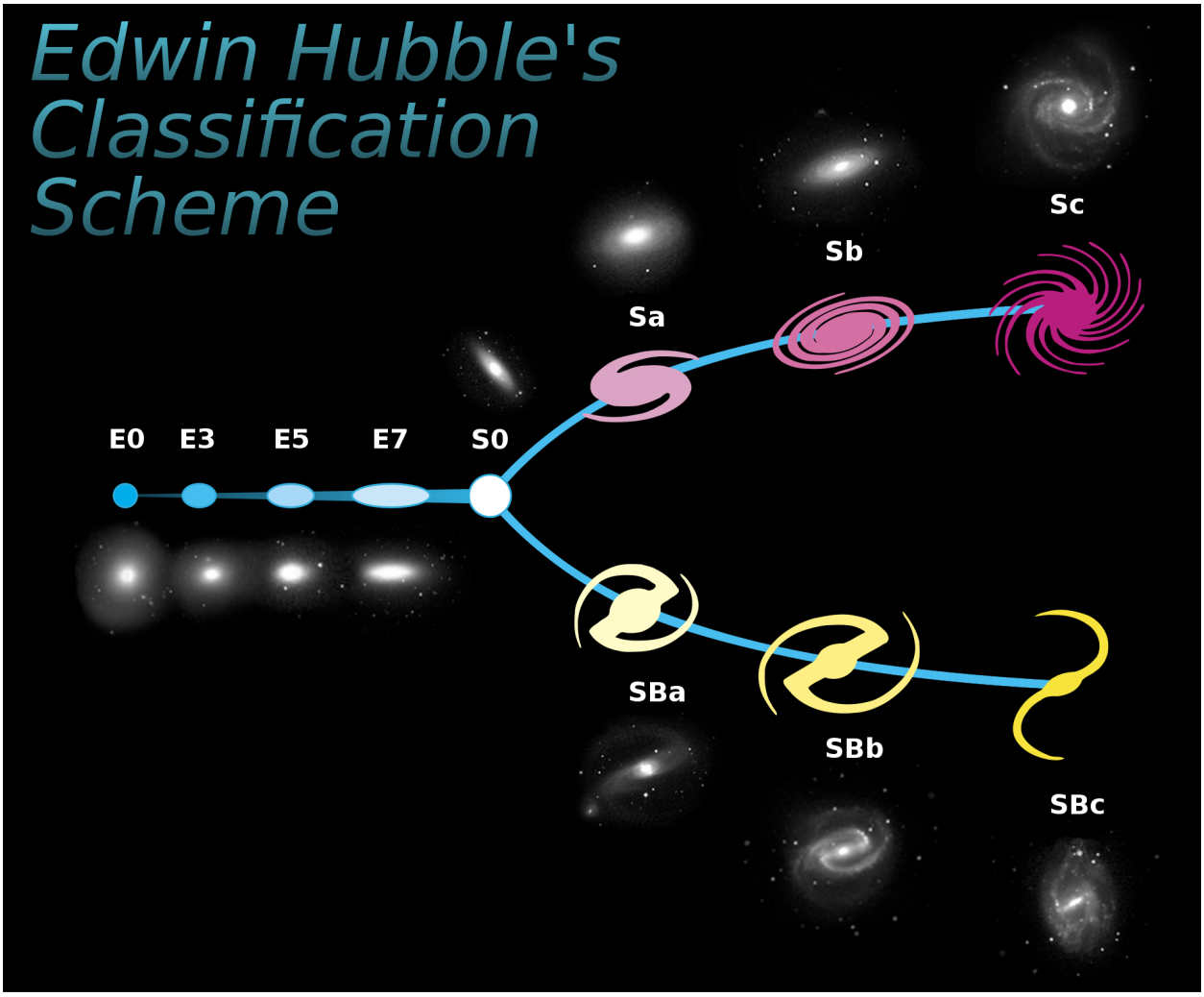

Figure 1.1: This graphic depicts Edwin Hubble's Classification Scheme, separating galaxies into ellipticals ("E") and spirals ("S"). The letters "a" and "b" signify how tight the spiral arms are, with "a" being the most tightly wound and "c" being the least. The letter "B" indicates if a galaxy is barred or not. Note, irregular and dwarf galaxies are not shown in this diagram. Credits: NASA; ESA

1.2 Nature of an Active Galactic Nucleus

It is widely accepted that massive galaxies host supermassive black holes (SMBHs) at their centers ($M > 10^6 M_\odot$; e.g., [96, 151]). Further, if SMBHs are fueled by sufficient accretion onto their cores, they can become an Active Galactic Nucleus (AGN; e.g. [241]). An AGN is one of the most luminous sources of electromagnetic (EM) radiation in the Universe; emitting radio waves to gamma rays (up to $L_{bol} \sim 10^{48}$ erg s^{-1}; e.g., [206, 207]). Moreover, since each band harnesses the ability to reveal unique AGN physics and attributes (e.g., orientation, accretion rate, and/or radio jets), the number of AGN classifications is extensive (> 50; Figure 1.2).

For example, the radio band is useful for probing AGNs with radio jets ($< 10\%$ of the total population of AGNs), where the jets are produced via synchrotron radiation from relativistic electrons spiraling along magnetic field lines and carried by plasma (e.g., [291]). Furthermore, optical and ultraviolet (UV) emission arise from the accretion disk. In fact, the AGN spectral energy distribution (SED) peaks in the UV for AGNs, where the "big blue bump" is a characteristic AGN feature, which is suspected to arise from optically thick thermal radiation from the accretion disk and/or free-free thermal emission (e.g., [240, 34, 14, 305]; Figure 1.3). Beyond the accretion disk, dust, which surrounds most AGNs, absorbs AGN radiation and re-emits it as infrared (IR) radiation. As a result, IR observations are advantageous for identifying obscured IR AGNs, which may be missed in optical surveys. Note, the AGN orientation angle impacts how much dust obscuration is observable, which plays a critical role in determining which emission lines can be used to detect AGNs (Section 1.3). Additionally, AGN X-rays are primarily emitted via inverse Compton scattering, which occurs when charged particles transfer energy to accretion disk photons. This process begins above the accretion disk in a region known as the AGN "corona". Finally, gamma rays, like radio waves, are emitted via AGN jets. To better comprehend how each band correlates to AGN detections, I present the largest AGN surface densities across

Class/Acronym	Meaning/Main properties
Quasar	Quasi-stellar radio source (originally)
Sey1	Seyfert 1, FWHM $\gtrsim$ 1,000 km s^{-1}
Sey2	Seyfert 2, FWHM $\lesssim$ 1,000 km s^{-1}
QSO	Quasi-stellar object
QSO2	Quasi-stellar object 2, high power Sey2
RQ AGN	Radio-quiet AGN
RL AGN	Radio-loud AGN
Jetted AGN	With strong relativistic jets
Non-jetted AGN	Without strong relativistic jets
Type 1	Sey1 and quasars
Type 2	Sey2 and QSO2
FR I	Fanaroff-Riley class I radio source
FR II	Fanaroff-Riley class II radio source
BL Lac	BL Lacertae object
Blazars	BL Lacs and FSRQs
BAL	Broad absorption line (quasar)
BLO	Broad-line object, FWHM $\gtrsim$ 1,000 km s^{-1}
BLAGN	Broad-line AGN, FWHM $\gtrsim$ 1,000 km s^{-1}
BLRG	Broad-line radio galaxy
CDQ	Core-dominated quasar
CSS	Compact steep spectrum radio source
CT	Compton-thick
FR 0	Fanaroff-Riley class 0 radio source
FSRQ	Flat-spectrum radio quasar
GPS	Gigahertz-peaked radio source
HBL/HSP	High-energy cutoff BL Lac/blazar
HEG	High-excitation galaxy
HPQ	High polarization quasar
Jet-mode	
IBL/ISP	Intermediate-energy cutoff BL Lac/blazar
LINER	Low-ionization nuclear emission-line regions
LLAGN	Low-luminosity AGN
LBL/LSP	Low-energy cutoff BL Lac/blazar
LDQ	Lobe-dominated quasar
LEG	Low-excitation galaxy
LPQ	Low polarization quasar
NLAGN	Narrow-line AGN, FWHM $\lesssim$ 1,000 km s^{-1}
NLRG	Narrow-line radio galaxy
NLS1	Narrow-line Seyfert 1
OVV	Optically violently variable (quasar)
Population A	
Population B	
Radiative-mode	
RBL	Radio-selected BL Lac
Sey1.5	Seyfert 1.5
Sey1.8	Seyfert 1.8
Sey1.9	Seyfert 1.9
SSRQ	Steep-spectrum radio quasar
USS	Ultra-steep spectrum source
XBL	X-ray-selected BL Lac
XBONG	X-ray bright optically normal galaxy

Figure 1.2: The major AGN classes, from [207].

the EM spectrum in Figure 1.4. Note, while the AGN SED peaks in the optical/UV, the largest AGN surface density is in the soft X-ray region, where there is the lowest amount of host galaxy contamination. Figure 1.5 provides a more comprehensive overview of the selection biases for each band.

Additionally, two "modes" of AGNs are proposed to exist: "kinetic"/ "radio"/ "radio loud" mode and "radiative"/ "quasar"/"wind"/ "radio-quiet" mode (e.g., [90, 161, 183]). The latter represents high luminosity AGNs, near the Eddington luminosity/ limit, which is the maximum AGN luminosity when there is a balance between the gravitational pull inwards and the radiation force outwards, and involves the clearing of cold gas away from the AGN. In contrast, the former represents lower luminosity AGNs, within more massive galaxies, that feature hot gas, and incorporate mechanical energy produced through powerful radio jets; [87] posits that this mode of AGNs heats hot intracluster gas and can reduce star-formation by an order of magnitude in the host galaxy. For reference, a schematic diagram showing the basic features of AGNs (e.g., the accretion disk, SMBH, and radio jets) are presented in Figure 1.6, and the Eddington Luminosity is defined as:

$$\mathrm{L_{EDD}} = \frac{4\pi \mathrm{GMc}}{\kappa} \tag{1.1}$$

where G is the gravitational constant, M is the mass of the central object, c is the speed of light, and κ is opacity.

Moreover, considering the tremendous power of AGNs, there is growing evidence that they play a vital role in influencing the evolution of their host galaxies and local environments. Specifically, the AGN processes that can impact the local AGN environment, termed "AGN feedback" (e.g., radiation, winds, outflows, and radio jets) can interact with the interstellar medium and can result in the heating or clearing of gas. In fact, several authors suggest that AGNs quench star-formation by disrupting the coalescence of dense, cool, molecular galactic gas (e.g., [257, 61, 266, 59, 128, 276, 156, 263, 176, 87]). Additionally, there is

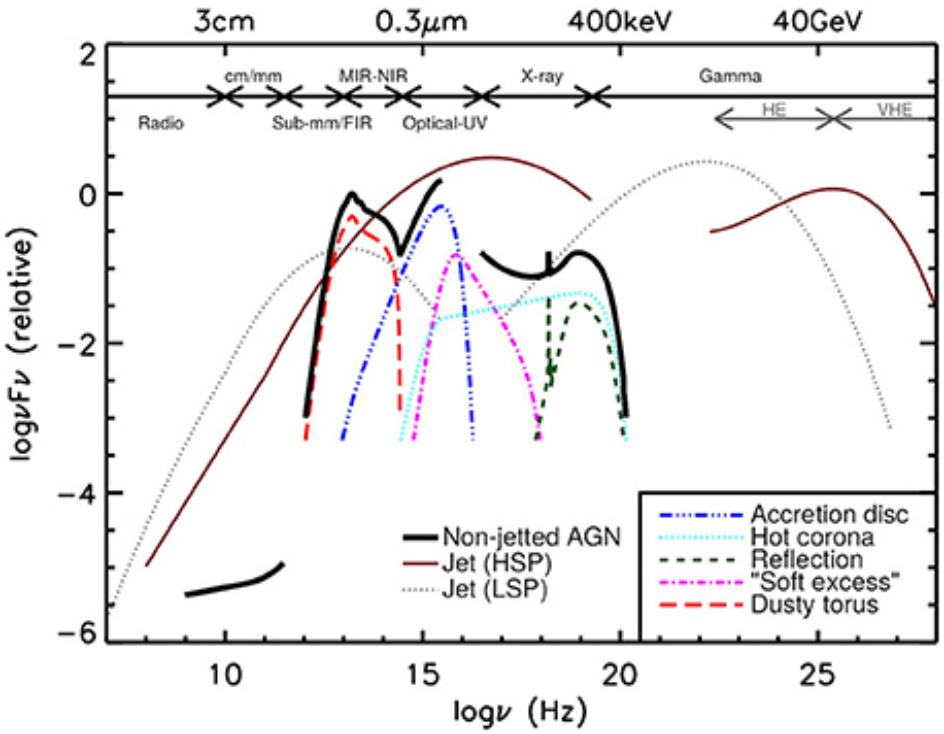

Figure 1.3: An approximate depiction of the AGN SED. The black curve showcases the total emission, and the other AGN elements are shown in separate colors. The AGN SED peaks in the ultraviolet. Adapted from [116] and reproduced by [207].

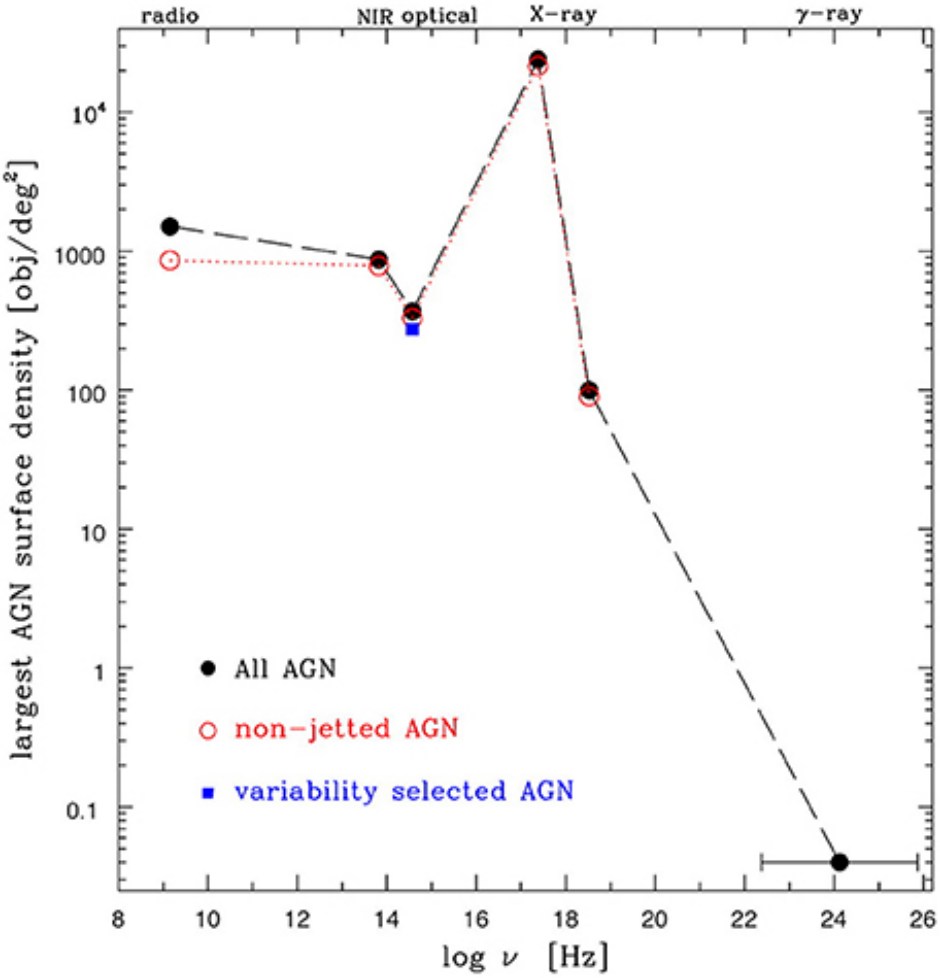

Figure 1.4: The largest AGN surface density across the entire EM spectrum. Black filled points represent all AGNs, open red points correspond to AGNs without jets, and the closed blue square marks the variability selected AGN. The peak in the soft X-ray band is due to relatively low host galaxy contamination at those frequencies. Figure from [207].

Band	Type	Physics	Selection biases/weaknesses	Key capabilities/strengths
Radio, $f_r \gtrsim 1$ mJy	Jetted	Jet	Non-jetted sources	High efficiency, no obscuration bias
Radio, $f_r \lesssim 1$ mJy	Jetted and non-jetted	Jet and SF	Host contamination	Completeness, no obscuration bias
IR	Type 1 and 2	Hot dust and SF	Completeness, reliability, host contamination, no dust	Weak obscuration bias, high efficiency
Optical	Type 1	Disk	Completeness, low-luminosity, obscured sources, host contamination	High efficiency, detailed physics from lines
X-ray	Type 1 and (most) 2	Corona	Very low-luminosity, heavy obscuration	Completeness, low host contamination
γ-ray	Jetted	Jet	Non-jetted, unbeamed sources	High reliability
Variability	All (in principle)	Corona, disk, jet	Host contamination, obscuration, cadence and depth of observations	Low-luminosity

Figure 1.5: A multi-wavelength overview of AGNs highlighting the different selection biases (weaknesses) and key capabilities (strengths). Figure from [207].

further compelling evidence in support of AGN feedback suppressing star-formation (e.g., [279, 117, 12]). The authors reveal a declining AGN luminosity and mass trend from a peak at z $\sim$ 2 - 2.5 to present day ($z = 0$). As outlined in [88], this appears to oppose the hierarchical cold dark matter universe (Section 1.1), where the most massive galaxies form in the present day. However, one possible solution to this is AGN feedback. As massive galaxies collide and merge through cosmic time, they supply large reservoirs of dense gas for star-formation and AGN accretion; however, AGN feedback may be depriving the AGN of matter to sustain further accretion, effectively turning the active galaxy quiescent (e.g. [140, 107, 67, 266, 33, 46]). As the gas dissipates, it leaves behind red, non star-forming elliptical galaxies (e.g., [266]). Such a process would account for the diminishing AGN luminosity and mass trends reported as a function of redshift from $z \sim 2$ - 2.5 to the present day ($z = 0$).

Furthermore, the interplay between AGN feedback and the host galaxy may account for the empirical correlation between SMBH mass and the stellar velocity dispersion in the galactic bulge (i.e. the "M-σ relationship"; e.g., [98, 95]). Moreover, it may create dense pockets of gas, which actually trigger star-formation (e.g.,[256, 281]). These possibilities underscore the exciting field of AGN feedback, and the potential impact of AGNs on the host galaxy.

The nature of AGN processes and their role in the growth of a galaxy is still an open ended question. Significant progress has been made to observe AGN feedback; yet, the plethora of modes and classes of AGNs suggests that further large-scale AGN studies are required to understand this complex phenomena. To resolve the true extent of AGN physics, a combination of observational efforts are required. Doing so will help reveal how AGNs can impact the star-formation, size, and structure of their host galaxies, in addition to other galaxy properties.

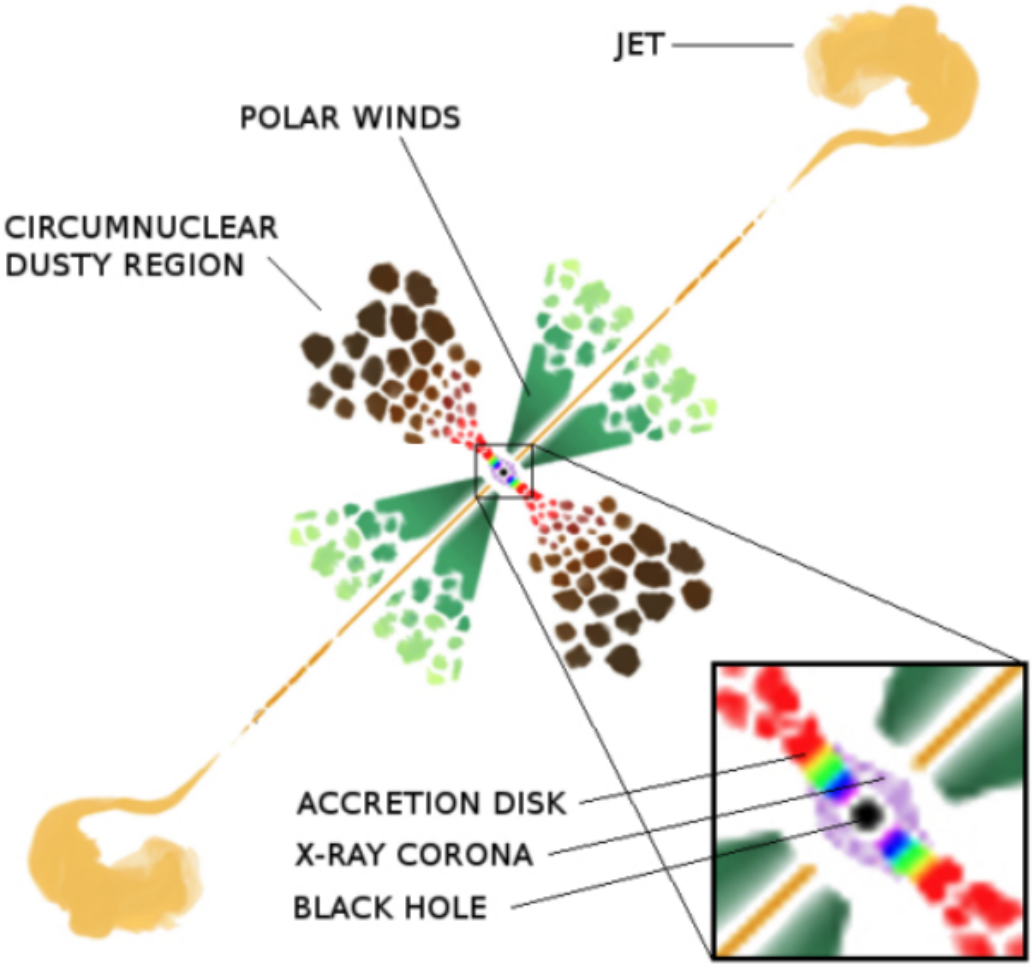

Figure 1.6: AGN Diagram (not to scale). The SMBH is at the center of the galaxy in black, the mutli-temperature accretion disk depicting infalling matter onto the SMBH is shown in rainbow colors, and the X-ray corona illuminating the accretion disk is in violet. The size of the disk ranges between $\sim 10^{-5}$ parsec to $\sim 10^{-2}$ parsec for a $10^8 M_\odot$ black hole. The circumnuclear dusty region is shown in dark brown and begins ~ 0.1 parsec, and the polar ionized winds (green) form < 1 parsec and can extend into the interstellar medium (shown in yellow-green) several hundred parsecs from the SMBH. Kiloparsec-sized radio jets are shown in yellow. Figure from [175].

1.3 AGN Selection Techniques

Despite the importance of AGNs in galaxy evolution, the AGNs themselves can be difficult to identify accurately. As shown in Figure 1.5, attempting to detect AGNs in each band of the EM spectrum has its own limitations and strengths. For example, radio wave observations are excellent tracers of AGN jets and are not significantly impeded by dust obscuration. However, they are weak at identifying non-jetted AGNs (90% of all AGNs) and AGNs that feature jets oriented outside of the observational field of view. Moreover, IR observations do not have to contend with a dust obscuration bias and are highly efficient; however, they are not strong AGN tracers when there is little dust surrounding the SMBH. Further, optical studies are also efficient, and extensive details on AGN physics can be inferred via optical lines (e.g., cloud velocity, SMBH mass, temperature, and density); though, low-luminosity sources, dust obscuration, and host galaxy contamination can impede their utility. Similarly, X-ray observations are challenging to use when the AGN is not very luminous or heavily dust obscured; however, X-rays face little host galaxy contamination. In addition, gamma rays are very reliable tracers of the high energy physics associated with AGNs, particularly those associated with AGN jets; yet, similar to radio waves, they are limited with observations of non-jetted AGNs. Finally, observing variable AGNs (i.e., AGNs that experience cycles of active accretion and quiescence) can help identify low-luminosity AGNs, where the variability stems from the corona, disk, and jet. Major drawbacks to using variability observations, however, are that host galaxy contamination, dust obscuration, cadence, and depth of observation can pose challenges for accurate AGN detection.

1.4 Optical Band AGN Detection

In this dissertation, I focus on the optical band of the EM spectrum. In this wavelength range, the Baldwin-Phillips-Terlevich emission-line ratio diagnostic diagrams (BPT diagrams; [143, 141, 145]) are the most prolific resources used for differentiating gas ionization

sources as star-forming, Seyfert (AGN), low-ionization nuclear emission-line region (LINER), or a composite of multiple ionization sources. They serve as the traditional AGN selection tool for most spectroscopic surveys. These diagrams operate by comparing line ratios between high and low ionization species, most commonly [OIII]λ5007/Hβ vs. [NII]λ6583/Hα ("[NII]/ Hα diagram" hereafter). Note, the optical "[NII]/ Hα diagram" can only be used for $z < 0.5$ galaxies; beyond which, [NII] is redshifted out of the optical band. As outlined in [278], massive stars account for the bulk of emission in star-forming galaxies, which translates to a well-defined upper limit on the intensities of the collisionally excited lines relative to the recombination lines; whereas AGNs feature far more energetic photons that are higher in intensity relative to the recombination lines. To distinguish between these two populations, BPT diagrams often employ two demarcations: 1) the [143] separation between galaxies with an extreme-UV ionizing radiation field dominated by AGN ($> 50\%$) and those powered by star-formation, and 2) the [141] empirical divide between AGN and star-formation sources, based on the location of the Sloan Digital Sky Survey 's (SDSS; [304]) star-forming galaxies. The galaxies between these two lines are referred to as composite galaxies, which may host a star-forming or AGN dominated emission line source. However, the drawback of BPT ionization ratios is that they can often be contaminated by diffuse ionized gas, extraplanar gas, photoionization by hot stars, metallicity, emission from post-AGB stars and star-formation, and shocks. These sources can elevate line flux ratios to be AGN-like, potentially leading to misclassification (e.g., [223, 224, 144, 301]).

On the other hand, one promising, yet still poorly understood avenue for identifying AGNs are coronal emission lines ("CLs"; so named because they were first observed in the solar corona). CLs are highly ionized species of gas with ionization potentials $\geq$ 100 eV (e.g., [NeV], [FeVII], and [FeX]). These lines require extremely high energies for production, above the limit of stellar emission (55 eV; e.g., [113]), may serve as unambiguous tracers for the strong ionizing continuum of AGN, and can provide direct insight into the nature of the host galaxy. Some studies suggest that CLs trace the AGN itself, since they find that

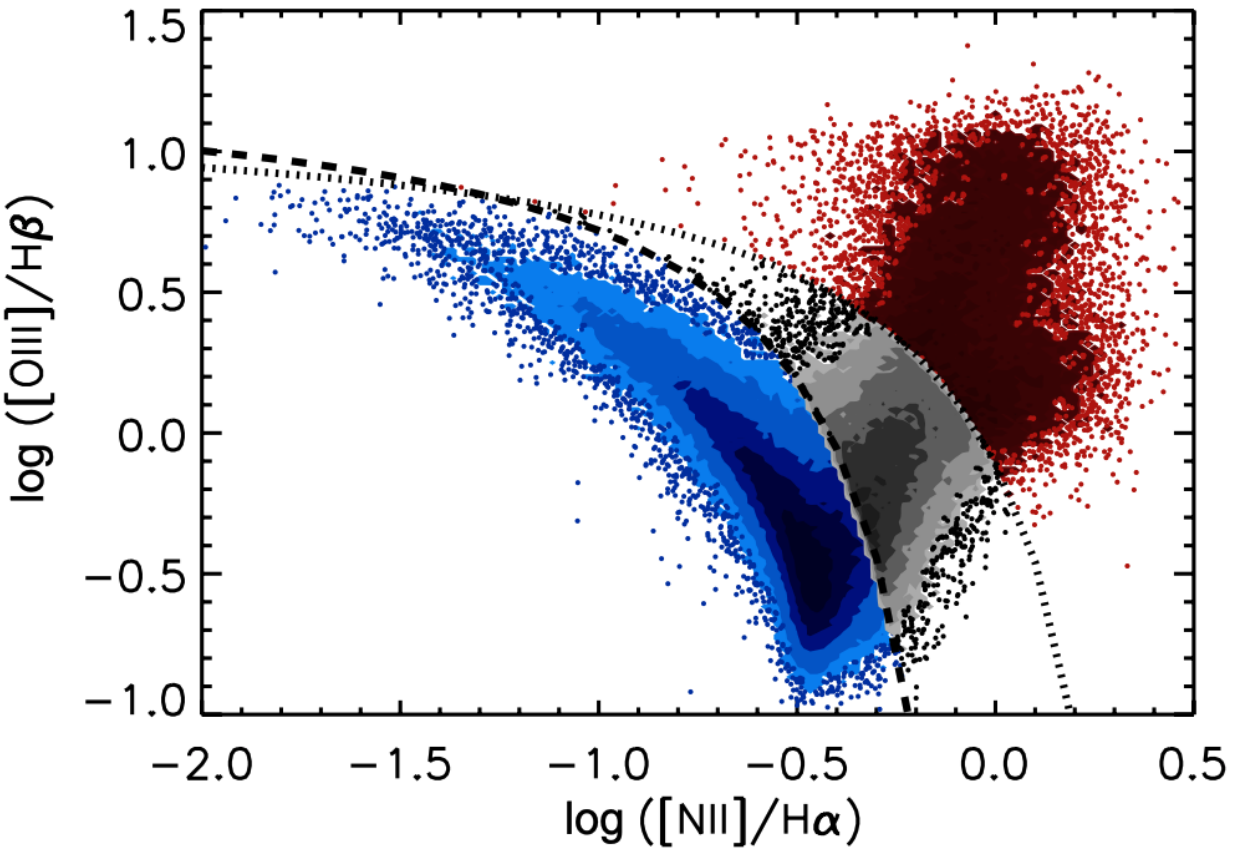

Figure 1.7: A sample log([OIII]/Hβ) vs. log([NII]/Hα) BPT diagram for a population of SDSS galaxies. The dashed curve shows the [141] empirical division between star-forming galaxies and AGNs. The dotted curve shows the [143] theoretical division. The blue points represent star-formation, the red points represent AGNs, and the gray, a composite of the two. Figure from [278].

CLs reside in a distinct zone of extremely hot and collisionally ionized plasma near AGNs (e.g., [232]). Moreover, [246] contend that a single CL with a given luminosity is enough to confirm the presence of an AGN. Using the spectral synthesis code `CLOUDY` ([93]), [246] model a CL emission-line-spectroscopy-spectrum, using precise models of dust, ionizing radiation fields, HII regions, molecular clouds, and densities. They also produce a set of simulated star-formation (i.e., "starburst") and AGN SEDs (Figure 1.8). In the figure, the SED of the starburst SED drops significantly in the UV part of the EM spectrum, producing an insignificant fraction of the total luminosity beyond a few tens of eV. In contrast, the model for the AGN SED, showing the labeled CLs along it, reaches much further than the SED of the starburst model - into the high energy X-ray band. This suggests that CLs strongly correlate with AGN activity.

In addition, the ionization sources of CLs are not yet fully understood because of the small number of CL emitting galaxies that have been studied in the optical band, primarily due to obscuration of the nuclear region (e.g., [105, 66, 244]). In fact, many studies are of a single CL galaxy, and one of the largest optical studies only analyzed ~ 10 CL galaxies ([180]). The authors analyzed the structure and physical properties of CLs using observations from NASA's Space Telescope Imaging Spectrograph/ *Hubble Space Telescope*. Using a sample of 10 pre-selected AGNs, they measured the bulk of CLs to lie within a 10 - 230 parsec radius from the nuclear core and determined that photoionization by the central continuum source (i.e. the AGN) was responsible for their production.

Here, I continue this effort to search for AGNs in the optical band. This is in part because of the extensive physics that can be determined using optical lines, but also due to the availability of the largest integral field unit (IFU) spectroscopic survey of galaxies to date, the SDSS's Mapping Nearby Galaxies at Apache Point Observatory (MaNGA) catalog ([36, 80, 159, 303, 29, 290]), which uses the SDSS 2.5 m telescope [111] at Apache Point Observatory in Sunspot, NM. Moreover, observations began in 2014 and the final data release recently became available, which contains the spectra for 10,010 nearby galaxies (0.01

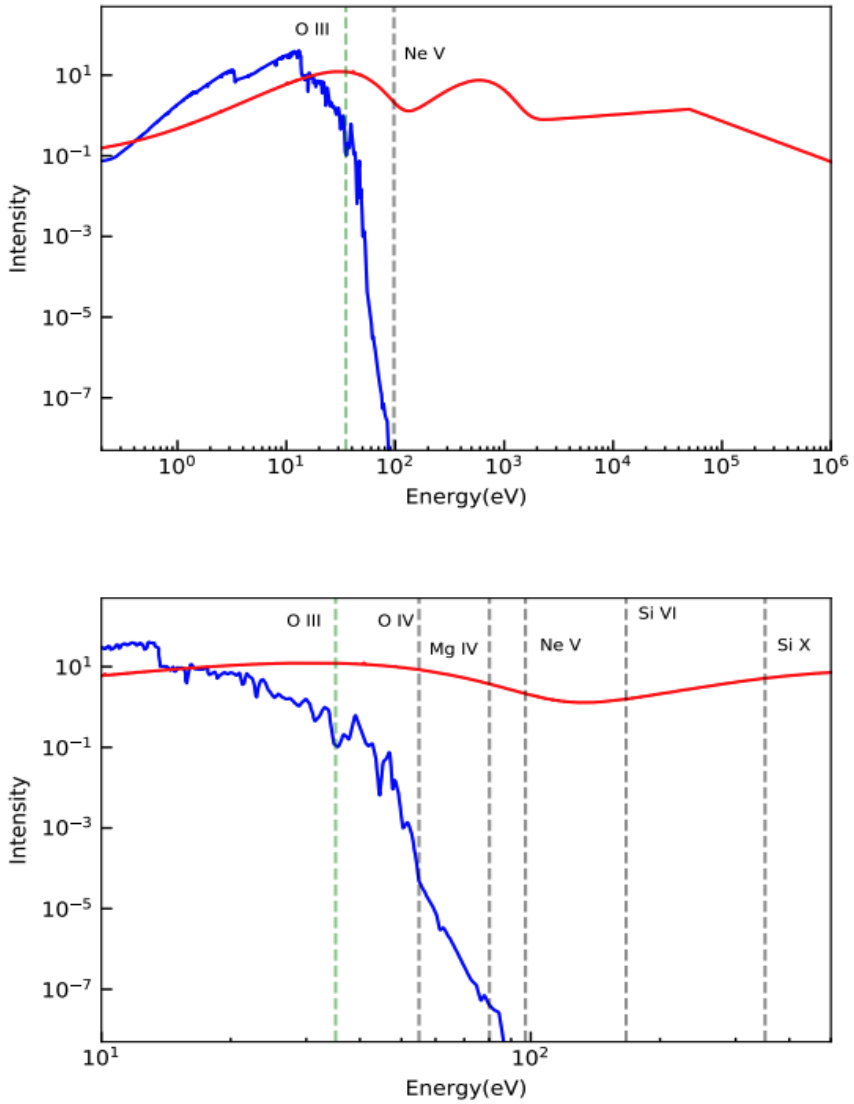

Figure 1.8: Top: starburst (blue) and AGN (red) SED models. The dotted vertical lines indicate the ionization potentials of [OIII] and [NeV] ions. Bottom Panel: Same as above, showing only the UV to soft X-ray component of the SEDs. The dotted vertical lines indicate the ionization potentials of [OIII], [OIV] , [MgIV] , [NeV] , [SiVI] , and [SiX]. In both, the AGN model and the labeled CLs extend well past the starburst model. Figure from [246].

$< z < 0.15$; average $z \approx 0.03$) with stellar mass distributions between 10^9 $M_\odot$ and 10^{12} $M_\odot$. The wavelength range of MaNGA spans 3622 Å - 10354 Å. Further, MaNGA uses IFU fiber-bundles grouped into hexagonal grids to produce spectroscopic maps out to at least 1.5 times the effective radius; the typical galaxy is mapped out to a radius of 15 kiloparsec, and the standard spatial resolution of 1 -2 kiloparsec ([80]). In comparison, previous SDSS surveys (e.g., SDSS-I to SDSS-III; [304, 82]) observed galaxies with small ($3''$ diameter) optical fibers. The resulting spectra only traced a small region close to the galactic center, potentially missing nuclear activity outside of this region.

Moreover, I consider The Unified Model of AGNs ([7, 280]; Figure 1.9). This model details the unique processes, features, and zones associated with AGNs. In this model, a sub parsec rotation dominated accretion disk is shown. In addition, there is the broad line region (BLR) 0.01 - 1 parsec from the SMBH. This is a high density region, with dust-free gas clouds moving at approximately Keplerian velocities $>$ 1,000 km s^{-1}. The distance of these clouds from the SMBH is luminosity dependent. Slightly further out, at 0.1 - 10 parsec, an axis-symmetric dusty torus resides, which features luminosity dependent dimensions. Beyond these regions is a much larger zone known as the narrow line region (NLR). Here, there are lower density and lower velocity ($<$ 1,000 km s^{-1}) ionized gas clouds, compared to the BLR. This region is vast, and extends from just outside the dusty torus to several kiloparsecs from the SMBH. Unlike the BLR, most of the gas in the NLR does contain dust. Finally, central jets are shown, which are often associated with radio wave and gamma ray emission. Further details on The Unified Model can be found in [28, 230, 212, 205].

AGNs can also primarily be categorized as Type I or Type II, depending on the orientation of the AGN and the properties of the emission lines observed for each. Type I are oriented pole-on and are observed to have broad (FWHM $\sim$ 1,000 - 20,000 km s^{-1}) emission lines. They are generally referred to as Seyfert 1 or "quasi-stellar objects". Classifying Type I AGNs, using the broad Hα and broad Hβ lines, for example, is very efficient when the BLR is not strongly dust obscured. On the other hand, Type II are oriented edge-on and

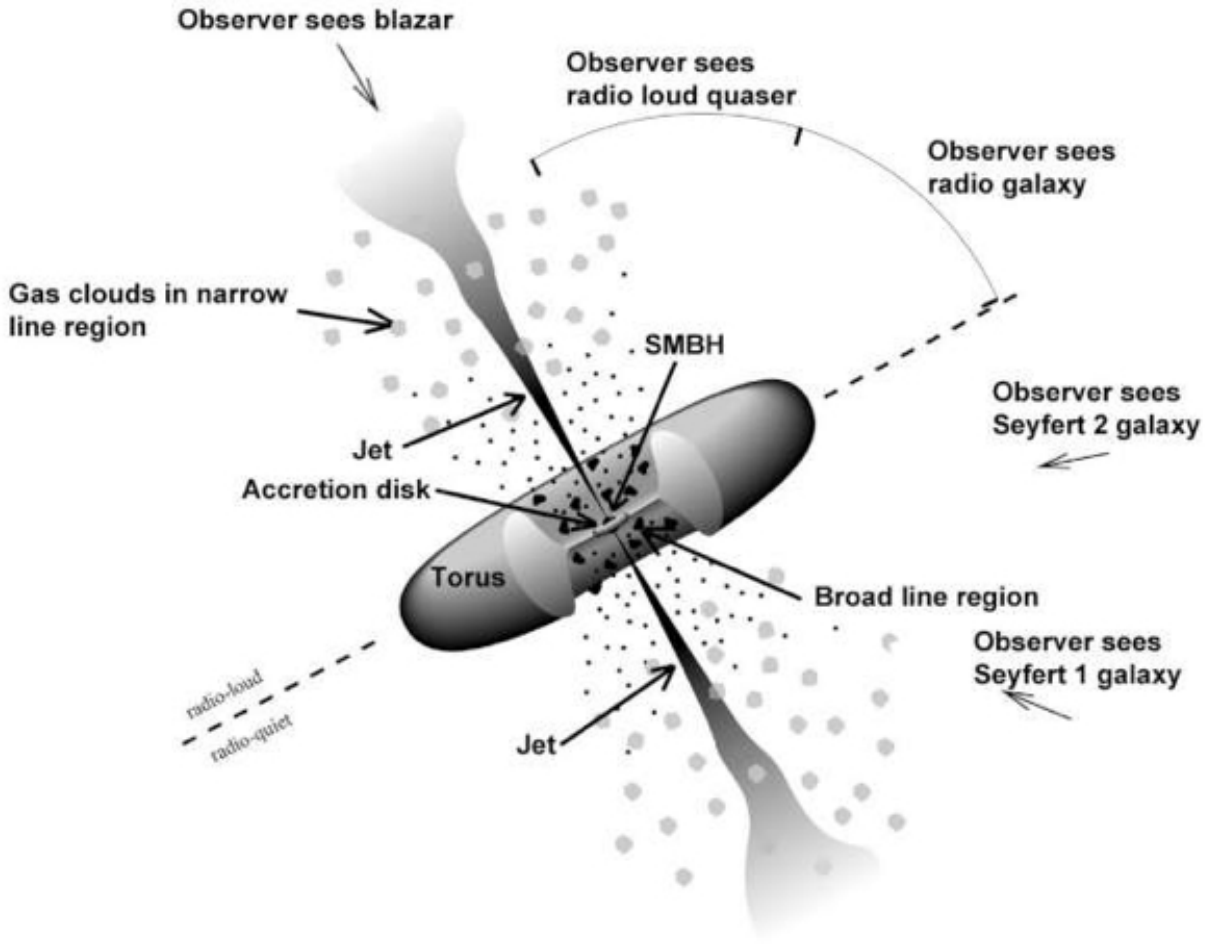

Figure 1.9: The Unified Model of AGNs ([7, 280]). The diagram showcases the fundamental attributes of an AGN, which include a central SMBH, a dusty torus, the BLR, the NLR, and bi-polar jets.

are observed to have narrow (FWHM $\sim$ 300 - 1,000 km s^{-1}) emission lines. However, without complimentary X-ray observations, for example, identifying AGNs using the NLR alone can be challenging. This is because star-formation can also produce strong narrow emission lines. As a result, I focus on the BLR as an additional tool to identify AGNs in MaNGA, in isolation and/or when there is a merging system and one or both of the galaxies features an AGN. I also explore the possibility of using BL detections to identify recoiling SMBHs in merging galaxy systems.

1.5 Dissertation Overview

In this introductory section, I presented an overview of the hierarchical evolution of galaxies, the nature of AGNs and their potential impacts on host galaxy evolution, and several existing AGN selection techniques. I also reviewed the need to refine AGN detections, particularly in the optical band, where dust obscuration and host galaxy contamination can lead to missed or misclassified AGN detections. BPT diagrams, in particular, are traditionally used for differentiating gas ionization sources as star-forming, Seyfert (AGNs), low-ionization nuclear emission-line region (LINER), or a composite of multiple ionization sources. The challenge of solely using BPT diagrams to detect AGNs is due to their line flux ratios often being contaminated by diffuse ionized gas, extraplanar gas, photoionization by hot stars, metallicity, emission from post-AGB stars, star-formation, and shocks, potentially leading to AGN misclassification. As a result, I focus on more accurate optical diagnostics of AGNs, such as CL and BL detections. To do so, I use the SDSS MaNGA catalog, which features IFU spectroscopy to provide spatially resolved galactic spectra for 10,010 unique galaxies, and spans a wavelength range of 3622 Å - 10354 Å.

In Chapters 2 and 3, I delve into my extensive work detecting CLs in MaNGA. These $\geq$ 100 eV emission lines are free of contamination by star-formation and can provide a path for stronger AGN identification, the first step in better comprehending the co-evolution of AGNs and their host galaxies. I create two MaNGA CL catalog versions, using two

different MaNGA data releases (containing 6,263 and 10,010 galaxies, respectively). In Chapter 2, I focus on the initial version of the CL catalog (10 CL galaxies) and evaluate the distances of the CLs from the galactic center, cross-match the sample with existing AGN catalogs, measure the average electron temperatures of the CL gas, and evaluate the ionization mechanism(s) of the CLs. In Chapter 3, I cross-match the final version of the CL catalog (71 CL galaxies) with one of the largest MaNGA AGN catalogs. After, I identify an AGN CL-detection-luminosity dependence and then analyze the role of dust extinction on CL detections.

In Chapter 4, I discuss my work detecting BLs in MaNGA. I present my catalog of BL galaxies (301 broad Hα galaxies and 801 broad Hβ galaxies; 1,042 unique BL galaxies), report the physical parameters of the BLs, and describe the effectiveness of using BLs to find companion AGNs and recoiling black holes. Paired with the CL detections, BL detections can help ensure accurate AGN identification, not only in MaNGA, but in other large-scale spectroscopic surveys of galaxies.

Finally, in Chapter 6, I summarize the conclusions of my dissertation and discuss possible future work. Specifically, I focus on multi-wavelength observations and the collective effort required to achieve unambiguous AGN detections, and to unravel the role of AGNs in their host galaxies.

Chapter 2

The Physics of the Coronal Line Region for Galaxies in MaNGA

This chapter was published in The Astrophysical Journal ([191]).

2.1 Introduction

An Active Galactic Nucleus (AGN), fueled by accretion onto its central supermassive black hole (SMBH; $M_{\rm BH} > 10^6 M_\odot$), is one of the most energetic phenomena in the observable universe; it can generate a bolometric luminosity $> 10^{48}$ erg s^{-1}, which can outshine the collective light of an entire host galaxy. The most powerful can also heat and photoionize gas tens of kpc away (e.g., [118, 181, 142, 164, 48]).

Moreover, feedback - the mechanism by which AGN processes (e.g., photoionization, radio jets, and winds) impact nearby matter - has been shown to influence the evolution of the host galaxy (e.g., [87, 134, 135, 237]). On one hand, AGN feedback may quench star formation and limit the host galaxy's growth (e.g., [126]). On the other, AGN feedback can impart extreme pressure on the neighboring interstellar medium and generate high density conditions favorable for star formation (e.g., [256]).

To unravel the dynamics of AGN-galactic co-evolution, reliable AGN identification is an essential first step. To address this, we consider the Unified Model of AGNs [7]. In this framework, an AGN is classified as either Type I or Type II. Type I are viewed pole-on and are observed to have broad (FWHM $>$ 1,000 km s^{-1}) and narrow (FWHM $<$ 1,000 km s^{-1}) emission lines, whereas Type II are viewed edge-on and are observed to only have narrow

emission lines. The physical structures that correspond to these regions are the broad line region (BLR) and the narrow line region (NLR), respectively.

The NLR is the largest observable structure in the UV, optical, and near-IR that is directly impacted by the ionizing radiation from an AGN. Measurements from a *Hubble Space Telescope* snapshot survey, in addition to ground based [OIII] observations, suggest this region extends hundreds of parsec (pc) to several kiloparsec (kpc) from the nuclear core (e.g., [186, 249, 188]). However, the NLR surrounding an AGN may feature active star formation, which can also produce narrow lines (e.g., [NII] λ6584 and [OIII] λ5007; see [242]). As a result, the NLR is not always an ideal tracer for exclusive AGN activity.

Comparatively, the BLR resides much closer to the SMBH (within $\sim$ 0.1 kpc; e.g., [158, 60]). The enhanced cloud velocities found in this region, near the accreting SMBH, provide reliable signatures for nuclear AGN activity. However, the BLR is not often spatially resolved in most existing spectroscopic surveys. Further, for Type II AGN, the BLR is often obscured by a dusty torus that can attenuate optical and UV emission (e.g., [122]).

For most AGNs, though, highly ionized species of gas with ionization potentials (IPs) $\gtrsim$ 100 eV (termed "coronal lines"; CLs; e.g., [FeVII] and [NeV]) are proposed to exist in the nuclear region between the compact BLR and the more extensive NLR (e.g., [252, 104]). These lines require extremely high energies for production, above the limit of stellar emission (55 eV; [113]), likely trace the strong ionizing continuum of an AGN [252], and have been linked to AGN-driven outflows (e.g., [188, 179, 234, 41]). As a result, detecting CLs may help identify AGNs and AGN-driven outflows in large spectroscopic galactic surveys, which are essential for understanding the influence of AGN feedback on the host galaxy.

CLs have been observed in the spectra of some AGNs; however, their nature and physical extent are still not very well understood (e.g., [210, 201, 215, 188]). Prior studies (e.g., [232]) suggest that they reside in a distinct zone of extremely hot and collisionally ionized plasma between the BLR and the NLR, in the coronal line region (CLR). Further, [180] analyzed the structure and physical properties of the CLR for 10 pre-selected AGNs.

They used the *Hubble Space Telescope*/Space Telescope Imaging Spectrograph to study [NeV] λ3427, [FeVII] λ3586, λ3760, λ6086, [FeX] λ6374, [FeXIV] λ5303, [FeXI] λ7892, and [SXII] λ7611 emission in their sample. They determined that the CLR extends between 10 - 230 pc from the nuclear core (similar to [188] and [228]). They also measured CLR electron temperatures to vary between 10,000 K - 20,000 K (below the pure AGN photoionization threshold of $\sim$ 20,000 K) and compared the ionization properties of the CLR to varying photoionization and shock models (e.g., [26, 79]). They concluded that AGN photoionization from a central source is the sole physical mechanism producing the lines in their sample. Moreover, [99] scanned the sixth Sloan Digital Sky Survey (SDSS) data release ([3]) and investigated the CLR in 63 AGNs with [FeX] λ6374 emission (IP = 233.60 eV), without an a priori assumption that emission would only be found in AGNs. They also studied [FeXI] λ7892 (IP = 262.10 eV) and [FeVII] λ6086 (IP = 99.10 eV) emission in these AGNs. They determined that photoionization is also the source of the CLs (inferred using X-ray observations from *Rosat*; [288, 287]). The authors then measured the extent of the CL emitting clouds in their sample and found that the lines with higher IPs (e.g., [FeX] and [FeXI]) feature larger FWHM values, consistent with the lines occupying a region closest to the BLR, at a scale comparable to the dusty torus. They determined that the lower IP [FeVII]-emitting regions feature narrower lines and likely merge with the traditional NLR.

Here, we use the SDSS's Mapping Nearby Galaxies at Apache Point Observatory (MaNGA) integral field unit (IFU) catalog, from the survey's fifteenth data release in its the fourth phase (SDSS-IV), to further evaluate the ionization mechanism(s) of the CLR and to better understand the relationship between CLs and AGN activity. Large IFU spectroscopic surveys are critical for studying CLs because they provide spatially resolved galactic spectra that can trace the full extent of the CLR. Additionally, MaNGA has observed 10,010 nearby galaxies, and the eighth data release of the catalog contains 6,263 unique galaxies, making it one of the largest IFU survey of galaxies currently available. With our custom pipeline, we detect 10 galaxies with emission from one or more CLs detected at $\geq 5\sigma$ above the con-

tinuum in at least 10 spaxels ($\sim 0.16\%$ of the sample), which makes it the most extensive such catalog of MaNGA CL galaxies to date.

This paper is outlined as follows: Section 2.2 details the technical components of the SDSS-IV MaNGA survey and its data pipeline, Section 2.3 describes the methodology we use to build the CL catalog and to analyze the physical properties of the CLR, Section 2.4 reviews our results, Section 2.5 provides interpretations of our findings, and Section 2.6 includes our conclusions and intended future work. All wavelengths are provided in vacuum and we assume a ΛCDM cosmology with the following values: $\Omega_M = 0.287$, $\Omega_\Lambda = 0.713$ and $H_0 = 69.3$ km s^{-1} Mpc^{-1}.

2.2 Observations

2.2.1 The MaNGA Survey

To conduct our analysis, we utilize the largest IFU spectroscopic survey of galaxies to date, the SDSS-IV MaNGA catalog [36, 80, 159, 303, 29, 290]. MaNGA began taking data in 2014 using the SDSS 2.5 m telescope [111], and has logged the spectra for 10,010 nearby galaxies ($0.01 < z < 0.15$; average $z \approx 0.03$) with stellar mass distributions between 10^9 $M_\odot$ and 10^{12} $M_\odot$. The spectra were taken at wavelengths between 3622 Å - 10354 Å, with a typical spectral resolution of ~ 2000 and a velocity resolution of 72 km s^{-1} (see [36]).

MaNGA relies upon dithered observations using IFU fiber-bundles, assembled individually from the Baryon Oscillation Spectroscopic Survey Spectrograph [259]. The IFUs are grouped into hexagonal grids with field-of-view (FoV) diameters between 12.″5 to 32.″5 - each distribution is matched to the apparent size of the target galaxy [36]. The exact configuration of the fiber-fed system consists of two 19-fiber IFUs (12.″5 FoV), four 37-fiber IFUs (17.″5 FoV), four 61-fiber IFUs (22.″5 FoV), two 91-fiber IFUs (27.″5 FoV), and five 127-fiber IFUs (32.″5 FoV). The resulting pluggable science and calibration IFUs generate galactic spectroscopic maps out to at least 1.5 times the effective radius; the typical galaxy is mapped out to a radius of 15 kpc. Each MaNGA spatial pixel, or spaxel, covers 0.″5 $\times$

0.″5 and the average full-width half maximum (FWHM) of the on-sky point spread function (PSF) is 2.″5, which corresponds to a typical spatial resolution of 1 -2 kpc [80].

2.2.2 MaNGA Data Reduction Pipeline

The MaNGA Data Reduction Pipeline (DRP) generates flux calibrated and sky-subtracted data for each galaxy in a FITS file format that is used for scientific analysis [159]. The resulting DRP data product is run through MaNGA's Data Analysis Pipeline (DAP; [294]) that provides spectral modeling and science data products, such as stellar kinematics (velocity and velocity dispersion), emission-line properties (kinematics, fluxes, and equivalent widths), and spectral indices (e.g., D4000 and Lick indices). The data products are publicly released periodically as MaNGA Product Launches (MPLs).

To construct our catalog of CL galaxies in MaNGA, we use MaNGA's eighth data release (MPL-8), which contains data for 6,263 unique galaxies.

2.3 Analysis

2.3.1 Spectral Fitting

The MaNGA DAP provides fits for prominent emission lines (e.g., the narrow components of Hα, Hβ, and [OIII] λ5007). However, it does not offer fits for the CLs of interest in this chapter (Table 2.1), which we select due to their high ionization potentials ($\gtrsim$ 100 eV), their presence within the wavelength range of MaNGA, and for comparison with prior CLR studies that featured these lines (e.g., [150, 8, 201, 235, 187, 180, 236]). As a result, we construct a custom pipeline to scan for [NeV] $\lambda\lambda$3347, 3427, [FeVII] $\lambda\lambda\lambda$3586, 3760, 6086, and [FeX] λ6374 emission at $\geq 5\sigma$ above the background continuum in the 6,623 galaxies in MPL-8. We use this high 5σ threshold to ensure we identify unambiguous CL emission.

We first access the DRP to extract the necessary data cubes for each MaNGA galaxy. The data cubes provide a spectrum for each individual spaxel across the FoV of each galaxy

(spaxel arrays vary between 32 × 32 spaxels to 72 × 72 spaxels, depending on IFU configuration). We then use the spectroscopic redshifts of each galaxy, adopted from the NASA Sloan Atlas catalogs using single-fiber measurements [30], to shift the spectra to rest vacuum wavelengths and to impose a minimum redshift threshold ($z_{\rm min}$) for CLs near the lower wavelength limit of MaNGA (3622 Å; Table 2.1). In some instances, CL rest wavelengths are redshifted out of MaNGA's spectral range.

Once the spectra are wavelength corrected, we analyze each individual spaxel for each galaxy and perform a polynomial fit on a narrow spectral region, $\sim$ 300 Å wide, of continuum near the CL to model the background stellar continuum and subtract it. We then attempt a single Gaussian fit on a $\sim$ 30 Å region centered on the rest wavelengths of the CLs. This wavelength range was shown to sufficiently capture the full extent of CL emission in our preliminary scans, even for CLs with FWHM $>$ 1,000 km s^{-1}. We subsequently determine the root mean square (RMS) flux of two continuum regions ($\sim$ 60 Å wide) that neighbor each target CL, free of absorption or emission lines, and require that CL amplitudes are detected at $\geq 5\sigma$ above the mean RMS flux values in these continuum regions. We consider the spectral resolution of MaNGA (R = $\lambda/\Delta\lambda \sim$ 1400 at 3600 Å; R $\sim$ 2000 at 6000 Å; [259]) to eliminate fits with $\Delta\lambda <$ 2.4 Å (for [NeV] $\lambda\lambda$3347, 3427), $<$ 2.6 Å (for [FeVII] $\lambda\lambda$3586, 3760), and $<$ 3 Å (for [FeVII] λ6086 and [FeX] λ6374; we do not detect the [FeX] λ6374 line using this criteria). We also require that each galaxy in our catalog features $>$ 10 CL-emitting spaxels to ensure we are detecting sources with definitive CL emission. We show an example of a single Gaussian fit for the [FeVII] λ3760 line in Figure 2.1.

2.3.2 Coronal Line Flux Maps

We use flux maps to trace the strength and distribution of the CLs in the CLR. To generate these maps, we use the integrated CL flux value from each spaxel for each CL galaxy. We show an example flux map in Figure 2.2.

For each MaNGA observation, the photometric center corresponds to the galactic center

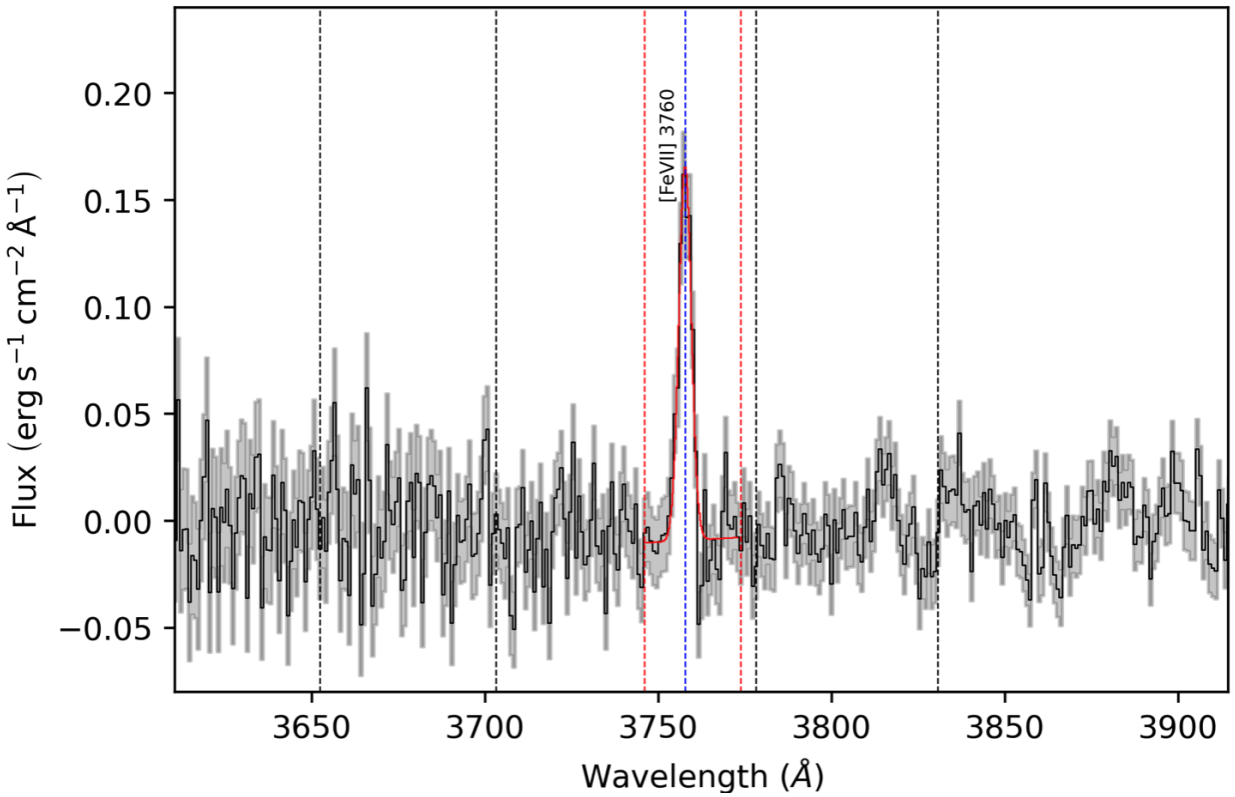

Figure 2.1: A sample spectrum from an individual spaxel showing the [FeVII] λ3760 line detected at $\geq 5\sigma$ above the continuum in J1349. The solid black line is the continuum subtracted spectrum, the shaded gray region is the uncertainty, the solid red line represents the best fit, the red dotted vertical lines mark the fitting window, the blue dotted line signifies the rest wavelength of the [FeVII] λ3760 line, and the two sets of black dotted vertical lines correspond to the neighboring continuum windows where the RMS flux values of the continuum are calculated.

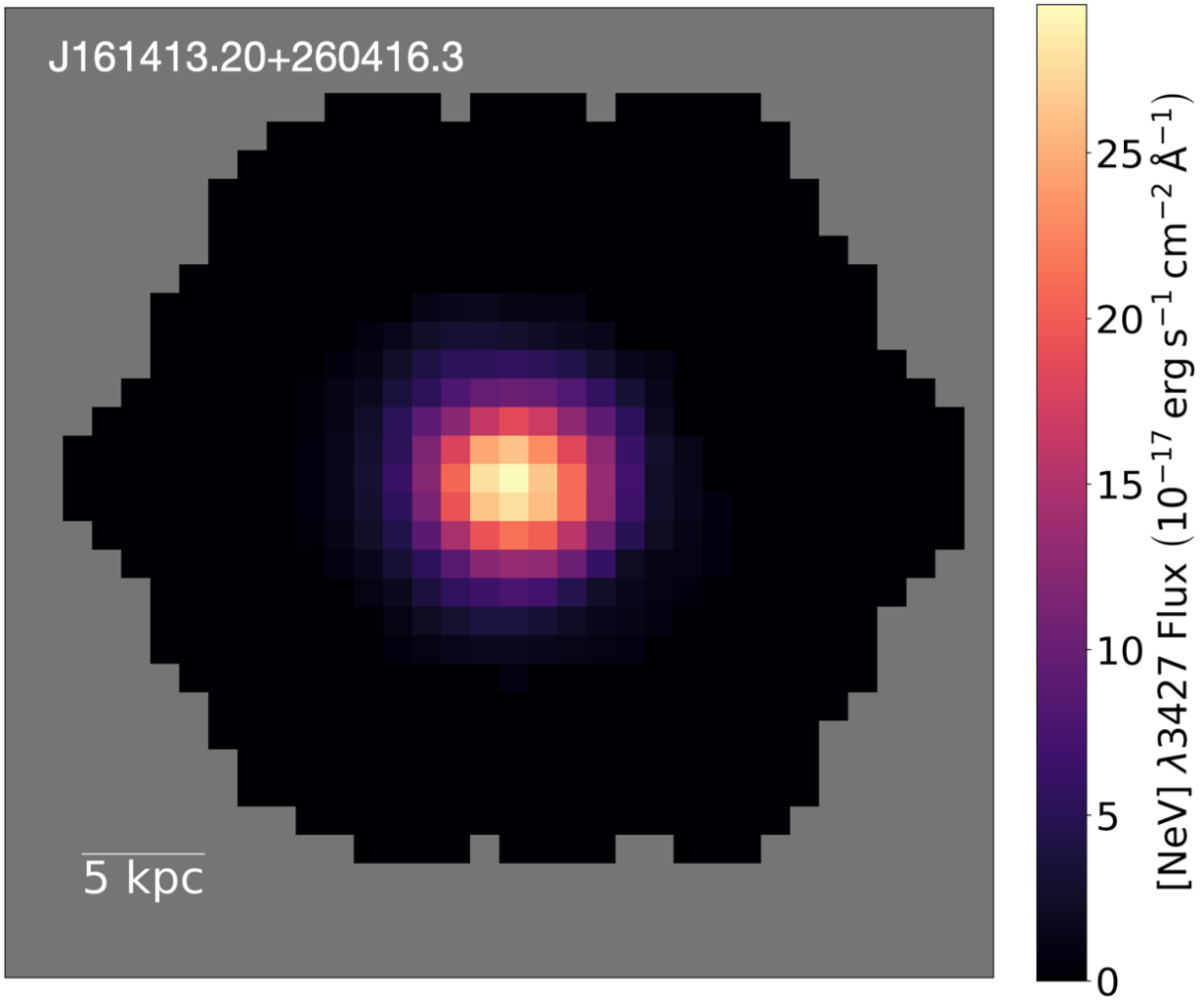

Figure 2.2: A sample CL flux map showing [NeV] λ3427 emission detected $\geq 5\sigma$ above the continuum in J1614. For this galaxy, the strongest [NeV] λ3427 emission is located near the center of the galaxy. The gray region is outside of the MaNGA FoV.

Table 2.1: Target CLs

Emission Line	Wavelength (Å)	IP (eV)	$z_{\min}$
[NeV]	3347	126.22	0.088
[NeV]	3427	126.22	0.063
[FeVII]	3586	125.0	0.016
[FeVII]	3760	125.0	-
[FeVII]	6086	125.0	-
[FeX]	6374	262.1	-

Note: Columns are (1) emission line, (2) rest wavelength, (3) ionization potential, and (4), minimum redshift value required for MaNGA detection.

([303]). We use this position and the galaxy's inclination angle to determine the de-projected galactocentric distance of each CL spaxel. The MaNGA DAP provides the ratio of the semi-minor to semi-major axes (b/a) for each galaxy, and we use this value to determine the cosine of each galaxy's inclination angle (i): cos(i)= b/a. The de-projected distance of each CL spaxel to the center of the galaxy is then measured by:

$$D_{\text{Spaxel}} = \sqrt{(x - x_{\text{center}})^2 + \big((y - y_{\text{center}}) * \cos(\text{i})\big)^2} \tag{2.1}$$

Next, we convert the spaxel distances to a physical unit (kpc) using the `astropy.cosmology` `Python` package. The resulting value corresponds to the distance of each CL emitting spaxel, and the coronal line distance (CLD) corresponds to the distance of each galaxy's most extended CL-emitting spaxel (from the galactic center).

2.3.3 Coronal Line Intensity Profiles

We explore CL intensity as a function of de-projected galactocentric distance to help determine the ionization mechanism(s) producing the CLs. We consider the study conducted by [302], which analyzed ionization sources in galaxies with spatially extended emission line regions. The authors measured integrated flux profiles for a system of ionizing sources and found that the strength of ionizing flux, as a function of galactocentric distance, should

decay with a power law index of α = -2 (i.e. obey the inverse square law) for pure AGN photoionization. They used this model to differentiate AGN photoionization from other sources (e.g., shocks). [274] also used this model to show that jet-induced shocks primarily ionize extended emission line regions along the axis of radio jets for several AGNs, and that AGN photoionization dominates within the nuclear regions. We fit a power law for each CL galaxy, and measure the best-fit power law index to help determine the ionization source(s) for the CLs. We present a sample power-law fit in Figure 2.3.

2.3.4 Stellar Shock Diagnostics

We consider the role of supernova remnant (SNR) shocks in our analysis to determine their role in the production of CL emission. The first SNR identified in an external galaxy was observed by [177, 178]. The authors relied upon the strength of the [SII] $\lambda\lambda$6717, 6731 doublet with respect to the Hα line to differentiate SNR shocks from photoionized regions. [71] and [73] refined this relation empirically, and determined that regions with [SII] $(\lambda6717 + \lambda6731)/\text{H}\alpha > 0.4$ feature SNR shocks. The use of this threshold is widely adopted to identify SNRs (e.g., [218, 78, 163, 27, 162]), and we employ it in our analysis. For each CL galaxy, we also divide the number of CL-emitting spaxels that feature SNRs by the total number of CL-emitting spaxels. The resulting value is the fraction of SNRs in each galaxy's CLR ("SNR Frac" in Table 2.2). We calculate this parameter to determine if elevated fractions of SNRs correspond to enhanced CL production, which would suggest that SNR shocks play a major role in the production of CLs. The MaNGA DAP provides flux measurements for the [SII] λ6717, [SII] λ6731, and Hα lines.

2.3.5 Electron Temperature and Electron Number Density Diagnostics

The electron temperatures and electron number densities of emission line regions provide direct insight into their ionization source(s). Specifically, temperatures between 10,000 K - 20,000 K are typical for photoionization equilibrium, as opposed to collisional shocks,

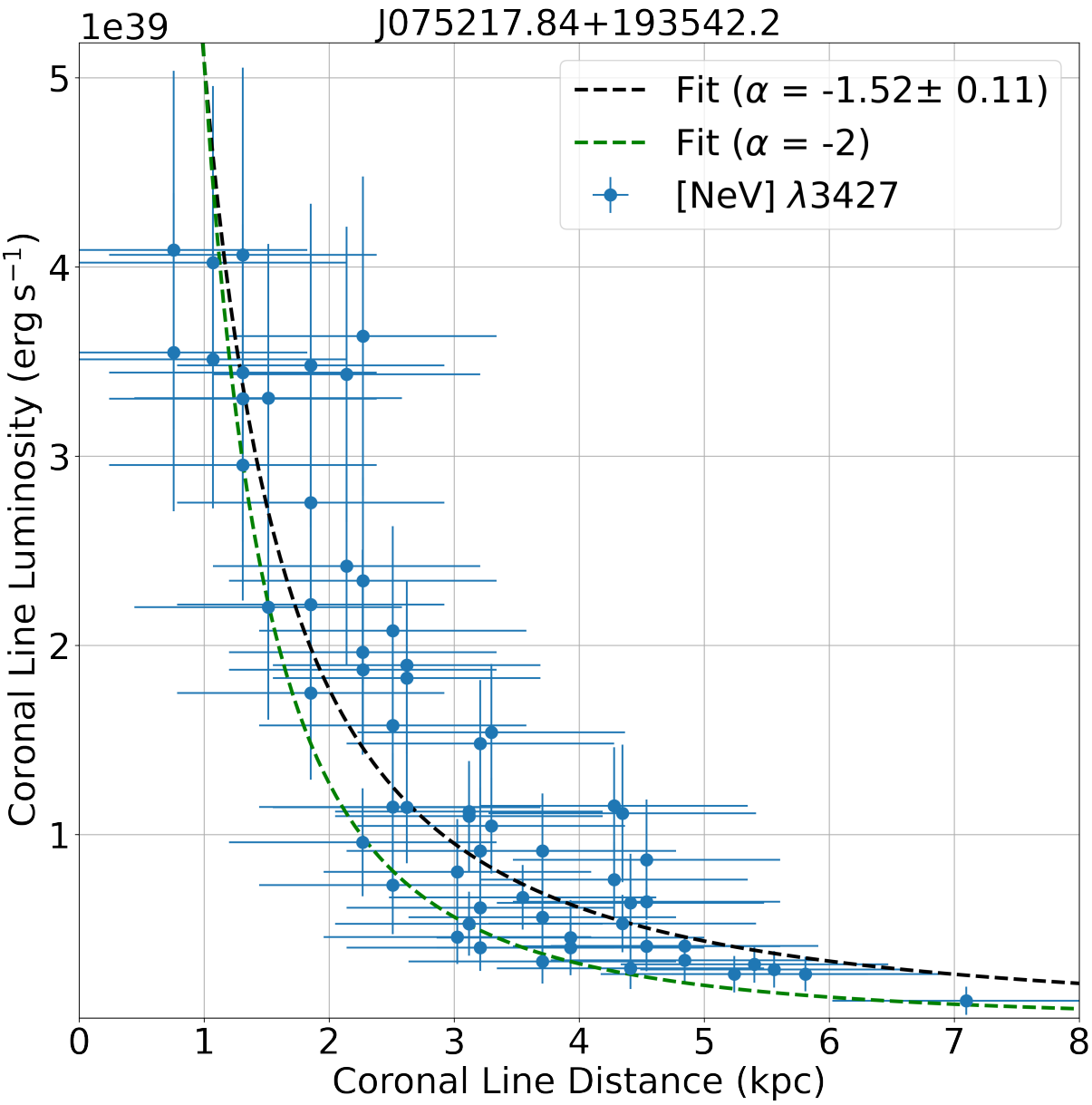

Figure 2.3: A sample plot of CL luminosity vs. de-projected galactocentric distance for the [NeV] λ3427 emitting spaxels in J0752. The black curve is the measured power-law fit for the data ($\alpha = -1.52$). The green curve is the model fit ($\alpha = -2$) for pure AGN photoionization.

for example, which can induce temperatures up to 10^6 K (e.g., [204]). Furthermore, number densities on the order of $n_e \approx 10^2$ - 10^4 cm^{-3} are typical of the NLR; $n_e > 10^9$ cm^{-3} for the BLR (e.g., [152]).

We measure these parameters for the CL galaxies in our sample using Pyneb, a `Python` package that evolved from the `IRAF` package `Nebular` [253, 168]. `Pyneb's` **getCrossTemDen** routine iterates over the temperature sensitive flux ratio [OIII] (λ5007 + λ4959)/λ4363 and the density sensitive flux ratio [SII] λ6717/ λ6731 to provide self-consistent temperature and density values. For intermediate densities ($n_e \approx 10^3$ cm^{-3}), which are found beyond the BLR:

$$\frac{j_{\lambda 6717}}{j_{\lambda 6731}} \propto \frac{n_e}{n_e^2} \propto n_e^{-1} \tag{2.2}$$

where j is the emissivity of each line and n_e is the electron number density. For the temperature sensitive ratio:

$$\frac{F(\lambda 4959 + \lambda 5007)}{F(\lambda 4363)} \approx \frac{7.33 \exp\left(3.29 \times 10^4 / T_e\right)}{1 + 4.5 \times 10^{-4}\, n_e\, T_e^{-\frac{1}{2}}} \tag{2.3}$$

where F is the flux of each line and T_e is the electron temperature.

We measure these line ratios for each CL emitting spaxel and use **getCrossTemDen** to determine the CLR temperatures and densities in our sample. The MaNGA DAP provides flux values for the [OIII] λ4959, [OIII] λ5007, [SII] λ6717, and [SII] λ6731 lines. However, it does not provide flux values for the [OIII] λ4363 line. We thus modify our spectral fitting routine outlined in Section 2.3.1 to measure [OIII] λ4363 in the CL emitting spaxels, if present. We note that the [OIII] λ4363 line is often blended with the Hγ line; as a result, we use a double Gaussian fit, where appropriate, to isolate [OIII] λ4363 emission. We show an example of a double Gaussian fit on the Hγ and [OIII] λ4363 lines in Appendix A.

2.3.6 Galaxy Morphology

To determine the morphological diversity of our sample and to uncover the link, if any, between CL emission and galaxy type, we use the MaNGA Morphologies from Galaxy

Zoo value-added catalog, which features data from Galaxy Zoo 2 (GZ2; [297]). GZ2 is a citizen science campaign with more than 16 million visual morphological classifications for $>$ 304,000 galaxies in SDSS.

We use the weighted vote fraction (outlined in [297]), which accounts for voter consistency, to identify CL galaxies as either elliptical ("smooth"; "E" in Table 2.2) or spiral ("features or disks"; "S" in Table 2.2). We also use this fraction to determine if a CL galaxy is in the process of merging ("m" in Table 2.2). We require a weighted vote fraction $\geq 50\%$ for each morphological classification. 4/10 CL galaxies in our sample do not have a GZ2 morphological classification and their morphologies are not apparent from a visual inspection (labeled '-' in Table 2.2).

2.3.7 AGN Bolometric Luminosity

Fueled by the accretion of gas onto supermassive black holes, AGNs emit their energy across the entire electromagnetic spectrum. The AGN bolometric luminosity can thus be a useful gauge for tracing the strength of their emission. If the bulk of CL emission is powered by AGN activity, we anticipate that the AGN bolometric luminosities of the CL galaxies will scale with their CL luminosities.

We determine the AGN bolometric luminosity for each CL-emitting spaxel using the [OIII] λ5007 flux values provided by the MaNGA DAP, and the procedure outlined in [209], which assumes [OIII] λ5007 emission comes from the AGN:

$$\log\left(\frac{\mathrm{L_{bol}}}{\mathrm{ergs^{-1}}}\right) = (0.5617 \pm 0.0978)\log\left(\frac{\mathrm{L_{[OIII]}}}{\mathrm{ergs^{-1}}}\right) + (21.186 \pm 4.164) \tag{2.4}$$

2.4 Results

In this section, we review the strength and spatial distribution of the CLs in our sample, investigate the role of SNR shocks in the production of the CLs, and present electron

temperature, electron density, and AGN bolometric luminosity measurements for the CLR. We then compare our sample with the largest existing MaNGA AGN catalog to determine if CL emission is unambiguously linked to AGN activity. Finally, we cross-match our sample with three existing MaNGA BPT AGN catalogs to help uncover if CLs can help identify AGNs in large spectroscopic surveys.

Overall, we detect 10 CL galaxies in our scan of MaNGA's MPL-8 (0.16% of the catalog) with CL emission detected at $\geq 5\sigma$ above the continuum in > 10 spaxels. This detection rate suggests that we will identify ~ 16 CL galaxies in the full survey of 10,010 galaxies. We provide the entire sample of CL galaxies in Table 2.2.

We measure the CLR to extend between 1.3 - 23 kpc from the galactic center, with an average distance of 6.6 kpc (distances traditionally associated with the NLR). In Appendix B, we present each CL galaxy's [OIII] λ5007 flux map to demonstrate the similar physical scales (several kpc) of the CLR and NLR.

Further, to ensure that CL emission is sufficiently resolved for each CL galaxy, we investigate the instrument PSF ($\sim 2.''5$ for MaNGA). We determine that the PSF for our sample varies between 536 pc to 3.2 kpc, with an average PSF of 1.7 kpc. 6/10 CL galaxies show well resolved and continuous emission beyond the instrument PSF. The remaining four CL galaxies, J0752 ([NeV] λ3427), J1535 ([FeVII] λ6086), J1714 ([NeV] λ3347), and J2051 ([NeV] λ3427) lack continuous CL emission within a $2.''5$ x $2.''5$ FoV. As a result, we consider the CLRs within these galaxies to be slightly below the instrument PSF, and not spatially resolved in our analysis. The CL emission in these galaxies may indeed still be spatially resolved (e.g., CL emission may be oriented along an ionization cone); however, we reason that the CLDs we present for these galaxies are upper estimates.

Table 2.2: MaNGA CL Galaxies

SDSS Name (1)	Redshift (z) (2)	Mor. (3)	Detected CL (4)	L_{Bol} (10^{44} erg s^{-1}) (5)	L_{CL} (10^{40} erg s^{-1}) (6)	CLD (kpc) (7)	SNR Frac (8)	α (9)
J073623.13+392617.7	0.12	-	[NeV] λ3427	21.5±0.1	5.2±0.4	5.4±1.1	-	-0.6±0.1
J075217.84+193542.2	0.12	-	[NeV] λ3427	49.0±0.2	9.8±0.4	7.1±1.1	1.0	-1.5±0.1
J090659.46+204810.0	0.11	S(m)	[FeVII] λ3586	4.9±0.1	3.70±0.03	10.0±1.0	0.36	-0.46±0.04
J134918.20+240544.9	0.02	-	[FeVII] λ3760	18.4±0.1	7.20±0.01	7.0±0.2	0.38	-0.84±0.03
J145420.10+470022.3	0.13	E(m)	[FeVII] λ3760	0.75±0.09	2.30±0.02	23.0±1.1	0.5	0.2±0.1
J153552.40+575409.4	0.03	E	[FeVII] λ6086	7.76±0.04	0.23±0.01	1.3±0.3	-	-1.3±0.2
J161413.20+260416.3	0.13	-	[NeV] λ3347	78.6±0.3	5.7±0.3	5.9±1.2	-	-0.6±0.1
J161413.20+260416.3	-	-	[NeV] λ3427	126.0±0.3	23.0±0.3	8.3±1.2	-	-1.2±0.1
J171411.63+575834.0	0.09	E	[NeV] λ3347	5.5±0.1	0.95±0.10	4.3±0.9	-	-0.9±0.2
J171411.63+575834.0	-	-	[NeV] λ3427	9.7±0.1	5.5±0.1	3.7±0.9	-	-0.9±0.1
J205141.54+005135.4	0.11	S	[NeV] λ3427	4.3±0.1	0.75±0.03	2.5±1.0	-	-0.6±0.1
J211646.34+110237.4	0.08	S	[NeV] λ3427	41.4±0.1	3.1±0.1	4.3±0.8	1.0	-1.2±0.1

Note: Columns are (1) CL galaxy SDSS name, (2) redshift from the NASA Sloan Atlas catalogs using single-fiber measurements [30], (3) Galaxy Zoo 2 morphology (if available), (4) detected CL in the galaxy, (5) AGN bolometric luminosity estimated from [OIII] measurements ([209]), (6) CL luminosity measured in this work, (7) galactocentric distance of the most extended CL-emitting spaxel, (8) fraction of SNRs in the CLR (if available), and (9) slope of the CL intensity profile.

2.4.1 The Strength and Distribution of the CLs

Extended emission line regions (1 kpc to 100 kpc from the galactic center) surrounding AGNs are expected to feature a variety of ionization mechanisms, which include photoionization and shocks (e.g., [274]). To determine the role that these ionization sources play in the production of CLs, we explore the strength and distribution of the CLs.

2.4.1.1 [NeV] $\lambda\lambda$3347, 3427

The [NeV] λ3347 line is produced from the same excitation level as [NeV] λ3427, but its relative flux $\big(100 \times$ CL Flux/Flux (Lyα); based on a composite quasar spectrum from [283]$\big)$ is 0.118 $\pm$ 0.008, approximately one-third of the [NeV] λ3427 line (0.405 $\pm$ 0.012; [283]). As a result, we expect to detect the stronger [NeV] λ3427 line in a higher fraction of MaNGA galaxies, which we do.

We measure [NeV] λ3427 emission in six galaxies from MPL-8: J1614, J1714, J0736, J0752, J2051, and J2116. In two of these galaxies, J1614 and J1714, we also measure [NeV] λ3347 emission. We present [NeV] $\lambda\lambda$3347, 3427 flux maps for J1614 (z = 0.13; no GZ2 classification) and J1714 (z = 0.09; elliptical) in Figure 2.4. For J1614, we identify extended [NeV] λ3347 emission out to 5.9 $\pm$ 2.9 kpc from the galactic center; 8.3 $\pm$ 3.9 kpc for [NeV] λ3427. For J1714, we measure [NeV] λ3347 emission out to 4.3 $\pm$ 2.2 kpc from the galactic center; 3.7 $\pm$ 2.2 kpc for [NeV] λ3427. We show the [NeV] λ3427 flux maps for J0736 (z = 0.12; no GZ2 classification; CLD = 5.4 $\pm$ 2.7 kpc), J0752 (z = 0.12; no GZ2 classification; CLD = 7.1 $\pm$ 2.7), J2051 (z = 0.11; spiral; CLD = 2.5 $\pm$ 2.5 kpc), and J2116 (z = 0.08; spiral; CLD = 4.3 $\pm$ 1.9 kpc) in Figure 2.5. In each galaxy, [NeV] $\lambda\lambda$3347, 3427 emission is predominantly concentrated within the galactic interior (within 2.″5 throughout the paper), suggesting that a central source governs CL production in these galaxies. We cross-match these galaxies with the largest existing MaNGA AGN catalog ("MaNGA AGN catalog"; [52]; AGN classifications determined using *WISE* mid-infrared color cuts, *Swift*/BAT hard X-ray

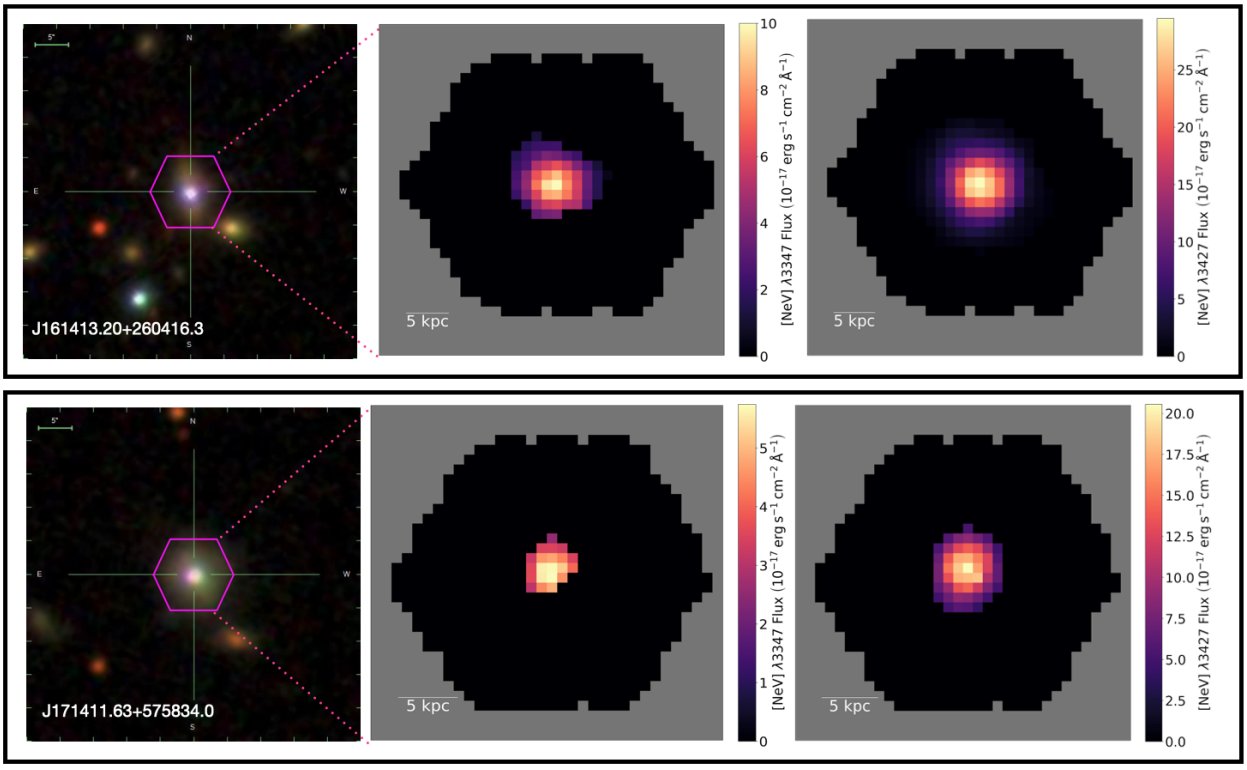

Figure 2.4: From top to bottom: SDSS optical image and CL flux maps for J1614 ([NeV] $\lambda\lambda$3347, 3427) and J1714 ([NeV] $\lambda\lambda$3347, 3427).

observations, NVSS/ FIRST 1.4 GHz radio observations, and SDSS broad emission lines; Section 2.5), and determine that all [NeV] $\lambda\lambda$3347, 3427 galaxies are classified as AGNs.

2.4.1.2 [FeVII] $\lambda\lambda\lambda$3586, 3760, 6086

[283] analyzed a homogeneous data set of over 2,200 quasar spectra from SDSS and created a variety of composite spectra from this sample. The authors determined that the relative fluxes for [FeVII] $\lambda\lambda\lambda$3760, 3586, 6086 are 0.078 $\pm$ 0.007, 0.100 $\pm$ 0.011, and 0.113 $\pm$ 0.016, respectively (σ = 0.018), which feature significantly less scatter than the [NeV] $\lambda\lambda$3347, 3427 lines (σ = 0.20). As a result, we expect to find a similar fraction of [FeVII] galaxies that emit each line, which we do.

We measure [FeVII] emission in four MPL-8 galaxies: J1454 ([FeVII] λ3760; z = 0.13; elliptical; merger), J1349 ([FeVII] λ3760; z = 0.02; no GZ2 classification), J0906 ([FeVII] λ3586; z = 0.11; spiral; merger), and J1535 ([FeVII] λ6086; z = 0.03; spiral). We present the flux distributions for these galaxies in Figure 2.5.

Previous studies (e.g., [203, 64, 65, 97]) posit that the CLR lies within a transition zone between the BLR ($\sim$ 0.1 kpc) and the NLR (several kpc). Here, we measure [FeVII] λ3760 flux in J1454 out to 23.0 $\pm$ 2.9 kpc (4.4σ above the mean of the CLD distribution; the largest in our sample). We also find that the bulk of the CLR in this galaxy is not spatially coincident with the galactic center. We determine that this galaxy is classified as a merger in GZ2 and we detect the companion southwest of the galactic center, well-aligned with the [FeVII] λ3760 emission. During the merging process, companion galaxies can be separated by tens of kpcs (e.g., [91]), which we reason likely accounts for the far-reaching CL emission in J1454 (see Section 2.4.1.3).

We measure [FeVII] λ3760 emission in J1349 out to 7.0 $\pm$ 0.6 kpc from the galactic center. The CL emission in this galaxy is most abundant within the galactic interior, but also extends throughout the southwest and northeast regions. No GZ2 classification is available for this galaxy, but its strong CL emission (1.2σ above the mean of the CL luminosity

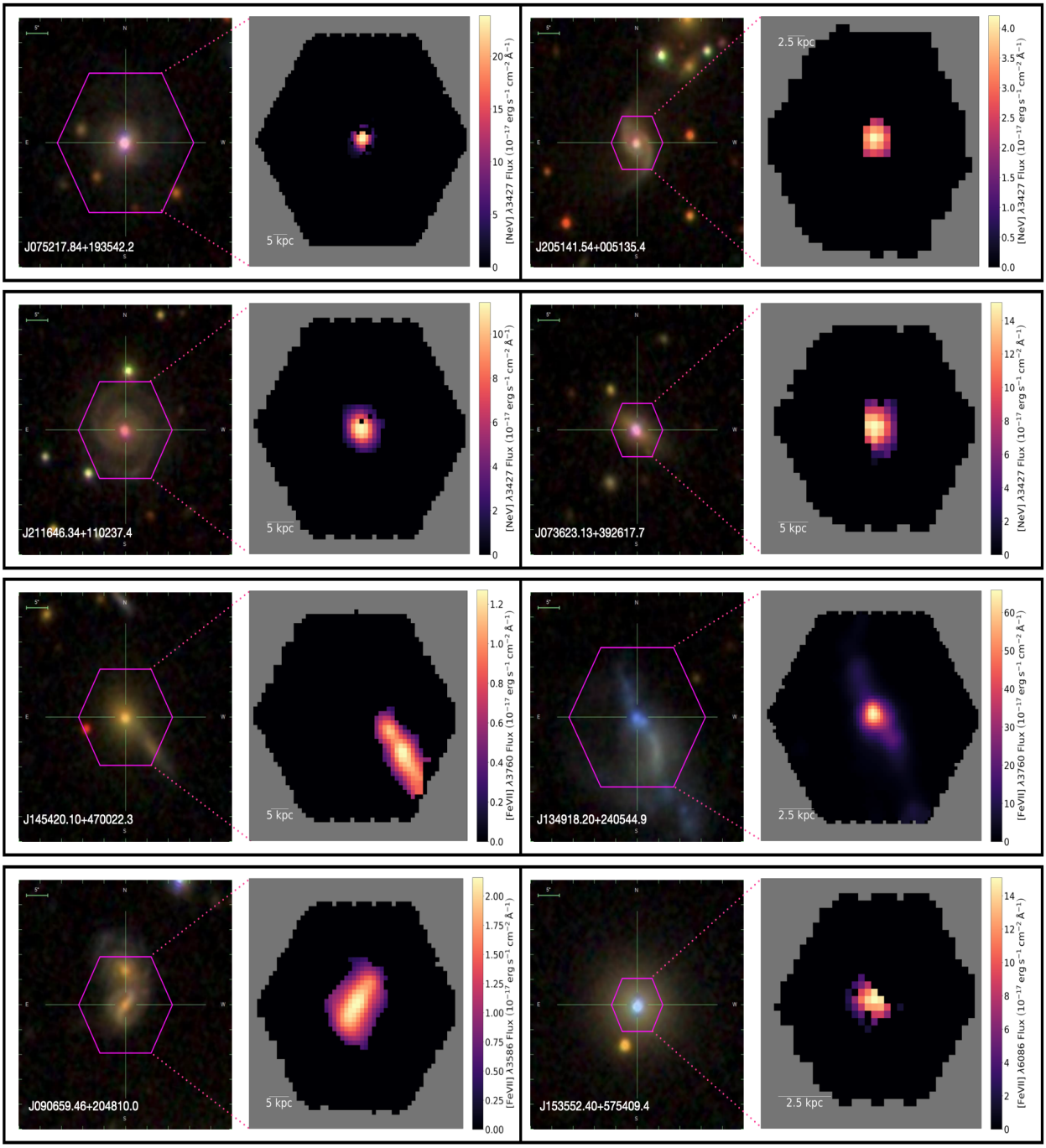

Figure 2.5: From left to right and top to bottom: the SDSS optical image and CL flux maps for J0752, J2051, J2116, J0736, J1454, J1349, J0906, and J1535. The CLDs for the CL mergers are the most extended in our sample (10.0 ± 2.5 kpc for J0906 and 23.0 ± 2.9 kpc for J1454). Merger-induced shocks are likely to be the primary ionization mechanism for these galaxies. The CL galaxies that host AGNs tend to have more compact CL emission that is predominantly within the galactic interior, which suggests AGN photoionization is the primary CL ionization mechanism for these galaxies.

distribution; Table 2.2) and its extended morphology make it a galaxy of peculiar interest in our analysis. We further analyze this galaxy in Section 2.4.4 and determine it to be an AGN candidate.

For J0906, we identify substantial [FeVII] λ3586 emission out to 10.0 $\pm$ 2.5 kpc from the galactic center (1.9σ above the mean of the CLD distribution; the second largest in our sample). We determine that this galaxy is a merger based on the GZ2 classification and identify elongated CL emission along an apparent central bar. We detect the companion in the northern region of this galaxy, partially within the MaNGA FoV.

We scan the MaNGA AGN catalog and find no AGN classification for J1454, J1349, or J0906 (two mergers; one unclassified morphology). We consider the likelihood that these galaxies are AGN candidates, to help determine if AGN processes are producing the CLs in these galaxies, in Section 2.4.4.

Moreover, prior studies show that gas inflows produced by mergers can generate widespread shocks that ionize gas on kpc and sub-kpc scales (e.g., [182]). As such, we also consider the influence of a companion galaxy to be a potential source of the far-reaching CL emission in the merging galaxies (Section 2.4.1.3).

For J1535 (a confirmed AGN in the MANGA AGN catalog), we detect [FeVII] λ6086 emission out to 1.3 $\pm$ 0.76 kpc. The CL distribution in J1535 strongly resembles the nuclear-bound [NeV] $\lambda\lambda$3347,3427 distributions (Section 2.4.1.1). If CLs are produced predominately by AGN photoionization, then we expect to find the bulk of CLs within the galactic interior, which is the case for this galaxy.

2.4.1.3 CL AGNs and CL Mergers

We find that the CL galaxies in our sample are either hosting an AGN (7; "CL AGNs"), undergoing a merger (2; "CL mergers"), or are unclassified (1; an AGN candidate; Section 2.4.4). The strength and distribution of the CL AGNs are consistent with AGN photoionization playing the most direct role in the production of the CLs, with merger-induced shocks

being a strong candidate for ionization, too. The CL AGN detection rate (70% - 80%) suggests that CLs are useful for identifying AGN in large spectroscopic surveys.

Additionally, we measure the CLDs of the CL mergers to be the most extended in our sample (10.0 ± 2.5 kpc for J0906 and 23.0 ± 2.9 kpc for J1454). The interactions between companion galaxies, which occur on the scale of tens of kpcs, can create tidal forces that drive gas towards the galactic centers, which can lead to shock excitation (e.g., [91]). These shocks are likely to impact both galaxies and account for the extended CL emission we see in the CL mergers. Moreover, the CL mergers may be relevant for AGN studies because infalling gas can fuel AGN activity, which can produce large-scale outflows and additional shocks that influence the host galaxy's evolution (e.g., [225]).

2.4.2 The Role of Stellar Shocks in the CLR

Shock ionization can result from a variety of phenomena, including, but not limited to, AGN activity (e.g., jets), gas inflows produced by mergers, and stellar winds generated by SNRs (e.g., [146]). We address the role of SNR shock ionization in the CLR, specifically, by investigating the populations of SNRs in the CLR. To execute this analysis, we adopt the approach outlined in Section 2.3.4.

Further, to better decipher the role of SNRs in the CLR, we plot the CL luminosity for each galaxy in our sample against the fraction of SNRs in their CLRs (Figure 2.6). We utilize the Pearson correlation coefficient to quantify our results. The coefficient ranges from -1 to +1, where 0 implies no correlation, -1 is indicative of a negative correlation, and +1 signifies a positive correlation. If CL luminosity and the fraction of SNRs are positively correlated, then SNRs likely play a critical role in the production of CLs.

We compute a Pearson correlation value of 0.3, implying a weak positive correlation between the fraction of SNRs in the CLR and the strength of the CLs. This suggests that a higher fraction of SNR shocks, on average, do not increase the strength of CL emission. We reason that AGN photoionization and merger-induced shocks are the dominant ionization

mechanisms producing the CLs, even for the CL galaxies that feature a 100% fraction of SNRs in their CL-emitting spaxels (Section 2.4.4). However, we do acknowledge the sparse amount of data in Figure 2.6 and a lack of a clear visual trend. While we expect photoionization and merger-induced shocks to have the most impact on the strength of the CLs, further analysis is required to definitively rule out the influence of SNRs in the CLR.

We also inspect the ionizing radiation field of the CL galaxies to determine the ionization mechanism(s) producing the CLR. We consider the r^{-2} ionizing radiation dilution characteristic of pure AGN photoionization (e.g., [274, 302]; Section 2.3.3), and compare the power law indexes of the CL luminosities to α = -2 (Table 2.2). We measure α to range between -1.8 $\pm$ 0.3 to -0.6 $\pm$ 0.1 for the CL AGNs (7) and -0.9 $\pm$ 0.1 to 0.2 $\pm$ 0.1 for the remaining sample (3). For both samples, the decay of ionizing radiation with increasing galactocentric distances is shallower than the profile expected for pure AGN photoionization. As a result, we reason that the CLs, even for the CL AGNs, likely feature a blend of ionization mechanisms that include, but are not limited to, SNRs and merger-induced shocks, which account for the extended nature of the CLR (Section 2.4). Further, we acknowledge that fluctuations in the density profile, as a function of galactocentric distance (Section 2.4.3; e.g., [222]), may influence the evolution of the ionizing radiation field, and that merger-driven shocks, AGN photoionization, and SNR shocks may not be the only CL ionization mechanisms; stochastic accretion, AGN light echoes, and AGN outflows are also possible mechanisms that can produce CL emission (e.g., [188, 298]).

2.4.3 Electron Temperatures and Electron Number Densities of the CLs

Previous studies (e.g., [180]) found that temperatures in the CLR range from 10,000 K - 20,000 K, consistent with pure AGN photoionization. However, beyond the $\sim$ 20,000 K threshold, up to 10^6 K, outflowing jets can collisionally ionize and heat gas clouds (via stellar and AGN shocks, for example; see [185]; Section 2.3.5). For these cases, kinetic energy must be supplied by an additional source (e.g., [204]). Moreover, intermediate electron densities

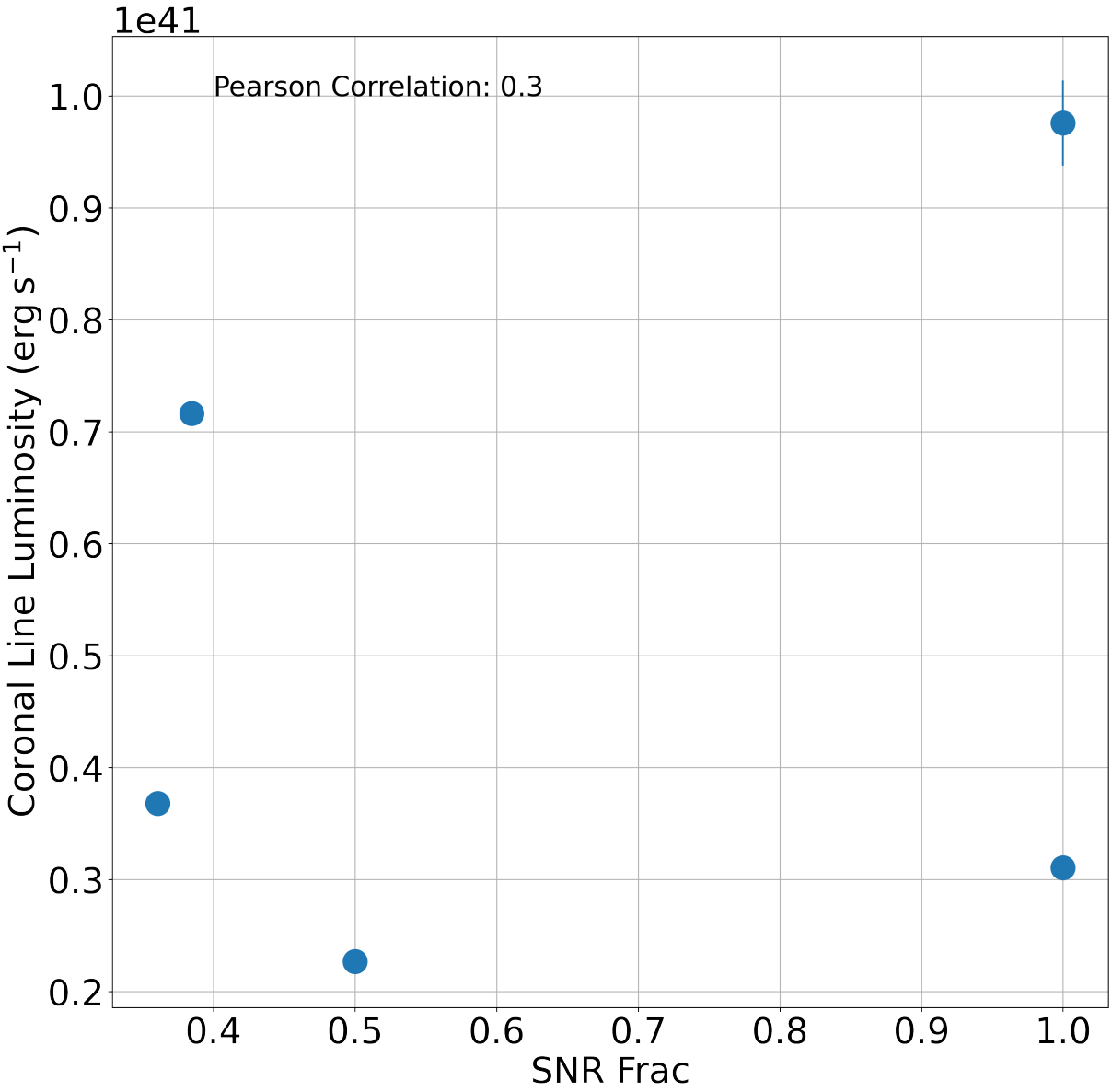

Figure 2.6: Total CL luminosity for each CL galaxy (with SNR emission in at least one CL spaxel) vs. the fraction of SNRs found in their respective CLRs. We measure a Pearson correlation value of 0.3, which suggests that, on average, higher fractions of SNRs do not produce more abundant CL emission. Due to the few data points and the lack of a clear visual trend, we consider these results preliminary. For some data points, CL luminosity uncertainties are too small to be visualized on the plot.

$n_e \approx 10^2$ - 10^4 cm^{-3} are typical of the NLR; $n_e > 10^9$ cm^{-3} for the BLR.

As a result, we measure the temperature and density profiles for the galaxies in our sample to better understand the nature of the CLR (Figure 2.7). For the density profiles, we acknowledge that recent studies (e.g., [13, 63]) report that electron number densities derived from the [SII] $\lambda\lambda$6717,6731 doublet may be underestimated. Thus, we consider our electron density measurements to be lower estimates.

For the temperature and density measurements, we require flux values for the [OIII] λ4363 line, but we only detect this line in 4/10 CL galaxies, which all host AGNs (Table 2.3). We also consider the fraction of spaxels in each galaxy's CLR that we can measure temperatures and densities for (the "Measurement Fraction" in Table 2.3). We find that the average CLR temperatures vary between 12,331 - 22,530 K, and that the average temperatures for 2/4 CL galaxies are consistent with pure photoionization. However, 2/4 feature temperatures slightly above the $\sim$ 20,000 K threshold (for J1535, we determine a temperature of 21,088 K in the single spaxel we could measure). We reason that for both of the CL AGNs with average temperatures above this limit, shock-induced compression and heating contribute to the production of the CLs (see [226] for a similar analysis of shocked emission in AGNs).

Additionally, we determine that the average CLR density varies between 244 - 586 cm^{-3}, typical of the NLR. This result is consistent with the CLDs extending well into the NLR (Section 2.4.1).

Table 2.3: Average CLR Electron Temperatures and Number Densities

SDSS Name	CL	Electron Temperature (K)	Electron Density (cm^{-3})	Measurement Fraction
(1)	(2)	(3)	(4)	(5)
J075217.84+193542.2	[NeV] λ3427	16,680	400	56%
J153552.40+575409.4	[FeVII] λ6086	21,088	586	3%
J161413.20+260416.3	[NeV] λ3347	22,530	355	36%
	[NeV] λ3427	19,533	244	38%
J211646.34+110237.4	[NeV] λ3427	12,331	414	51%

Note: Columns are (1) CL galaxy SDSS name, (2) detected CL, (3) average CLR electron temperature, (4) average CLR electron temperature, and (5) the fraction of spaxels in each galaxy's CLR that we can measure temperatures and densities for.

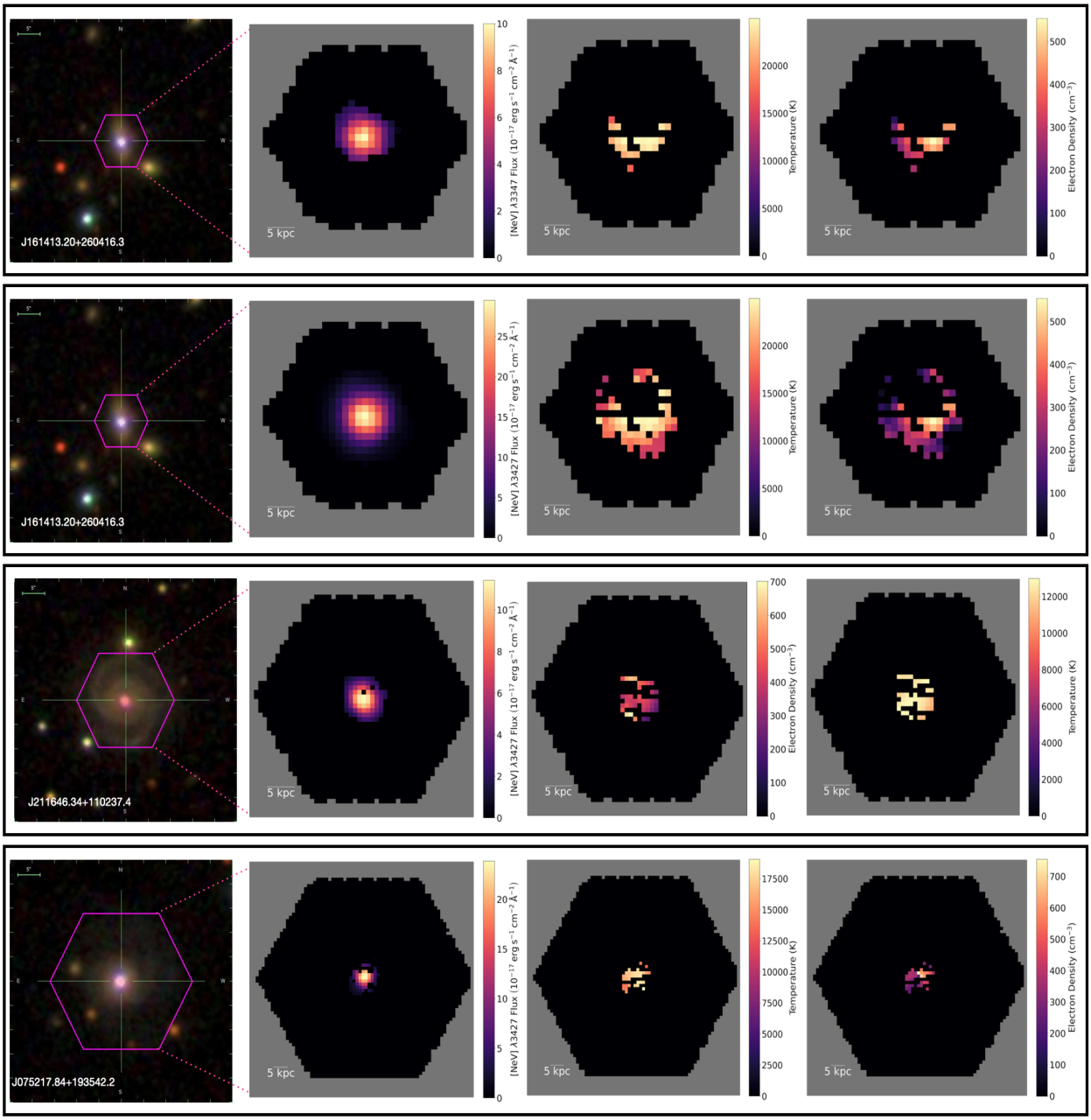

Figure 2.7: Left to right and top to bottom: SDSS optical image, and CL flux, temperature, and density maps for J1614 ([NeV] λ3347), J1614 ([NeV] λ3427), J2116 ([NeV] λ3427), and J0752 ([NeV] λ3427).

2.4.4 AGN Bolometric Luminosity

AGN bolometric luminosity measures the total luminosity emitted by an AGN across all wavelengths. It effectively traces the accretion efficiency, which is the fraction of accreted mass on the SMBH that is radiated, and offers direct insight into AGN power (e.g., [217]). If CLs provide definitive evidence for AGN activity, then the CL luminosity of each CL-emitting spaxel should broadly scale with its bolometric luminosity. We explore this relation using the method outlined in Section 2.3.7, and present our results in Figure 2.8. For galaxies with multiple CL detections, we plot each CL independently. We identify a strong positive correlation between CL and bolometric luminosities for our full sample (Pearson value of 0.9). In general, the strength of the CLR (measured by CL emission) scales with bolometric luminosity.

We then perform a linear regression on the full sample of CL galaxies. We use the R^2 statistic to quantify our results. This is a statistical measure that uses the sample's variance to determine how close the data are to the fitted regression line. It varies between 0 and 1, where 0 implies high variability of the data (i.e. a poor model fit) and 1 suggests low variability (i.e. a good fit). We measure R^2 for our sample to be 0.7, which suggests that CL luminosity is dependent on AGN bolometric luminosity, for the majority of our sample. Additionally, we measure the residuals to determine how well the data fit the regression line. We calculate the quantity R_f as the ratio of the residuals to the predicted regression values for each data point (Table 2.4). This dimensionless quantity measures the deviation of the data points relative to their predicted model values.

We first analyze the CL AGNs and determine that they fit the regression well, as we expect, with R_f values < 3. We then target the CL galaxies that have not been classified as an AGN in the MaNGA AGN catalog, which are either undergoing a merger (J1454 and J0906) or are unclassified (J1349). We do so to identify if these are outliers in our sample of CL galaxies, and to determine if they are potential AGN candidates. J1454 and J0906 are

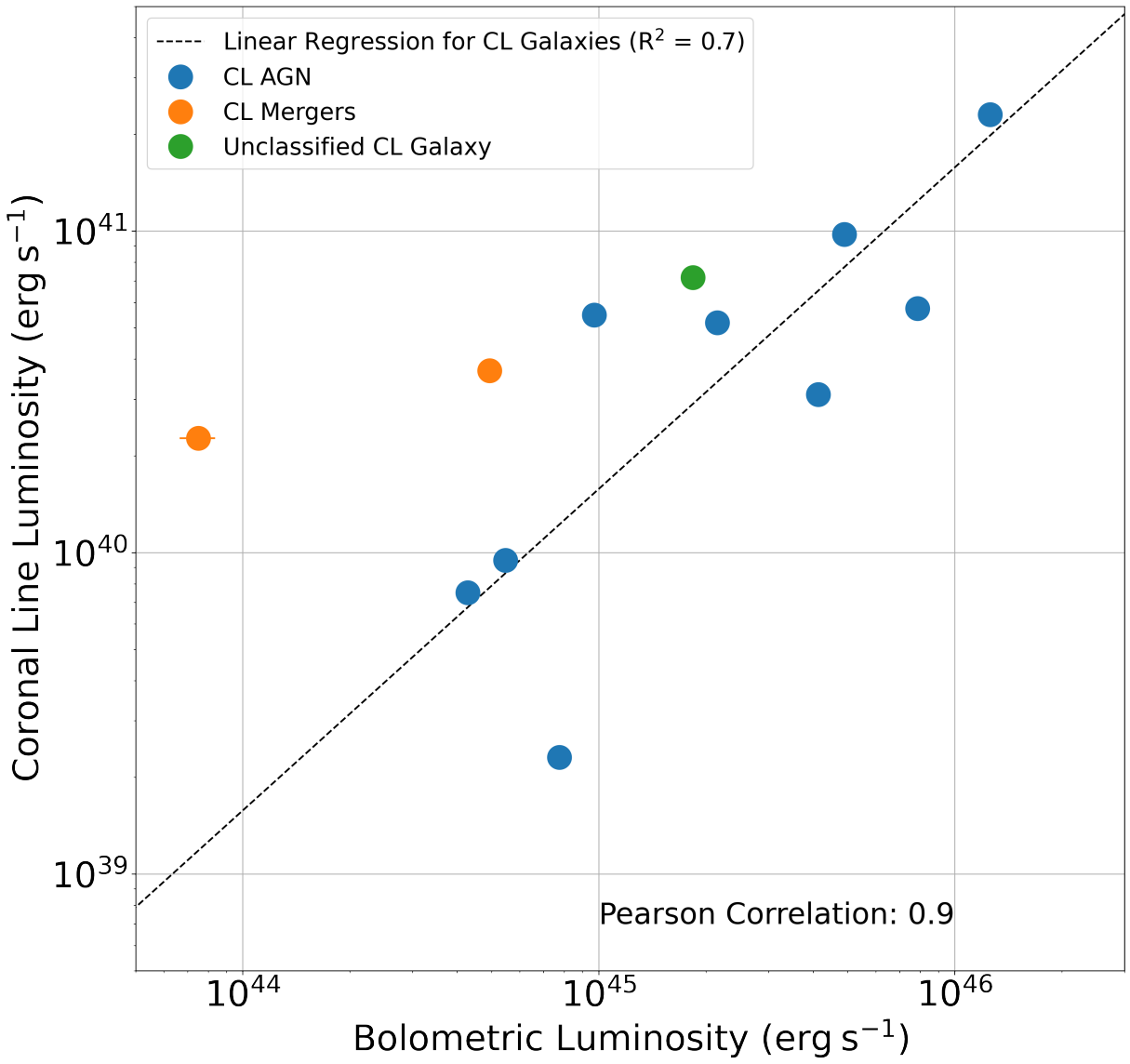

Figure 2.8: Total CL luminosity plotted against bolometric luminosity for all CL galaxies. The black line in the linear regression fit to the data. The blue data points are the CL AGNs, the orange are the CL mergers, and the green is the unclassified CL galaxy J1349. For some data points, CL and bolometric luminosity uncertainties are too low to be visualized on the plot.

marked by the orange data points in Figure 2.8; J1349 in green. We measure R_f values for J1454 and J0906 to be 8.1σ and 1.7σ above the mean of the R_f distribution, respectively - the two highest in our sample. This suggests that J1454 is not a strong AGN candidate, and that J0906 requires further analysis to determine if it hosts an AGN. On the other hand, J1349 ($R_f = 1.5$) is within 1σ of the mean of the distribution. We consider this galaxy to be an AGN candidate due to its proximity to the regression line.

We deduce that CLs are strong tracers of AGNs, but perhaps not perfect since we also find that galaxy mergers (which may not host an AGN) can also feature a CLR.

2.4.5 MaNGA AGN Catalog Comparison

Several authors suggest that CLs are common features in the spectra of AGNs and provide unambiguous signatures for AGN activity due to their high production energies (e.g., [150, 216, 180, 157, 188]). We use a catalog of confirmed AGNs in MaNGA to test the robustness of CLs as AGN identifiers (Table 2.5).

[52] assembled the largest existing catalog of AGNs in MaNGA to date. The authors used *WISE* mid-infrared color cuts, *Swift*/BAT hard X-ray observations, NVSS/ FIRST 1.4 GHz radio observations, and SDSS broad emission lines to create their sample. In total, they reported 406 unique AGNs in MPL-8.

Mid-infrared emission, generated by the heated dust which encompasses an AGN, is a reliable probe for obscured and unobscured AGN activity. As a result, they used observations from the *Wide-Field Infrared Survey Explorer* (*WISE*; [299]) to help identify AGNs. They considered the four bands observed with *WISE* (3.4 μm (W1), 4.6 μm (W2), 12 μm (W3), and 22 μm (W4)) and apply a 75% reliability criteria of W1 - W2 $>$ 0.486 exp$\{0.092$(W2 - 13.07)$^2\}$ and W2 $>$ 13.07, or W1 - W2 $>$ 0.486 and W2 $\leq$ 13.07 ([10]) for their analysis. They identified 67 WISE AGNs in MaNGA.

To trace the hot X-ray corona around an AGN, the authors used the catalog assembled by [199], which consists of $\sim$ 1,000 AGNs observed by the *Swift* Observatory's Burst Alert

Table 2.4: R_f Values for the CL Luminosity vs. Bolometric Luminosity Relationship

SDSS Name	CL	R_f
J073623.13+392617.7	[NeV] λ3427	0.53
J075217.84+193542.2	[NeV] λ3427	0.26
J090659.46+204810.0	[FeVII] λ6086	3.7
J134918.20+240544.9	[FeVII] λ3760	1.5
J145420.10+470022.3	[FeVII] λ6086	18.0
J153552.40+575409.4	[FeVII] λ6086	0.81
J161413.20+260416.3	[NeV] λ3347	0.54
	[NeV] λ3427	0.16
J171411.63+575834.0	[NeV] λ3347	0.10
	[NeV] λ3427	2.6
J205141.54+005135.4	[NeV] λ3427	0.11
J211646.34+110237.4	[NeV] λ3427	0.52

Table 2.5: CL Galaxies Found in the MaNGA AGN Catalog

SDSS Name	AGN Detection Method
J073623.13+392617.7	*WISE*, Broad
J075217.84+193542.2	*WISE*, BAT
J153552.40+575409.4	*WISE*, BAT, Broad
J161413.20+260416.3	*WISE*, BAT, Broad
J171411.63+575834.0	*WISE*, Broad
J205141.54+005135.4	*WISE*, Broad
J211646.34+110237.4	*WISE*, Broad

Telescope (BAT) in the ultra hard X-ray (14 - 195 keV). The authors found 17 AGNs from this catalog in MaNGA.

Further, radio studies are unique in their ability to detect strong emission emanating from AGN radio jets. [25] used observations from the 1.4 GHz NRAO Very Large Array Sky Survey (NVSS; [56]) and the Faint Images of the Radio Sky at Twenty Centimeters (FIRST; [15]) to detect AGNs in the SDSS's seventh data release (DR7). They differentiated AGN activity from star formation emission using the correlation between the 4000 Å break strength and radio luminosity per stellar mass, emission line diagnostics, and the relation between Hα and radio luminosity ([15]). [52] found 325 radio AGNs from this catalog in MaNGA.

Broad Balmer emission lines (FWHM $>$ 1,000 km s^{-1}) also serve as useful signatures for AGN activity. The high velocity clouds which produce these lines provide clear evidence of high density gas in close proximity to the SMBH. [200] assembled a catalog of nearby ($z \leq 2$) Type I AGNs in SDSS's seventh data release using the broad Hα emission line, and [52] identified 55 broad line AGNs from this catalog in MaNGA.

We cross match our sample with the 406 unique MaNGA AGNs reported by [52] and find 7 CL galaxies in it (70% of our sample). We consider CLs to be a strong tracer of AGN activity since the majority of our CL galaxies are confirmed to host an AGN. Additionally, the remaining 30% of our sample are galaxies of interest. J1349 is an AGN candidate (Section 2.4.4), and J1454 and J0906 are undergoing mergers, which can induce strong gas inflows that can eventually trigger the activation of AGNs and fuel large-scale AGN outflows (e.g., [225]).

2.4.6 BPT AGN Catalog Comparison

Baldwin-Phillips-Terlevich optical emission line diagnostic diagrams (BPT diagrams; [11, 143, 145, 141]) incorporate line ratios between high and low ionization species (e.g., [OIII] λ5007/$H\beta$ vs. [NII] λ6584/Hα or [OIII] λ5007/$H\beta$ vs. [SII] (λ6717 + λ6731)/Hα) to distinguish gas ionization sources as star forming, Seyfert (AGN), low-ionization nuclear

emission-line region (LINER), or a composite of multiple ionization sources. They serve as the traditional AGN selection tool for most spectroscopic surveys.

[220], [239], and [301] used these diagrams to identify AGN candidates in MaNGA's MPL-5, which contains data cubes for 2,727 unique galaxies. We scan these catalogs to identify the fraction of CL galaxies found within them. We do so to determine the strength of the BPT diagrams as an AGN selection tool, and to assess if CLs can help provide accurate AGN identifications in MaNGA (and similar spectroscopic surveys). We acknowledge that each BPT catalog may not have exhaustively scanned MPL-5 (e.g., spectroscopic data may not have been available for all galaxies during each analysis; [220]). As a result, we consider our findings preliminary.

A primary drawback of BPT diagrams is their inability to distinguish low ionization AGNs from post-AGB stars. [220] used the equivalent width of Hα (EW Hα) to mitigate this issue. [45] first determined that galaxies with EW H$\alpha < 3$ Å are predominantly ionized by post-AGB stars, rather than AGNs. As a result, [220] used this threshold to analyze single-fiber (within the central 3″) MPL-5 galaxy observations. They identified 62 AGNs above this limit, which were also reported as Seyfert or LINER (which have been shown to strongly link with AGN activity; e.g., [125]) on the BPT diagrams. We scan this catalog for the CL AGNs that are in MPL-5 (J1714; J0736; J2116; J1535) and determine that 0/4 are present.

[239] also used BPT diagrams to analyze the spectroscopic properties of ionized gas within the central (within 3″) of the MPL-5 galaxies. The authors similarly used EW Hα values to differentiate AGN from post-AGB star ionization regions. However, they relaxed the 3 Å criteria used by [220] and [45], and only considered galaxies with EW H$\alpha < 1.5$ Å to be primarily ionized by post-AGB stars (to include weaker AGN). Additionally, the authors excluded galaxies below the Kauffmann demarcation curve, which is an empirical tracer of HII regions - used to isolate star forming sources on BPT diagrams ([143, 145]). Using these constrains, they reported 98 AGNs in MPL-5. We find that 1/4 CL AGN, that

are in MPL-5, are in this catalog (J2116).

Finally, [301] analyzed each spaxel for every galaxy in MPL-5 and created spatially resolved BPT-diagrams. They weighted the summed fraction of spaxels categorized as either AGN, LINER, or composite in each galaxy (e.g., AGN spaxels were given an 80% weight and composite spaxels were given a 20% weight). The authors then performed cuts on Hα surface brightness and Hα EW. Hα surface brightness is a reliable tracer of diffuse hot ionized gas; however, emission line ratios are often enhanced in regions with low Hα surface brightness (which can mimic AGN and LINER emission; e.g., [114]). As a result, they excluded spaxels with Hα surface brightnesses $< 10^{37}$ erg s^{-1} kpc^{-2}. They also elevated the minimum EW Hα threshold to 5 Å to further reduce potential stellar contamination (below this limit post-AGB stars are considered to be the primary ionization mechanism). They found 303 AGN candidates, and we identify 2/4 CL AGNs, that are in MPL-5, in their sample (J1535 and J2116). [301] acknowledged that BPT ionization ratios can be impacted by diffuse ionized gas, extraplanar gas, photoionization by hot stars, metallicity, and shocks. These sources can elevate line flux ratios to produce AGN-like features, potentially leading to misclassification (e.g., [223, 224, 144]).

We determine that the [220], [239], and [301] catalogs feature 0/4, 1/4, and 2/4 CL AGN(s) (in MPL-5), respectively. The low fraction of CL AGNs in these catalogs suggests that CL detections may be useful for identifying AGNs missed by traditional BPT diagrams. We will conduct a more thorough review in a forthcoming publication (Negus et al., in prep) and determine the BPT classifications for all of the CL-emitting spaxels in our sample. We will also compare our findings with future MaNGA BPT AGN catalogs that scan a more complete sample of MaNGA galaxies. This will help us build a deeper understanding of the CL galaxies, and will enable us to more closely evaluate the strength of BPT diagrams as AGN classifiers.

2.5 Discussion

In this chapter, we analyze 10 CL galaxies from MaNGA's MPL-8. With our detection rate (0.16%), we expect to find at least $\sim$ 16 CL galaxies with CL emission at $\geq 5\sigma$ above the continuum, in at least 10 spaxels, in the final MaNGA catalog of $\sim$ 10,000 galaxies. We anticipate that the majority of these CL galaxies will be confirmed as AGNs or AGN candidates, and that the remaining will be CL mergers.

We determine that AGN photoionization is likely the dominant ionization mechanism for the CLs in our sample, which is consistent with results found in previous studies (e.g., [99, 180]). As a result, we consider CLs to be a useful tracer for AGN identification, which is a critical step in constraining the role of AGN feedback in the host galaxy's evolution. On the other hand, we also determine that CLs can be featured in merging galaxies that may not host an AGN (20% of our catalog), likely through gas inflows that trigger shocks and extend the reach of the CLR. However, these CL galaxies may still be useful for understanding feedback within galaxies since mergers can initiate galaxy winds, fuel AGNs, stimulate star formation, and impact a galaxy's gas supply (e.g., [266, 49, 225]).

Further, [69] studied CL emission in four nearby AGNs and reported a co-spatial distribution of CL emission with radio jets. [187] also modeled the location and kinematics of the CLR in a sample of AGNs and declared that the bulk of these regions corresponded to outflows. These AGN processes, in addition to shocks, may be additional CL ionization mechanisms that can account for the extended emission we report.

Finally, prior CL studies measured these lines to lie between the BLR and the NLR (e.g., [180, 232]), or on the order of hundreds of pc (e.g., [188, 228]). Here, we measure the CLR to be far more extended, out to distances of 1.3 - 23 kpc from the galactic center and well into the NLR. We do consider the possibility that the CL emission in the CL galaxies can be smeared (to distances much larger than the FWHM of the PSF) by seeing from the atmosphere, the telescope, and/ or the instruments (e.g., [43]). In Section 2.4, we

show that beam smearing is possible for 4/10 CL galaxies and consider their CLDs to be upper estimates. However, the remaining population of 6 CL galaxies feature continuous and well resolved CL emission. Among this sample, the CL galaxy with the most extended CL emission is spatially resolved and extends out to 23 kpc. As such, the extent of the CLR that we report (1.3 - 23 kpc from the galactic center) is unlikely to be impacted significantly by beam smearing.

2.6 Summary and Future Work

We assemble the largest catalog of MaNGA CL galaxies to date. With our custom pipeline, we detect 10 CL galaxies exhibiting emission from one or more CLs ([NeV] λ3347, [NeV] λ3427, [FeVII] λ3586, [FeVII] λ3760, or [FeVII] λ6086 in this chapter) detected at $\geq 5\sigma$ above the background continuum in at least 10 spaxels.

Our primary results are the following:

(1) CL emission extends 1.3 - 23 kpc from the galactic center, with an average distance of 6.6 kpc (well into the traditional NLR).

(2) Across our entire sample, CL luminosity diminishes exponentially from the galactic center with -1.8 $\pm$ 0.3 $\leq \alpha \leq$ 0.2 $\pm$ 0.1. We compare this to the power law index expected for pure AGN photoionization ($\alpha = -2$), and reason that shocks (e.g., merger-induced and from SNRs) can also produce CLs and increase α to values > -2.

(3) The average CLR electron temperature ranges between 12,331 K - 22,530 K. Shock-induced compression and heating must necessarily elevate these temperatures beyond the threshold for photoionization ($\sim$ 20,000 K).

(4) The average CLR electron number density is on the order of $\sim 10^2$ cm^{-3}, consistent with the CLR occupying the NLR, beyond the BLR.

(5) CL luminosity strongly correlates with bolometric luminosity (Pearson value of 0.9) for our sample. This is consistent with AGN activity primarily regulating the strength of CLs.

(6) The CL mergers (J1454 and J0906) deviate most significantly ($R_f > 3$) from the linear regression fit performed on CL luminosity vs. bolometric luminosity. J1454, 8.1σ above the mean of the R_f distribution, is not a strong AGN candidate based on this result. J0906, 1.7σ above the mean of the R_f distribution, requires further analysis to determine if it hosts an AGN.

(7) 7 CL galaxies (70% of our catalog) are confirmed AGNs. One CL galaxy is also an AGN candidate. CLs are strong, but perhaps not perfect, indicators of AGN activity.

(8) Several CL AGNs are not found in existing BPT AGN catalogs. Our preliminary results suggests that CL detections may be useful for helping to identify AGNs missed by traditional BPT diagrams.

We will conduct a full review of the CLR kinematics in a forthcoming publication to determine the role of outflows in the production of CLs. Specifically, we will trace the bulk motion of galactic outflows (i.e. jets), study the dynamics of gas inflows that result from mergers, and measure the rotation and cloud velocities of gas near the galactic core using MaNGA's DAP.

We will also scan MPL-11, the final MaNGA data release that contains 10,010 galaxies, and append our sample of CL galaxies with any additional CL galaxy detections. We will then determine which CLs are most suitable for identifying high luminosity AGNs, and proceed to investigate the role of dust extinction on optical CL detections. Ultimately, we seek to ensure we identify all CL galaxy candidates and to build the most complete sample of CL galaxies in MaNGA.

Chapter 3

A Catalog of 71 Coronal Line Galaxies in MaNGA: [NeV] is an Effective AGN Tracer

This chapter was published in The Astrophysical Journal ([192]).

3.1 Introduction

Active Galactic Nucleus (AGN) feedback, the process by which an active accretion disk converts gravitational energy into radiative or mechanical energy (e.g., AGN-induced photoionization, outflows, shocks, winds, and jets), has been shown to dynamically influence the evolution of a host galaxy (e.g., the tight correlation between stellar velocity dispersion and black hole mass and the quenching of star formation; e.g., [95, 98, 127, 87, 151, 120]). However, the full spatial extent, ionization properties, and impact of AGN feedback on the host galaxy have yet to be fully unraveled.

The Unified Model of AGN ([7, 280]) provides a fundamental architecture for understanding the evolution of AGN feedback. In this model, an AGN is either Type I or Type II. Type I are viewed pole-on and are observed to have broad (FWHM $>$ 1,000 km s^{-1}) and narrow (FWHM $<$ 1,000 km s^{-1}) emission lines, whereas Type II are viewed edge-on and are observed to only have narrow emission lines. These regions are termed the broad-line region (BLR) and the narrow-line region (NLR), respectively.

In [191], we considered The Unified Model before investigating the "coronal line region" (CLR), an area surrounding a supermassive black hole (SMBH; $M_{BH} > 10^6$ $M_\odot$) that

produces highly ionized species of gas with ionization potentials (IPs) $\geq$ 100 eV (termed "coronal lines" (CLs) since they were first observed in the solar corona). CLs are suspected to primarily originate from the strong ionizing continuum of an AGN; in particular, nuclear CLs are produced in the inner edge of the dusty torus and extended CLs are tied to the presence of a jet or AGN-driven outflows (due to the highly energetic nature of these processes; e.g., [233, 215, 99, 187, 180, 232, 188, 104, 228]).

Further, CLs in the mid-infrared have been extensively used to probe for AGNs, and to subsequently analyze their physical environments, within dusty galaxies (e.g., [100, 272, 9, 170, 293, 62]). In fact, several studies have shown that AGNs, even those missed by optical surveys (due to obscuration, for example), are uncovered by observations of infrared CLs (e.g., [243, 246, 238]). Additionally, since CL emission from Type II supernovae is infrequent, weak, and short lived, CL infrared observations have been particularly useful for accurately identifying CL emission exclusively from AGNs (e.g., [260]).

In regard to optical studies, Baldwin-Phillips-Terlevich diagnostics diagrams ([11, 286, 143, 145]) are predominantly used to differentiate emission-line sources as star-forming, AGN, or a composite of the two. However, diffuse ionized gas, extraplanar gas, photoionization by hot stars, metallicity, and shocks can elevate sources beyond the star formation threshold and potentially lead to AGN misclassification (e.g., [301]).

Moreover, while the NLR is the largest observable structure directly affected by an AGN's ionizing radiation (out to several kpcs; e.g., [188]), star formation can also produce some of the narrow lines usually associated with AGN (e.g., [OIII] λ5007; "[OIII]" hereafter). Further, while the BLR provides definitive evidence of AGN activity, due to the elevated cloud velocities, its compact radial extent ($\approx$ 0.1 kpc; e.g., [158]) is often spatially unresolved in most spectroscopic surveys. On the other hand, CLs require energies well above the limit of stellar emission (55 eV; [113]) and are typically spatially resolved beyond the BLR and well into the NLR (e.g., [191]). If CLs can provide accurate AGN identification in optical spectroscopic surveys of galaxies, as they have been shown to do in infrared surveys, then

detecting them may be a critical step in constraining the complexities of AGN feedback (e.g., [184]).

The Sloan Digital Sky Survey's (SDSS) Mapping Nearby Galaxies at Apache Point Observatory catalog (MaNGA; [36]) has provided an unprecedented lens into the dynamic environments that surround the SMBHs of nearly 10,010 nearby ($0.01 < z < 0.15$; average $z \approx 0.03$) galaxies. Using integral field spectroscopy (IFS), MaNGA provides a 1 - 2 kpc spatial sampling across the field of view of each observed galaxy, which offers direct insight into the spatial extent, ionization properties, and the environmental impact of AGN feedback. For reference, previous SDSS surveys (e.g., SDSS-I to SDSS-III; [304, 82]) observed galaxies with small (3" diameter) optical fibers. The resulting spectra only traced a small region close to the galactic center, potentially missing nuclear activity outside of this region. [303] further report that 80% of SDSS galaxies observed with a single fiber have less than 36% of their light covered. Moreover, long-slit spectroscopic surveys of galaxies also reveal limited spatial information, since only narrow elongated regions of each galaxy are observed (e.g., [196]). In contrast, MaNGA offers the ability to capture spatially extended galactic features, which can reveal off-nuclear activity and large-scale emission line regions.

In [191], we scanned for [NeV] $\lambda\lambda$3347, 3427, [FeVII] $\lambda\lambda\lambda$3586, 3760, 6086, and [FeX] λ6374 emission at $\geq 5\sigma$ above the background continuum in the 6,623 galaxies from MaNGA's eighth data release (MPL-8). We identified 10 CL galaxies in MPL-8, the largest such catalog at the time; seven of which were confirmed to host an AGN, which suggests that CL emission can be useful for tracing AGN activity. The remaining three visually appear to be undergoing galactic mergers. We also found that the average spatial extent of the CLR from the nuclear center is 6.6 kpc - well into the NLR. Further, we measured the average electron number density of the CLRs in our sample to be on the order of $\approx 10^2$ cm^{-3}, also consistent with the CLR occupying the traditional NLR, beyond the BLR (typical NLR densities range from 10^1 - 10^7 cm^{-3}; e.g., [212, 221]).

However, we also reported a range of power-law indices (α) above the threshold ex-

pected for pure AGN photoionization ($\alpha = -2$; we measured -1.8 $\pm$ 0.3 $\leq \alpha \leq$ 0.2 $\pm$ 0.1), and electron temperature values slightly above the threshold for pure AGN photoionization ($T_e = 20,000$ K; [203]). We found that the average CLR electron temperatures varied between 12,331 K - 22,530 K. These results suggest that shock-induced compression and heating may also play a role in the production of CLs.

Comparatively, [180] investigated the CLR for 10 pre-selected AGNs. They used the *Hubble Space Telescope*/Space Telescope Imaging Spectrograph to study [NeV] λ3427, [FeVII] $\lambda\lambda\lambda$3586, 3760, 6086, [FeX] λ6374, [FeXIV] λ5303, [FeXI] λ7892, and [SXII] λ7611 emission in their sample. The authors deduced that AGN photoionization is the main driving mechanism for the CLs. Moreover, [99] used the sixth SDSS data release ([3]) to analyze the CLR in 63 AGNs with [FeX] λ6374 (IP = 233.60 eV), [FeXI] λ7892 (IP = 262.10 eV), and [FeVII] λ6086 (IP = 99.10 eV) emission. They used X-ray observations from *Rosat* ([288, 287]) to similarly posit that AGN photoionization is the main ionization source of the CLs. Finally, [219] executed the first systematic survey of twenty optical CLs in the spectra of nearly 1 million galaxies from the eighth SDSS data release ([5]). The authors found that CL emission is extremely rare ($\approx 0.03\%$ of the sample show at least one CL), and that the highest ionization potential CLs tend to be found in lower mass galaxies. They reasoned that this finding is consistent with theory that hotter accretion disks are produced by lower mass black holes, which typically reside in lower mass galaxies.

Here, we use MaNGA's eleventh, and final, data release (MPL-11; 10,010 unique galaxies) to further resolve the physics of the CLR, and to better understand the relationship between the production of CLs and AGN activity. With our custom pipeline, we identify 71 unique galaxies with emission from [NeV] $\lambda\lambda$3347, 3427, [FeVII] $\lambda\lambda\lambda$3586, 3760, 6086, and/or [FeX] λ6374 detected at $\geq 5\sigma$ above the continuum, which makes it the most extensive such catalog of MaNGA CL galaxies to date.

This paper is outlined as follows: Section 3.2 details the technical components of the SDSS-IV MaNGA survey and its data pipeline, Section 3.3 describes the methodology we

use to build the CL catalog and to analyze the physical properties of the CLR, Section 3.4 reviews our results, Section 3.5 provides interpretations of our findings, and Section 3.6 includes our conclusions and intended future work. All wavelengths are provided in vacuum and we assume a ΛCDM cosmology with the following values: $\Omega_M = 0.287$, $\Omega_\Lambda = 0.713$ and $H_0 = 69.3$ km s^{-1} Mpc^{-1}.

3.2 Observations

3.2.1 Sample of Galaxies

We assemble our sample from the SDSS-IV MaNGA catalog ([36, 80, 159, 303, 29, 290]). MaNGA observations occurred between 2014 to 2020, using the SDSS 2.5 m telescope ([111]). The IFS survey contains data for 10,010 nearby galaxies ($0.01 < z < 0.15$; average $z \approx 0.03$) with stellar mass distributions between 10^9 $M_\odot$ and 10^{12} $M_\odot$. The spectra were taken at wavelengths between 3622 Å - 10354 Å, with a typical spectral resolving power of ≈ 2000, corresponding to a velocity resolution of 72 km s^{-1} (see [36]).

MaNGA contains spectroscopic maps out to at least 1.5 times the effective radius; the typical galaxy is mapped out to a radius of 15 kpc. Each MaNGA spatial pixel, or spaxel, covers $0.''5 \times 0.''5$, and the average full-width half maximum (FWHM) of the on-sky point spread function (PSF) is $2.''5$, which corresponds to a typical spatial resolution of 1 -2 kpc ([80]).

3.2.2 MaNGA Data Analysis Pipeline

The MaNGA Data Analysis Pipeline (DAP; [294]) offers publicly available high-level data products. The MaNGA DAP algorithms have been in development since 2014 and its main outputs are stellar kinematics, fluxes and kinematics of prominent emission lines, and continuum spectral indices. To measure each parameter, the DAP relies on spectral fitting with pPXF ([38, 39]), where each fit features a blend of stellar templates with a multiplicative

polynomial component to the stellar continuum. In particular, the DAP incorporates the MILESHC stellar templates library ([294]) to fit the stellar kinematics.

The inputs for the DAP are data reduced by the MaNGA Data Reduction Pipeline (DRP). The DRP is fed spectra from the MaNGA fiber-feed system, which consists of 17 IFUs: two 19-fiber IFUs, four 37-fiber IFUs, four 61-fiber IFUs, two 91-fiber IFUs, and five 127-fiber IFUs (see [80] for a more detailed description). The DRP subsequently wavelength, flux, and astrometrically calibrates the spectra.

3.3 Analysis

3.3.1 CL Continuum Subtraction and Emission Line Fitting

We scan for [NeV] $\lambda\lambda$3347, 3427, [FeVII] $\lambda\lambda\lambda$3586, 3760, 6086, and [FeX] λ6374 emission to better understand their effectiveness as AGN indicators. These CLs are selected because MaNGA's DAP does not provide emission line measurements for them. As a result, we expand upon the custom pipeline detailed in [191] to measure these CLs in MPL-11. Note, all 10 CL galaxies reported in [191] are recovered using the new MPL-11 pipeline.

3.3.1.1 CL Stellar Continuum Subtraction

To measure the stellar kinematics, and subsequently subtract the stellar continuum for each CL galaxy's observed spectra, we use pPXF ([40, 38, 39]). pPXF performs a polynomial fit on each galaxy's spectrum while masking gas emission lines. For each fit, we use the MILES[1] stellar templates library to represent the stellar population synthesis model. This library contains $\approx$ 1,000 stars, with spectra obtained by the *Isaac Newton Telescope*. These spectra cover the wavelength range of 3525 Å - 7500 Å at a 2.5 Å FWHM resolution.

We first access the DRP to extract the necessary data cubes for each MaNGA galaxy before performing the pPXF stellar continuum subtraction. The data cubes provide a spec-

[1] http://miles.iac.es/

trum for each individual spaxel across the FoV of each galaxy. We then use the spectroscopic redshifts of each galaxy, adopted from the NASA Sloan Atlas catalogs ([30]), to adjust the spectra to rest vacuum wavelengths. We also use a minimum redshift threshold ($z_{\min}$) for CLs near the lower wavelength limit of MaNGA (3622 Å; Table 3.1) to ensure CLs of interest are not shifted out of MaNGA's spectral coverage. For [NeV] $\lambda\lambda$3347, 3427 and [FeVII] λ3586, $\approx$ 93% (9,152), $\approx$ 83% (8,096), and $\approx$ 3% (229) of the MPL-11 galaxies, respectively, feature redshifts that place each CL out of MaNGA's spectral range; as a result, we are unable to scan for [NeV] $\lambda\lambda$3347, 3427 and [FeVII] λ3586 in these respective galaxies.

We then apply a mask to each datacube, such that the imported wavelength range for each spectrum matches the wavelength range of the stellar templates library (3525 Å-7500 Å). Next, we normalize each spectrum by dividing fluxes in this wavelength range by each spectrum's median flux value (to avoid numerical issues; see [39] for a more detailed discussion). Subsequently, we define a typical instrument resolution of $\approx$ 2.5 Å, construct a set of Gaussian emission line templates (to mask emission lines; provided by pPXF), and fit the stellar templates. Note, for the CLs near the lower limit of the mask (3525 Å; e.g., [NeV] $\lambda\lambda$3347, 3427 and [FeVII] λ3586), we perform a custom stellar continuum fit and subtraction before measuring the target emission line. In these instances, we execute a polynomial fit on a narrow spectral region, $\approx$ 300 Å wide, of continuum (free of prominent absorption or emission lines) near the rest wavelength of the target CL to model the background stellar continuum and subtract it from the spectrum.

3.3.1.2 [NeV] and [FeVII] Emission Line Measurements

Once the spectra are stellar continuum subtracted, we attempt a single Gaussian fit on a $\approx$ 30 Å region centered on the rest wavelengths of the CLs ([FeX]λ6374 being the exception; see Section 3.3.1.3). We found that this wavelength range is adequate for capturing the full extent of CL emission in our preliminary scans. We then determine the root mean square (RMS) flux of two continuum regions ($\approx$ 60 Å wide) that neighbor each target CL, free of

absorption or emission lines, and require that CL amplitudes are detected at $\geq 5\sigma$ above the mean RMS flux values in these continuum regions. We consider the spectral resolution of MaNGA (R = $\lambda/\Delta\lambda \approx 1400$ at 3600 Å; R $\approx$ 2000 at 6000 Å; [259]) to eliminate fits with $\Delta\lambda \lessapprox 2.4$ Å (for [NeV] $\lambda\lambda$3347, 3427), $\lessapprox 2.6$ Å(for [FeVII] $\lambda\lambda$3586, 3760), and $\lessapprox 3$ Å(for [FeVII] λ6086 and [FeX] λ6374). We provide an example of a single Gaussian fit for the [FeVII] λ3586 line in Figure 3.1.

3.3.1.3 [FeX] Emission Line Measurements

For [FeX] λ6374, the broad blue wing of this line is often blended with [OI] λ6364 due to their close proximity. Consequently, we attempt a double Gaussian fit to isolate the [FeX] λ6374 line. If this routine does not successfully fit both lines with $\geq 5\sigma$ confidence, then we attempt a single Gaussian fit and apply the method used in [99] and [236], whereby the emission line ratio [OI] λ6300/λ6364 is used to determine if the [OI] λ6364 and [FeX] λ6374 lines are blended. Specifically, from atomic physics, if [OI] λ6300/λ6364 = 3, then the [OI] λ6364 line is free from contamination (see also [85] for a full review). If [FeX] λ6374 emission is present and blended with [OI] λ6364, it will reduce the [OI] λ6300/λ6364 ratio below three. The MaNGA DAP provides flux values for both [OI] λ6364 and [OI] λ6300 lines. We adopt this method and require this ratio to be below three when fitting for [FeX] λ6374 with a single Gaussian fit to avoid confusing [OI] λ6364 and [FeX] λ6374 emission. Once we isolate the [FeX] λ6374 emission, we impose the same thresholds used to identify the [NeV] and [FeVII] emission lines (e.g., amplitudes $\geq 5\sigma$; Section 3.3.1.2).

3.3.2 Coronal Line Flux Maps

Similar to [191], we create custom CL flux maps to analyze the strength and distribution of the CLs in the CLR. We create these maps using the integrated CL flux value from each spaxel for each CL galaxy (Figure 3.2).

The center of each MaNGA observation corresponds to the galactic center ([303]). We

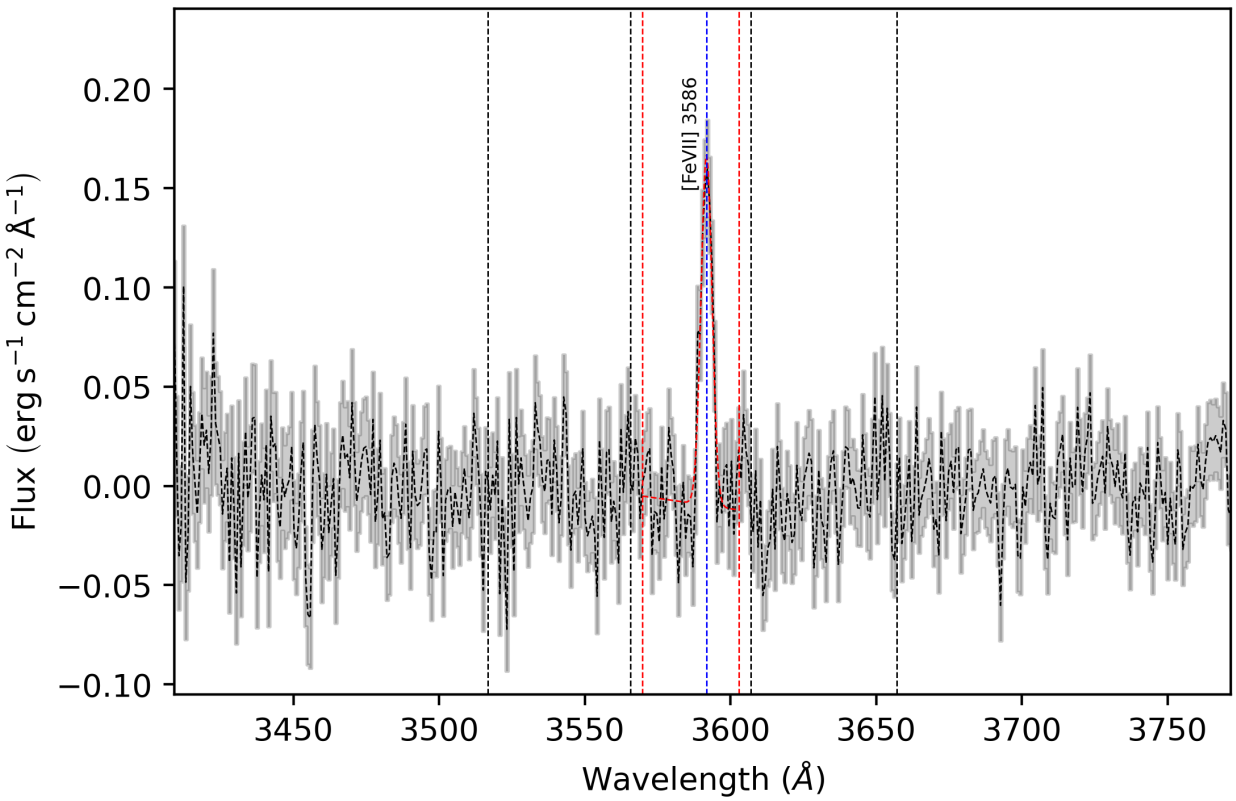

Figure 3.1: A sample spectrum from an individual spaxel showing the [FeVII] λ3586 line detected at $\geq 5\sigma$ above the continuum in J0906. The dotted black line is the continuum subtracted spectrum, the shaded gray region is the uncertainty, the solid red line represents the best fit, the red dotted vertical lines mark the fitting window, the blue dotted line signifies the rest wavelength of the [FeVII] λ3586 line, and the two sets of black dotted vertical lines correspond to the neighboring continuum windows where the RMS flux values of the continuum are calculated.

Table 3.1: CLs

Emission Line	Wavelength (Å)	IP (eV)	$z_{\min}$
[NeV]	3347	97.1	0.088
[NeV]	3427	97.1	0.061
[FeVII]	3586	99.1	0.016
[FeVII]	3760	99.1	-
[FeVII]	6086	99.1	-
[FeX]	6374	233.6	-

Note: Columns are (1) emission line, (2) rest wavelength, (3) ionization potential, and (4) minimum redshift value required for MaNGA detection.

use this position and the galaxy's inclination angle to determine the de-projected galactocentric distance of each CL spaxel. We do acknowledge that the CL gas may not be restricted to the galactic disk; i.e., the CL emission may associated with an ionization "cone" and therefore, in these instances, the de-projected distances are approximations.

The MaNGA DAP provides the ratio of the semi-minor to semi-major axes (b/a) for each galaxy, and we use this value to determine the cosine of each galaxy's inclination angle (i): cos(i)= b/a. The de-projected distance of each CL spaxel to the center of the galaxy is then measured by:

$$\mathrm{CLD} = \sqrt{(\mathrm{x} - \mathrm{x_{center}})^2 + \big((\mathrm{y} - \mathrm{y_{center}}) * \cos(\mathrm{i})\big)^2} \tag{3.1}$$

where x is the projected distance between the spaxel and the galaxy center measured along the galaxy's major axis, and y for the minor axis.

We then convert spaxel distances to a physical unit (kpc) using the `astropy.cosmology` Python package. The resulting value corresponds to the coronal line distance (CLD) of each CL emitting spaxel from the galactic center. Further, the minimum coronal line distance ($\mathrm{CLD_{min}}$) corresponds to the distance of each galaxy's closest CL-emitting spaxel from the galactic center. Finally, the maximum coronal line distance ($\mathrm{CLD_{max}}$) corresponds to the distance of each galaxy's most distant CL-emitting spaxel from the galactic center.

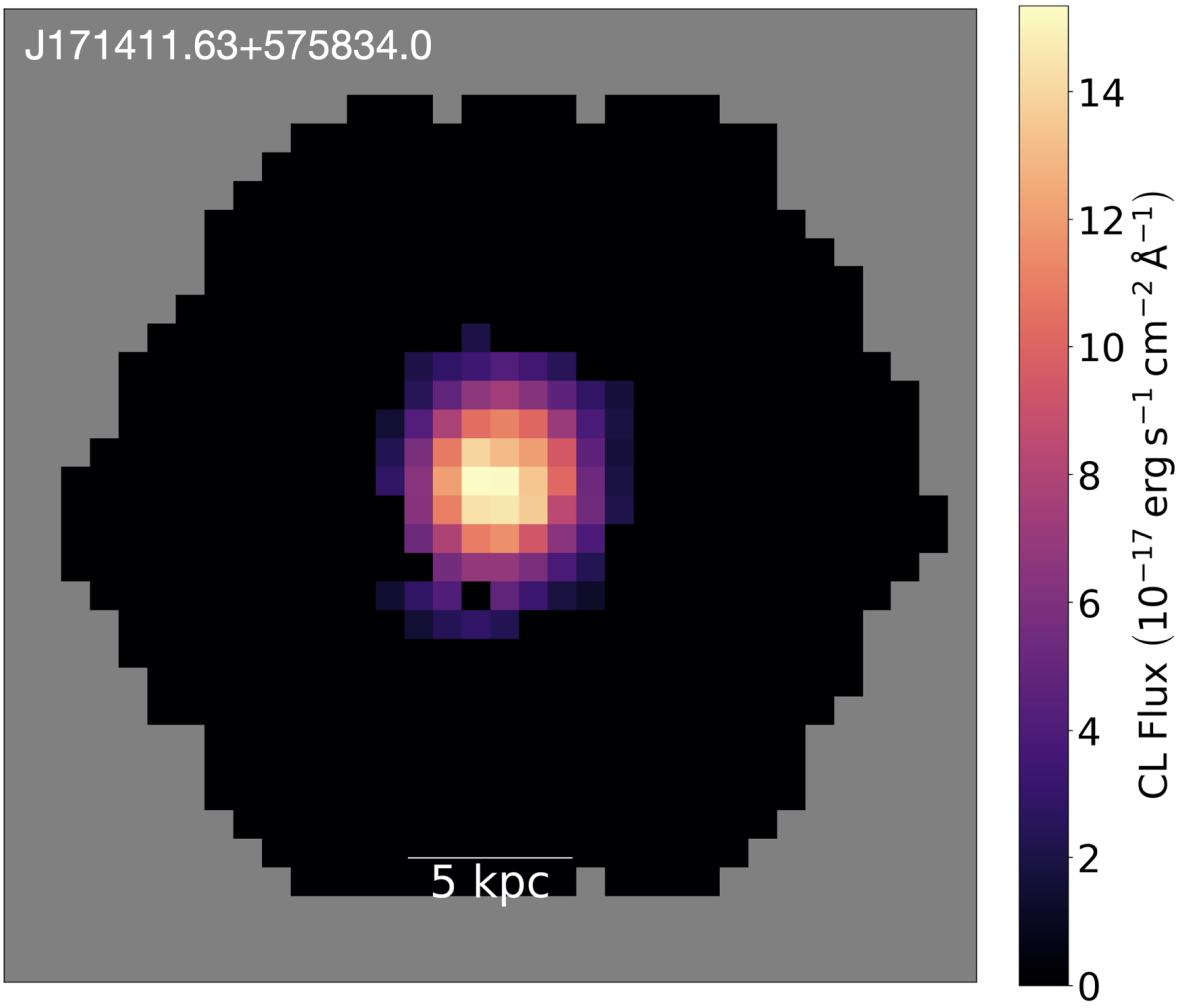

Figure 3.2: A sample CL flux map showing [NeV] λ3427 emission detected $\geq 5\sigma$ above the continuum in J1714. For this galaxy, the strongest [NeV] λ3427 emission is located near the center of the galaxy. The gray region is outside of the MaNGA FoV and the black region are spaxels with no CL emission. North is up, south is down, east is to the left, and west is to the right.

3.3.3 Galaxy Morphology

To uncover the correlation, if any, between CL emission and galaxy morphology (e.g., spiral and elliptical), we use the MaNGA Morphologies Galaxy Zoo value-added catalog to classify the morphologies of the galaxies in our sample. This catalog features data from Galaxy Zoo 2, a "citizen science" catalog with more than 16 million visual morphological classifications for $>$ 304,000 galaxies in SDSS (GZ2; [297]),

The weighted vote fraction (discussed in [297]) accounts for voter consistency when participants select morphological classifications, and we require this fraction to be $\geq 50\%$ before assigning a morphological classification (e.g., "E" for elliptical, or "S" for spiral). We also use the weighted vote fraction to determine if a CL galaxy features a bar, and/or is categorized as odd ("b" and"o", respectively).

In addition, to determine the fraction of CL galaxies undergoing a merger, we consider the analysis being performed by [195] ("Nevin catalog" hereafter). The authors determine the merger probability for each of the 1.3 million galaxies in the SDSS DR16 photometric sample, using a statistical learning tool that is built on a linear discriminant analysis framework, which is trained to separate mock images of simulated merging and non-merging galaxies using imaging predictors (see [194] for a full review). We investigate the MPL-11 galaxies from the broader SDSS DR16 Nevin catalog, and classify a CL galaxy as a merger if the Nevin catalog gives it a merger value (p_{merg}) > 0.5.

3.3.4 AGN Bolometric and [OIII] Luminosities

The AGN bolometric luminosity effectively traces the energetic output of an AGN (across the entire electromagnetic spectrum). To compare the luminosity of the CL AGN candidates with other known AGN candidates, we thus consider the bolometric luminosity parameter.

We determine the AGN bolometric luminosity for each CL galaxy using the summed

[OIII] flux values ($F_{[\mathrm{OIII}]}$) across the entire galaxy (provided by the MaNGA DAP), and the procedure outlined in [209], which assumes [OIII] emission comes from an AGN:

$$\log\left(\frac{\mathrm{L_{bol}}}{\mathrm{ergs^{-1}}}\right) = (0.5617 \pm 0.0978)\log\left(\frac{\mathrm{L_{[OIII]}}}{\mathrm{ergs^{-1}}}\right) + (21.186 \pm 4.164) \tag{3.2}$$

where $L_{[\mathrm{OIII}]} = F_{[\mathrm{OIII}]}(4\pi R^2)$ and R is the DAP provided luminosity distance based on redshift and a standard cosmology of $\Omega_M = 0.3$ and $\Omega_\Lambda = 0.7$ (redshift is also measured by the DAP).

We then measure the total [OIII] luminosity (using the summed [OIII] fluxes across the entire galaxy) for each CL galaxy in our sample. Next, we compare the [OIII] luminosities of the CLs in our pipeline (Section 3.4.3) to determine the relative strength of [OIII] for each CL. We do so to assess if specific CLs are preferentially found in higher or lower luminosity [OIII]-emitting galaxies, which is useful to determine if CLs uniformly trace all AGN, or if there may be an [OIII] luminosity dependence.

3.3.5 Narrow-Line BPT Diagnostics Diagrams

Baldwin-Phillips-Terlevich optical emission-line diagnostic diagrams (BPT diagrams; [11, 286, 143, 145]) are widely accepted to be effective tools for categorizing gas ionization sources as star-forming, Seyfert (AGN), low-ionization nuclear emission-line region (LINER), or a composite of multiple ionization sources. They serve as the traditional AGN selection tool for most spectroscopic surveys. Specifically, these diagrams compare line ratios between high and low ionization species, most commonly [OIII] λ5007/Hβ vs. [NII] λ6583/Hα ("[NII]/ Hα diagram" hereafter).

In this chapter, we construct spatially resolved narrow-line BPT diagnostic diagrams for the CL galaxies to better constrain the ionization sources of the CLs. To do so, we require emission line measurements for the [NII] λ6583, [OIII] λ5007, Hα, and Hβ emission lines. The DAP measures the continuum subtracted flux for each of these emission lines. Note, these fluxes account for galactic reddening using the E(B-V) values determined by the DRP, which assumes an [198] reddening law.

Once we determine the necessary emission line flux measurements, we compute the ratios for the [NII]/ Hα diagram, for each CL-emitting spaxel. We then use these values to create custom spatially-resolved BPT maps, whereby we present the BPT-classification for each CL-emitting spaxel within the MaNGA FoV, for each CL galaxy. Figure 3.3 shows an example BPT map.

3.3.6 Dust Attenuation

[187] investigated the [FeVII] λ6086, [FeX] λ6374, and [FeXI] λ7892 emission lines in the Seyfert 1 galaxy Ark 564. The authors used the photoionization code CLOUDY ([94]) to determine the location and kinematics of these lines. They found that the CLs are launched from a dusty torus near the SMBH, where the gas is quickly accelerated. Moreover, using the CLOUDY models, they determined that some iron carrying grains are destroyed during the initial acceleration of the gas.

To follow up on the analysis performed by [187], and to better understand the role of dust grains on the potential depletion of the iron CLs, we use the E(B - V) color excess index. This index traces the degree of interstellar reddening caused by photons that are scattered off of dust; in essence, it measures the difference between an object's observed color index and its intrinsic color index. E(B - V) values for each CL galaxy are provided by the MaNGA DRP (using [248] maps), and assume the extinction law provided by [198].

3.3.7 Shock Diagnostics

We explore the role of shocks (e.g., supernova remnant (SNR) and [OI] λ6300 ("[OI]" hereafter) shocks) in our analysis to elucidate the role of collisional excitation in the production CLs (e.g., [210]). To do so, we consider the strength of the [SII] $\lambda\lambda$6717, 6731 doublet with respect to the Hα line, which has traditionally been used to differentiate SNR shocks from photoionized regions. Specifically, [71] and [73] first determined that regions with [SII] $(\lambda 6717 + \lambda 6731)/\mathrm{H}\alpha > 0.4$ can be used to identify SNR shocks. Additionally, the [OI] emis-

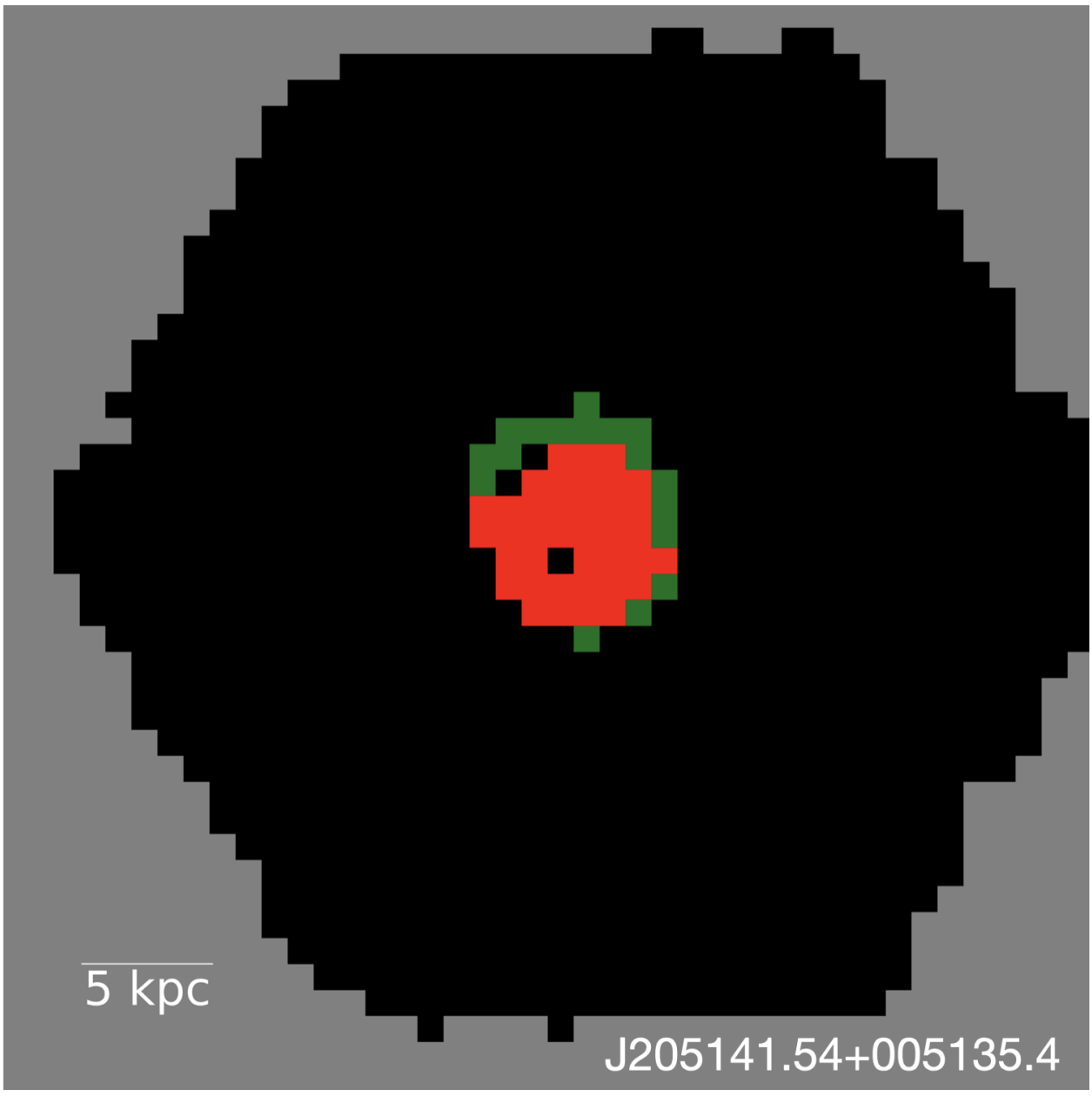

Figure 3.3: A sample BPT map showing AGN spaxels in red and composite spaxels in green, for CL-emitting spaxels in J2051 (a [NeV] λ3427 galaxy). The gray region is outside of the MaNGA FoV and the black region are spaxels with no CL emission. North is up, south is down, east is to the left, and west is to the right.

sion line is generally a strong tracer of shock excitation, and line flux ratios with [OI]/Hα> 0.1 indicate that shocks with velocities 160-300 km s $^{-1}$ are the main excitation source of [OI] (e.g., [77, 6, 91, 223, 224, 226, 51]). The MaNGA DAP provides flux measurements for the [SII] $\lambda\lambda$6717, 6731, [OI], and Hα emission lines.

3.4 Results

In this section, we report the main findings for the CL galaxies in our sample. First, we present the fraction of confirmed AGN in the CL galaxies. Then, we analyze the spatial distribution and extent of the CLs. Next, we inspect the CL galaxy bolometric and [OIII] luminosities to deduce the effectiveness of using each species for accurate AGN identification. After, we assess the BPT classification of the CL-emitting spaxels. Finally, we investigate the role of dust extinction and shocks in the CLR to determine the impact of dust grains on CL emission, and to further constrain the ionization source(s) of the CLs.

In total, we find 71 galaxies with CL emission at $\geq 5\sigma$ above the background continuum in MaNGA's MPL-11 (33 feature [NeV] emission, 39 feature [FeVII] emission, and 4 feature [FeX] emission). Note, in our sample, 40 unique CL galaxies with either [NeV] λ3427, [FeVII], or [FeX] emission, or a combination of the three, feature redshifts below the $z_{\rm min}$ threshold for [NeV] λ3347 ($z_{\rm min} = 0.088$); further, 24 unique CL galaxies with either [FeVII] or [FeX] emission feature redshifts below the $z_{\rm min}$ threshold for [NeV] λ3427 ($z_{\rm min} = 0.061$). Therefore, we are unable to scan for [NeV] λ3347 or [NeV] λ3427 in these respective galaxies. In general, most of the MPL-11 galaxies feature redshifts that place [NeV] $\lambda\lambda$3347, 3427 out of MaNGA's spectral range (see Section 3.3.1.1).

Moreover, in light of the extensive work to detect AGNs using infrared CLs, we cross-matched our catalog of 71 unique CL galaxies with the infrared CL catalogs presented in [100], [272], [9] [170], [293], [62], [105]. We do not identify any of the MaNGA CL galaxies in these samples.

For 63/71 CL galaxies with GZ2 classifications (89%), we determine a nearly even

fraction of spirals and ellipticals (48% and 52%, respectively). In addition, we measure the average size of the CLR (from the galactic center) for [NeV] $\lambda\lambda$3347, 3427, [FeVII] $\lambda\lambda\lambda$3586, 3760, 6086, and [FeX] λ6374 to be 1.9 kpc, 2.3 kpc, 3.7 kpc, 5.3 kpc, 4.1 kpc, and 2.5 kpc, respectively (Table 3.2). Further, we find that the vast majority of [NeV] galaxies feature at least one CL-emitting spaxel in their nuclear regions (98.5%; 2.″5 x 2.″5 FoV surrounding the central spaxel), whereas [FeVII] and [FeX] galaxies generally feature a smaller fraction (73% and 75%, respectively). The corresponding fraction of confirmed AGN in these galaxies (determined by comparing our sample to the largest catalog of confirmed MaNGA AGN; Section 3.4.1) is 94%, 14%, and 25%, respectively.

3.4.1 MaNGA AGN Comparison

Comerford et al. (in prep) provide the most complete sample of AGN in MaNGA's MPL-11 (see [52] for a full review of their MPL-8 MaNGA AGN catalog). The authors compile a catalog of MaNGA AGN that were detected using SDSS broad emission lines, NVSS/ FIRST 1.4 GHz radio observations, *WISE* mid-infrared color cuts, and *Swift*/BAT hard X-ray observations.

Broad Balmer emission lines (FWHM $>$ 1,000 km s^{-1}) are strong tracers of the rapidly rotating, high density gas, near the SMBH. They serve as reliable tracers for AGN activity. [200] assembled a catalog of nearby ($z \leq 2$) Type I AGN in SDSS's seventh data release using the broad Hα emission line, and Comerford et al. (in prep) identify 78 broad line AGN from this catalog in MPL-11.

Powerful AGN radio jets can expand several kpcs from the SMBH, and can thus serve as strong signatures for AGN activity. As a result, detecting the radio emission from these sources is a great tool for accurate AGN identification. [25] used observations from the 1.4 GHz NRAO Very Large Array Sky Survey (NVSS; [56]) and the Faint Images of the Radio Sky at Twenty Centimeters (FIRST; [15]) to detect AGN in the SDSS's seventh data release (DR7). They differentiated AGN activity from star formation emission using the correlation

between the 4000 Å break strength and radio luminosity per stellar mass, emission line diagnostics, and the relation between Hα and radio luminosity ([15]). Comerford et al. (in prep) find 221 radio AGN from this catalog in MPL-11.

Heated dust that surrounds an AGN can produce mid-infrared emission, which can expose obscured and unobscured AGN activity. Comerford et al. (in prep) thus rely upon observations from the *Wide-Field Infrared Survey Explorer* (*WISE*; [299]) to help identify AGN. They consider the four bands observed with *WISE* (3.4 μm (W1), 4.6 μm (W2), 12 μm (W3), and 22 μm (W4)) and apply a 75% reliability criteria of W1 - W2 $>$ 0.486 exp$\{0.092(\text{W2 - } 13.07)^2\}$ and W2 $>$ 13.07, or W1 - W2 $>$ 0.486 and W2 $\leq$ 13.07 ([10]) to select AGN. Comerford et al. (in prep) detect 130 *WISE* AGN in MPL-11.

X-ray emission produced by AGN generally result from inverse Compton scattering of low energy UV photons by energetic electrons from the accretion disk (e.g., [7, 112, 124]). Therefore, X-rays can be a useful indicator of AGN activity. Accordingly, the authors use the X-ray catalog assembled by [199], which consists of $\approx$ 1,000 AGN observed by the *Swift Observatory's* Burst Alert Telescope (BAT) in the ultra hard X-ray (14 - 195 keV), to detect AGN. Comerford et al. (in prep) uncover 30 AGN from this catalog in MPL-11.

We compare our CL sample to the AGN catalog reported by Comerford et al. (in prep; "Comerford sample" hereafter) and cross-match 35 CL galaxies in it (52% of our sample). Further, we consider the fraction of CL galaxies with confirmed AGN by specific CL species. We determine that 94% (31/33) of the [NeV] galaxies host an AGN; 14% (5/36) of the [FeVII] galaxies and 25% (1/4) of the [FeX] galaxies. Overall, 35 unique CL galaxies host a confirmed AGN; 80% (28/35) are confirmed with *WISE* observations, 63% (22/35) with broad Balmer emission lines, 14% (5/35) with NVSS observations, and 11% (4/35) with BAT AGN.

All of the [NeV] λ3347 galaxies feature an AGN and [NeV] λ3427 emission, and of the five [FeVII] galaxies with a confirmed AGN, two (J0736 and J1714) also feature both [NeV] $\lambda\lambda$3347, 3427 emission. Further, two of the remaining three [FeVII] galaxies with a

Table 3.2: Spatial Properties for the CL Galaxies

Detected CL (1)	Wavelength (Å) (2)	Confirmed Galaxies (3)	Nuclear Emission (%) (4)	CLD_{min} kpc (5)	CLD_{max} kpc (6)	CLD_{avg} kpc (7)
[NeV]	3347	8	100	0.52	5.3	1.9
[NeV]	3427	33	97	0.34	19	2.3
[FeVII]	3586	4	100	0.10	9.6	3.7
[FeVII]	3760	16	56	0.11	36	5.3
[FeVII]	6086	19	63	0.10	21	4.1
[FeX]	6374	4	75	0.60	4.9	2.5

Note: Columns are (1) detected CL, (2) rest wavelength, (3) number of galaxies with CL emission detected, (4) percentage of CL galaxies with at least one CL-emitting spaxel in a nuclear 2.″5 FoV, (5) the average CLD (distance of CL-emitting spaxel from the galaxy center), (6) the distance of the furthest CL-emitting spaxel from the galaxy center, and (7) the distance of the closest CL-emitting spaxel from the galaxy center.

confirmed AGN (J0807 and J1157) feature emission from more than one [FeVII] emission line (J0807 features [FeVII] $\lambda\lambda\lambda$3586, 3760, 6086 emission; J1157 features [FeVII] $\lambda\lambda$3586, 3760 emission). The final [FeVII] galaxy with a confirmed AGN exclusively features [FeVII] λ6086 emission, and the sole [FeX] galaxy with a confirmed AGN (J1628) exclusively features [FeX] emission.

Provided that 80% of the CL galaxies in our sample are confirmed to host an AGN via *WISE* diagnostics, we consider the fact that these *WISE* diagnostics are likely to miss low luminosity AGN (e.g., [10]). Perhaps, one possible explanation for the discrepancy in AGN across the CLs in our sample is that [NeV] traces high-luminosity AGN, while [FeVII] and [FeX] may possibly trace low-luminosity AGN. We explore this further in Sections 3.4.3 and 3.4.5.

3.4.2 Spatial Distribution and Extent of the CLs

To better constrain the ionization source(s) of the CLs, we first map the measured fluxes of the CLs within the MaNGA FoV for each CL galaxy (Figure 3.2). These flux maps provide a snapshot of the orientation, extent, and intensity of CL emission for the galaxies in

our sample. Then, we compute the de-projected distance of each CL spaxel from the nuclear center of each galaxy (i.e. the photometric center; Section 3.3.2) to determine the distance of each CL-emitting spaxel from the galaxy center. Finally, we define the nuclear region of each CL galaxy to be a 2.″5 x 2.″5 aperture (5 x 5 spaxel grid; where each spaxel covers a 0.″5 x 0.″5 FoV) surrounding the central spaxel.

If AGN photoionization is the primary mechanism producing the CLs, it is likely that CL emission is predominantly within the nuclear region of each galaxy, close to the SMBH and the accretion disk (e.g., [99, 180]). On the other hand, if shocks, AGN outflows, or stellar processes play an active role in generating CLs, we anticipate that CL emission will not be found exclusively in the nuclear region. Rather, we would expect to find emission in regions off-center or off-axis from the SMBH and the galaxy's rotational plane (see [191] for more discussion).

To analyze the CL distribution within the nuclear region of the CL galaxies, we measure the fraction of CL galaxies with at least one CL emitting spaxel in their center, for each CL (Table 3.2). We find that the vast majority of [NeV] $\lambda\lambda$3347, 3427 galaxies feature at least one [NeV]-emitting spaxel in their nuclear regions (100% and 97%, respectively). This finding is consistent with our results in Section 3.4.1, that [NeV] is a strong tracer of AGN activity (i.e. CL emission is likely dominated by AGN photoionization near the SMBH). Comparatively, the fraction of CL galaxies with nuclear emission from [FeVII] $\lambda\lambda\lambda$3586, 3760, or 6086 varies significantly more (100%, 56%, and 63%, respectively).

In Figure 3.4, we present a sample of CL flux maps for six representative CL galaxies. In three of the galaxies (J1104, J1349, and J2152), it is apparent that the source of the CLs is within the nuclear region, as the CL flux is concentrated here. However, for the three remaining galaxies (J0023, J1613, and J0920), the CL-emitting spaxels are highly offset from the nuclear region. Based on the orientation of the CL flux in J0023 and J0920, it is possible that AGN outflows are generating the CL since the CL emission is generally perpendicular to the orbital plane of each galaxy. For the J1613 observation, we determine that several optical

emission lines (e.g., [OIII] and Hα) measured in the secondary galaxy (with the featured "CL emission"; southwest of J1613 in the MaNGA FoV) have large velocity shifts ($>$ 2,000 km s^{-1}) compared to the center of J1613, which suggests this may not be a companion galaxy (i.e., this is not a merging system; J1613 is not in the Nevin catalog). As a result, the "CL emission" in this galaxy is likely from a separate emission line, from a background galaxy with a different redshift than the primary galaxy. For J1349, we acknowledge that there appears to be a visual companion galaxy near the nuclear region; it is possible that both merger induced shocks and AGN photoionization could be producing the CL emission. In addition, we suspect that dust grains may also have a significant impact on the presence of [FeVII] and [FeX] emission in our sample. In Section 3.4.5, we review the likelihood of iron depletion by dust grains more thoroughly.

We also compute the CLDs for the CL galaxies. The CLD, which is the distance of each CL-emitting spaxel from the galactic center, reveals the physical scale of the CLR for each CL galaxy. We measure the average CLDs for [NeV] $\lambda\lambda$3347, 3427 to be 1.9 kpc and 2.3 kpc, respectively; 3.7 kpc, 5.3 kpc, and 4.1 kpc for [FeVII] $\lambda\lambda\lambda$3586, 3760, 6086, respectively; 2.5 kpc for [FeX]λ6374. We find no correlation between IPs and CLDs (IP = 233.6 eV for [FeX], IP =97.1 eV for [NeV], and IP = 99.1 eV for [FeVII]). Moreover, for the [NeV] galaxies, the minimum and maximum distances of each CL-emitting spaxel from the nuclear center (labeled CLD$_{min}$ and CLD$_{max}$ in Table 3.2) ranges between 340 pc to 19 kpc, 100 pc to 36 kpc for the [FeVII] galaxies, and 600 pc to 4.9 kpc for the [FeX] galaxies. These large variances in CL distance suggest that the CLR extends from just beyond the BLR ($\approx$ 0.1 kpc) and well into the NLR (several kpcs).

Finally, to confirm that CL emission is indeed resolved for each CL galaxy, we consider the instrument PSF ($\approx 2.''5$ for MaNGA), and find that 60/71 CL galaxies show resolved and continuous emission in excess of the typical instrument PSF. The remaining 11 CL galaxies (J0205, J1010, J1117, J1317, J1344, J1416, J1604, J1626, J1628, J1658, and J1649) lack CL emission in excess of the typical instrument PSF. We reason that these CLRs are below

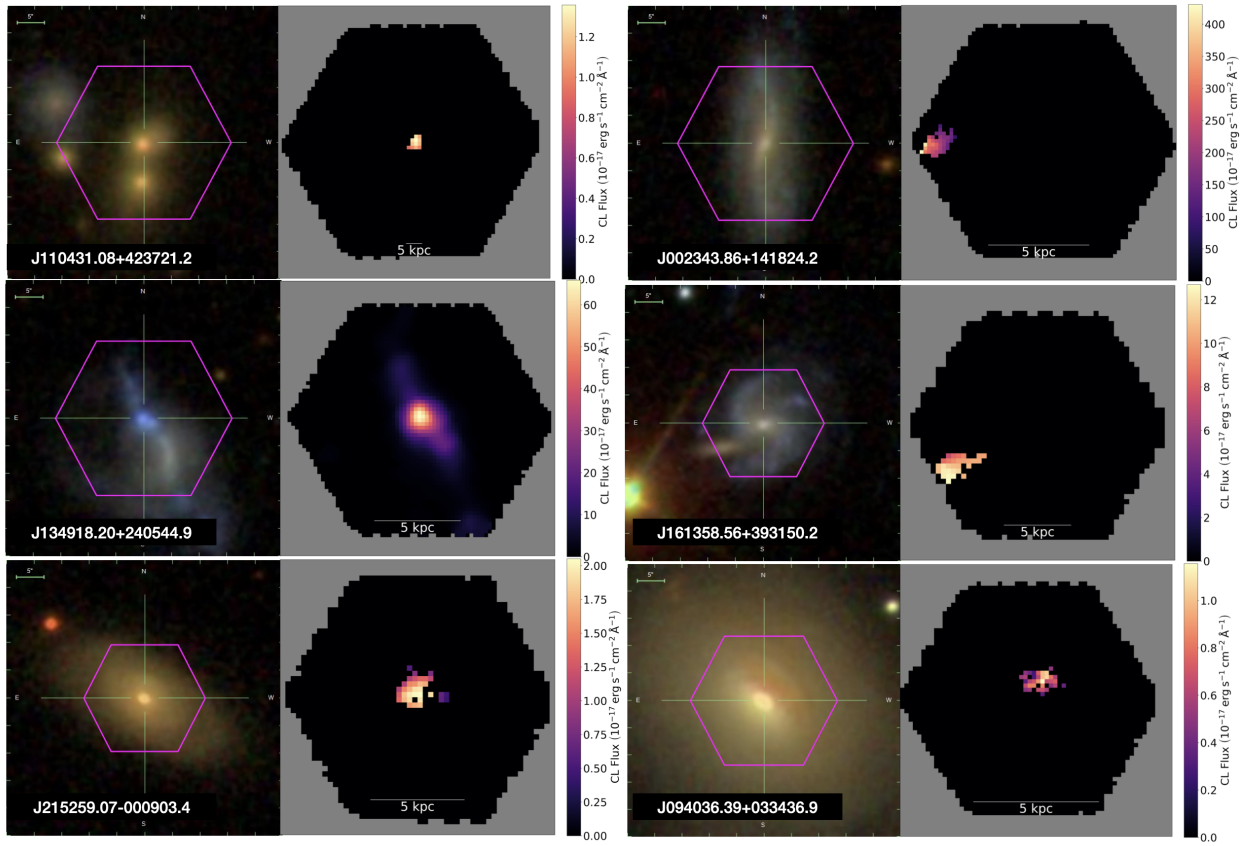

Figure 3.4: CL flux maps for 6/71 CL galaxies in our sample. From top to bottom and left to right: J1104 ([NeV] λ3427 map), J0023 ([FeVII] λ3760 map), J1349 ([FeVII] λ3760 map), J1613 ([FeVII] λ3760 map), J2152 ([FeVII] λ6086 map), and J0940 ([FeVII] λ6086 map). For J0023 and J0940, the maps display CL emission spatially offset from the galaxy center. For each galaxy, the emission is offset perpendicular to the rotational plane of the galaxy, suggestive of the source of the CLs being AGN outflows. For J1349 we observe a possible companion galaxy and consider the possibility that these two galaxies to be undergoing a merger. For the J1613 observation, we determine that several optical emission lines (e.g., [OIII] and Hα) measured in the secondary galaxy (with the featured "CL emission"; southwest of J1613 in the MaNGA FoV) have large velocity shifts ($>$ 2,000 km s^{-1}) compared to the center of J1613, which suggests this may not be a companion galaxy (i.e., this is not a merging system; J1613 is not in the Nevin catalog). As a result, the "CL emission" in this galaxy is likely from a separate emission line, from a background galaxy with a different redshift than the primary galaxy. For J1104 and J2152, CL emission is concentrated towards the galaxy center, likely produced by AGN photoionization.

the instrument PSF, and not spatially resolved. As discussed in [191], these CLRs may still be spatially resolved by other instruments (e.g., [180] and their use of STIS/HST optical spectra), and it is also possible that CL emission may be oriented along an ionization cone; however here we consider the CLDs of these galaxies to be upper limits.

3.4.3 AGN Bolometric and [OIII] Luminosities

AGN bolometric luminosity, which scales with [OIII] luminosity, is effectively the "power" of an AGN. As outlined in [209], [OIII] emission is the most utilized line for measuring bolometric luminosity, due its strength in most AGN spectra and the relatively weak blending of emission from photoionized gas in star forming regions with the line (e.g., [121, 120]).

Therefore, to help resolve the discrepancy between the differing fractions of confirmed AGN in our sample (Section 3.4.1; 94% of the [NeV] galaxies feature a confirmed AGN, 14% for the [FeVII] galaxies, and 25% of the [FeX] galaxies; for CL galaxies with multiple CLs, we measure this fraction independently for each CL), and to evaluate the overall effectiveness of using CL detections to identify AGN, we consider the bolometric and [OIII] luminosities of the CL galaxies, and further inspect the Comerford sample of MaNGA AGN. In particular, we compare the mean bolometric luminosities of the CL galaxies ($L_{\rm bol}$; using the summed [OIII] flux across the entire galaxy; Section 4.3.3) with the total population of MPL-11 AGN in the Comerford sample (Section 3.4.1; Figure 3.5).

We find that the mean bolometric luminosity for the [NeV] galaxies (mean $z = 0.10$; median $z = 0.11$), $\log(L_{\rm bol}) = 44.5$ erg s^{-1}, is consistent with the mean value of Comerford's population of MaNGA galaxies that host an AGN ($\log(L_{\rm bol}) = 44.6$ erg s^{-1}). On the other hand, we measure the mean bolometric luminosities of the [FeVII] galaxies (mean $z = 0.06$; median $z = 0.05$) and the [FeX] galaxies (mean $z = 0.07$; median $z = 0.06$) to be an order of magnitude lower than the mean $\log(L_{\rm bol})$ value of the Comerford sample ($\log(L_{\rm bol}) = 43.7$ erg s^{-1} and $\log(L_{\rm bol}) = 43.5$ erg s^{-1} for the [FeVII] and [FeX] galaxies, respectively). Note,

we also present the [OIII] luminosity distribution for the CL galaxies in Figure 3.6 (the mean [OIII] luminosity for the [NeV] galaxies is 41.5 erg s^{-1}; 40.1 erg s^{-1} and 39.8 erg s^{-1} for the [FeVII] and [FeX] galaxies, respectively). We reason that the [FeVII] and [FeX] galaxies may be preferentially tracing lower luminosity AGN in MaNGA, which are generally more difficult to detect in multi-wavelength observations.

However, we find that the five [FeVII] galaxies with a confirmed AGN (J0736, J0807, J1157, J1535, and J1714) all feature relatively high [OIII] luminosities of $\log(L_{[OIII]}) \gtrapprox 41$ erg s^{-1}. Additionally, the three remaining [FeVII] galaxies with [OIII] luminosities at or above this limit (without confirmed AGN) are J0906, J1349, and J2152. Both J0906 and J1349 visually appear to be actively undergoing a merger; J2152 shows no apparent companion galaxy. We reason that, for the [FeVII] galaxies in our sample, the $\log(L_{[OIII]})$ cutoff of ≈ 41 erg s^{-1} is a useful threshold for identifying confirmed AGN (from the Comerford sample) and may also be helpful for detecting mergers. Further, for the [NeV] galaxies, J1344 features the lowest [OIII] luminosity ($\log(L_{[OIII]}) = 40.6$ erg s^{-1}) and in fact hosts a confirmed AGN. We consider the [OIII] luminosity threshold for the [FeVII] galaxies ($\log(L_{[OIII]}) \approx 41$ erg s^{-1}) to be similar for the [NeV] galaxies.

We also determine that the two [NeV] galaxies (J1658 and J1104) that do not feature a confirmed AGN (out of 33 total [NeV] galaxies), feature [OIII] luminosities of $\log(L_{[OIII]}) = 41.2$ erg s^{-1} and $\log(L_{[OIII]}) = 41.4$ erg s^{-1}, respectively. Considering these high [OIII] luminosities, and the high [NeV] AGN detection rate (94%), we propose that these two galaxies are strong AGN candidates.

On the other hand, the one [FeX] galaxy with a confirmed AGN, J1628, features an [OIII] luminosity of $\log(L_{[OIII]}) = 39.8$ erg s^{-1} (the remaining three [FeX] galaxies, which do not host a confirmed AGN, also have log([OIII]) luminosities < 40 erg s^{-1}). Consequently, while we consider the $\log(L_{[OIII]}) \approx 41$ erg s^{-1} threshold useful for identifying CL galaxies with a confirmed AGN, it is important to acknowledge that CL galaxies with a confirmed AGN can have [OIII] luminosities below this limit.

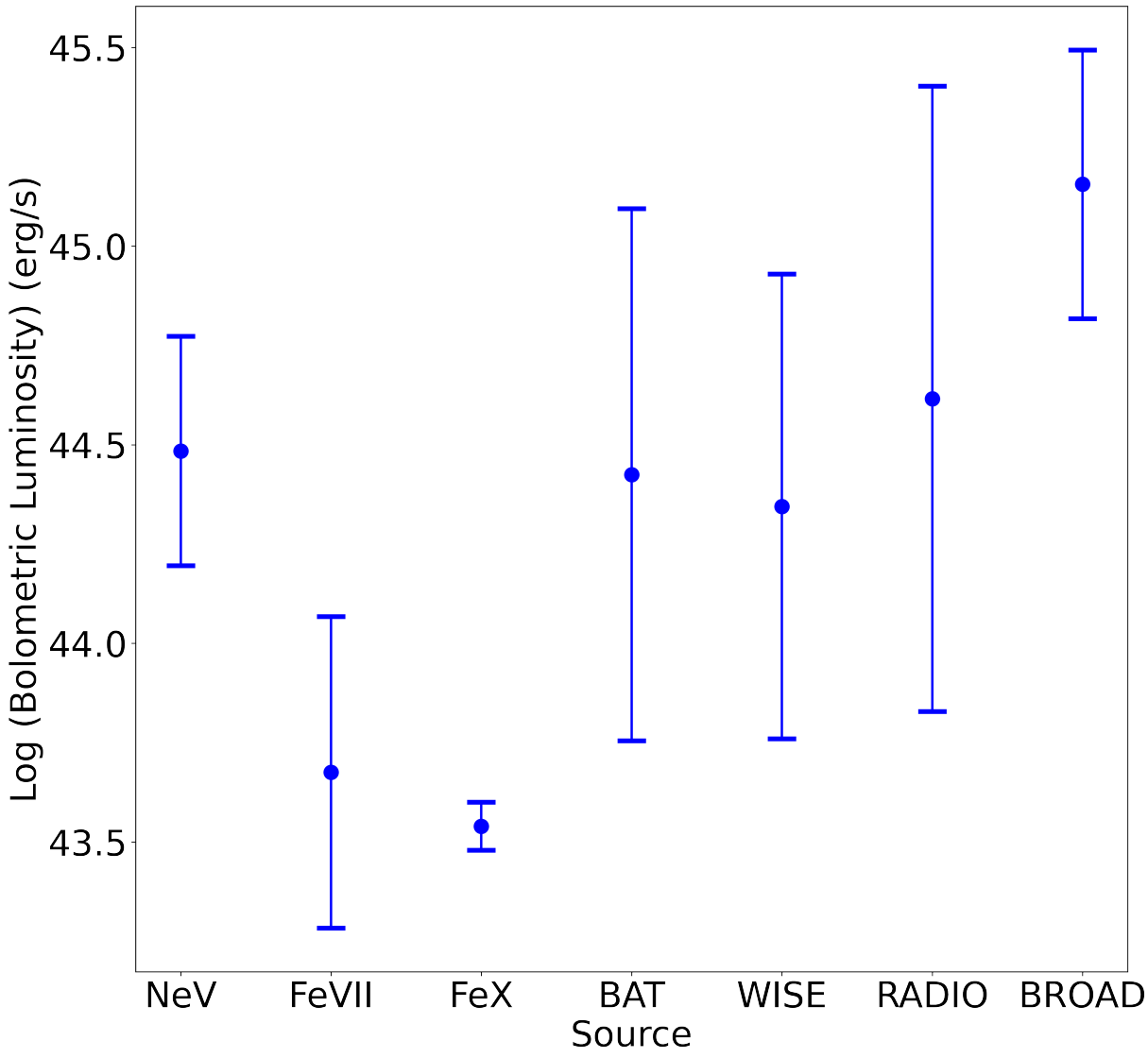

Figure 3.5: Average mean bolometric luminosities for the 71 CL galaxies in our sample (analyzed by each CL species; [NeV], [FeVII], and [FeX]), compared to the MaNGA galaxies confirmed to feature an AGN in the Comerford sample. The AGN in the Comerford sample were verified using SDSS broad emission lines, NVSS/ FIRST 1.4 GHz radio observations, *WISE* mid-infrared color cuts, and *Swift*/BAT hard X-ray observations. The mean bolometric luminosity of the [NeV] galaxies, $\log(L_{\rm bol}) = 44.5$ erg s^{-1}, is consistent with the AGN reported in the Comerford sample (mean $\log(L_{\rm bol}) = 44.6$ erg s^{-1} for the Comerford sample). However, the [FeVII] and [FeX] galaxies feature mean bolometric luminosities an order of magnitude lower ($\log(\rm L_{bol}) \leq 43.7$ erg s^{-1}) than the Comerford sample. We suspect that the [FeVII] and [FeX] emission lines may primarily be detecting low luminosity AGN in MaNGA.

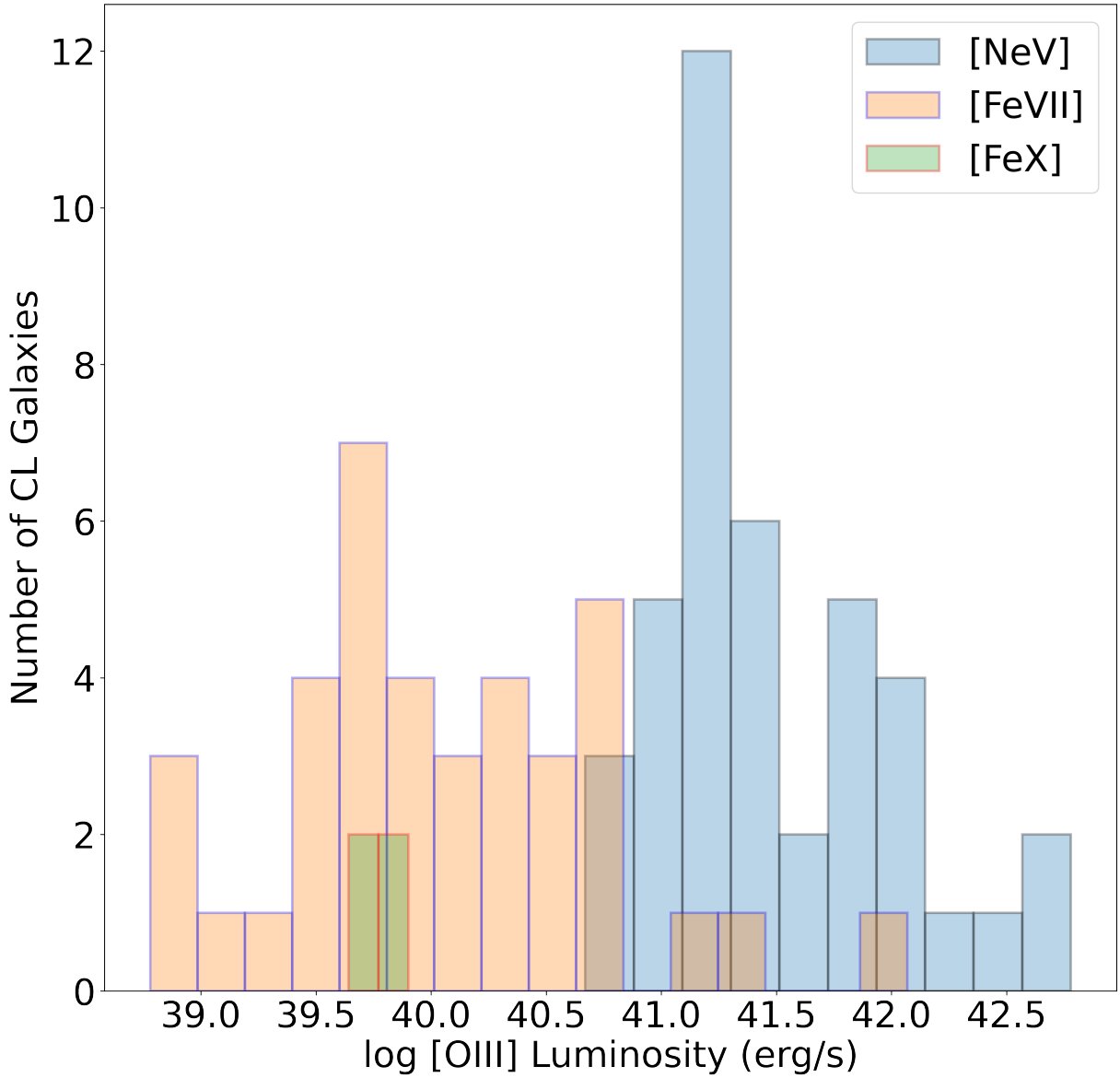

Figure 3.6: The log([OIII]) luminosity distribution for the 71 CL galaxies. The blue, orange, and green histograms represent the [NeV], [FeVII], and [FeX] galaxies in our sample, respectively. [NeV] emitting galaxies tend to have higher [OIII] luminosities than [FeVII] or [FeX], which suggests that these galaxies may host higher luminosity AGN. The mean of the [NeV] log([OIII]) luminosity distribution is 41.5 erg s^{-1}; 40.1 erg s^{-1} and 39.8 erg s^{-1} for [FeVII] and [FeX], respectively.

3.4.4 BPT Analysis

The BPT diagram has long served as the standard tool for identifying ionization mechanisms in emission line sources (e.g, [11, 286, 143, 145]). While effects such as stellar shocks and emission from post-AGB stars are liable to elevate SF sources beyond the AGN threshold (see [302, 19, 4] for a further discussion), we nonetheless explore the BPT classification for each CL-emitting spaxel to help pin down the source of CL emission in our sample. To do so, we compute the log([OIII]/Hβ) and log([NII]/Hα) ratios required for the [NII]/Hα diagram (Section 3.3.5). Using the thresholds outlined in [145], we categorize each CL spaxel as either [HII] (i.e. star forming), AGN, or a composite of the two. Note, for some CL-spaxels, the DAP reports negative values for the necessary emission line fluxes, likely because the emission lines of interest yield low flux levels and the DAP's subtraction of the stellar continuum results in a net absorption at the expected wavelength of the emission line. As such, we exclude these spaxels from our analysis.

For the [NeV], [FeVII], and [FeX] emission lines, we determine that, on average, the majority of CL-emitting spaxels are AGN or composite (Table 3.3). For [NeV] $\lambda\lambda$3347, 3427 we find that 87.5% and 90% of these spaxels are classified as AGN, respectively; 12.5% and 10% composite, respectively; 0% SF for both. Moreover, we measure the BPT ratios for the [FeVII] $\lambda\lambda\lambda$3586, 3760, 6086 spaxels, and find that 78.5%, 80.3%, and 67.9% of these spaxels are classified as AGN, respectively; 19%, 5.8%, and 19.7% composite, respectively; 2.5%, 13.9%, and 12.5% SF, respectively. For [FeX] λ6374, 88.3% of the CL-emitting spaxels are classified as AGN; 0% composite; 11.7% SF. In total, 100% of the [NeV] spaxels in our sample are either BPT AGN or BPT composite, 91% of the [FeVII] spaxels, and 88.3% of the [FeX] spaxels. These results suggest that the CLs are perhaps useful tracers of AGN, and that the lack of confirmed AGN in our [FeVII] and [FeX] galaxies may trace back to the nearly bimodal log([OIII]) and bolometric luminosity distributions presented in Section 3.4.3 (i.e. [FeVII] and [FeX] may generally be found in low luminosity AGN that are potentially missed by traditional AGN detection techniques; though, it is also possible that [FeVII] and [FeX] may not host an AGN at all). We explore this possibility, and the corresponding

Table 3.3: BPT Classifications for the CL Galaxies

Detected CL	Rest Wavelength Å	Confirmed CL Galaxies	Confirmed AGN	Confirmed AGN Fraction %	[NII] AGN Fraction %	[NII] Composite Fraction %	[NII] SF Fraction %
(1)	(2)	(3)	(4)	(5)	(6)	(7)	(8)
[NeV]	λ3347	8	8	100	87.5	12.5	0
	λ3427	33	31	94	90	10	0
[FeVII]	λ3586	4	3	75	78.5	19	2.5
	λ3760	16	2	13	80.3	5.8	13.9
	λ6086	19	3	16	67.9	19.7	12.5
[FeX]	λ6374	4	1	25	88.3	0	11.7

Note: Columns are (1) detected CL, (2) rest wavelength, (3) the number of galaxies that feature emission from the respective line, (4) the fraction of galaxies that host a confirmed AGN, (5) the average fraction of [NII] AGN BPT spaxels, (6) the average fraction of [NII] Composite BPT spaxels, and (7) the average fraction of [NII] SF BPT spaxels.

impact of dust extinction on iron CL emission in Section 3.4.5.

3.4.5 The Impact of Dust on CL Emission

The role of dust extinction (i.e. the impact of dust grains) on CL emission has yet to be fully unraveled. [187] suggest that dust grains can potentially deplete heavier CL species (e.g., iron). Further, [92] posit that there are three primary effects of dust on line formation: 1) emission lines weaken due to the absorption of the incident continuum by dust, 2) grains photoelectrially heat the gas, and 3) some of the gas-phase elements (e.g., iron) are depleted (see also [251, 261, 47, 154]). Comparatively, [92] contend that neon (a noble gas; i.e. a species of gas with a full outer shell of valence electrons, and thus less chemical reactivity) is significantly less depleted by dust grains, and therefore [NeV] is emitted almost fully outside the grain sublimation radii. Here, we consider the likelihood that a significant population of iron CL photons are destroyed by dust in our sample.

To explore the role of dust extinction on CL emission in our sample, and to determine its relevance for the discrepancy between the fraction of confirmed AGN in the [NeV] galaxies (94%) vs. the [FeVII] and [FeX] galaxies (14% and 25% respectively; Section 3.4.1), we use the E(B - V) color excess index, which traces interstellar reddening (Section 3.3.6). The MaNGA DRP provides this index for each galaxy in MPL-11, and we use it to determine if there is a correlation between the dust content of each CL galaxy and its CL emission. We present our findings in Table 3.4.

In particular, we find the mean E(B - V) values for the [FeVII] $\lambda\lambda$3760, 6086 galaxies to be the lowest (i.e. feature less dust grains) across our sample (0.029 and 0.039, respectively). Because iron is susceptible to destruction by dust grains, particularly in the nuclear region where the presence of dust is greater (also due to dust in the NLR), these relatively low values provide a viable explanation for the presence of [FeVII] $\lambda\lambda$3760, 6086 emission in these galaxies; for reference, our sample contains 16 [FeVII] λ3760 galaxies and 19 [FeVII] λ6086 galaxies. Comparatively, the [NeV] $\lambda\lambda$3347, 3427, [FeVII] λ3586, and [FeX] λ6374

Table 3.4: CLR Dust Attenuation

Detected CL (1)	Wavelength (Å) (2)	Average E(B-V) Value (3)
[NeV]	3347	0.057
	3427	0.045
[FeVII]	3586	0.045
	3760	0.029
	6086	0.039
[FeX]	6374	0.049

Note: Columns are (1) detected CL, (2) rest wavelength, and (3) average E(B-V) values, for each CL, reported by MaNGA's DRP.

galaxies feature higher mean E(B- V) values; 0.057, 0.045, 0.045, and 0.049, respectively. The corresponding number of iron CL-emitting galaxies found in these galaxies is only nine in total (J0736 features emission from both [NeV] lines, as well as [FeVII] λ3586 emission; J1714 features emission from both [NeV] lines, as well as [FeVII] λ6086 emission; J0807 features emission from [FeVII] $\lambda\lambda\lambda$3586, 3760, 6086; J1157 features emission from [FeVII] $\lambda\lambda$3586, 3760; J0906 features emission from [FeVII] λ3586; J1628, J2311, J1649, and J1720 exclusively feature emission from [FeX] λ6374). We suspect that emission from the iron CL species is being diminished within these relatively dusty galaxies, which provides a physical explanation for the low number of iron CL galaxies in the high E(B - V) value galaxies (E(B - V) $\geq$ 0.045; nine iron CL galaxies) vs. the low E(B - V) galaxies (E(B - V) $<$ 0.039; 34 iron CL galaxies).

Furthermore, [83] considered the correlation between the AGN dusty torus and AGN bolometric luminosity. They proposed that the dusty torus diminishes at $\log(L_{\rm bol}) \lessapprox 42$ erg s^{-1}, due to mass accretion no longer being able to sustain the necessary cloud outflow rate, which effectively results in a decrease in column density (see also [44, 296, 173]). While the cloud component of the AGN is not immediately extinguished below this threshold, the authors contend that the cloud outflow rate at $\log(L_{\rm bol}) \lessapprox 42$ erg s^{-1} is less than the

necessary "standard" observed in higher luminosity AGN. As a result, we consider the L_{bol} values for the CL species (Figure 3.5, mean $\log(L_{bol}) \geq 44.3$ erg s^{-1} for [NeV] galaxies; mean $\log(L_{bol}) \leq 43.7$ erg s^{-1} for the [FeVII] and [FeX] galaxies) to conclude that the lower L_{bol} values correlate with a diminishing dusty torus, which results in less destruction of iron by dust grains. Accordingly, we detect more iron CLs in these low luminosity sources. On the other hand, the [NeV] galaxies feature higher L_{bol} values, which likely correspond to their elevated E(B - V) values. Likewise, since L_{bol} scales with L_{OIII}, this reasoning elucidates the nearly bimodal $\log(L_{OIII})$ distribution of the [NeV] vs. the [FeVII] and [FeX] galaxies (Figure 3.6; the mean of the [NeV] log([OIII]) luminosity distribution is 41.5 erg s^{-1}; 40.1 erg s^{-1} and 39.8 erg s^{-1} for [FeVII] and [FeX], respectively).

3.4.6 SNR, [OI], and Merger-Induced Shocks in the CLR

Astrophysical shocks can result from a variety of mechanisms, which include, but are not limited to, galaxy collisions, SNRs, cloud-cloud collisions, expanding HII regions, and outflows from young stellar objects (see [6] for a further review). To deduce the role of shocks in the CLR, we consider the [SII] $(\lambda6717 + \lambda6731)/\mathrm{H}\alpha$ and [OI]$\lambda6300/\mathrm{H}\alpha$ ratios for each CL-emitting spaxel in our sample (values > 0.4 indicate SNR shocks and values > 0.1 trace [OI] shocks, respectively; Section 3.3.7).

We also investigate the fraction of CL galaxies actively undergoing a merger using the Nevin et al., catalog (Table 3.5; Table 3.7; Section 3.3.3). In [191], we found that the 3/10 CL galaxies without a confirmed AGN were all strong merger candidates (J0906, J1349, and J1454). Therefore, we consider the possibility that companion galaxies can drive gas inflows towards the galactic centers, resulting in merger-induced shock excitation (e.g., [91]) that may also produce CLs. Using the Nevin catalog, here we determine that 32/66 of the CL galaxies (48%; 5 CL galaxies are not reported in the Nevin catalog: J0752, J0920, J1306, J1613, and J2132) have $\mathrm{p_{merg}}$ values > 0.5 - indicative of an ongoing merger.

Further, we present our SNR and [OI] shocks results in Tables 3.9 and 3.10. Overall, we find that the fraction of SNR and [OI] shocks do not vary significantly for the CL galaxies. In particular, on average and across all CL species, 42% of the CL-emitting spaxels in the CL galaxies with a confirmed AGN feature SNR shocks (35% feature [OI] shocks), whereas 56% of the CL-emitting spaxels in the CL galaxies without a confirmed AGN feature SNR shocks (49% feature [OI] shocks). Further, on average and across all CL species, 32% of the CL-emitting spaxels in the CL galaxies undergoing a merger feature SNR shocks (38% feature [OI] shocks). On the other hand, 36% of the CL-emitting spaxels in the CL galaxies not undergoing a merger feature SNR shocks (27% feature [OI] shocks). Finally, on average and across all CL species, 41% of the CL-emitting spaxels in the CL galaxies with nuclear CL emission feature SNR shocks (32% feature [OI] shocks). Comparatively, 27% of the CL-emitting spaxels in the CL galaxies without nuclear CL emission feature SNR shocks (44% feature [OI] shocks).

Table 3.5: Morphological and Merger Classifications of the CL Galaxies (Continued)

SDSS Name	Detected CL(s)	Redshift	Morphology	Merger
(1)	(2)	(3)	(4)	(5)
J001938.78+144201.1	[FeVII]λ6086	0.116	E	N
J002343.86+141824.2	[FeVII]λ3760	0.018	S(b)	N
J020557.03+004623.9	[FeVII]λ6086	0.042	E	N
J021257.59+140610.2	[NeV]λ3427	0.062	-	N
J030639.57+000343.1	[NeV]λ3427	0.107	E	Y
J072656.07+410136.0	[NeV]λ3427	0.129	S(b)	Y
J073623.13+392617.7	[NeV]λ3347, [NeV]λ3427, [FeVII]λ3586	0.118	-	Y
J074128.48+442431.6	[NeV]λ3427	0.132	E	N
J075217.84+193542.2	[NeV]λ3427	0.117	-	-
J075756.71+395936.1	[NeV]λ3427	0.066	E(o)	Y
J080018.53+461112.3	[FeVII]λ3760	0.061	E	N
J080403.40+404809.3	[NeV]λ3427	0.126	S	Y
J080543.32+252710.9	[FeVII]λ3760	0.072	E	Y
J080707.18+361400.5	[FeVII]λ3586, [FeVII]λ3760, [FeVII]λ6086	0.032	S	N
J080859.19+364112.9	[FeVII]λ6086	0.03	E	Y
J084002.36+294902.6	[NeV]λ3427	0.065	E	N
J085208.48+511845.8	[FeVII]λ3760	0.115	S	N
J085601.94+572327.4	[FeVII]λ6086	0.041	S(bo)	N

Note: Columns are (1) SDSS Name, (2) detected CL(s), (3) redshift, (4) GZ2 morphological classifications; "E" is for elliptical, "S" is for spiral, "b" is for bar, "o" is for odd, and "-" indicates no morphological classification was assigned, and (5) the merger classification from the Nevin catalog; "Y" marks galaxies with $p_{merg} > 0.5$, "N" identifies galaxies with $p_{merg} \leq 0.5$, and "-" represents galaxies that are not in the Nevin catalog.

Table 3.6: Morphological and Merger Classifications of the CL Galaxies (Continued)

SDSS Name	Detected CL(s)	Redshift	Morphology	Merger
(1)	(2)	(3)	(4)	(5)
J085835.98+013149.5	[NeV]λ3427	0.107	S(b)	Y
J090659.46+204810.0	[FeVII]λ3586	0.109	S(o)	N
J092002.85+054407.7	[FeVII]λ6086	0.038	S(b)	-
J092739.77+050312.5	[NeV]λ3427	0.126	S	N
J094036.39+033436.9	[FeVII]λ6086	0.016	-	Y
J101042.59+061157.0	[NeV]λ3427	0.098	E(o)	Y
J103825.16-002331.1	[NeV]λ3347, [NeV]λ3427	0.096	S(o)	Y
J105439.31+475144.2	[NeV]λ3427	0.073	S(b)	N
J105759.31+404940.6	[FeVII]λ6086	0.024	E	Y
J110431.08+423721.2	[NeV]λ3427	0.126	E(o)	Y
J111403.52+472653.4	[FeVII]λ3760	0.113	E	Y
J111711.79+465134.0	[FeVII]λ3760	0.061	E	N
J111724.94+443347.8	[FeVII]λ3760	0.066	E	N
J111803.22+450646.8	[NeV]λ3347, [NeV]λ3427	0.107	E(o)	Y
J112043.79+534337.4	[FeVII]λ6086	0.107	E	N
J115710.68+221746.2	[FeVII]λ3586, [FeVII]λ3760	0.052	S(b)	N
J122443.43+442438.8	[NeV]λ3427	0.126	E	Y
J123521.03+422002.6	[FeVII]λ6086	0.039	E	N
J130626.65+451720.4	[FeVII]λ6086	0.051	E	-

Note: Columns are (1) SDSS Name, (2) detected CL(s), (3) redshift, (4) GZ2 morphological classifications; "E" is for elliptical, "S" is for spiral, "b" is for bar, "o" is for odd, and "-" indicates no morphological classification was assigned, and (5) the merger classification from the Nevin catalog; "Y" marks galaxies with $p_{merg} > 0.5$, "N" identifies galaxies with $p_{merg} \leq 0.5$, and "-" represents galaxies that are not in the Nevin catalog.

Table 3.7: Morphological and Merger Classifications of the CL Galaxies (Continued)

SDSS Name	CL	Redshift	Morphology	Merger
(1)	(2)	(3)	(4)	(5)
J131730.11+474659.3	[FeVII]λ3760	0.027	E	N
J134401.90+255628.3	[NeV]λ3427	0.062	S(b)	N
J134918.20+240544.9	[FeVII]λ3760	0.021	-	Y
J141623.14+381127.4	[NeV]λ3427	0.135	-	Y
J142004.29+470716.8	[NeV]λ3427	0.07	S(b)	N
J144454.24+522648.5	[FeVII]λ3760	0.146	E	N
J145420.10+470022.3	[FeVII]λ3760	0.126	E(o)	Y
J151600.58+342119.1	[NeV]λ3427	0.125	S(o)	Y
J151856.39+332152.2	[FeVII]λ6086	0.069	E	N
J153552.40+575409.4	[FeVII]λ6086	0.03	E(o)	N
J160455.20+280956.9	[NeV]λ3427	0.077	S	Y
J161301.62+371714.9	[NeV]λ3427	0.069	S(b)	Y
J161358.56+393150.2	[FeVII]λ3760	0.038	S	-
J161413.20+260416.3	[NeV]λ3347, [NeV]λ3427	0.131	-(o)	Y
J162428.39+483548.0	[FeVII]λ6086	0.057	E(o)	Y
J162621.91+405442.7	[FeVII]λ3760	0.03	S(o)	Y
J162845.89+252938.0	[FeX]λ6374	0.04	E	N

Note: Columns are (1) SDSS Name, (2) detected CL(s), (3) redshift, (4) GZ2 morphological classifications; "E" is for elliptical, "S" is for spiral, "b" is for bar, "o" is for odd, and "-" indicates no morphological classification was assigned, and (5) the merger classification from the Nevin catalog; "Y" marks galaxies with $p_{merg} > 0.5$, "N" identifies galaxies with $p_{merg} \leq 0.5$, and "-" represents galaxies that are not in the Nevin catalog.

Table 3.8: Morphological and Merger Classifications of the CL Galaxies (Continued)

SDSS Name	CL	Redshift	Morphology	Merger
(1)	(2)	(3)	(4)	(5)
J162908.95+383256.6	[FeVII]λ6086	0.033	E	N
J163014.63+261223.3	[NeV]λ3347, [NeV]λ3427	0.131	S(b)	N
J163053.84+243343.5	[FeVII]λ6086	0.063	E	Y
J163430.87+374143.6	[NeV]λ3427	0.099	E	N
J164956.39+351243.5	[FeX]λ6374	0.1	E	N
J165810.10+622456.3	[NeV]λ3427	0.119	S(b)	N
J171411.63+575834.0	[NeV]λ3347, [NeV]λ3427, [FeVII]λ6086	0.093	E	Y
J172032.02+280602.9	[FeX]λ6374	0.083	-	Y
J205141.54+005135.4	[NeV]λ3347, [NeV]λ3427	0.106	S	Y
J211646.34+110237.4	[NeV]λ3427	0.081	S	Y
J212401.89-002158.6	[NeV]λ3427	0.062	S(b)	Y
J212900.75+001057.3	[FeVII]λ3760	0.133	E(o)	N
J213227.90+100816.9	[NeV]λ3427	0.063	S(o)	-
J215259.07-000903.4	[FeVII]λ6086	0.028	S	N
J223338.41+131243.6	[NeV]λ3347, [NeV]λ3427	0.093	S	Y
J231142.05+150638.2	[FeX]λ6374	0.04	S(o)	N
J232538.54+152115.8	[FeVII]λ6086	0.041	S	N

Note: Columns are (1) SDSS Name, (2) detected CL(s), (3) redshift, (4) GZ2 morphological classifications; "E" is for elliptical, "S" is for spiral, "b" is for bar, "o" is for odd, and "-" indicates no morphological classification was assigned, and (5) the merger classification from the Nevin catalog; "Y" marks galaxies with $p_{merg} > 0.5$, "N" identifies galaxies with $p_{merg} \leq 0.5$, and "-" represents galaxies that are not in the Nevin catalog.

Table 3.9: SNR Shocks

Detected CL (1)	Wavelength (Å) (2)	CL AGN SNR Shocks (3)	CL Non-AGN SNR Shocks (4)	CL Mergers SNR Shocks (5)	CL Non-Mergers SNR Shocks (6)	CL Nuclear SNR Shocks (7)	CL Non-Nuclear SNR Shocks (8)
[NeV]	3347	13%	-	14%	0%	13%	-
[NeV]	3427	33%	100%	30%	50%	39%	0%
[FeVII]	3586	3%	38%	0%	8%	12%	-
[FeVII]	3760	6%	55%	49%	49%	52%	45%
[FeVII]	6086	95%	42%	64%	41%	61%	25%
[FeX]	6374	100%	45%	36%	67%	67%	36%

Note: Columns are (1) detected CL, (2) rest wavelength, (3) percentage of CL-emitting spaxels in the CL Galaxies with a confirmed AGN that feature SNR shocks, (4) percentage of CL-emitting spaxels in the CL Galaxies without a confirmed AGN that feature SNR shocks, (5) percentage of CL-emitting spaxels in the CL Galaxies undergoing a merger that feature SNR shocks, (6) percentage of CL-emitting spaxels in the CL Galaxies not undergoing a merger that feature SNR shocks, (7) percentage of CL-emitting spaxels in the CL Galaxies with nuclear CL emission (See Section 3.4.2) that feature SNR shocks, and (8) percentage of CL-emitting spaxels in the CL Galaxies without nuclear CL emission that feature SNR shocks. "-" indicates an empty sample set.

Table 3.10: [OI] Shocks

Detected CL (1)	Wavelength (Å) (2)	CL AGN SNR Shocks (3)	CL Non-AGN [OI] Shocks (4)	CL Mergers [OI] Shocks (5)	CL Non-Mergers [OI] Shocks (6)	CL Nuclear [OI] Shocks (7)	CL Non-Nuclear [OI] Shocks
[NeV]	3347	25%	-	29%	0%	25%	-
[NeV]	3427	29%	100%	33%	31%	35%	0%
[FeVII]	3586	4%	12%	0%	6%	6%	-
[FeVII]	3760	3%	28%	20%	26%	25%	25%
[FeVII]	6086	50%	36%	45%	33%	31%	49%
[FeX]	6374	100%	67%	100%	67%	67%	100%

Note: Columns are (1) detected CL, (2) rest wavelength, (3) percentage of CL-emitting spaxels in the CL Galaxies with a confirmed AGN that feature [OI] shocks, (4) percentage of CL-emitting spaxels in the CL Galaxies without a confirmed AGN that feature [OI] shocks, (5) percentage of CL-emitting spaxels in the CL Galaxies undergoing a merger that feature [OI] shocks, (6) percentage of CL-emitting spaxels in the CL Galaxies not undergoing a merger that feature [OI] shocks, (7) percentage of CL-emitting spaxels in the CL Galaxies with nuclear CL emission (See Section 3.4.2) that feature [OI] shocks, and (8) percentage of CL-emitting spaxels in the CL Galaxies without nuclear CL emission that feature [OI] shocks. "-" indicates an empty sample set.

We find clear evidence of SNR and [OI] shocks in the CL-emitting spaxels of each CL species in our sample. However, the fraction of these shocks does not strongly trace CL galaxies with or without: a confirmed AGN, a companion galaxy, or nuclear CL emission. We reason that SNR and [OI] shocks may be viable CL-emission mechanisms; however, they are not likely dominant, and we find little evidence that they produce CLs away from the nuclear region, in the absence of a confirmed AGN, or when a merging companion galaxy is present.

3.5 Discussion

Based on our findings, we reason that the efficacy of using CLs to detect AGN varies by species of CL. While the ionization potential of each CL is $\geq$ 100 eV (Table 3.1; well above the 55 eV threshold for pure star formation; consistent with the strong continuum of an AGN being the ionization source), we find that certain CLs are better at identifying higher luminosity AGN than others ($\log(L_{[OIII]}) \gtrapprox 41$ erg s^{-1}). In particular, [NeV] emission is predominately present in higher [OIII] luminosity galaxies that feature a confirmed AGN (mean $\log(L_{[OIII]}) = 41.5$ erg s^{-1} for the [NeV] galaxies; 94% of the [NeV] galaxies host a confirmed AGN). On the other hand, we detect [FeVII] and [FeX] emission in lower [OIII] luminosity galaxies with fewer confirmed AGNs (mean $\log(L_{[OIII]}) \leq 40.1$ erg s^{-1} for both CLs; 14% and 25% confirmed AGN for the [FeVII] and [FeX] galaxies, respectively).

We reason that the destruction of iron CLs by dust grains, which we find is inversely proportional to AGN bolometric luminosity (the dusty torus diminishes at $\log(L_{bol}) \lessapprox 42$ erg s^{-1}; e.g., [83]), may be directly impacting [FeVII] and [FeX] emission; the CL galaxies with the lowest E(B-V) values yield the most iron CL detections (nine iron CL galaxies with E(B - V) $\geq$ 0.045; 34 iron CL galaxies with (E(B - V) $<$ 0.039). We posit that if the [FeVII] and [FeX] galaxies host AGNs, that they may be lower luminosity AGNs, which are potentially too weak to be detected via SDSS broad emission lines, NVSS/ FIRST 1.4 GHz radio observations, *WISE* mid-infrared color cuts, and *Swift*/BAT hard X-ray observations.

We determine that there are primarily two distinct populations of CL galaxies in our sample: 1) a subset of CL galaxies that emit [NeV] (33/71 CL galaxies), with relatively high [OIII] and bolometric luminosities, and a high fraction of confirmed AGN (94%), and 2) a group of CL galaxies that emit [FeVII] and [FeX] (40/71 CL galaxies), with relatively low [OIII] and bolometric luminosities, and a low fraction of confirmed AGN (14% and 25%, respectively).

Overall, we consider the similar IPs of [NeV] and [FeVII] (97.1 eV and 99.1 eV, respectively), the high IP of [FeX] (233.6 eV), and our BPT analysis (100% of the [NeV] spaxels in our sample are either BPT AGN or BPT composite, 91% of the [FeVII] spaxels, and 88.3% of the [FeX] spaxels; Table 3.3), to deduce that each CL in our sample is likely linked to AGN activity, but that [FeVII] and [FeX] emission may preferentially be found in less luminous AGN (we also consider the possibility that some of the iron CL emission may not exclusively be produced by AGN; e.g., shocks may also play a role). We conclude that the BPT diagram is generally effective at tracing large populations of AGN; however, [NeV], in particular, can also be used as an additional resource to help trace AGN, specifically for instances where one or more of the optical BPT line ratios is unable to be determined.

Moreover, [92] reported CL critical densities between 10^7 - 10^{10} cm^{-3}, which suggest that the CLR is a region between the classical NLR and the BLR. The authors also indicate that lower ionization CLs (e.g., [NeV] and [FeVII]; IPs $\approx$ 100 eV) are more likely to form in lower density gas that should be spatially resolved. In contrast, higher ionization CLs (e.g., [FeX]; IP = 233.6 eV) form in a region closer to the nucleus where the ionizing flux, and ionization parameters, are higher (i.e., these CLs form in denser, more efficiently emitting regions). Here we determine that the average size of the CLR for [NeV] $\lambda\lambda$3347, 3427, [FeVII] $\lambda\lambda\lambda$3586, 3760, 6086, and [FeX] λ6374 is 1.9 kpc, 2.3 kpc, 3.7 kpc, 5.3 kpc, 4.1 kpc, and 2.5 kpc, respectively (Table 3.2) - well into the NLR for all CL species. With the enhanced capabilities of IFS, which enables us to spatially resolve the CLR, we find that the CLR for the galaxies in MaNGA is larger than reported in previous works (tens to hundreds of pcs;

e.g. [215, 180, 188, 232]).

Finally, while the bulk of the CL galaxies in our sample feature CL emission in their nuclear regions (within a central 2.″5 x 2.″5 FoV; Section 3.4.2; Table 3.2), a significant fraction do not, which is inconsistent with pure AGN photoionization. In Section 3.4.6, we show that [OI] and SNR shocks are present in the CL-emitting spaxels of each CL species. However, the fraction of SNR and [OI] shocks, across all CL species, do not significantly vary for the CL galaxies with or without nuclear CL emission. We reason, instead, that AGN radio jets or outflows may be interacting with gas clouds away from the nuclear region, ionizing them, and producing the non-centric CL emission we uncover in our sample (Figure 3.4; e.g., [275, 188]). It is also possible that this CL emission is tracing a different species of gas, that is not a CL, from a non-companion galaxy within the MaNGA FoV (at a different redshift than the target galaxy; e.g., J1613 - Figure 3.4).

3.6 Summary and Future Work

We construct the most extensive sample of MaNGA CL galaxies to date. With our custom pipeline, we measure emission from [NeV] λ3347, [NeV] λ3427, [FeVII] λ3586, [FeVII] λ3760, [FeVII] λ6086, and/or [FeX] λ6374 at $\geq 5\sigma$ above the background continuum in 71 galaxies in MaNGA's MPL-11 catalog of 10,010 unique galaxies.

Our main findings are:

(1) The average size of the CLR for [NeV], [FeVII], and [FeX] is 1.9 kpc, 3.8 kpc, and 2.5 kpc, respectively - beyond the BLR and into the traditional NLR.

(2) The fraction of [NeV], [FeVII], and [FeX] galaxies with at least one CL-emitting spaxel in their nuclear 2.″5 region is 98.5%, 73%, and 75%, respectively. Nuclear CL emission is preferentially found in [NeV] galaxies.

(3) We identify two main populations of CL galaxies: 1) galaxies that mostly feature [NeV] emission (33/71 CL galaxies), with relatively high [OIII] and bolometric lu-

minosities (mean [NeV] log([OIII]) luminosity = 41.5 erg s^{-1}; mean [NeV] log(L_{bol}) = 44.5 erg s^{-1}), and a high fraction of confirmed AGN (94%), and 2) galaxies that predominately emit [FeVII] and [FeX] (40/71 CL galaxies), with relatively low [OIII] and bolometric luminosities (mean [FeVII] and [FeX] log([OIII]) luminosities are 40.1 erg s^{-1} and 39.8 erg s^{-1}, respectively; mean [FeVII] and [FeX] log(L_{bol}) values are 43.7 erg s^{-1} and 43.5 erg s^{-1}, respectively), and a low fraction of confirmed AGN (14% and 25%, respectively).

(4) 100% of the [NeV] spaxels in our sample are either BPT AGN or BPT composite, 91% of the [FeVII] spaxels, and 88.3% of the [FeX] spaxels. The CLs are strong tracers of BPT AGN and BPT composite sources.

(5) We detect a low number of iron CL galaxies in high E(B - V) value galaxies (E(B - V) $\geq$ 0.045; nine iron CL galaxies) vs. low E(B - V) galaxies (E(B - V) $<$ 0.039; 34 iron CL galaxies). We reason that the destruction of iron CLs by dust grains, which is inversely proportional to AGN bolometric luminosity, may likely be depleting [FeVII] and [FeX] emission, particularly in the nuclear region where the presence of dust is greater. The [FeVII] and [FeX] galaxies may be tracing lower luminosity AGN, which are possibly too weak to be confirmed by traditional AGN detection techniques.

(6) SNR and [OI] shock excitation are viable CL production mechanisms; however, they are not likely primary, as the abundance of SNR and [OI] shocks does not vary significantly across our sample for galaxies with or without: nuclear CL emission, an AGN, or a merging companion.

We will explore the CLR kinematics in a future publication to better comprehend the role of outflows on CL production. In particular, we will use [OIII] flux maps to evaluate the likelihood that AGN outflows produce CL emission, provided the strong correlation between [OIII] emission and AGN outflows (e.g., [273, 54]). Further, we will measure the rotation

and cloud velocities of the gas for each CL galaxy (to determine how the bulk motion of gas in the CL galaxies correlates with CL emission), and also analyze the emission line profiles of the CLs to determine if, for example, the CLs feature any blue shifted emission - indicative of outflows.

Moreover, additional multi-wavelength observations of the CLs would help deduce their nature. X-ray observations from *Chandra*, for example, would allow us to better confirm the population of low luminosity AGN in the CL galaxies. This will help to determine the effectiveness of using CL emission as an unambiguous tracer of AGN in large-scale spectroscopic surveys of galaxies. Finally, our work here is also relevant for motivating near IR measurements of additional CLs that are observable by the *James Webb Space Telescope*, particularly in cases where optical CLs may be obscured.

Chapter 4

A Catalog of Broad Hα and Hβ Emitters in MaNGA

4.1 Introduction

The search for large populations of Active Galactic Nuclei (AGNs) in spectroscopic surveys has been extensive in recent years, and these efforts have utilized multiple bands of the electromagnetic spectrum (e.g., Radio, IR, Visible, and X-ray; e.g., [207, 52]). A primary motivation for assembling catalogs with robust populations of AGNs is to better decipher the relationship between central supermassive black holes (SMBHs; $M_{\rm BH} > 10^6 M_\odot$) and their parent galaxies (e.g., the M-σ relationship; [256, 126, 98, 95]). Further, SMBH mass has also been shown to correlate tightly with the mass and luminosity of the host galaxy's galactic bulge (e.g., [174, 106, 17, 70]).

Additionally, several authors present evidence that AGN feedback effectively suppresses star formation (e.g., [257, 61, 266, 59, 128, 276, 156, 263, 176, 87]), while others contend that it may actually stimulate star formation in certain regimes (e.g., [256, 281]). However, the true nature of these processes remains elusive. To address this, extensive samples of AGNs can serve to shed light on how well defined AGN parameters, like AGN luminosity and SMBH mass, correlate to features of the host galaxy, which include, but are not limited to: morphology, presence of a companion, and/or stellar properties.

Broad emission lines (BLs) in the optical and UV bands can help ensure accurate AGN identification, as they are fundamental signatures of an AGN. These lines are produced in a high density region, termed the broad line region (BLR). The BLR is close to the AGN

accretion disk and contains gas clouds that move near Keplerian velocities $>$ 1,000 km s^{-1} (e.g., [74, 147, 60]). Further, the outer edge of the BLR terminates at the hot dusty torus of the AGN, within 0.01 - 1 parsec of the SMBH (e.g., [193]). Further, depending on the orientation of the AGN and the properties of the emission lines observed for each, an AGN can be classified as Type I or Type II. Type I are oriented pole-on and are observed to have BLs.

On the other hand, Type II are oriented edge-on and are observed to have narrow emission lines (NLs; FWHM $\sim$ 300 - 1,000 km s^{-1}) in a lower density region, termed the narrow line region (NLR). The NLR is just beyond the dusty torus, out to several kiloparsecs from the SMBH (see The Unified Model of AGNs; [7, 280]). However, in the NLR, star-formation can produce strong narrow emission lines that mimic AGN emission (e.g., [242]). As a result, classifying Type I AGNs using BLs, the broad Hα and broad Hβ lines, for example, is typically more reliable than narrow lines at identifying AGNs (e.g., [200, 165]).

With the rise of the Sloan Digital Sky Survey (SDSS; [304, 82, 29]), a vast abundance of galactic spectra have been made available. With this large population of galactic spectra, multiple BL AGN catalogs have emerged. For example, [165] report a new sample of 14,584 BL AGN at $z < 0.35$, which are detected from the SDSS's Seventh Data Release (DR7). After performing a thorough procedure to remove the stellar continuum, they investigated Hα and Hβ emission lines. The authors predominately use broad Hα emission in their study and compute Hα luminosities between $10^{38.5}$ - $10^{44.3}$ erg s^{-1}, FWHMs between 500 - 34,000 km s^{-1}, and virial SMBH masses, estimated from the BL measurements, between $10^{5.1}$ - $10^{10.3}$ M$_\odot$. Further, [250] compiled a catalog of 105,783 unique quasars from the SDSS's Seventh Data Release. These quasars were spectroscopically confirmed, luminous (M$_i < 22.0$), and featured at least one line with FWHM $>$ 1,000 km s^{-1}. Also, [200] discovered 1,835 BL AGNs in SDSS's DR7 at $z < 0.2$. They measured broad Hα emission (FWHM $>$ 800 km s^{-1} for their sample) in these galaxies and used observations from the *Chandra X-Ray Observatory* ([86]) to confirm the AGNs. Finally, [208] assembled a BL AGN catalog of 21,877 galaxies using

the extended Baryon Oscillation Spectroscopic Survey (eBOSS), from the SDSS's fifteenth data release in its fourth phase (SDSS-IV; [29]).

Generally, for catalogs of Type I BL AGN, a standard line width of 1,000 km s^{-1} is used to differentiate the BLR from the NLR (e.g., [115, 86]). However, it is important to note that low-luminosity AGNs and low-mass SMBHs can feature BL widths below this threshold. As referenced in [165], some low-mass SMBHs, which have been confirmed to be AGNs using X-ray observations (e.g., [109, 75, 166]), can have widths as low as 500 km s^{-1}. Here, we primarily target AGNs with a high enough luminosity and SMBH mass to place their line widths above 1,000 km s^{-1}. We acknowledge that our sample may miss the weaker AGN and lower mass SMBHs below this threshold.

Moreover, existing galaxy formation models suggest that galaxies evolve through frequent mergers with companion galaxies. (e.g., [289]). During these mergers, the two SMBHs at the galaxy centers lose energy via dynamical friction and gravitationally begin to coalesce (see Section 4.3.4). In some cases, one or both of the SMBHs may actively be accreting matter as an AGN. If both are AGNs, then the pair is termed "dual AGN" ([101, 49, 55]). A small quantity of dual AGNs are presently known. On the other hand, if one of the galaxies is an AGN and the other quiescent, the AGN is termed an "offset AGN" ([50]). One way to detect an AGN in a merging system is to use BL detections. For example, if we detect BLs outside of the nuclear region of a target galaxy, and within the nuclear region of a companion galaxy, it is an indication that the companion hosts an AGN (i.e., this is an offset AGN detection).

Additionally, if we detect BLs near, but spatially offset from the nuclear region of a galaxy, and measure an offset velocity for the line profile, but no companion is visible, we may detect a recoiling black hole. These objects result from the mergers of binary SMBHs with unequal masses and arbitrary spins. As the binaries merge, they produce highly energetic gravitational radiation, which can also transport linear and angular momentum. In some cases, a net flux of linear momentum will be emitted by the system and the final SMBH will

experience a gravitational recoil (e.g., [211, 18, 123]).

In this chapter, we add to the existing population of SDSS AGNs using the SDSS-IV Mapping Nearby Galaxies at Apache Point Observatory (MaNGA) integral field unit (IFU) catalog ([36]). MaNGA is a large-scale spectroscopic survey that has observed 10,010 nearby galaxies. With our pipeline, we detect 301 broad Hα-emitting galaxies and 802 broad Hβ emitting galaxies at $\geq 5\sigma$ above the continuum, with line widths $>$ 1,000 kms^{-1} and BL emission in at least 1 spaxel. In total, we detect 1,042 unique BL galaxies (60 BL galaxies feature both Hα and Hβ emission). Here, we report the physical parameters of these BL galaxies (e.g., BL luminosities, BL FWHMs, and SMBH masses). We also detect 35 broad Hα galaxies and 77 broad Hβ galaxies with emission from a companion, rather than the MaNGA target galaxy (i.e., offset AGNs). We find that 3 offset AGNs feature both broad Hα and Hβ emission, leading to 109 unique offset AGNs in our sample.

This paper is outlined as follows: Section 4.2 covers the details of the SDSS-IV MaNGA survey and its data pipeline, Section 4.3 reviews the techniques we use to build the BL catalog and to analyze the physical properties of the BLR, Section 4.4 overviews our results, Section 4.5 features the interpretations of our findings, and Section 4.6 provides our conclusions and intended future work. All wavelengths are provided in vacuum and we assume a ΛCDM cosmology with the following values: $\Omega_M = 0.287$, $\Omega_\Lambda = 0.713$ and $H_0 = 69.3$ km s^{-1} Mpc^{-1}.

4.2 Galaxy Observations

4.2.1 MaNGA Catalog

To assemble a statistically significant sample of BL galaxies, we utilize the largest IFU spectroscopic survey of galaxies to date, the SDSS-IV MaNGA catalog ([36]). MaNGA uses the SDSS 2.5 m telescope [111], and has observed the spectra for 10,010 nearby galaxies ($0.01 < z < 0.15$; average $z \approx 0.03$) with stellar mass distributions between 10^9 $M_\odot$ and 10^{12} $M_\odot$. The wavelength range of MaNGA spans 3622 Å - 10354 Å, with a typical spectral

resolution of $\sim$ 2000 and a velocity resolution $\sigma = 72$ km s^{-1} ([36, 159]).

MaNGA uses IFU fiber-bundles grouped into hexagonal grids with field-of-view (FoV) diameters between 12.″5 to 32.″5, where the size of the bundles corresponds to the apparent size of the target galaxy ([36]). Specifically, the system is comprised of two 19-fiber IFUs (12.″5 FoV), four 37-fiber IFUs (17.″5 FoV), four 61-fiber IFUs (22.″5 FoV), two 91-fiber IFUs (27.″5 FoV), and five 127-fiber IFUs (32.″5 FoV). The MaNGA observations generate spectroscopic maps out to at least 1.5 times the effective radius, with an average footprint of $\sim$ 500 arcsec^2 per IFU; the typical galaxy is mapped out to a radius of 15 kpc. Each MaNGA spatial pixel, or spaxel, covers 0.″5 $\times$ 0.″5 and the average FWHM of the on-sky point spread function (PSF) is 2.″54, which corresponds to a typical spatial resolution of 1 -2 kpc ([80]).

4.2.2 MaNGA Data Reduction Pipeline

The MaNGA Data Reduction Pipeline (DRP) produces sky-subtracted spectrophotometrically calibrated spectra in a FITS file format that is used for scientific analysis ([159]). The resulting DRP data product is run through MaNGA's Data Analysis Pipeline (DAP; [294]) that provides three-dimensional data cubes that combine dithered observations. The data cubes offer science data products, such as stellar kinematics, emission-line parameters (e.g., fluxes and equivalent widths), and spectral indices (e.g., D4000 and Lick indices). The data products are publicly released periodically as MaNGA Product Launches (MPLs). To construct our catalog of BL galaxies in MaNGA, we use MaNGA's eleventh, and final, data release (MPL-11), which contains data for 10,010 unique galaxies.

4.3 Analysis

4.3.1 Stellar Continuum Fit and Subtraction and Spectral Fitting

The MaNGA DAP provides fits for prominent emission lines (e.g., the narrow components of the Hα, Hβ, and [OIII] λ5007 lines). However, it does not offer fits for the broad Hα and Hβ components (FWHM $>$ 1,000 km s^{-1}). As a result, we create a custom pipeline to scan for broad Hα and Hβ emission in MaNGA.

The initial step in our pipeline is accessing the DRP to retrieve the data cubes for each MaNGA galaxy. The data cubes provide a spectrum for each individual spaxel across the FoV of each galaxy (spaxel arrays vary between 32 $\times$ 32 spaxels to 72 $\times$ 72 spaxels, depending on IFU configuration). We then use the spectroscopic redshifts of the stellar component of each galaxy, provided by the DAP (`STELLAR_Z` parameter), to shift the spectra to rest vacuum wavelengths ($\lambda_{\rm rest}$ = 4862 Å for Hβ and $\lambda_{\rm rest}$ = 6562 Å for Hα). Then, to subtract the stellar continuum for each BL galaxy's corrected spectra, we use the software package `pPXF` ([38, 39]). `pPXF` performs a polynomial fit on each galaxy's spectrum while masking prominent emission and absorption features. To fit the stellar population synthesis model on each fit, we use the MILES[1] stellar templates library. This library features $\approx$ 1,000 stars, with spectra obtained by the *Isaac Newton Telescope*, and covers the wavelength range of 3525 Å - 7500 Å at a 2.5 Å FWHM resolution.

We then apply a mask to each datacube, such that the imported wavelength range for each spectrum matches the wavelength range of the stellar templates library (3525 Å-7500 Å). Next, we normalize each spectrum by dividing fluxes in this wavelength range by each spectrum's median flux value (to avoid numerical issues; similar to [192]; see [39] for a more detailed discussion). Subsequently, we define a typical instrument resolution of $\approx$ 2.5 Å, construct a set of Gaussian emission line templates (to mask emission lines; provided by `pPXF`), and fit the stellar templates.

[1] http://miles.iac.es/

Then, we use the spectroscopic analysis `Python` package `PySpecKit` ([102, 103]) to perform a multi-Gaussian scan for the broad Hα and broad Hβ emission-line components at $\geq 5\sigma$ above the background continuum, with FWHMs $>$ 1,000 km s^{-1}, in the 10,010 galaxies in MPL-11. For the Hα fits, we first fit the [NII] $\lambda\lambda$6549, 6585 and [SII] $\lambda\lambda$6718, 6732 doublets. The widths of all NLs are tied to the widths of [SII]. Then, we fit NL and BL components to the Hα line. We proceed to analyze only the BL fit on the Hα line, which has been isolated by subtracting the continuum and blending lines. For the Hβ line, we only fit NL and BL components to the line profile and analyze the BL results. We use the conservative 5σ and 1,000 km s^{-1} thresholds to ensure we identify definitive BL emission.

In addition, in some instances, it can be challenging to accurately measure the width of the broad Hα line, especially near the strong neighboring emission lines of [NII] $\lambda\lambda$6549,6585. Due to the complexities of this, we follow the procedure performed by [200]. In particular, we calculate a ratio between the mean fluxes of two spectral regions near Hα: 6460 - 6480 Å and 6523 - 6543 Å. The former is near Hα but not too close to be mixed with Hα emission, which makes it a good proxy for the continuum near Hα. The latter region is closer to the Hα line and is a good tracer of the broadening of the Hα line. Once this ratio is computed for each fit, we require that this value be $>$ 1 for all MaNGA galaxies, and pass our other requirements, in order to be considered a broad Hα detection. In [200], this threshold proved to recover the strongest broad Hα detections. Figures 4.1 and 4.2 show examples of broad Hα and Hβ fits from our pipeline

4.3.2 Broad Line Flux/ Velocity Maps and Line Luminosities

We create custom BL flux and velocity maps to analyze the strength and distribution of the BLs, and their cloud velocities, in our sample. We create these maps using the integrated BL flux value and measured FWHM from each spectrum for each spaxel for each BL galaxy. We measure these values during the spectral fitting routine outlined in Section 4.3. An example broad Hα flux and velocity map is shown in Figure 4.3 (see Appendix C for an

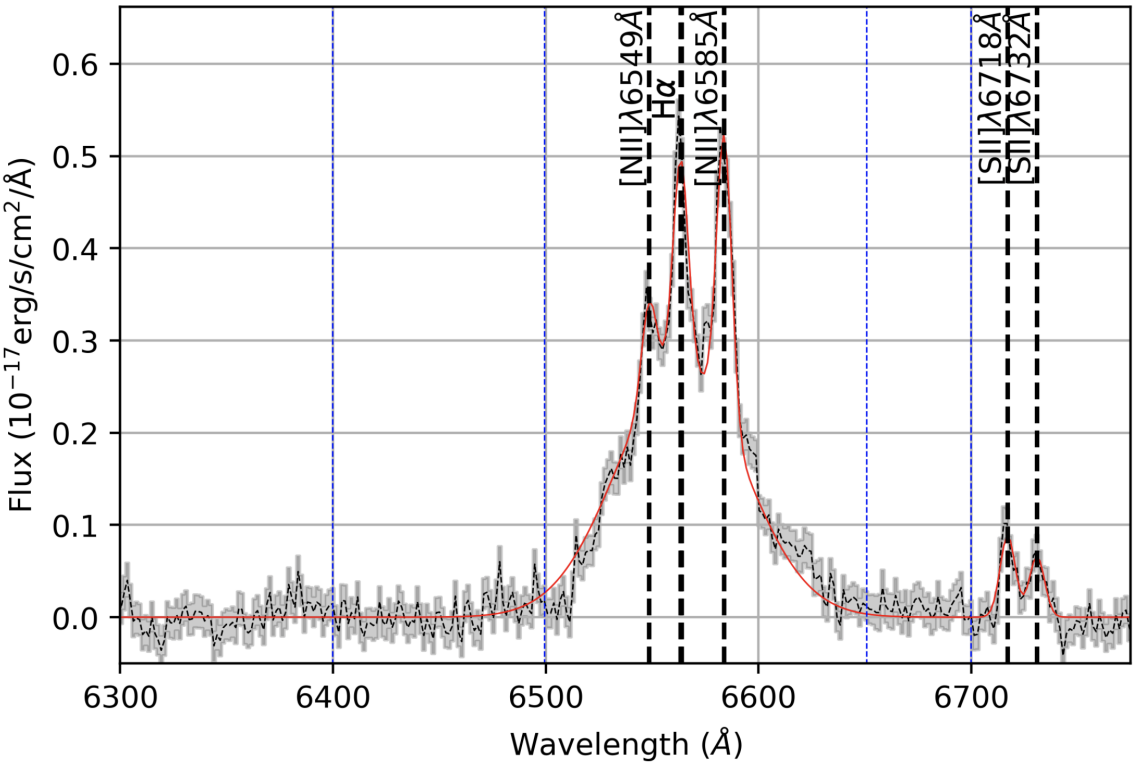

Figure 4.1: A sample spectrum from an individual spaxel showing the broad Hα line detected at $\geq 5\sigma$ above the continuum in J004730.34+154149.4. The dotted black line is the stellar continuum subtracted spectrum, the shaded gray region is the uncertainty, the solid red line represents the best fit, the bold dashed black lines signify the rest wavelengths of the Hα, [NII] $\lambda\lambda$6549, 6585, and [SII] $\lambda\lambda$6718, 6732 lines, and the two sets of blue dotted vertical lines correspond to the neighboring continuum windows where the RMS flux values of the continuum are calculated

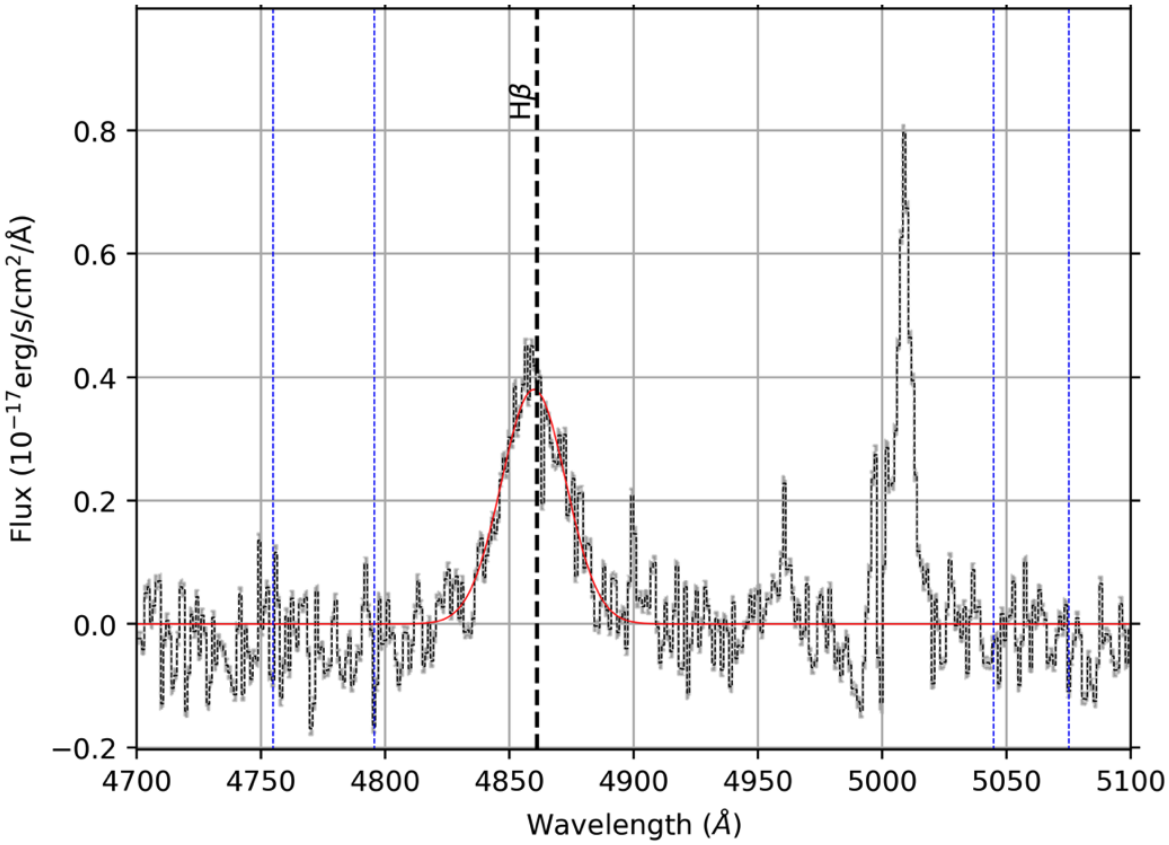

Figure 4.2: A sample spectrum from an individual spaxel showing the broad Hβ line detected at $\geq 5\sigma$ above the continuum in J171411.63+575834.0. The dotted black line is the stellar continuum subtracted spectrum, the shaded gray region is the uncertainty, the solid red line represents the best fit, the bold dashed black lines signifies the rest wavelength of the Hβ line, and the two sets of blue dotted vertical lines correspond to the neighboring continuum windows where the RMS flux values of the continuum are calculated

example broad Hβ flux and velocity map). Note, these BL flux maps trace the presence of an AGN, oriented so that the central SMBH is viewed directly. The observed fluxes depend only on the angle between the observational line of sight and the dusty torus (which can obscure these lines).

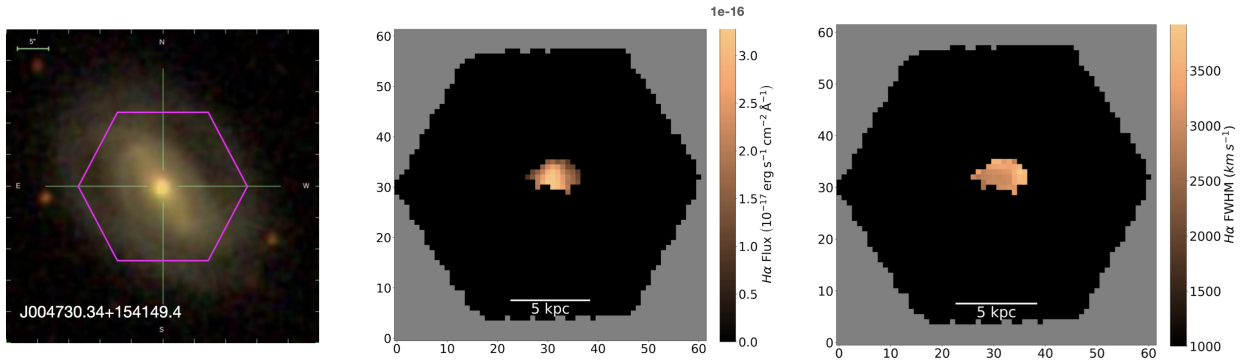

Figure 4.3: From left to right, an example SDSS optical image from MaNGA, a custom generated broad Hα flux map, and a custom generated broad Hα FWHM map for J004730.34+154149.4. The gray region is outside of the MaNGA FoV and the black region are spaxels with no BL emission. North is up and east is to the left.

As reviewed in [200], some theoretical frameworks propose an AGN luminosity dependence for the fraction of observed Type I AGN. In several models, a receding dusty torus is considered, whereby nuclear luminosity determines the dust sublimation radius. Specifically, the more luminous an AGN is, the further the dusty torus is pushed away, which expands the torus' inner radius; consequently, the opening angle of the torus increases if the height of the torus is fixed (e.g., [160, 89, 258]). This underscores the importance of determining AGN luminosity measurements in our sample. Moreover, evaluating the AGN luminosities for our sample will help us determine the the range of broad Hα and broad Hβ luminosities for the BL galaxies in MaNGA above our FWHM cutoff of 1,000 km s^{-1}.

We determine the line luminosity for each spaxel using Equation 4.1 and Equation 4.2:

$$L_{H\alpha} = F_{H\alpha}(4\pi R^2) \tag{4.1}$$

$$L_{H\beta} = F_{H\beta}(4\pi R^2) \tag{4.2}$$

where $F_{H\alpha}$ is the measured Hα flux from our spectral fits, $F_{H\beta}$ is the measured Hβ flux from our spectral fits, and R is the DAP provided luminosity distance based on the galaxy redshift.

4.3.3 SMBH Masses and Stellar Velocity Dispersions

Based on the virial method, which assumes the BLR is virialized, SMBH masses can be estimated with broad Hα and Hβ luminosities. These mass measurements, for example, are critical in the larger context of resolving the role of SMBHs in their host galaxy's evolution (e.g., the M-σ relationship, which is the empirical correlation between a galaxy's SMBH mass and the stellar velocity dispersion of its galactic bulge; [98, 95]). Here, we use the SMBH mass estimator from [108]. The SMBH mass is derived using the broad Hα and broad Hβ luminosities in Equations 4.3 and 4.4:

$$M_{\rm BH} = (1.3 \pm 0.3) \times 10^6 \big(\frac{L_{H\alpha}}{10^{42}{\rm ergs}^{-1}}\big)^{0.57\pm0.06} \big(\frac{\rm FWHM_{H\alpha}}{10^3{\rm kms}^{-1}}\big)^{2.06\pm0.06} M_\odot \tag{4.3}$$

$$M_{\rm BH} = (3.6 \pm 0.2) \times 10^6 \big(\frac{L_{H\beta}}{10^{42}{\rm ergs}^{-1}}\big)^{0.56\pm0.02} \big(\frac{\rm FWHM_{H\beta}}{10^3{\rm kms}^{-1}}\big)^{2} M_\odot \tag{4.4}$$

where $L_{H\alpha}$ is the luminosity of the broad Hα component (Equation 4.1), $L_{H\beta}$ is the luminosity of broad Hβ component (Equation 4.2), $FWHM_{H\alpha}$ is the median broad Hβ FWHM value measured across all BL spaxels for each BL galaxy, and $FWHM_{H\beta}$ is the median broad Hα FWHM value measured across all BL spaxels for each BL galaxy.

Finally, to confirm the correlation between SMBH mass and stellar velocity dispersion, we determine the stellar velocity dispersion for each galaxy. We use the `STELLAR_SIGMA_1RE` parameter from the MaNGA DAP to determine this value for each BL galaxy. This value is the flux-weighted mean stellar velocity dispersion of all spaxels within 1 effective radius

("Re"; i.e., the radius from within which half of the galaxy light is contained). Note, we only use this value for galaxies with BL emission from the target MaNGA galaxy, not from a companion galaxy whose velocity dispersion has not been measured by the DAP.

4.3.4 Hα and Hβ Offset Velocities and Companion Galaxies

SMBHs are suspected to form and grow through two primary paths: 1) active accretion, whereby nearby gas accumulates onto the central engine, and 2) and hierarchical merging of separate SMBHs through large-scale mergers (e.g., [151]). As detailed in [35], the byproduct of mergers is the formation of a gravitationally bound SMBH system, where each galaxy's SMBH moves towards the center of the system because of dynamical friction ([42]). However, near 10 parsecs, dynamical friction fails to effectively decrease the pair's angular momentum, and alternative processes dictate the binary orbital dynamics. Within 0.1 pc, gravitational radiation drives the remaining angular momentum out of the system and causes the SMBHs to finally merge ([16]). Finally, after coalescence, the remnant black hole is liable to recoil due to the emission of the gravitational waves and the properties of the original SMBHs (e.g., unequal spins and unequal masses; [37, 31]). For reference, the maximum recoil velocity identified in fully relativistic simulations of black hole mergers is up to $\sim$ 4,000 - 5,000 km s^1 ([37, 167]). Moreover, if a SMBH is recoiling, and features an AGN, the BLR should be gravitationally bound to the system, and there should be an observable systemic Doppler shift of the BLs.

In addition, a clear correlation between mergers and AGN fueling has been empirically shown in some studies (e.g. [153, 84, 245]). In the context of recoiling black holes that result from mergers, the displacement of SMBH from the nuclear center can alter AGN feedback at the galaxy center, emphasizing the importance of finding recoiling black holes in the context of SMBH-galaxy co-evolution. Note, AGN outflows and/or relativistic jets may also produce systemic Doppler shifts of the BLs in some instances (e.g., [148]). This underscores the need to search for, and analyze, BL velocities offset from the velocity of the stellar continuum of

the MaNGA galaxies in our sample.

We also consider both offset and dual AGN, where the former signifies one galaxy in a merging system hosts an AGN, and the latter signifies that both do. If offset AGNs exist in merging systems in our sample, we expect to find BL emission in either the target or companion galaxy. For reference, we anticipate a slight velocity offset for the companion, as it is likely at a slightly different redshift than the target galaxy. On the other hand, if dual AGN are in merging systems in our sample, we expect to find BL emission both in the target galaxy and the companion, or in two companion galaxies if we detect a triple merging system.

Therefore, we calculate the offset velocities of the Hα and Hβ BLs using Equation 4.5:

$$\Delta v_{\rm BL} = c\,\big(\frac{z_{\rm BL} - z_{\rm sys}}{1 + z_{\rm sys}}\big) \tag{4.5}$$

where z_{BL} is the redshift of the stellar component of the target galaxy provided by the MaNGA DAP (`STELLAR_Z`), z is the redshift we measure for each observed line profile, and c is the speed of light.

Finally, to further determine if a possible connection exists between BL emission and the presence of a companion galaxy, we consider if a BL galaxy is merging or not based on the sample produced by [195] ("Nevin catalog" hereafter). The authors calculate the merger probability for the 1.3 million galaxies in the SDSS DR16 photometric sample, using imaging predictors that have been trained to separate mock images of simulated merging and non-merging galaxies (see [194]). We analyze the BL galaxies in the SDSS DR16 Nevin catalog, and classify a BL galaxy as a merger if the Nevin catalog gives it a merger value $(\rm p_{merg}) > 0.5$.

4.4 Results

In this section, we present our findings for the BL galaxies in MaNGA. In total, we find 301 galaxies (median $z = 0.046$) with broad Hα emission at $\geq 5\sigma$ above the background continuum, with FWHM values $> 1{,}000$ km s^{-1}, in MaNGA's MPL-11; 801 galaxies (median $z = 0.56$) with broad Hβ emission. In total, we detect 1,042 unique BL galaxies; 60 feature both Hα and Hβ emission. For the Hα galaxies, we detect 35 offset AGNs, where the BL emission comes solely from a companion galaxy ($\sim 12\%$), not the target MaNGA galaxy; 77 for the Hβ galaxies ($\sim 10\%$). Note, 3 offset AGNs feature both broad Hα and Hβ emission, leading to 109 unique offset AGNs in our sample. We also measure the broad Hα luminosities for our sample to range between 10^{37} - 10^{42} erg s^{-1}; the median broad Hα luminosity is 10^{38} erg s^{-1}. Additionally, we measure the broad Hβ luminosities for our sample to range between 10^{36} - 10^{42} erg s^{-1}; the median broad Hβ luminosity is 10^{38} erg s^{-1}.

4.4.1 BL Intensities and Cloud Velocities

Understanding the properties of the BLs in our sample can help clarify the dynamics of the AGNs which produce them. Specifically, the line intensity and line widths of each BL can help trace the features of an AGN (e.g., the strength of the AGN and the BLR radius).

In our sample of BL galaxies, we measure broad Hα luminosities between 10^{37} - 10^{42} erg s^{-1}. For the broad Hβ sample, we measure broad Hβ luminosities between 10^{36} - 10^{42} erg s^{-1}. We display histograms of these results in Figure 4.4, and find that the majority of the BL AGNs in MaNGA feature broad Hα and Hβ luminosities $\sim 10^{38}$ erg s^{-1}. Additionally, we determine that the broad Hα galaxies are more luminous, with a median luminosity of 9.7×10^{38} erg s^{-1}, which is $\sim 25\%$ higher than the median luminosity, 2.4×10^{38} erg s^{-1}, of the Hβ galaxies. Note, previous studies have suggested that the profiles of the Balmer lines can vary from one another, indicative of higher density and higher velocity zones of the BLR (e.g., [254, 255, 58, 282]). We contend that this may be a viable explanation for the higher

broad Hα luminosities in our sample.

Furthermore, in low density and low optical depth gas, Hβ emission is effective at tracing the ionizing continuum luminosity (e.g., the 5100 Å luminosity; [136]). Moreover, some studies show a strong dependence between the ionizing AGN flux and Hβ emission in the BLR. This is attributed to the effective temperature at the disk radius, which corresponds to the location of the BLR. As inferred from the Hβ line, this temperature is 1,000 Kelvin, close to the threshold that dust can exist at (see [137, 300, 24, 60, 23, 292]). As a result, broad Hβ emission is often used to determine the size of the BLR (termed "Reverberation Mapping"; e.g., [212, 300, 136]; Equation 4.6). This is one example, of many (e.g., the broad Hα/Hβ ratio can also be used as a dust extinction estimator; e.g., [76]), that showcases how BL luminosities can elucidate the physics of the BLR. For reference, the size of the BLR can be derived using the following:

$$\mathrm{Log\ R_{BLR}\ (light-days)} = (1.381 \pm 0.080) + (0.684 \pm 0.106)\ \mathrm{Log}\ \big(\frac{\mathrm{L_{H\beta}}}{10^{42}\ \mathrm{erg\ s^{-1}}}\big) \qquad (4.6)$$

where $\mathrm{R_{BLR}}$ is the radius of the BLR and $\mathrm{L}_{H\beta}$ is the luminosity of the broad Hβ component. We calculate $\mathrm{R_{BLR}}$ values between 0.01 - 46 light days for our Hβ sample, with a median radius of 0.1 light days (0.02 pc). Comparatively, [300] investigated 34 AGNs with z between 0.002 - 0.371 and $\mathrm{L_{H\beta}}$ values between 10^{39} - 10^{43} erg s^{-1}. The authors report $\mathrm{R_{BLR}}$ values between 1.4 - 387 light days. Since the lower range of our broad Hβ luminosities is 10^{36} erg s^{-1}, three order of magnitude lower than the lowest Hβ luminosity in the [300] sample (10^{39} erg s^{-1}), and the top range of our broad Hβ luminosities is 10^{42}, one order of magnitude lower than the [300] sample (10^{43} erg s^{-1}), we reason that our $\mathrm{R_{BLR}}$ values are consistent with [300] and are reasonable approximations.

Additionally, for the Hα line, we calculate FWHMs between 1,010 km s^{-1} - 4,919 km s^{-1}, with a median FWHM of 2,079 km s^{-1}. For the Hβ line, we calculate FWHMs between 1,001 km s^{-1} - 5,849 km s^{-1}, with a median FWHM of 1,146 km s^{-1}. These elevated velocities provide direct evidence of the rapidly rotating gas clouds near the accreting SMBH, clear

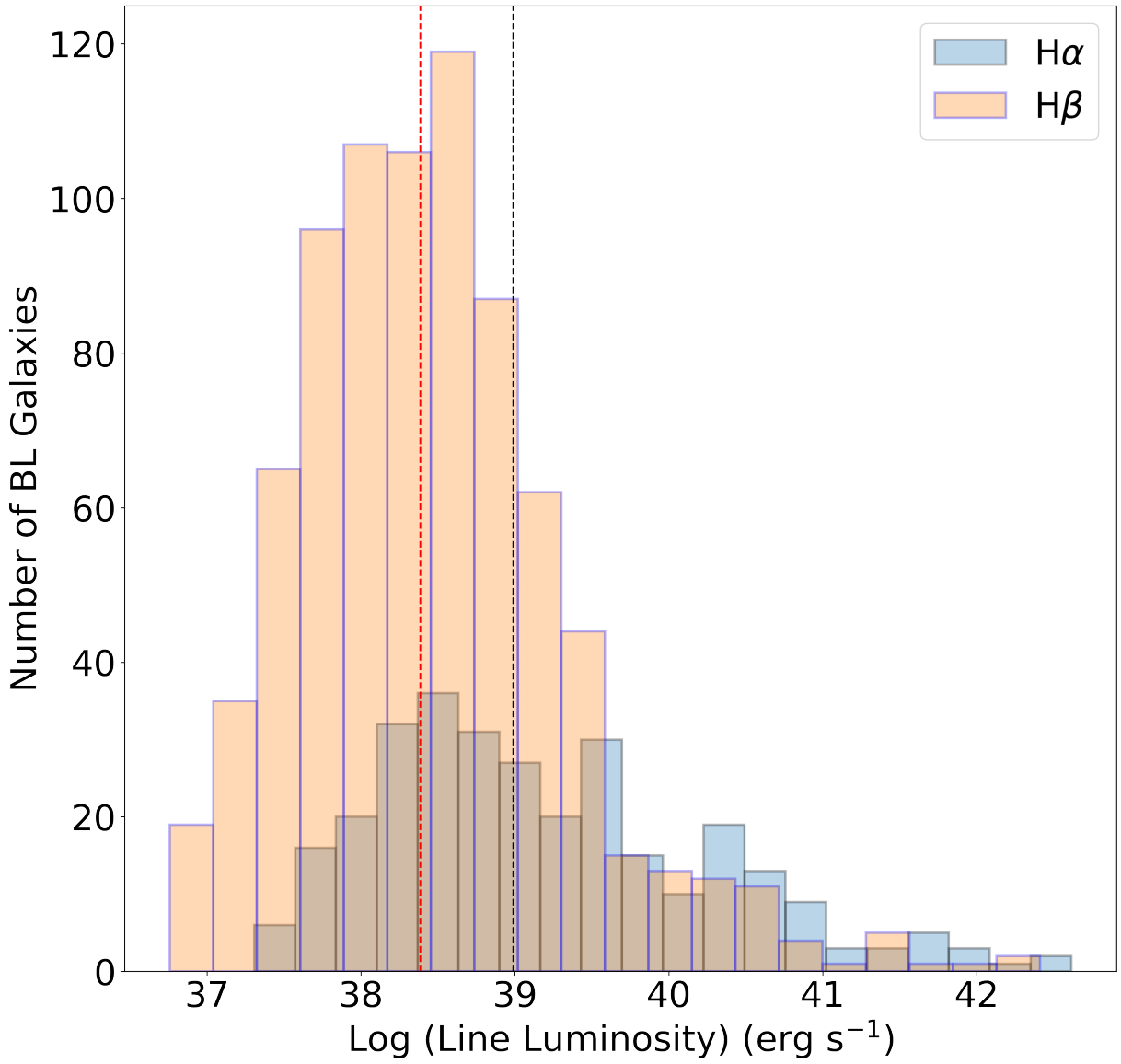

Figure 4.4: BL Luminosity distribution for the BL galaxies. The blue histogram represents the 301 broad Hα galaxies and the orange histogram represents the 801 broad Hβ galaxies. The dotted black line marks the median luminosity (9.7×10^{38} erg s^{-1}) for the Hα sample, whereas the red dashed line marks the median luminosity (2.4×10^{38} erg s^{-1}) for the Hβ sample.

tracers of AGN activity.

4.4.2 SMBH Mass Estimates

Virial SMBH masses for low-redshift AGNs can typically be estimated using measurements of the optical continuum strength (e.g., the luminosity of the continuum at 5100 Å) and the width of the broad Hβ line (e.g., [108]). However, systematic uncertainties and difficulties measuring these quantities can make this method challenging. Additionally, if the optical continuum of radio-loud AGNs is enhanced by emission from AGN jets, the continuum and SMBH masses will be systematically over-estimated (e.g., [108]). Therefore, [108] analyzed a sample of SDSS BL AGNs and proposed a new formalism for calculating SMBH masses using BL measurements. In their sample of $\sim$ 3,000 AGNs, they found that: Hα luminosity scales nearly linearly with the optical continuum luminosity, there is a definitive correlation between Hα and Hβ line widths (i.e. FWHMs), and that SMBH masses can be estimated solely using observations of the broad Hα emission line (Equation 4.3). They also uncovered that the Hβ emission line can also be solely used if Hα emission is not available (Equation 4.4). As a result, we use Equations 4.3 and 4.4 to convert the broad Hα and broad Hβ luminosities to SMBH masses for the BL galaxies in our sample.

Doing so, we measure SMBH masses for the Hα galaxies to range between 10^5 - 10^9 $M_\odot$, with a median mass of 10^7 $M_\odot$. Further, for the Hβ galaxies, we measure SMBH masses to vary between 10^5 - 10^9 $M_\odot$, with a median mass of 10^6 $M_\odot$ (Figure 4.5). Note, for the 60 BL galaxies with broad Hα and Hβ emission, we compute SMBH mass measurements using only the broad Hα emission-line components.

Furthermore, we compare the SMBH masses of our sample to the velocity dispersions of their host galaxies. We do so to test the M-σ relationship for our sample, which is the empirical correlation between a galaxy's SMBH mass and the stellar velocity dispersion of its galactic bulge ([98, 95]). We present our results for the Hα galaxies in Figure 4.6. Similar to our analysis of FWHM vs. SMBH mass (measured from the broad Hα line), we use

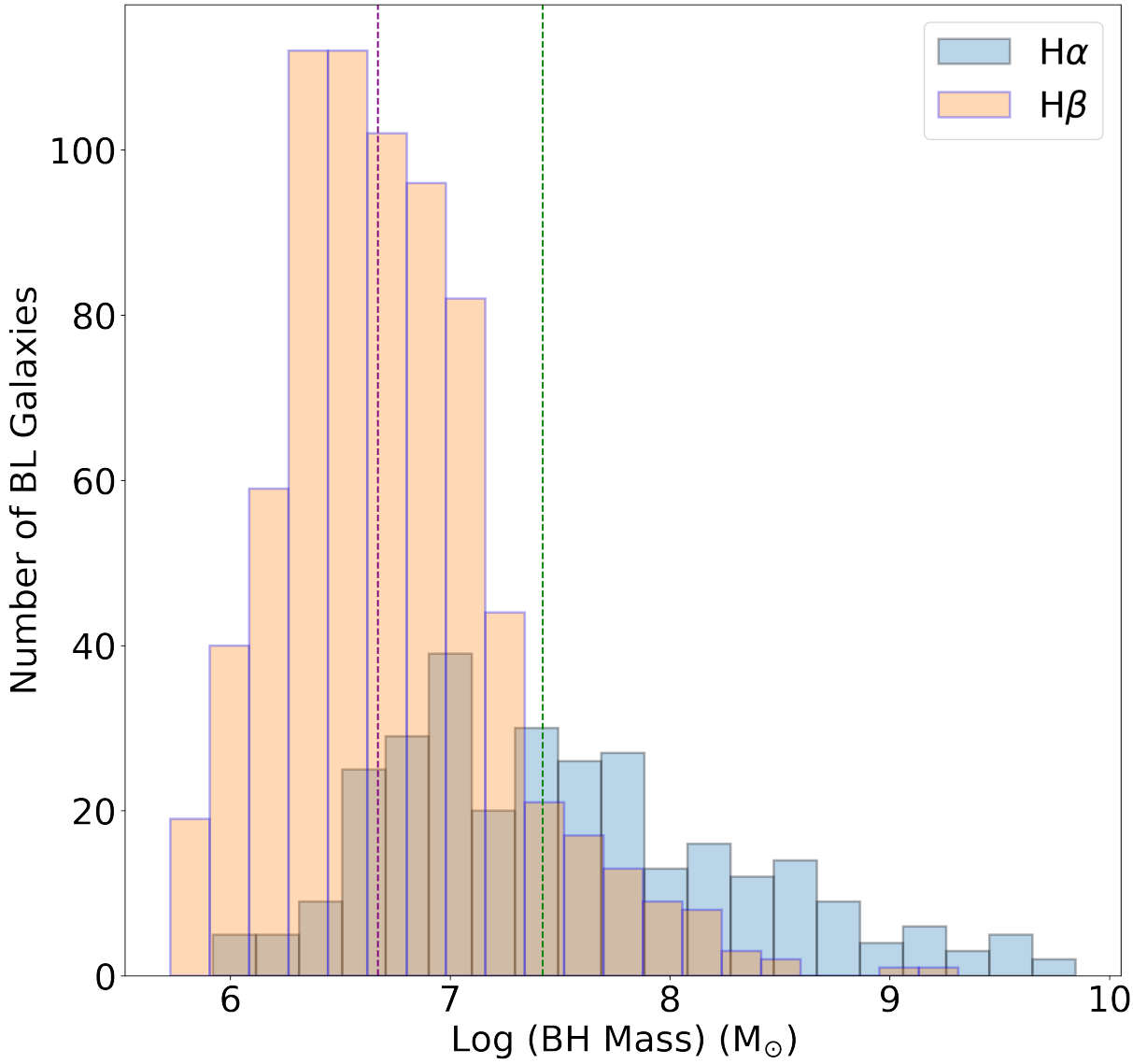

Figure 4.5: SMBH Mass distribution for the BL galaxies. The blue histogram represents the 301 broad Hα galaxies (60 of which also feature broad Hβ emission); the orange histogram represents 761 broad Hβ galaxies (with only broad Hβ emission). The dotted green line marks the median SMBH mass for the Hα sample (2.6×10^7 $M_\odot$), whereas the purple dashed line marks the median SMBH mass for the Hβ sample (4.7×10^6 $M_\odot$). For the 60 BL galaxies with broad Hα and Hβ emission, we compute SMBH mass measurements using only the broad Hα emission-line components.

the Pearson correlation to quantify our results. We measure a Pearson coefficient between velocity dispersion and SMBH mass to be 0.44. This suggests a positive correlation between the two parameters, and confirms that SMBH mass and stellar velocity are correlated in our sample, as expected.

However, we note that for the Hβ sample, where we measure SMBH masses using the broad Hβ line, we determine a Pearson coefficient of 0.04 (Figure 4.7). While this corresponds to a positive correlation, it is weaker than reported in the literature ([98, 95]). We reason that because the broad Hα galaxies feature higher mass SMBHs (median SMBH mass of 10^7 $M_\odot$ for the broad Hα galaxies; 10^6 for the broad Hβ galaxies), the M-σ relationship is likely tighter.

4.4.3 BL Mergers and Recoiling SMBH Candidates

The BL velocity profiles may feature a blend of many different components, which include, but are not limited to, Doppler motions, inflows/ outflows (possibly induced by mergers), shocks, rotation, or even a recoiling black hole. These velocity features can manifest to make the final profile a combination of many components (e.g., [214, 149]).

For our sample of BL galaxies, the BL Gaussian fits we use specifically trace the Doppler motions within the gravitational influence of the SMBH within the target galaxy, centered in MaNGA's field of view (e.g., [148]). However, we determine that a small population of BL profiles trace the BLR in a companion galaxy. Using the Nevin catalog (Section 4.3.4), we determine that 122 out of 275 broad Hα galaxies, which we could determine a merger classification for, are currently undergoing a galaxy merger (44%). Moreover, out of these 122 merging systems, we scan for the systems with BL emission from the companion galaxy outside of the target galaxy's nuclear region, which we define as the central 2.″5 region. Using these constraints, we identify 35 broad Hα offset AGNs and present an example of three offset AGNs in Figure 4.8. We showcase the optical SDSS images for the galaxies, as well as the broad Hα flux and broad Hα FWHM values for the companion galaxies. The full

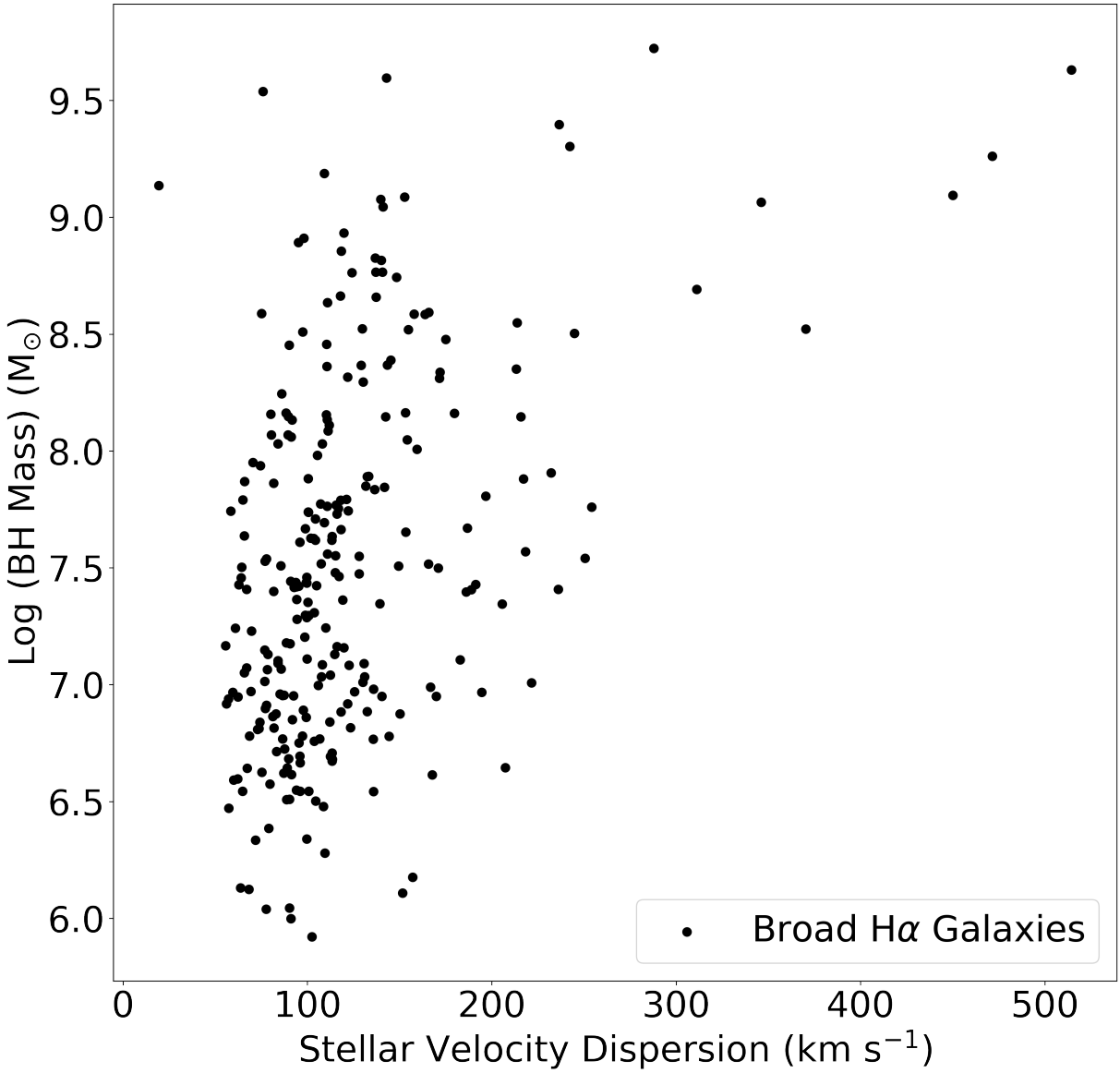

Figure 4.6: SMBH mass vs. stellar velocity dispersion. The black data points represent the broad Hα MaNGA galaxies. We use the flux-weighted mean stellar velocity dispersion of all spaxels within 1 R_e of the target galaxy (from the MaNGA DAP). The SMBH mass estimates are derived from the broad Hα luminosities (Equation 4.3). Note, we have removed the galaxies with BL emission solely from a companion galaxy, not the target MaNGA galaxy (Section 4.4.3).

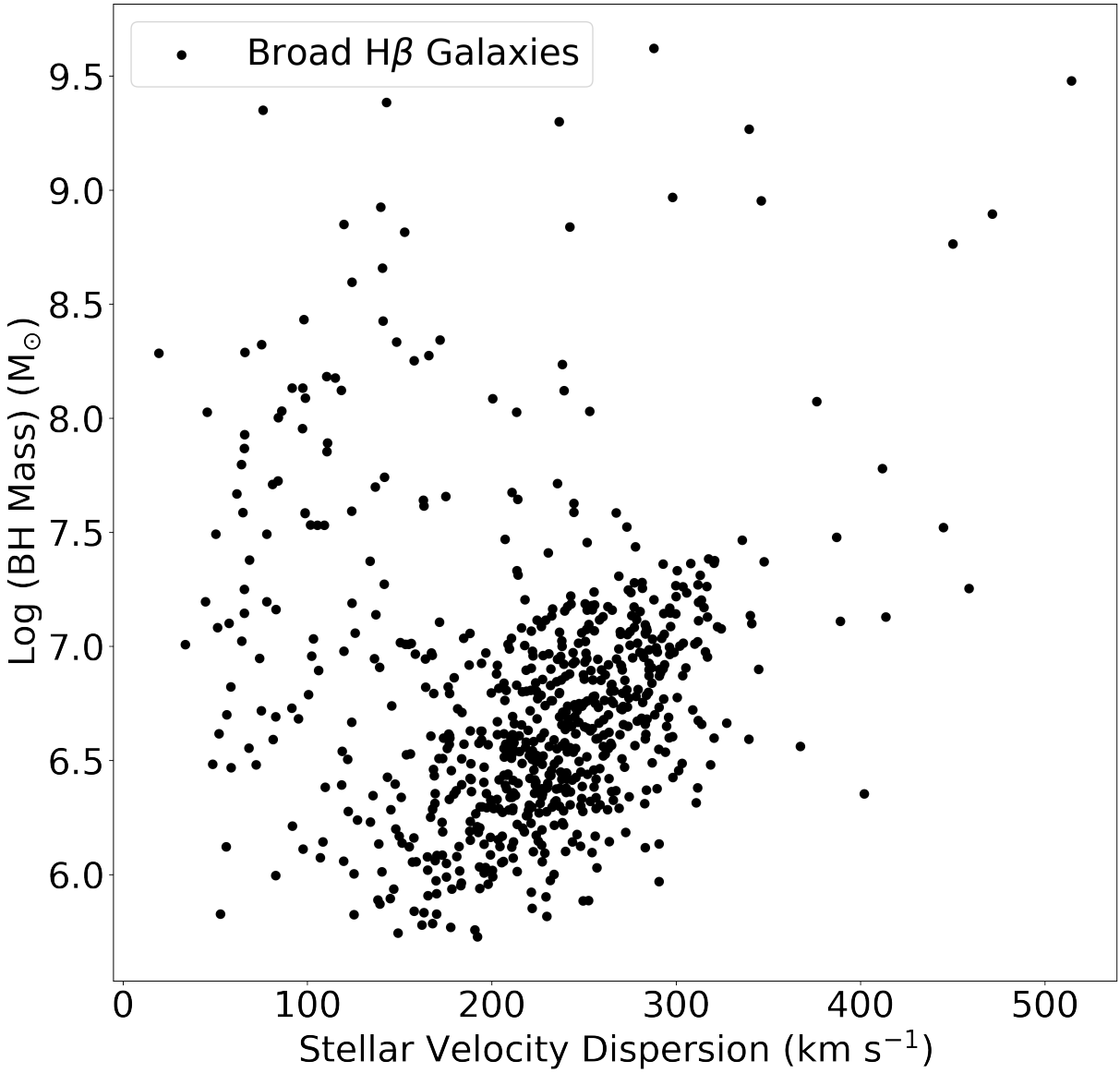

Figure 4.7: SMBH mass vs. stellar velocity dispersion. The black data points represent the broad Hβ MaNGA galaxies. We use the flux-weighted mean stellar velocity dispersion of all spaxels within 1 R_e of the target galaxy (from the MaNGA DAP). The SMBH mass estimates are derived from the broad Hβ luminosities (Equation 4.4). Note, we have removed the galaxies with BL emission solely from a companion galaxy, not the target MaNGA galaxy (Section 4.4.3).

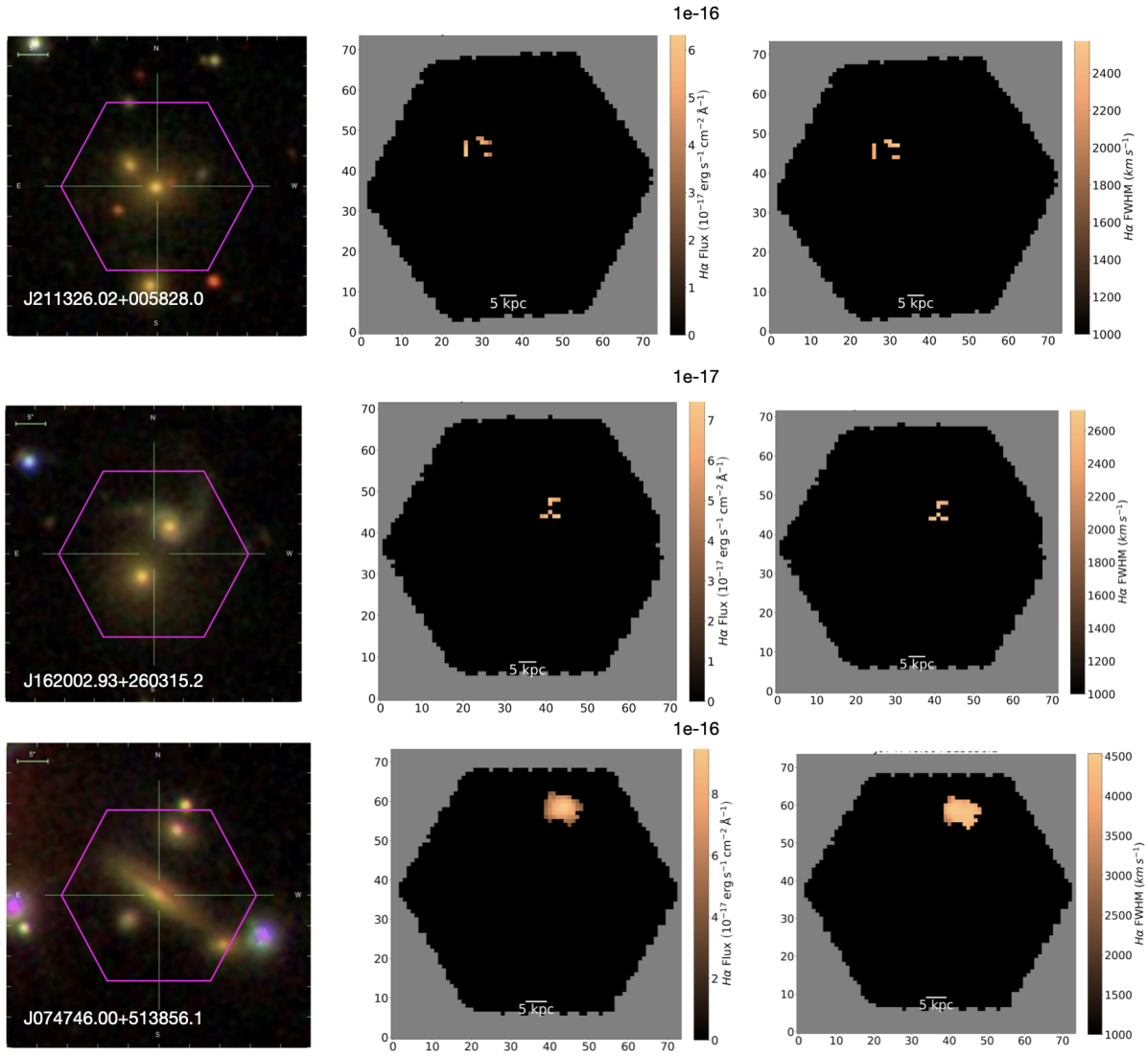

Figure 4.8: BL flux and velocity maps for 3/35 BL galaxies in our sample with broad Hα emission from a companion galaxy, not the target MaNGA galaxy. From top to bottom and left to right: SDSS optical images, broad Hα flux maps, and broad Hα FWHM maps for J211326.02+005828.0, J162002.93+260315.2, and J074746.00+513856.1.

list of broad Hα companion galaxies is provided in Appendix D. Note, for the entire sample, we do not detect any dual broad Hα candidates.

Likewise, we use the Nevin catalog to detect mergers in the Hβ sample. We find that 313 out of 722 broad Hβ galaxies, that we could determine a merger classification for, are experiencing a galaxy merger (43%). Further, we apply the same criteria as we did for the broad Hα galaxies to search for offset broad Hβ AGNs (BL emission from a companion outside of the central 2.″5 region). We detect 77 broad Hβ offset AGNs in our sample. Note, 3 offset AGNs feature both broad Hα and Hβ emission, leading to 109 unique offset AGNs in our sample. In addition, we display the optical SDSS images, as well as the broad Hβ fluxes and broad Hβ FWHMs for the companion galaxies in Figure 4.9. For J005620.79+135143.6, we identify broad Hβ emission in two companion galaxies. The full list of broad Hβ companion galaxies is provided in Appendix D. For the entire sample, we detect one dual broad Hβ candidate - J005620.79+135143.6.

Comparatively, we use the Nevin catalog to scan the total MaNGA catalog. We identify 2518 mergers, out of the 9582 MaNGA galaxies with a Nevin catalog merger classification (26%). As a result, it is evident that the broad Hα and Hβ galaxies trace a higher fraction of merging galaxies compared to the full MaNGA catalog (18% and 17% more, respectively). This is consistent with the analyses performed by [270, 271]. The authors posit that during the galaxy merging process, gas and dust are driven toward the centers of the merging galaxy pairs, which triggers SMBH growth, and funnels matter to accrete onto one or both of the SMBHs, leading to AGN activation. The authors compile a catalog of 204 offset and dual AGNs with a median $z \sim 1.15$ and stellar bulge separations < 20 kpc, using the Advanced Camera for Surveys on the *Hubble Space Telescope*. They find that AGN activation is primarily stagnant between 20 - 14 kpc, has a bump between 14 - 11 kpc, drops slightly from 11 - 4 kpc, and increases substantially from 3 - 2 kpc. We reason that the interactions between merging galaxies in our BL catalog, where the typical MaNGA footprint is mapped out to a radius of 15 kpc, may trigger some of the AGNs we detect due to the dynamical

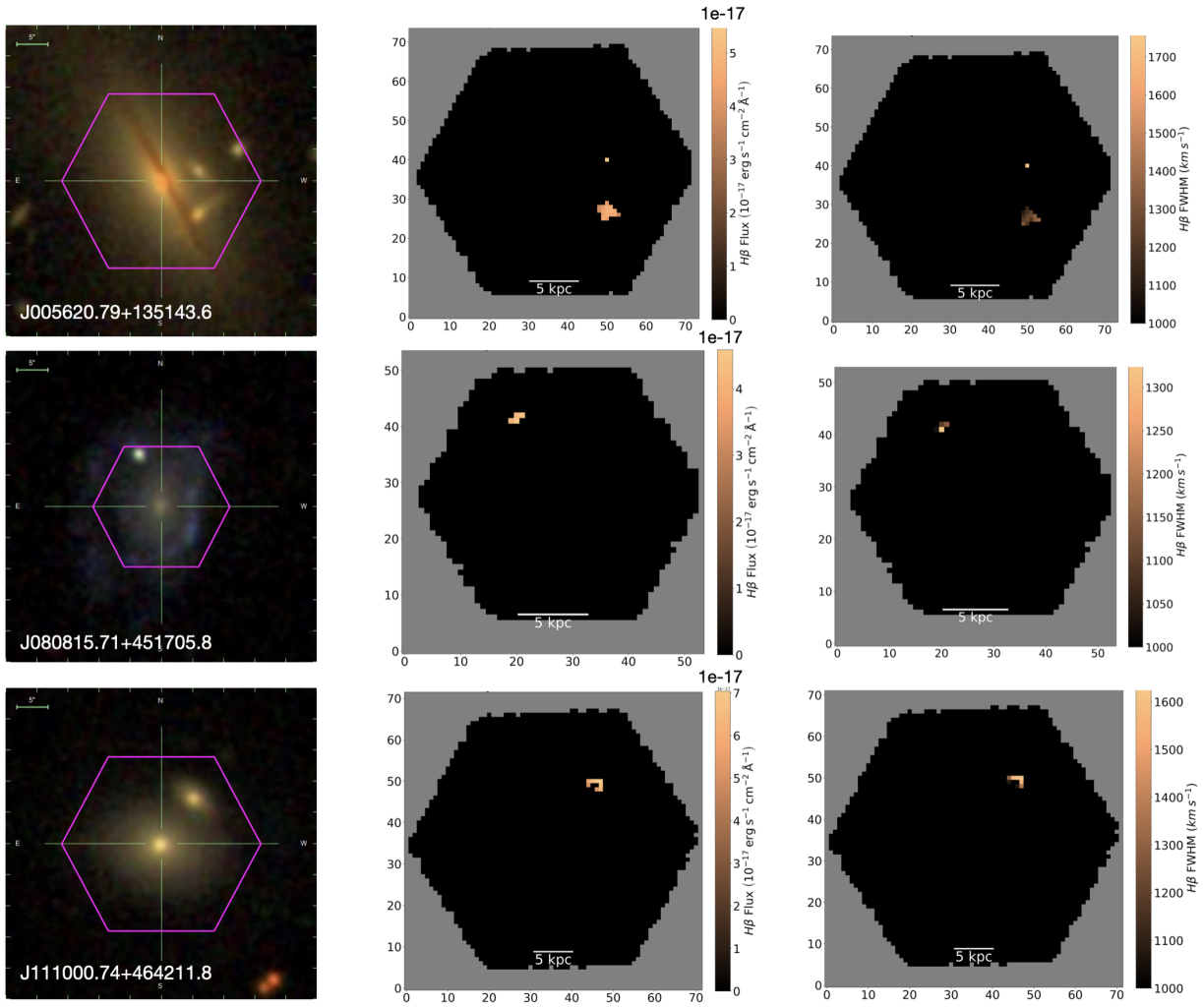

Figure 4.9: BL flux and velocity maps for 3/77 BL galaxies in our sample with broad Hβ emission from a companion galaxy, not the target MaNGA galaxy. From top to bottom and left to right: SDSS optical images, broad Hβ flux maps, and broad Hβ FWHM maps for J005620.79+135143.6, J080815.71+451705.8, and J111000.74+464211.8. In J005620.79+135143.6, we detect broad Hβ emission in two companion galaxies.

interactions between galaxies. This may account for the higher merger fraction in our BL sample.

Finally, for merging galaxy systems, near 10 parsecs, dynamical friction fails to effectively decrease the pair's angular momentum, and within 0.1 pc, gravitational radiation drives the remaining angular momentum out of the system and causes the SMBHs to finally merge. After coalescence, the remnant black hole is liable to recoil (sometimes at velocities > 1,000 km s^{-1}) due to the emission of gravitational waves. Further, if the recoiling SMBH features an AGN, the BLR should be gravitationally bound to the system, and there should be an observable systemic Doppler shift of the BLs. As a result, we search for evidence of recoiling SMBHs in our sample. To do so, we use Equation 4.5 to identify BL galaxies that feature velocities offset from the velocity of the stellar continuum of the target galaxy, which cannot be solely attributed to a companion galaxy. We find 48 broad Hα galaxies with velocity offsets > 1,000 km s^{-1}. Comparatively, we find 217 broad Hβ galaxies that meet this criteria. From these two populations, we perform a visual inspection and identify five recoiling black hole candidates (J021035.31+125505.6, J075347.89+374208.8, J082505.71+470915.8, J082529.04+470800.6, and J170259.70+333316.2; Appendix E), where the BL emission does not clearly come from a companion galaxy, and the BL emission is off-nuclear.

4.5 Discussion

We investigate 310 broad Hα galaxies and 801 broad Hβ galaxies in MaNGA's MPL-11 (1,042 unique BL galaxies), which contains 10,010 unique galaxies. We measure the broad Hα luminosity for our sample to range between 10^{37} - 10^{42} erg s^{-1}, and measure the broad Hβ luminosities for our sample to range between 10^{36} - 10^{42} erg s^{-1}. These BL galaxies represent the population of Type I AGN in MaNGA, which are AGNs oriented pole-on. The broad emission we measure directly traces the high velocity clouds found near the AGN accretion disk.

However, while Hα is the strongest line in the Balmer series and is one of the most

reliable signatures of a Type I AGN, we note that the multifaceted Hα-[NII] complex, which produces some blending of the Hα and [NII] line profiles and can create asymmetric broad Hα profiles, which may lead to some some missed broad Hα detections. This may account for the discrepancy in the number of broad Hα (301) vs. Hβ (801) galaxies we detect.

Further, we investigate the BL properties within these galaxies to better understand the properties of the BLR. For example, we use the empirical relation between Hβ emission and the size of the BLR (e.g., [300]) to measure the size of the BLR for the Hβ galaxies. We find that the BLR for these galaxies ranges between 0.01 - 46 light days, with a median radius of 0.1 light days (0.02 pc).

In addition, while some BL catalogs report that low-luminosity AGNs and low-mass SMBHs can feature BL widths as low as 500 km s^{-1} (e.g., [165]), we use the more typical line width of 1,000 km s^{-1} to differentiate the BLR from the NLR (consistent with [115, 86]). Using this threshold, we measure broad Hα FWHMs between 1,010 km s^{-1} - 4,919 km s^{-1}, with a median FWHM of 2,079 km s^{-1}. For the broad Hβ galaxies, we calculate broad Hβ FWHMs between 1,001 km s^{-1} - 5,849 km s^{-1}, with a median FWHM of 1,146 km s^{-1}. Doing so, we avoid potential contamination by star-formation, which can produce strong narrow emission lines $<$ 1,000 km s^{-1}(e.g., [242]).

Furthermore, as outlined in [108], SMBH masses can be estimated solely from observations of the broad Hα or Hβ emission line. As a result, we measure SMBH masses for the Hα galaxies to range between 10^5 - 10^9 M$_\odot$; 10^5 - 10^9 M$_\odot$ for the Hβ galaxies. These measurements help us identify a positive correlation between SMBH mass and velocity dispersion, consistent with [98, 95].

Finally, we investigate the BL galaxies in our sample with BL emission from a companion galaxy, not the target MaNGA galaxy (i.e., offset AGNs). We detect 109 unique offset AGNs in our sample. Further, we find that 122 out of 275 broad Hα galaxies, which we could determine a merger classification for, are currently undergoing a galaxy merger (44%). Similarly, 313 out of 722 broad Hβ galaxies, that we could determine a merger classification

for, are experiencing a galaxy merger (43%). Compared to the merger fraction in MaNGA (26%), the BL galaxies trace a higher fraction of mergers. We reason that during the galaxy merging process, gas and dust are driven toward the centers of the merging galaxy pairs, which triggers SMBH growth, and funnels matter to accrete onto one or both of the SMBHs, leading to AGN activation (e.g., [270, 271]). This may account for the higher merger fractions, compared to the full MaNGA sample (26%), for the BL galaxies. We also inspect the candidate BL galaxies that may host a recoiling SMBH in our sample. We identify 5 BL galaxies that may potentially be recoiling SMBHs. These galaxies feature off-nuclear BL emission, systemic offset velocities $>$ 1,000 km s^{-1}, and have BLs that are not clearly from a companion galaxy.

4.6 Summary and Future Work

We build one of the largest catalogs of broad Hα and Hβ galaxies in MaNGA to date, using our custom pipeline, which measures BL emission at $\geq 5\sigma$ above the background continuum, and with FWHM values $>$ 1,000 km s^{-1}.

Our primary findings are:

(1) The radius of the BLR ranges between 0.01 - 46 light days, with a median radius of 0.1 light days (0.02 pc) for our Hβ sample.

(2) Broad Hα luminosities vary between 10^{37} - 10^{42} erg s^{-1}; 10^{36} - 10^{42} erg s^{-1} for the broad Hβ galaxies. Further, broad Hα galaxies are more luminous, with a median luminosity of 9.7×10^{38} erg s^{-1}, which is $\sim$ 25% higher than the median luminosity (2.4×10^{38} erg s^{-1}) of the Hβ galaxies.

(3) Broad Hα FWHMs vary between 1,010 km s^{-1} - 4,919 km s^{-1}, with a median FWHM of 2,079 km s^{-1}; 1,001 km s^{-1} - 5,849 km s^{-1}, with a median FWHM of 1,146 km s^{-1} for the broad Hβ galaxies.

(4) SMBH masses for the Hα galaxies range between 10^5 - 10^9 $M_\odot$, with a median mass of 10^7 $M_\odot$; 10^5 - 10^9 $M_\odot$, with a median mass of 10^6 $M_\odot$ for the Hβ galaxies.

(5) The Pearson coefficient for FWHM and SMBH mass for the Hα galaxies is 0.82 (0.72 for the Hβ galaxies), which implies a positive correlation, as expected from Equation 4.3 and 4.4.

(6) The Pearson coefficient between velocity dispersion and SMBH mass is 0.44 for the Hα galaxies. This suggests a positive correlation between the two parameters, and confirms that SMBH mass and stellar velocity are correlated in our sample, as expected. However, the Pearson coefficient for the broad Hβ sample is 0.04, weaker than reported in prior studies.

(7) 122 out of 275 broad Hα galaxies, which we could determine a merger classification for, are currently undergoing a galaxy merger (44%). Similarly, 313 out of 722 broad Hβ galaxies, that we could determine a merger classification for, are experiencing a galaxy merger (43%). Both are well above the merger fraction in the full MaNGA sample (26%). We reason that this is likely due to merger-induced AGN fueling in our sample.

(8) 35 broad Hα galaxies feature offset AGNs; 77 broad Hβ galaxies feature offset AGNs. 3 offset AGNs feature both broad Hα and Hβ emission, leading to 109 unique offset AGNs in our sample.

(9) 5 BL galaxies have off-nuclear BL emission, velocities $>$ 1,000 km s^{-1} offset from the velocity of the stellar continuum of the target galaxy, and BL emission not clearly from a companion galaxy. These attributes make them recoiling SMBH candidates.

BL detection in large spectroscopic surveys offers a powerful tool for identifying AGNs, and for comprehending the AGN physics closest to the accretion disk, which is essential for unraveling the nature of AGN-galaxy co-evolution.

Future work to enhance these efforts could include: 1) a thorough investigation of the kinematic properties of the BLR, and 2) multi-wavelength observations of the BL AGN in MaNGA. Exploring the kinematics of the BL profiles in more depth (e.g., measuring the asymmetries of the line profiles and analyzing double-peaked BLs) can shed insight on how various BL velocity components manifest. These include, but are not limited to, a blend of Doppler motions, inflows/ outflows (possibly induced by mergers), shocks, rotation, or even a recoiling black hole. To further evaluate the kinematics of the BLs and to determine their relationship with feedback, constructing additional velocity maps (similar to the flux maps) for each BL galaxy would help to reveal the kinematic gradients of the gas (0.″5 x 0.″5 resolution; provided by MaNGA's DAP). This could help differentiate shocks from photoionized regions (e.g., shock velocities $\geq$ 500 km s^{-1}; [57]). Moreover, outflowing winds can be identified by inspecting asymmetric and broadened Gaussian profiles. Finally, X-ray observations, from *Chandra*, for example, would be useful for verifying the AGNs in our BL sample, and in particular, confirming the population of offset and dual AGNs.

Chapter 5

Dissertation Summary and Future Work

In this dissertation, I have presented the work I completed during my Ph.D. The core of this work focused on accurate AGN identification in the optical band, since existing optical AGN methods (e.g, BPT Diagrams) are liable to contamination by diffuse ionized gas, extraplanar gas, photoionization by hot stars, metallicity, emission from post-AGB stars and star formation, and shocks, leading to AGN misclassification.

To address this, I used CLs as an AGN tracer. These are highly ionized species of gas with IPs $\geq$ 100 eV (e.g., [NeV], [FeVII], and [FeX]), which require extremely high energies for production, above the limit of stellar emission.

In Chapter 2, I considered that the fundamental nature and extent of the CLR, which may serve as a vital tracer for AGN activity, remain unresolved. I explored previous studies, which suggested that the CLR is produced by AGN-driven outflows and occupies a distinct region between the broad line region and the narrow line region, which places it tens to hundreds of parsecs from the galactic center. Then, I investigated 10 CL emitting galaxies from the SDSS-IV MaNGA catalog with emission from one or more CLs detected at $\geq 5\sigma$ above the continuum in at least 10 spaxels. I found that the CLR is far more extended, reaching out to 1.3 - 23 kpc from the galactic center. Moreover, I cross-matched the sample of 10 CL galaxies with the largest existing MaNGA AGN catalog and identified 7 in it; two of the remaining three are galaxy mergers and the final one is an AGN candidate. Further, I measured the average CLR electron temperatures to range between 12,331 K -

22,530 K, slightly above the typical threshold for pure AGN photoionization ($\sim$ 20,000 K) and indicative of shocks (e.g., merger-induced or from supernova remnants) in the CLR. In this chapter, I reasoned that ionizing photons emitted by the central continuum source (i.e. AGN photoionization) primarily generate the CLs, and that energetic shocks are an additional ionization mechanism that may produce the most extended CLRs I measured.

In Chapter 3, I further considered that despite the importance of AGN in galaxy evolution, accurate AGN identification is often challenging. To build upon the analyses in Chapter 2, and to determine if CLs are in fact strong AGN tracers, I assembled and analyzed the largest catalog of optical CL galaxies using the MaNGA catalog. I detected CL emission in 71 MaNGA galaxies, out of the 10,010 unique galaxies from the final MaNGA catalog, with $\geq 5\sigma$ confidence. In the sample, I measured [NeV] $\lambda\lambda$3347, 3427, [FeVII] $\lambda\lambda\lambda$3586, 3760, 6086, and [FeX] λ6374 emission and cross-matched the CL galaxies with a catalog of AGNs that were confirmed with BL, X-ray, IR, and radio observations. I found that [NeV] emission, compared to [FeVII] and [FeX] emission, is best at identifying high luminosity AGNs. Moreover, I found that the CL galaxies with the least dust extinction yield the most iron CL detections. I posited that the bulk of the iron CLs are destroyed by dust grains in the galaxies with the highest [OIII] luminosities in the sample, and that AGNs in the galaxies with low [OIII] luminosities are possibly too weak to be detected using traditional techniques.

In addition, to complement the search for CLs in MaNGA, I focused on BLs (FWHMs $>$ 1,000) observed in Type I AGNs, which are oriented pole-on, in Chapter 4. Since the broad Hα and broad Hβ lines are incredibly efficient at tracing AGNs when the BLR is not strongly dust obscured, I scanned for them in MaNGA as well. I found 301 broad Hα galaxies and 801 broad Hβ galaxies. In total, I detected 1,042 unique BL galaxies; 60 feature both Hα and Hβ emission. I found that the radius of the BLR ranges between 0.01 - 46 light days, with a median radius of 0.1 light days (0.02 pc) for our Hβ sample. I also determined that the broad Hα luminosities vary between 10^{37} - 10^{42} erg s^{-1}; 10^{36} - 10^{42} erg s^{-1} for the

broad Hβ galaxies. Further, I reported that broad Hα galaxies are more luminous, with a median luminosity of 9.7×10^{38} erg s^{-1}, which is $\sim 25\%$ higher than the median luminosity (2.4×10^{38} erg s^{-1}) of the Hβ galaxies. Then, I calculated broad Hα FWHMs to vary between 1,010 km s^{-1} - 4,919 km s^{-1}, with a median FWHM of 2,079 km s^{-1}; 1,001 km s^{-1} - 5,849 km s^{-1}, with a median FWHM of 1,146 km s^{-1} for the Hβ galaxies. My analysis then focused on the SMBH masses for the BL sample, and I found that the SMBH masses for the Hα galaxies range between 10^5 - 10^9 M$_\odot$, with a median mass of 10^7 M$_\odot$; 10^5 - 10^9 M$_\odot$, with a median mass of 10^6 M$_\odot$ for the Hβ galaxies. In addition, I identified that 122 out of 275 broad Hα galaxies, which I could determine a merger classification for, are currently undergoing a galaxy merger (44%). Similarly, I found that 313 out of 722 broad Hβ galaxies, that I could determine a merger classification for, are experiencing a galaxy merger (43%). Both are well above the merger fraction in the full MaNGA sample (26%), and suggests AGN fueling for the mergers in our sample. Finally, I reported that 35 broad Hα galaxies host offset AGNs; 77 for the broad Hβ galaxies. 3 offset AGNs feature both broad Hα and Hβ emission, leading to 109 unique offset AGNs in our sample. Ultimately, I concluded that BLs are indeed strong tracers of the high velocities clouds near the AGN accretion disk, and may even be able to trace recoiling BHs.

Regarding future work with the CLs, *Chandra* observations would be advantageous. For example, for the 71 CL galaxies with [NeV] or [FeVII] emission, some have nuclear CL emission only while others have spatially-offset CL emission that could be associated with outflows or shocks. To help understand whether [NeV] and [FeVII] lines are definitively tracing AGN activity, I cross–matched the CLs galaxies with AGN detections from *WISE* mid-infrared color cuts, SDSS BLs, *Swift*/BAT hard X-ray observations, and NVSS/ FIRST 1.4 GHz radio observations ([53]). Surprisingly, I found that most of the [NeV] galaxies have confirmed AGNs (31/33), with most of the detections coming from *WISE*. In contrast, most of the [FeVII] galaxies do not have confirmed AGNs (only 3/34; one detected in *WISE*; one detected in *WISE* and broad lines; one detected in *WISE*, broad lines, and *Swift*; all three

have nuclear [FeVII] emission). Both [NeV] and [FeVII] have similar ionization potentials (97.1 eV and 99.1 eV, respectively), and while [NeV] has been suggested as an AGN tracer before, [FeVII] is not well studied in the literature. One possibility is that the galaxies with nuclear [FeVII] have central AGNs, while in the off-nuclear [FeVII] galaxies the [FeVII] emission is produced by outflows or shocks, either associated with AGNs or other phenomena such as star formation and mergers

As I reviewed in Section 3.4.5, I suspect that dust obscuration may be playing a role. I reasoned that emission from the iron CL species is being diminished within dusty galaxies, which provides a physical explanation for the low number of iron CL galaxies with nuclear emission in high E(B - V) value galaxies. I also considered the correlation between the AGN dusty torus and AGN bolometric luminosity. I found that the lower L_{bol} values correlate with a diminishing dusty torus, which results in less destruction of nuclear iron by dust grains; I detected more iron CLs in these low luminosity sources. On the other hand, the [NeV] galaxies feature higher L_{bol} values, which likely correspond to their elevated E(B - V) values. I concluded that [NeV] traces high-luminosity AGNs while [FeVII] traces low-luminosity AGNs; the expected bolometric luminosities of the AGNs (traced by [OIII] flux; [119]) in the [FeVII] galaxies are $\sim$ two orders of magnitude smaller, on average, than those of the [NeV] galaxies.

I recently won a *Chandra* proposal to observe five [FeVII]-emitting MaNGA galaxies with *Chandra*(100 ks total). Observing these [FeVII] galaxies will allow me to definitively elucidate the origin(s) of CL production in these galaxies, and to better understand the efficacy of CLs as AGN tracers. Two targets have nuclear [FeVII] emission and three targets have [FeVII] emission that is $7''$ to $14''$ off nuclear. X-ray observations are required to identify any AGNs present in these galaxies, as these five galaxies do not have BLs, are not radio loud, and do not have mid-infrared AGN detections (perhaps because they host low-luminosity AGNs). *Chandra* is required for its excellent spatial resolution, which can pinpoint if the AGN is nuclear or associated with the off-nuclear [FeVII] emission and whether

there are soft X-rays associated with the off-nuclear emission. The *Chandra* observations, when combined with the MaNGA observations, will reveal whether the [FeVII] emission is produced by AGNs, AGN outflows, or outflows and shocks associated with star formation or galaxy mergers.

To make the most efficient use of *Chandra*, I selected the [FeVII] galaxies with high estimated 2-10 keV fluxes ($> 3 \times 10^{-14}$ erg cm^{-2} s^{-1}; estimated from the [OIII] flux spatially coincident with the [FeVII] emission and the established Type 2 AGN [OIII] to X-ray scaling relation; [119]). The five targets, shown in Figure 5.1, include two galaxies with nuclear [FeVII] emission (J1349 and J2152) and three galaxies with off-nuclear [FeVII] emission (J0023, J1613, and J0920; the spatial offsets range from $7''$ to $14''$, or 5 kpc to 7 kpc). These galaxies represent the overall fractions of [FeVII] galaxies in MaNGA with nuclear (40%) vs. off-nuclear (60%) [FeVII] emission. This also underscores the need for *Chandra*'s spatial resolution to pinpoint whether X-rays are associated with the nucleus or the off-nuclear emission. Further, two of the targets appear to be ongoing galaxy mergers (J1349 and J1613).

The primary goals of my *Chandra* data analysis will be to determine if any X-ray AGNs are present, and then to measure the AGN properties. Ultimately, I will determine whether the [FeVII] CL is an indicator of AGNs, outflows, shocks, or a combination of these effects. The *Chandra* and MaNGA observations will distinguish between the following possibilities:

(1) The [FeVII] emission is produced by AGNs. In this case I would find an X-ray AGN that is spatially coincident with the [FeVII] emission in the MaNGA observations. To test the hypothesis that [FeVII] emission is associated with lower luminosity AGNs on average, I will compare the AGN bolometric luminosities to those of the [NeV] galaxies with confirmed AGNs.

(2) The [FeVII] emission is produced by AGN outflows. If I find an X-ray AGN at the galaxy center while the [FeVII] emission is mostly off-nuclear, then this is evidence

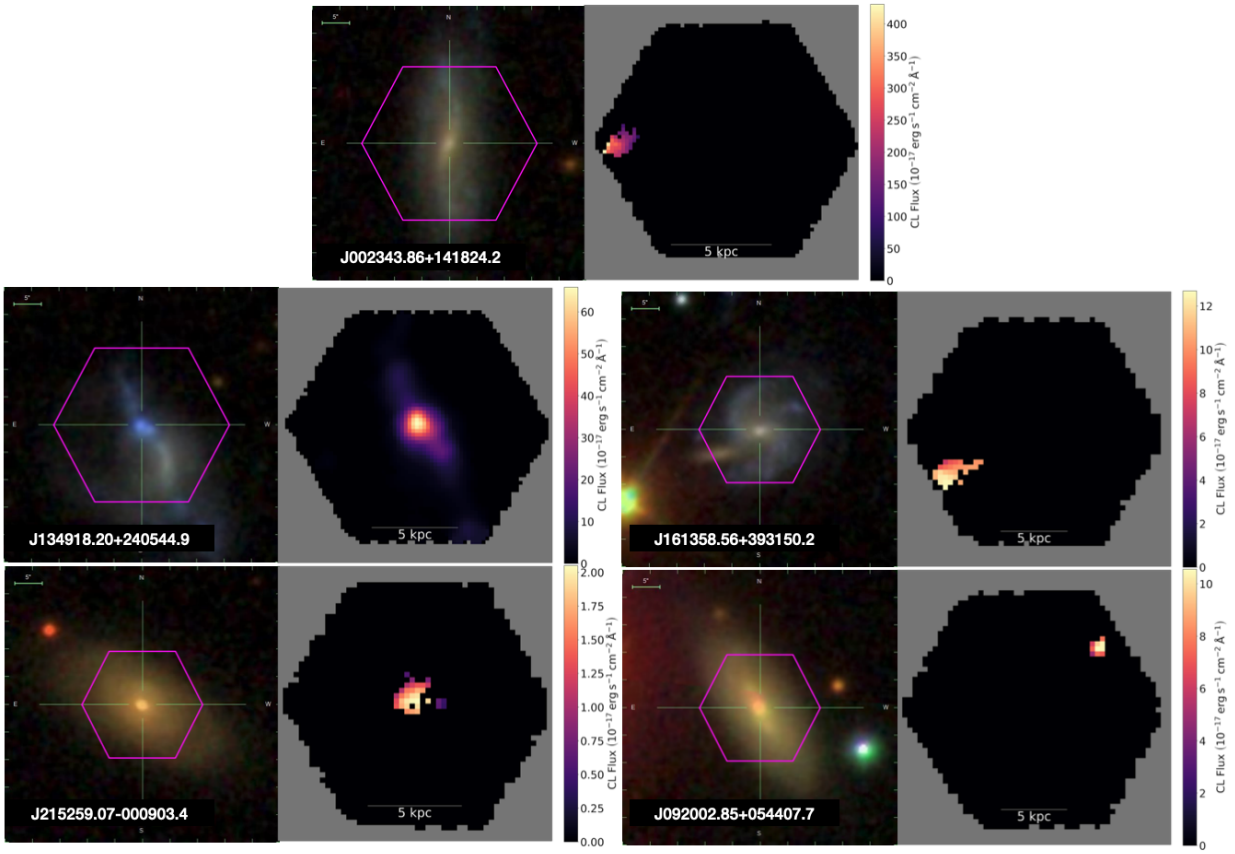

Figure 5.1: From left to right and top to bottom: SDSS optical image and corresponding [FeVII] flux map for J0023, J1349, J1613, J2152, and J0920, the targets of my *Chandra* observations. The purple hexagons show the footprint of MaNGA observations.

for the [FeVII] emission tracing AGN outflows. In this case I might also detect soft X-rays associated with the outflows and the [FeVII] emission. To help identify that the outflows are AGN instead of star formation driven, there are other markers I can search for in the MaNGA observations; for example, the ionized gas associated with the outflow (this could include other species such as [OIII]) typically have a conical morphology for AGN outflows, as opposed to the wide, chimney-shapes morphology typical of star formation driven outflows (e.g., [197]).

(3) The [FeVII] emission is produced by outflows or shocks associated with star formation or mergers. If I do not detect an X-ray AGNs, then the [FeVII] emission is likely produced by star formation driven outflows, supernova remnant (SNR) shocks, or merger-induced shocks. I can help distinguish between these scenarios by using the MaNGA observations to create maps of the spatial distribution of star formation, measure [S II]/Hα line flux ratios to trace SNR shocks (e.g., [72]), and measure [OI]/Hα line flux ratios to trace shocks due to mergers (e.g., [227].

Finally, observations of infrared CLs are an exciting pathway for identifying AGNs. This is for two reasons: 1) hot massive stars do not generate photons energetic enough to generate IR CLs (e.g., [SIV], [CaVIII], [OIV], and [S III]), and 2) IR emission from Type II supernovae is rare, extremely weak, and short lived (e.g., [110, 20]). Also, IR CLs are less sensitive to dust obscuration than optical lines and are less likely to be contaminated by host galaxy stellar emission. As outlined in [246], the *Infrared Space Observatory* (ISO) and the *Spitzer* missions have uncovered significant populations of CL AGNs in galaxies with optically "normal" nuclear spectra (e.g., [169, 100, 285, 105]. With the *James Webb Space Telescope*, observations in the 1 - 30 μm band are now possible, beyond the capabilities of the *ISO* or *Spitzer*. This will provide a tantalizing opportunity to scan for even larger populations of IR CLs to help better detect AGNs, and ultimately, determine their astrophysical significance in the context of galaxy evolution.

Bibliography

[1] Tom Abel, Michael L. Norman, and Piero Madau. Photon-conserving Radiative Transfer around Point Sources in Multidimensional Numerical Cosmology. Astrophysical Journal, 523(1):66–71, September 1999.

[2] Kurt L. Adelberger, Charles C. Steidel, Mauro Giavalisco, Mark Dickinson, Max Pettini, and Melinda Kellogg. A Counts-in-Cells Analysis Of Lyman-break Galaxies At Redshift Z ~3. Astrophysical Journal, 505(1):18–24, September 1998.

[3] Jennifer K. Adelman-McCarthy, Marcel A. Agüeros, Sahar S. Allam, Carlos Allende Prieto, Kurt S. J. Anderson, Scott F. Anderson, James Annis, Neta A. Bahcall, C. A. L. Bailer-Jones, Ivan K. Baldry, J. C. Barentine, Bruce A. Bassett, Andrew C. Becker, Timothy C. Beers, Eric F. Bell, Andreas A. Berlind, Mariangela Bernardi, Michael R. Blanton, John J. Bochanski, William N. Boroski, Jarle Brinchmann, J. Brinkmann, Robert J. Brunner, Tamás Budavári, Samuel Carliles, Michael A. Carr, Francisco J. Castander, David Cinabro, R. J. Cool, Kevin R. Covey, István Csabai, Carlos E. Cunha, James R. A. Davenport, Ben Dilday, Mamoru Doi, Daniel J. Eisenstein, Michael L. Evans, Xiaohui Fan, Douglas P. Finkbeiner, Scott D. Friedman, Joshua A. Frieman, Masataka Fukugita, Boris T. Gänsicke, Evalyn Gates, Bruce Gillespie, Karl Glazebrook, Jim Gray, Eva K. Grebel, James E. Gunn, Vijay K. Gurbani, Patrick B. Hall, Paul Harding, Michael Harvanek, Suzanne L. Hawley, Jeffrey Hayes, Timothy M. Heckman, John S. Hendry, Robert B. Hindsley, Christopher M. Hirata, Craig J. Hogan, David W. Hogg, Joseph B. Hyde, Shin-ichi Ichikawa, Željko Ivezić, Sebastian Jester, Jennifer A. Johnson, Anders M. Jorgensen, Mario Jurić, Stephen M. Kent, R. Kessler, S. J. Kleinman, G. R. Knapp, Richard G. Kron, Jurek Krzesinski, Nikolay Kuropatkin, Donald Q. Lamb, Hubert Lampeitl, Svetlana Lebedeva, Young Sun Lee, R. French Leger, Sébastien Lépine, Marcos Lima, Huan Lin, Daniel C. Long, Craig P. Loomis, Jon Loveday, Robert H. Lupton, Olena Malanushenko, Viktor Malanushenko, Rachel Mandelbaum, Bruce Margon, John P. Marriner, David Martínez-Delgado, Takahiko Matsubara, Peregrine M. McGehee, Timothy A. McKay, Avery Meiksin, Heather L. Morrison, Jeffrey A. Munn, Reiko Nakajima, Jr. Neilsen, Eric H., Heidi Jo Newberg, Robert C. Nichol, Tom Nicinski, Maria Nieto-Santisteban, Atsuko Nitta, Sadanori Okamura, Russell Owen, Hiroaki Oyaizu, Nikhil Padmanabhan, Kaike Pan, Changbom Park, Jr. Peoples, John, Jeffrey R. Pier, Adrian C. Pope, Norbert Purger, M. Jordan Raddick, Paola Re Fiorentin, Gordon T. Richards, Michael W. Richmond, Adam G.

Riess, Hans-Walter Rix, Constance M. Rockosi, Masao Sako, David J. Schlegel, Donald P. Schneider, Matthias R. Schreiber, Axel D. Schwope, Uroš Seljak, Branimir Sesar, Erin Sheldon, Kazu Shimasaku, Thirupathi Sivarani, J. Allyn Smith, Stephanie A. Snedden, Matthias Steinmetz, Michael A. Strauss, Mark SubbaRao, Yasushi Suto, Alexander S. Szalay, István Szapudi, Paula Szkody, Max Tegmark, Aniruddha R. Thakar, Christy A. Tremonti, Douglas L. Tucker, Alan Uomoto, Daniel E. Vanden Berk, Jan Vandenberg, S. Vidrih, Michael S. Vogeley, Wolfgang Voges, Nicole P. Vogt, Yogesh Wadadekar, David H. Weinberg, Andrew A. West, Simon D. M. White, Brian C. Wilhite, Brian Yanny, D. R. Yocum, Donald G. York, Idit Zehavi, and Daniel B. Zucker. The Sixth Data Release of the Sloan Digital Sky Survey. The Astrophysical Journal Supplement Series, 175(2):297–313, April 2008.

[4] Christopher J. Agostino and Samir Salim. Crossing the Line: Active Galactic Nuclei in the Star-forming Region of the BPT Diagram. Astrophysical Journal, 876(1):12, May 2019.

[5] Hiroaki Aihara, Carlos Allende Prieto, Deokkeun An, Scott F. Anderson, Éric Aubourg, Eduardo Balbinot, Timothy C. Beers, Andreas A. Berlind, Steven J. Bickerton, Dmitry Bizyaev, Michael R. Blanton, John J. Bochanski, Adam S. Bolton, Jo Bovy, W. N. Brandt, J. Brinkmann, Peter J. Brown, Joel R. Brownstein, Nicolas G. Busca, Heather Campbell, Michael A. Carr, Yanmei Chen, Cristina Chiappini, Johan Comparat, Natalia Connolly, Marina Cortes, Rupert A. C. Croft, Antonio J. Cuesta, Luiz N. da Costa, James R. A. Davenport, Kyle Dawson, Saurav Dhital, Anne Ealet, Garrett L. Ebelke, Edward M. Edmondson, Daniel J. Eisenstein, Stephanie Escoffier, Massimiliano Esposito, Michael L. Evans, Xiaohui Fan, Bruno Femenía Castellá, Andreu Font-Ribera, Peter M. Frinchaboy, Jian Ge, Bruce A. Gillespie, G. Gilmore, Jonay I. González Hernández, J. Richard Gott, Andrew Gould, Eva K. Grebel, James E. Gunn, Jean-Christophe Hamilton, Paul Harding, David W. Harris, Suzanne L. Hawley, Frederick R. Hearty, Shirley Ho, David W. Hogg, Jon A. Holtzman, Klaus Honscheid, Naohisa Inada, Inese I. Ivans, Linhua Jiang, Jennifer A. Johnson, Cathy Jordan, Wendell P. Jordan, Eyal A. Kazin, David Kirkby, Mark A. Klaene, G. R. Knapp, Jean-Paul Kneib, C. S. Kochanek, Lars Koesterke, Juna A. Kollmeier, Richard G. Kron, Hubert Lampeitl, Dustin Lang, Jean-Marc Le Goff, Young Sun Lee, Yen-Ting Lin, Daniel C. Long, Craig P. Loomis, Sara Lucatello, Britt Lundgren, Robert H. Lupton, Zhibo Ma, Nicholas MacDonald, Suvrath Mahadevan, Marcio A. G. Maia, Martin Makler, Elena Malanushenko, Viktor Malanushenko, Rachel Mandelbaum, Claudia Maraston, Daniel Margala, Karen L. Masters, Cameron K. McBride, Peregrine M. McGehee, Ian D. McGreer, Brice Ménard, Jordi Miralda-Escudé, Heather L. Morrison, F. Mullally, Demitri Muna, Jeffrey A. Munn, Hitoshi Murayama, Adam D. Myers, Tracy Naugle, Angelo Fausti Neto, Duy Cuong Nguyen, Robert C. Nichol, Robert W. O'Connell, Ricardo L. C. Ogando, Matthew D. Olmstead, Daniel J. Oravetz, Nikhil Padmanabhan, Nathalie Palanque-Delabrouille, Kaike Pan, Parul Pandey, Isabelle Pâris, Will J. Percival, Patrick Petitjean, Robert Pfaffenberger, Janine Pforr, Stefanie Phleps, Christophe Pichon, Matthew M. Pieri, Francisco Prada, Adrian M. Price-Whelan, M. Jordan Raddick, Beatriz H. F. Ramos,

Céline Reylé, James Rich, Gordon T. Richards, Hans-Walter Rix, Annie C. Robin, Helio J. Rocha-Pinto, Constance M. Rockosi, Natalie A. Roe, Emmanuel Rollinde, Ashley J. Ross, Nicholas P. Ross, Bruno M. Rossetto, Ariel G. Sánchez, Conor Sayres, David J. Schlegel, Katharine J. Schlesinger, Sarah J. Schmidt, Donald P. Schneider, Erin Sheldon, Yiping Shu, Jennifer Simmerer, Audrey E. Simmons, Thirupathi Sivarani, Stephanie A. Snedden, Jennifer S. Sobeck, Matthias Steinmetz, Michael A. Strauss, Alexander S. Szalay, Masayuki Tanaka, Aniruddha R. Thakar, Daniel Thomas, Jeremy L. Tinker, Benjamin M. Tofflemire, Rita Tojeiro, Christy A. Tremonti, Jan Vandenberg, M. Vargas Magaña, Licia Verde, Nicole P. Vogt, David A. Wake, Ji Wang, Benjamin A. Weaver, David H. Weinberg, Martin White, Simon D. M. White, Brian Yanny, Naoki Yasuda, Christophe Yeche, and Idit Zehavi. The Eighth Data Release of the Sloan Digital Sky Survey: First Data from SDSS-III. Astrophysical Journal, Supplement, 193(2):29, April 2011.

[6] Mark G. Allen, Brent A. Groves, Michael A. Dopita, Ralph S. Sutherland, and Lisa J. Kewley. The MAPPINGS III Library of Fast Radiative Shock Models. Astrophysical Journal, Supplement, 178(1):20–55, September 2008.

[7] Robert Antonucci. Unified models for active galactic nuclei and quasars. Annual Review of Astronomy and Astrophysics, 31:473–521, January 1993.

[8] I. Appenzeller and S. J. Wagner. Forbidden high-ionization lines in QSO spectra. Astronomy and Astrophysics, 250:57, October 1991.

[9] L. Armus, V. Charmandaris, H. W. W. Spoon, J. R. Houck, B. T. Soifer, B. R. Brandl, P. N. Appleton, H. I. Teplitz, S. J. U. Higdon, D. W. Weedman, D. Devost, P. W. Morris, K. I. Uchida, J. van Cleve, D. J. Barry, G. C. Sloan, C. J. Grillmair, M. J. Burgdorf, S. B. Fajardo-Acosta, J. G. Ingalls, J. Higdon, L. Hao, J. Bernard-Salas, T. Herter, J. Troeltzsch, B. Unruh, and M. Winghart. Observations of Ultraluminous Infrared Galaxies with the Infrared Spectrograph (IRS) on the Spitzer Space Telescope: Early Results on Markarian 1014, Markarian 463, and UGC 5101. Astrophysical Journal, Supplement, 154(1):178–183, September 2004.

[10] R. J. Assef, D. Stern, G. Noirot, H. D. Jun, R. M. Cutri, and P. R. M. Eisenhardt. The WISE AGN Catalog. The Astrophysical Journal Supplement Series, 234(2):23, February 2018.

[11] J. A. Baldwin, M. M. Phillips, and R. Terlevich. Classification parameters for the emission-line spectra of extragalactic objects. Publications of the ASP, 93:5–19, February 1981.

[12] A. J. Barger, L. L. Cowie, R. F. Mushotzky, Y. Yang, W. H. Wang, A. T. Steffen, and P. Capak. The Cosmic Evolution of Hard X-Ray-selected Active Galactic Nuclei. Astronomical Journal.

[13] Dalya Baron and Hagai Netzer. Discovering AGN-driven winds through their infrared emission - II. Mass outflow rate and energetics. Monthly Notices of the RAS, 486(3):4290–4303, July 2019.

[14] Richard Barvainis. The Case for an Optically Thin Thermal Big Blue Bump. Astrophysical Journal.

[15] Robert H. Becker, Richard L. White, and David J. Helfand. The FIRST Survey: Faint Images of the Radio Sky at Twenty Centimeters. Astrophysical Journal, 450:559, September 1995.

[16] M. C. Begelman, R. D. Blandford, and M. J. Rees. Massive black hole binaries in active galactic nuclei. Nature, 287(5780):307–309, September 1980.

[17] A. Beifiori, S. Courteau, E. M. Corsini, and Y. Zhu. On the correlations between galaxy properties and supermassive black hole mass. Monthly Notices of the RAS, 419(3):2497–2528, January 2012.

[18] Jacob D. Bekenstein. Gravitational-Radiation Recoil and Runaway Black Holes. Astrophysical Journal, 183:657–664, July 1973.

[19] Francesco Belfiore, Roberto Maiolino, Claudia Maraston, Eric Emsellem, Matthew A. Bershady, Karen L. Masters, Renbin Yan, Dmitry Bizyaev, Médéric Boquien, Joel R. Brownstein, Kevin Bundy, Niv Drory, Timothy M. Heckman, David R. Law, Alexandre Roman-Lopes, Kaike Pan, Letizia Stanghellini, Daniel Thomas, Anne-Marie Weijmans, and Kyle B. Westfall. SDSS IV MaNGA - spatially resolved diagnostic diagrams: a proof that many galaxies are LIERs. Monthly Notices of the RAS, 461(3):3111–3134, September 2016.

[20] Robert A. Benjamin and Harriet L. Dinerstein. Near-Infrared Spectroscopy of Classical Novae in the Coronal Phase. Astronomical Journal, 100:1588, November 1990.

[21] A. J. Benson, C. G. Lacey, C. S. Frenk, C. M. Baugh, and S. Cole. Heating of galactic discs by infalling satellites. Monthly Notices of the RAS, 351(4):1215–1236, July 2004.

[22] Andrew J. Benson. Galaxy formation theory. Physics Reports, 495(2-3):33–86, October 2010.

[23] Misty C. Bentz, Kelly D. Denney, Catherine J. Grier, Aaron J. Barth, Bradley M. Peterson, Marianne Vestergaard, Vardha N. Bennert, Gabriela Canalizo, Gisella De Rosa, Alexei V. Filippenko, Elinor L. Gates, Jenny E. Greene, Weidong Li, Matthew A. Malkan, Richard W. Pogge, Daniel Stern, Tommaso Treu, and Jong-Hak Woo. The Low-luminosity End of the Radius-Luminosity Relationship for Active Galactic Nuclei. Astrophysical Journal, 767(2):149, April 2013.

[24] Misty C. Bentz, Bradley M. Peterson, Hagai Netzer, Richard W. Pogge, and Marianne Vestergaard. The Radius-Luminosity Relationship for Active Galactic Nuclei: The Effect of Host-Galaxy Starlight on Luminosity Measurements. II. The Full Sample of Reverberation-Mapped AGNs. Astrophysical Journal, 697(1):160–181, May 2009.

[25] P. N. Best and T. M. Heckman. On the fundamental dichotomy in the local radio-AGN population: accretion, evolution and host galaxy properties. Monthly Notices of the RAS, 421(2):1569–1582, April 2012.

[26] L. Binette, A. S. Wilson, and T. Storchi-Bergmann. Excitation and temperature of extended gas in active galaxies. II. Photoionization models with matter-bounded clouds. Astronomy and Astrophysics, 312:365–379, August 1996.

[27] William P. Blair, P. Frank Winkler, and Knox S. Long. The Magellan/IMACS Catalog of Optical Supernova Remnant Candidates in M83. The Astrophysical Journal Supplement Series, 203(1):8, November 2012.

[28] R. D. Blandford. Physical processes in active galactic nuclei. In R. D. Blandford, H. Netzer, L. Woltjer, T. J. L. Courvoisier, and M. Mayor, editors, Active Galactic Nuclei, pages 161–275, January 1990.

[29] Michael R. Blanton, Matthew A. Bershady, Bela Abolfathi, Franco D. Albareti, Carlos Allende Prieto, Andres Almeida, Javier Alonso-García, Friedrich Anders, Scott F. Anderson, Brett Andrews, Erik Aquino-Ortíz, Alfonso Aragón-Salamanca, Maria Argudo-Fernández, Eric Armengaud, Eric Aubourg, Vladimir Avila-Reese, Carles Badenes, Stephen Bailey, Kathleen A. Barger, Jorge Barrera-Ballesteros, Curtis Bartosz, Dominic Bates, Falk Baumgarten, Julian Bautista, Rachael Beaton, Timothy C. Beers, Francesco Belfiore, Chad F. Bender, Andreas A. Berlind, Mariangela Bernardi, Florian Beutler, Jonathan C. Bird, Dmitry Bizyaev, Guillermo A. Blanc, Michael Blomqvist, Adam S. Bolton, Médéric Boquien, Jura Borissova, Remco van den Bosch, Jo Bovy, William N. Brandt, Jonathan Brinkmann, Joel R. Brownstein, Kevin Bundy, Adam J. Burgasser, Etienne Burtin, Nicolás G. Busca, Michele Cappellari, Maria Leticia Delgado Carigi, Joleen K. Carlberg, Aurelio Carnero Rosell, Ricardo Carrera, Nancy J. Chanover, Brian Cherinka, Edmond Cheung, Yilen Gómez Maqueo Chew, Cristina Chiappini, Peter Doohyun Choi, Drew Chojnowski, Chia-Hsun Chuang, Haeun Chung, Rafael Fernando Cirolini, Nicolas Clerc, Roger E. Cohen, Johan Comparat, Luiz da Costa, Marie-Claude Cousinou, Kevin Covey, Jeffrey D. Crane, Rupert A. C. Croft, Irene Cruz-Gonzalez, Daniel Garrido Cuadra, Katia Cunha, Guillermo J. Damke, Jeremy Darling, Roger Davies, Kyle Dawson, Axel de la Macorra, Flavia Dell'Agli, Nathan De Lee, Timothée Delubac, Francesco Di Mille, Aleks Diamond-Stanic, Mariana Cano-Díaz, John Donor, Juan José Downes, Niv Drory, Hélion du Mas des Bourboux, Christopher J. Duckworth, Tom Dwelly, Jamie Dyer, Garrett Ebelke, Arthur D. Eigenbrot, Daniel J. Eisenstein, Eric Emsellem, Mike Eracleous, Stephanie Escoffier, Michael L. Evans, Xiaohui Fan, Emma Fernández-Alvar, J. G. Fernandez-Trincado, Diane K. Feuillet, Alexis Finoguenov, Scott W. Fleming, Andreu Font-Ribera, Alexander Fredrickson, Gordon Freischlad, Peter M. Frinchaboy, Carla E. Fuentes, Lluís Galbany, R. Garcia-Dias, D. A. García-Hernández, Patrick Gaulme, Doug Geisler, Joseph D. Gelfand, Héctor Gil-Marín, Bruce A. Gillespie, Daniel Goddard, Violeta Gonzalez-Perez, Kathleen Grabowski, Paul J. Green, Catherine J. Grier, James E. Gunn, Hong Guo, Julien Guy, Alex Hagen, ChangHoon Hahn, Matthew

Hall, Paul Harding, Sten Hasselquist, Suzanne L. Hawley, Fred Hearty, Jonay I. Gonzalez Hernández, Shirley Ho, David W. Hogg, Kelly Holley-Bockelmann, Jon A. Holtzman, Parker H. Holzer, Joseph Huehnerhoff, Timothy A. Hutchinson, Ho Seong Hwang, Héctor J. Ibarra-Medel, Gabriele da Silva Ilha, Inese I. Ivans, KeShawn Ivory, Kelly Jackson, Trey W. Jensen, Jennifer A. Johnson, Amy Jones, Henrik Jönsson, Eric Jullo, Vikrant Kamble, Karen Kinemuchi, David Kirkby, Francisco-Shu Kitaura, Mark Klaene, Gillian R. Knapp, Jean-Paul Kneib, Juna A. Kollmeier, Ivan Lacerna, Richard R. Lane, Dustin Lang, David R. Law, Daniel Lazarz, Youngbae Lee, Jean-Marc Le Goff, Fu-Heng Liang, Cheng Li, Hongyu Li, Jianhui Lian, Marcos Lima, Lihwai Lin, Yen-Ting Lin, Sara Bertran de Lis, Chao Liu, Miguel Angel C. de Icaza Lizaola, Dan Long, Sara Lucatello, Britt Lundgren, Nicholas K. MacDonald, Alice Deconto Machado, Chelsea L. MacLeod, Suvrath Mahadevan, Marcio Antonio Geimba Maia, Roberto Maiolino, Steven R. Majewski, Elena Malanushenko, Viktor Malanushenko, Arturo Manchado, Shude Mao, Claudia Maraston, Rui Marques-Chaves, Thomas Masseron, Karen L. Masters, Cameron K. McBride, Richard M. McDermid, Brianne McGrath, Ian D. McGreer, Nicolás Medina Peña, Matthew Melendez, Andrea Merloni, Michael R. Merrifield, Szabolcs Meszaros, Andres Meza, Ivan Minchev, Dante Minniti, Takamitsu Miyaji, Surhud More, John Mulchaey, Francisco Müller-Sánchez, Demitri Muna, Ricardo R. Munoz, Adam D. Myers, Preethi Nair, Kirpal Nandra, Janaina Correa do Nascimento, Alenka Negrete, Melissa Ness, Jeffrey A. Newman, Robert C. Nichol, David L. Nidever, Christian Nitschelm, Pierros Ntelis, Julia E. O'Connell, Ryan J. Oelkers, Audrey Oravetz, Daniel Oravetz, Zach Pace, Nelson Padilla, Nathalie Palanque-Delabrouille, Pedro Alonso Palicio, Kaike Pan, John K. Parejko, Taniya Parikh, Isabelle Pâris, Changbom Park, Alim Y. Patten, Sebastien Peirani, Marcos Pellejero-Ibanez, Samantha Penny, Will J. Percival, Ismael Perez-Fournon, Patrick Petitjean, Matthew M. Pieri, Marc Pinsonneault, Alice Pisani, Radosław Poleski, Francisco Prada, Abhishek Prakash, Anna Bárbara de Andrade Queiroz, M. Jordan Raddick, Anand Raichoor, Sandro Barboza Rembold, Hannah Richstein, Rogemar A. Riffel, Rogério Riffel, Hans-Walter Rix, Annie C. Robin, Constance M. Rockosi, Sergio Rodríguez-Torres, A. Roman-Lopes, Carlos Román-Zúñiga, Margarita Rosado, Ashley J. Ross, Graziano Rossi, John Ruan, Rossana Ruggeri, Eli S. Rykoff, Salvador Salazar-Albornoz, Mara Salvato, Ariel G. Sánchez, D. S. Aguado, José R. Sánchez-Gallego, Felipe A. Santana, Basílio Xavier Santiago, Conor Sayres, Ricardo P. Schiavon, Jaderson da Silva Schimoia, Edward F. Schlafly, David J. Schlegel, Donald P. Schneider, Mathias Schultheis, William J. Schuster, Axel Schwope, Hee-Jong Seo, Zhengyi Shao, Shiyin Shen, Matthew Shetrone, Michael Shull, Joshua D. Simon, Danielle Skinner, M. F. Skrutskie, Anže Slosar, Verne V. Smith, Jennifer S. Sobeck, Flavia Sobreira, Garrett Somers, Diogo Souto, David V. Stark, Keivan Stassun, Fritz Stauffer, Matthias Steinmetz, Thaisa Storchi-Bergmann, Alina Streblyanska, Guy S. Stringfellow, Genaro Suárez, Jing Sun, Nao Suzuki, Laszlo Szigeti, Manuchehr Taghizadeh-Popp, Baitian Tang, Charling Tao, Jamie Tayar, Mita Tembe, Johanna Teske, Aniruddha R. Thakar, Daniel Thomas, Benjamin A. Thompson, Jeremy L. Tinker, Patricia Tissera, Rita Tojeiro, Hector Hernandez Toledo, Sylvain de la Torre, Christy Tremonti, Nicholas W. Troup, Octavio Valenzuela, Inma

Martinez Valpuesta, Jaime Vargas-González, Mariana Vargas-Magaña, Jose Alberto Vazquez, Sandro Villanova, M. Vivek, Nicole Vogt, David Wake, Rene Walterbos, Yuting Wang, Benjamin Alan Weaver, Anne-Marie Weijmans, David H. Weinberg, Kyle B. Westfall, David G. Whelan, Vivienne Wild, John Wilson, W. M. Wood-Vasey, Dominika Wylezalek, Ting Xiao, Renbin Yan, Meng Yang, Jason E. Ybarra, Christophe Yèche, Nadia Zakamska, Olga Zamora, Pauline Zarrouk, Gail Zasowski, Kai Zhang, Gong-Bo Zhao, Zheng Zheng, Zheng Zheng, Xu Zhou, Zhi-Min Zhou, Guangtun B. Zhu, Manuela Zoccali, and Hu Zou. Sloan Digital Sky Survey IV: Mapping the Milky Way, Nearby Galaxies, and the Distant Universe. Astronomical Journal, 154(1):28, July 2017.

[30] Michael R. Blanton, Eyal Kazin, Demitri Muna, Benjamin A. Weaver, and Adrian Price-Whelan. Improved Background Subtraction for the Sloan Digital Sky Survey Images. Astronomical Journal, 142(1):31, July 2011.

[31] Laura Blecha, Debora Sijacki, Luke Zoltan Kelley, Paul Torrey, Mark Vogelsberger, Dylan Nelson, Volker Springel, Gregory Snyder, and Lars Hernquist. Recoiling black holes: prospects for detection and implications of spin alignment. Monthly Notices of the RAS, 456(1):961–989, February 2016.

[32] G. R. Blumenthal, S. M. Faber, J. R. Primack, and M. J. Rees. Formation of galaxies and large-scale structure with cold dark matter. Nature, 311:517–525, October 1984.

[33] R. G. Bower, A. J. Benson, R. Malbon, J. C. Helly, C. S. Frenk, C. M. Baugh, S. Cole, and C. G. Lacey. Breaking the hierarchy of galaxy formation. Monthly Notices of the RAS, 370(2):645–655, August 2006.

[34] Joel N. Bregman. Continuum radiation from active galactic nuclei. Astronomy and Astrophysics Reviews, 2(2):125–166, January 1990.

[35] Peter Breiding, Sarah Burke-Spolaor, Michael Eracleous, Tamara Bogdanović, T. Joseph W. Lazio, Jessie Runnoe, and Steinn Sigurdsson. The Search for Binary Supermassive Black Holes among Quasars with Offset Broad Lines Using the Very Long Baseline Array. Astrophysical Journal, 914(1):37, June 2021.

[36] Kevin Bundy, Matthew A. Bershady, David R. Law, Renbin Yan, Niv Drory, Nicholas MacDonald, David A. Wake, Brian Cherinka, José R. Sánchez-Gallego, Anne-Marie Weijmans, Daniel Thomas, Christy Tremonti, Karen Masters, Lodovico Coccato, Aleksandar M. Diamond-Stanic, Alfonso Aragón-Salamanca, Vladimir Avila-Reese, Carles Badenes, Jésus Falcón-Barroso, Francesco Belfiore, Dmitry Bizyaev, Guillermo A. Blanc, Joss Bland-Hawthorn, Michael R. Blanton, Joel R. Brownstein, Nell Byler, Michele Cappellari, Charlie Conroy, Aaron A. Dutton, Eric Emsellem, James Etherington, Peter M. Frinchaboy, Hai Fu, James E. Gunn, Paul Harding, Evelyn J. Johnston, Guinevere Kauffmann, Karen Kinemuchi, Mark A. Klaene, Johan H. Knapen, Alexie Leauthaud, Cheng Li, Lihwai Lin, Roberto Maiolino, Viktor Malanushenko, Elena Malanushenko, Shude Mao, Claudia Maraston, Richard M. McDermid, Michael R.

Merrifield, Robert C. Nichol, Daniel Oravetz, Kaike Pan, John K. Parejko, Sebastian F. Sanchez, David Schlegel, Audrey Simmons, Oliver Steele, Matthias Steinmetz, Karun Thanjavur, Benjamin A. Thompson, Jeremy L. Tinker, Remco C. E. van den Bosch, Kyle B. Westfall, David Wilkinson, Shelley Wright, Ting Xiao, and Kai Zhang. Overview of the SDSS-IV MaNGA Survey: Mapping nearby Galaxies at Apache Point Observatory. Astrophysical Journal, 798(1):7, January 2015.

[37] Manuela Campanelli, Carlos O. Lousto, Yosef Zlochower, and David Merritt. Maximum Gravitational Recoil. Physical Review Letters, 98(23):231102, June 2007.

[38] Michele Cappellari. pPXF: Penalized Pixel-Fitting stellar kinematics extraction. Astrophysics Source Code Library, record ascl:1210.002, October 2012.

[39] Michele Cappellari. Improving the full spectrum fitting method: accurate convolution with Gauss-Hermite functions. Monthly Notices of the RAS, 466(1):798–811, April 2017.

[40] Michele Cappellari and Eric Emsellem. Parametric Recovery of Line-of-Sight Velocity Distributions from Absorption-Line Spectra of Galaxies via Penalized Likelihood. Publications of the ASP, 116(816):138–147, February 2004.

[41] F. C. Cerqueira-Campos, A. Rodríguez-Ardila, R. Riffel, M. Marinello, A. Prieto, and L. G. Dahmer-Hahn. Coronal-line forest active galactic nuclei - I. Physical properties of the emission-line regions. Monthly Notices of the RAS, 500(2):2666–2684, January 2021.

[42] S. Chandrasekhar. Dynamical Friction. I. General Considerations: the Coefficient of Dynamical Friction. Astrophysical Journal, 97:255, March 1943.

[43] Jianhang Chen, Yong Shi, Ross Dempsey, David R. Law, Yanmei Chen, Renbin Yan, Longji Bing, Sandro B. Rembold, Songlin Li, Xiaoling Yu, Rogemar A. Riffel, Joe R. Brownstein, and Rogério Riffel. The spatial extension of extended narrow line regions in MaNGA AGN. Monthly Notices of the RAS, 489(1):855–867, October 2019.

[44] M. Chiaberge, A. Capetti, and A. Celotti. The HST view of FR I radio galaxies: evidence for non-thermal nuclear sources. Astronomy and Astrophysics, 349:77–87, September 1999.

[45] R. Cid Fernandes, G. Stasińska, M. S. Schlickmann, A. Mateus, N. Vale Asari, W. Schoenell, and L. Sodré. Alternative diagnostic diagrams and the 'forgotten' population of weak line galaxies in the SDSS. Monthly Notices of the RAS, 403(2):1036–1053, April 2010.

[46] Luca Ciotti, Jeremiah P. Ostriker, and Daniel Proga. Feedback from Central Black Holes in Elliptical Galaxies. III. Models with Both Radiative and Mechanical Feedback. Astrophysical Journal, 717(2):708–723, July 2010.

[47] N. R. Collins, S. B. Kraemer, D. M. Crenshaw, F. C. Bruhweiler, and M. Meléndez. Physical Conditions in the Narrow-Line Region of Markarian 3. II. Photoionization Modeling Results. Astrophysical Journal, 694(2):765–788, April 2009.

[48] Julia M. Comerford, R. Scott Barrows, Francisco Müller-Sánchez, Rebecca Nevin, Jenny E. Greene, David Pooley, Daniel Stern, and Fiona A. Harrison. An Active Galactic Nucleus Caught in the Act of Turning Off and On. Astrophysical Journal, 849(2):102, November 2017.

[49] Julia M. Comerford, Brian F. Gerke, Jeffrey A. Newman, Marc Davis, Renbin Yan, Michael C. Cooper, S. M. Faber, David C. Koo, Alison L. Coil, D. J. Rosario, and Aaron A. Dutton. Inspiralling Supermassive Black Holes: A New Signpost for Galaxy Mergers. Astrophysical Journal, 698(1):956–965, June 2009.

[50] Julia M. Comerford and Jenny E. Greene. Offset Active Galactic Nuclei as Tracers of Galaxy Mergers and Supermassive Black Hole Growth. Astrophysical Journal, 789(2):112, July 2014.

[51] Julia M. Comerford, James Negus, R. Scott Barrows, Dominika Wylezalek, Jenny E. Greene, Francisco Müller-Sánchez, and Rebecca Nevin. Toward a More Complete Optical Census of Active Galactic Nuclei via Spatially Resolved Spectroscopy. Astrophysical Journal, 927(1):23, March 2022.

[52] Julia M. Comerford, James Negus, Francisco Müller-Sánchez, Michael Eracleous, Dominika Wylezalek, Thaisa Storchi-Bergmann, Jenny E. Greene, R. Scott Barrows, Rebecca Nevin, Namrata Roy, and Aaron Stemo. A Catalog of 406 AGNs in MaNGA: A Connection between Radio-mode AGNs and Star Formation Quenching. Astrophysical Journal, 901(2):159, October 2020.

[53] Julia M. Comerford, James Negus, Francisco Müller-Sánchez, Michael Eracleous, Dominika Wylezalek, Thaisa Storchi-Bergmann, Jenny E. Greene, R. Scott Barrows, Rebecca Nevin, Namrata Roy, and Aaron Stemo. A catalog of 406 agns in manga: A connection between radio-mode agns and star formation quenching. The Astrophysical Journal, 901(2):159, Oct 2020.

[54] Julia M. Comerford, Rebecca Nevin, Aaron Stemo, Francisco Müller-Sánchez, R. Scott Barrows, Michael C. Cooper, and Jeffrey A. Newman. The Origin of Double-peaked Narrow Lines in Active Galactic Nuclei. IV. Association with Galaxy Mergers. Astrophysical Journal, 867(1):66, November 2018.

[55] Julia M. Comerford, David Pooley, R. Scott Barrows, Jenny E. Greene, Nadia L. Zakamska, Greg M. Madejski, and Michael C. Cooper. Merger-driven Fueling of Active Galactic Nuclei: Six Dual and Offset AGNs Discovered with Chandra and Hubble Space Telescope Observations. Astrophysical Journal, 806(2):219, June 2015.

[56] J. J. Condon, W. D. Cotton, E. W. Greisen, Q. F. Yin, R. A. Perley, G. B. Taylor, and J. J. Broderick. The NRAO VLA Sky Survey. Astronomical Journal, 115(5):1693–1716, May 1998.

[57] M. Contini and S. M. Viegas. A Grid of Composite Models for the Simulation of the Emission-Line Spectra from the Narrow-Line Regions of Active Galaxies. The Astrophysical Journal Supplement Series, 132(2):211–232, February 2001.

[58] D. Michael Crenshaw. Profiles and Profile Ratios in Seyfert 1 Galaxies. Astrophysical Journal, Supplement, 62:821, December 1986.

[59] Darren J. Croton, Volker Springel, Simon D. M. White, G. De Lucia, C. S. Frenk, L. Gao, A. Jenkins, G. Kauffmann, J. F. Navarro, and N. Yoshida. The many lives of active galactic nuclei: cooling flows, black holes and the luminosities and colours of galaxies. Monthly Notices of the RAS, 365(1):11–28, January 2006.

[60] B. Czerny and K. Hryniewicz. The origin of the broad line region in active galactic nuclei. Astronomy and Astrophysics, 525:L8, January 2011.

[61] Claudio Dalla Vecchia, Richard G. Bower, Tom Theuns, Michael L. Balogh, Pasquale Mazzotta, and Carlos S. Frenk. Quenching cluster cooling flows with recurrent hot plasma bubbles. Monthly Notices of the RAS, 355(3):995–1004, December 2004.

[62] K. M. Dasyra, L. C. Ho, L. Armus, P. Ogle, G. Helou, B. M. Peterson, D. Lutz, H. Netzer, and E. Sturm. High-Ionization Mid-Infrared Lines as Black Hole Mass and Bolometric Luminosity Indicators in Active Galactic Nuclei. Astrophysical Journal, Letters, 674(1):L9, February 2008.

[63] R. Davies, D. Baron, T. Shimizu, H. Netzer, L. Burtscher, P. T. de Zeeuw, R. Genzel, E. K. S. Hicks, M. Koss, M. Y. Lin, D. Lutz, W. Maciejewski, F. Müller-Sánchez, G. Orban de Xivry, C. Ricci, R. Riffel, R. A. Riffel, D. Rosario, M. Schartmann, A. Schnorr-Müller, J. Shangguan, A. Sternberg, E. Sturm, T. Storchi-Bergmann, L. Tacconi, and S. Veilleux. Ionized outflows in local luminous AGN: what are the real densities and outflow rates? Monthly Notices of the RAS, 498(3):4150–4177, November 2020.

[64] M. M. De Robertis and D. E. Osterbrock. An analysis of the narrow-line profiles in high ionization Seyfert galaxies. Astrophysical Journal, 286:171–185, November 1984.

[65] M. M. De Robertis and D. E. Osterbrock. An Analysis of the Narrow-Line Profiles in Seyfert 2 Galaxies. Astrophysical Journal, 301:727, February 1986.

[66] A. Del Moro, D. M. Alexander, J. R. Mullaney, E. Daddi, M. Pannella, F. E. Bauer, A. Pope, M. Dickinson, D. Elbaz, P. D. Barthel, M. A. Garrett, W. N. Brandt, V. Charmandaris, R. R. Chary, K. Dasyra, R. Gilli, R. C. Hickox, H. S. Hwang, R. J. Ivison, S. Juneau, E. Le Floc'h, B. Luo, G. E. Morrison, E. Rovilos, M. T. Sargent, and Y. Q. Xue. GOODS-Herschel: radio-excess signature of hidden AGN activity in distant star-forming galaxies. Astronomy and Astrophysics, 549:A59, January 2013.

[67] T. Di Matteo, E. Quataert, S. W. Allen, R. Narayan, and A. C. Fabian. Low-radiative-efficiency accretion in the nuclei of elliptical galaxies. Monthly Notices of the RAS, 311(3):507–521, January 2000.

[68] Antonaldo Diaferio, Guinevere Kauffmann, Jörg M. Colberg, and Simon D. M. White. Clustering of galaxies in a hierarchical universe - III. Mock redshift surveys. Monthly Notices of the RAS, 307(3):537–552, August 1999.

[69] Y. Diaz and A. Rodríguez-Ardila. Origin of high ionization lines in active galactic nuclei. Boletin de la Asociacion Argentina de Astronomia La Plata Argentina, 61:186–188, August 2019.

[70] Xuheng Ding, John Silverman, Tommaso Treu, Andreas Schulze, Malte Schramm, Simon Birrer, Daeseong Park, Knud Jahnke, Vardha N. Bennert, Jeyhan S. Kartaltepe, Anton M. Koekemoer, Matthew A. Malkan, and David Sanders. The Mass Relations between Supermassive Black Holes and Their Host Galaxies at 1 ¡ z ¡ 2 HST-WFC3. Astrophysical Journal, 888(1):37, January 2020.

[71] S. Dodorico. The identification of supernova remnants in nearby galaxies. Mem. Societa Astronomica Italiana, 49:485–496, September 1978.

[72] S. Dodorico. The identification of supernova remnants in nearby galaxies. Mem. Societa Astronomica Italiana, 49:485–496, September 1978.

[73] S. Dodorico, M. A. Dopita, and P. Benvenuti. A catalogue of supernova remnant candidates in nearby galaxies. Astronomy and Astrophysics, Supplement, 40:67–80, April 1980.

[74] Christine Done and Julian H. Krolik. Kinematics of the Broad Emission Line Region in NGC 5548. Astrophysical Journal, 463:144, May 1996.

[75] Xiao-Bo Dong, Luis C. Ho, Weimin Yuan, Ting-Gui Wang, Xiaohui Fan, Hongyan Zhou, and Ning Jiang. A Uniformly Selected Sample of Low-mass Black Holes in Seyfert 1 Galaxies. Astrophysical Journal, 755(2):167, August 2012.

[76] Xiaobo Dong, Tinggui Wang, Jianguo Wang, Weimin Yuan, Hongyan Zhou, Haifeng Dai, and Kai Zhang. Broad-line Balmer decrements in blue active galactic nuclei. Monthly Notices of the RAS, 383(2):581–592, January 2008.

[77] M. A. Dopita. Optical emission from shock waves. I. Abundances in N49. Astrophysical Journal, 209:395–401, October 1976.

[78] M. A. Dopita, L. Binette, S. Dodorico, and P. Benvenuti. Radiative shock-wave theory. I. Chemical abundance diagnostics and galactic abundance gradients. Astrophysical Journal, 276:653–666, January 1984.

[79] Michael A. Dopita and Ralph S. Sutherland. Spectral Signatures of Fast Shocks. I. Low-Density Model Grid. The Astrophysical Journal Supplement Series, 102:161, January 1996.

[80] N. Drory, N. MacDonald, M. A. Bershady, K. Bundy, J. Gunn, D. R. Law, M. Smith, R. Stoll, C. A. Tremonti, D. A. Wake, R. Yan, A. M. Weijmans, N. Byler, B. Cherinka, F. Cope, A. Eigenbrot, P. Harding, D. Holder, J. Huehnerhoff, K. Jaehnig, T. C. Jansen, M. Klaene, A. M. Paat, J. Percival, and C. Sayres. The MaNGA Integral Field Unit Fiber Feed System for the Sloan 2.5 m Telescope. Astronomical Journal, 149(2):77, February 2015.

[81] J. S. Dunlop and J. A. Peacock. The redshift cut-off in the luminosity function of radio galaxies and quasars. Monthly Notices of the RAS, 247:19, November 1990.

[82] Daniel J. Eisenstein, David H. Weinberg, Eric Agol, Hiroaki Aihara, Carlos Allende Prieto, Scott F. Anderson, James A. Arns, Éric Aubourg, Stephen Bailey, Eduardo Balbinot, Robert Barkhouser, Timothy C. Beers, Andreas A. Berlind, Steven J. Bickerton, Dmitry Bizyaev, Michael R. Blanton, John J. Bochanski, Adam S. Bolton, Casey T. Bosman, Jo Bovy, W. N. Brandt, Ben Breslauer, Howard J. Brewington, J. Brinkmann, Peter J. Brown, Joel R. Brownstein, Dan Burger, Nicolas G. Busca, Heather Campbell, Phillip A. Cargile, William C. Carithers, Joleen K. Carlberg, Michael A. Carr, Liang Chang, Yanmei Chen, Cristina Chiappini, Johan Comparat, Natalia Connolly, Marina Cortes, Rupert A. C. Croft, Katia Cunha, Luiz N. da Costa, James R. A. Davenport, Kyle Dawson, Nathan De Lee, Gustavo F. Porto de Mello, Fernando de Simoni, Janice Dean, Saurav Dhital, Anne Ealet, Garrett L. Ebelke, Edward M. Edmondson, Jacob M. Eiting, Stephanie Escoffier, Massimiliano Esposito, Michael L. Evans, Xiaohui Fan, Bruno Femenía Castellá, Leticia Dutra Ferreira, Greg Fitzgerald, Scott W. Fleming, Andreu Font-Ribera, Eric B. Ford, Peter M. Frinchaboy, Ana Elia García Pérez, B. Scott Gaudi, Jian Ge, Luan Ghezzi, Bruce A. Gillespie, G. Gilmore, Léo Girardi, J. Richard Gott, Andrew Gould, Eva K. Grebel, James E. Gunn, Jean-Christophe Hamilton, Paul Harding, David W. Harris, Suzanne L. Hawley, Frederick R. Hearty, Joseph F. Hennawi, Jonay I. González Hernández, Shirley Ho, David W. Hogg, Jon A. Holtzman, Klaus Honscheid, Naohisa Inada, Inese I. Ivans, Linhua Jiang, Peng Jiang, Jennifer A. Johnson, Cathy Jordan, Wendell P. Jordan, Guinevere Kauffmann, Eyal Kazin, David Kirkby, Mark A. Klaene, G. R. Knapp, Jean-Paul Kneib, C. S. Kochanek, Lars Koesterke, Juna A. Kollmeier, Richard G. Kron, Hubert Lampeitl, Dustin Lang, James E. Lawler, Jean-Marc Le Goff, Brian L. Lee, Young Sun Lee, Jarron M. Leisenring, Yen-Ting Lin, Jian Liu, Daniel C. Long, Craig P. Loomis, Sara Lucatello, Britt Lundgren, Robert H. Lupton, Bo Ma, Zhibo Ma, Nicholas MacDonald, Claude Mack, Suvrath Mahadevan, Marcio A. G. Maia, Steven R. Majewski, Martin Makler, Elena Malanushenko, Viktor Malanushenko, Rachel Mandelbaum, Claudia Maraston, Daniel Margala, Paul Maseman, Karen L. Masters, Cameron K. McBride, Patrick McDonald, Ian D. McGreer, Richard G. McMahon, Olga Mena Requejo, Brice Ménard, Jordi Miralda-Escudé, Heather L. Morrison, Fergal Mullally, Demitri Muna, Hitoshi Murayama, Adam D. Myers, Tracy Naugle, Angelo Fausti Neto, Duy Cuong Nguyen, Robert C. Nichol, David L. Nidever, Robert W. O'Connell, Ricardo L. C. Ogando, Matthew D. Olmstead, Daniel J. Oravetz, Nikhil Padmanabhan, Martin Paegert, Nathalie Palanque-Delabrouille, Kaike Pan, Parul Pandey, John K. Parejko, Isabelle Pâris, Paulo Pellegrini, Joshua Pepper, Will J. Percival, Patrick Petitjean, Robert

Pfaffenberger, Janine Pforr, Stefanie Phleps, Christophe Pichon, Matthew M. Pieri, Francisco Prada, Adrian M. Price-Whelan, M. Jordan Raddick, Beatriz H. F. Ramos, I. Neill Reid, Celine Reyle, James Rich, Gordon T. Richards, George H. Rieke, Marcia J. Rieke, Hans-Walter Rix, Annie C. Robin, Helio J. Rocha-Pinto, Constance M. Rockosi, Natalie A. Roe, Emmanuel Rollinde, Ashley J. Ross, Nicholas P. Ross, Bruno Rossetto, Ariel G. Sánchez, Basilio Santiago, Conor Sayres, Ricardo Schiavon, David J. Schlegel, Katharine J. Schlesinger, Sarah J. Schmidt, Donald P. Schneider, Kris Sellgren, Alaina Shelden, Erin Sheldon, Matthew Shetrone, Yiping Shu, John D. Silverman, Jennifer Simmerer, Audrey E. Simmons, Thirupathi Sivarani, M. F. Skrutskie, Anže Slosar, Stephen Smee, Verne V. Smith, Stephanie A. Snedden, Keivan G. Stassun, Oliver Steele, Matthias Steinmetz, Mark H. Stockett, Todd Stollberg, Michael A. Strauss, Alexander S. Szalay, Masayuki Tanaka, Aniruddha R. Thakar, Daniel Thomas, Jeremy L. Tinker, Benjamin M. Tofflemire, Rita Tojeiro, Christy A. Tremonti, Mariana Vargas Magaña, Licia Verde, Nicole P. Vogt, David A. Wake, Xiaoke Wan, Ji Wang, Benjamin A. Weaver, Martin White, Simon D. M. White, John C. Wilson, John P. Wisniewski, W. Michael Wood-Vasey, Brian Yanny, Naoki Yasuda, Christophe Yèche, Donald G. York, Erick Young, Gail Zasowski, Idit Zehavi, and Bo Zhao. SDSS-III: Massive Spectroscopic Surveys of the Distant Universe, the Milky Way, and Extra-Solar Planetary Systems. Astronomical Journal, 142(3):72, September 2011.

[83] Moshe Elitzur and Isaac Shlosman. The AGN-obscuring Torus: The End of the "Doughnut" Paradigm? Astrophysical Journal, Letters, 648(2):L101–L104, September 2006.

[84] Sara L. Ellison, David R. Patton, J. Trevor Mendel, and Jillian M. Scudder. Galaxy pairs in the Sloan Digital Sky Survey - IV. Interactions trigger active galactic nuclei. Monthly Notices of the RAS, 418(3):2043–2053, December 2011.

[85] A. Elmhamdi. Oxygen Issue in Core Collapse Supernovae. Acta Astronomica, 61(2):179–198, June 2011.

[86] Ian N. Evans, Francis A. Primini, Kenny J. Glotfelty, Craig S. Anderson, Nina R. Bonaventura, Judy C. Chen, John E. Davis, Stephen M. Doe, Janet D. Evans, Giuseppina Fabbiano, Elizabeth C. Galle, II Gibbs, Danny G., John D. Grier, Roger M. Hain, Diane M. Hall, Peter N. Harbo, Xiangqun Helen He, John C. Houck, Margarita Karovska, Vinay L. Kashyap, Jennifer Lauer, Michael L. McCollough, Jonathan C. McDowell, Joseph B. Miller, Arik W. Mitschang, Douglas L. Morgan, Amy E. Mossman, Joy S. Nichols, Michael A. Nowak, David A. Plummer, Brian L. Refsdal, Arnold H. Rots, Aneta Siemiginowska, Beth A. Sundheim, Michael S. Tibbetts, David W. Van Stone, Sherry L. Winkelman, and Panagoula Zografou. The Chandra Source Catalog. Astrophysical Journal, Supplement, 189(1):37–82, July 2010.

[87] A. C. Fabian. Observational Evidence of Active Galactic Nuclei Feedback. Annual Review of Astronomy and Astrophysics, 50:455–489, Sep 2012.

[88] A. C. Fabian. Observational Evidence of Active Galactic Nuclei Feedback. Annual Review of Astronomy and Astrophysics, 50:455–489, September 2012.

[89] H. Falcke and P. L. Biermann. The jet-disk symbiosis. I. Radio to X-ray emission models for quasars. Astronomy and Astrophysics, 293:665–682, January 1995.

[90] B. L. Fanaroff and J. M. Riley. The morphology of extragalactic radio sources of high and low luminosity. Monthly Notices of the RAS, 167:31P–36P, May 1974.

[91] C. L. Farage, P. J. McGregor, M. A. Dopita, and G. V. Bicknell. Optical IFU Observations of the Brightest Cluster Galaxy NGC 4696: The Case for a Minor Merger and Shock-excited Filaments. Astrophysical Journal, 724(1):267–284, November 2010.

[92] Jason W. Ferguson, Kirk T. Korista, and Gary J. Ferland. Physical Conditions of the Coronal Line Region in Seyfert Galaxies. Astrophysical Journal, Supplement, 110(2):287–297, June 1997.

[93] G. J. Ferland, M. Chatzikos, F. Guzmán, M. L. Lykins, P. A. M. van Hoof, R. J. R. Williams, N. P. Abel, N. R. Badnell, F. P. Keenan, R. L. Porter, and P. C. Stancil. The 2017 Release Cloudy. Revista Mexicana de Astronomia y Astrofisica, 53:385–438, October 2017.

[94] G. J. Ferland, K. T. Korista, D. A. Verner, J. W. Ferguson, J. B. Kingdon, and E. M. Verner. CLOUDY 90: Numerical Simulation of Plasmas and Their Spectra. Publications of the ASP, 110(749):761–778, July 1998.

[95] L. Ferrarese and D. Merritt. A Fundamental Relation between Supermassive Black Holes and Their Host Galaxies. Astrophysical Journal, Letters, 539:L9–L12, August 2000.

[96] Laura Ferrarese and Holland Ford. Supermassive Black Holes in Galactic Nuclei: Past, Present and Future Research. Space Science Reviews, 116(3-4):523–624, February 2005.

[97] A. V. Filippenko and J. P. Halpern. NGC 7213 : a key to the nature of liners? Astrophysical Journal, 285:458–476, October 1984.

[98] K. Gebhardt, R. Bender, G. Bower, A. Dressler, S. M. Faber, A. V. Filippenko, R. Green, C. Grillmair, L. C. Ho, J. Kormendy, T. R. Lauer, J. Magorrian, J. Pinkney, D. Richstone, and S. Tremaine. A Relationship between Nuclear Black Hole Mass and Galaxy Velocity Dispersion. Astrophysical Journal, Letters, 539:L13–L16, August 2000.

[99] Jonathan M. Gelbord, James R. Mullaney, and Martin J. Ward. AGN with strong forbidden high-ionization lines selected from the Sloan Digital Sky Survey. Monthly Notices of the RAS, 397(1):172–189, July 2009.

[100] R. Genzel, D. Lutz, E. Sturm, E. Egami, D. Kunze, A. F. M. Moorwood, D. Rigopoulou, H. W. W. Spoon, A. Sternberg, L. E. Tacconi-Garman, L. Tacconi, and N. Thatte. What Powers Ultraluminous IRAS Galaxies? Astrophysical Journal, 498(2):579–605, May 1998.

[101] Brian F. Gerke, Jeffrey A. Newman, Jennifer Lotz, Renbin Yan, P. Barmby, Alison L. Coil, Christopher J. Conselice, R. J. Ivison, Lihwai Lin, David C. Koo, Kirpal Nandra, Samir Salim, Todd Small, Benjamin J. Weiner, Michael C. Cooper, Marc Davis, S. M. Faber, and Puragra Guhathakurta. The DEEP2 Galaxy Redshift Survey: AEGIS Observations of a Dual AGN at z = 0.7. Astrophysical Journal, Letters, 660(1):L23–L26, May 2007.

[102] Adam Ginsburg and Jordan Mirocha. PySpecKit: Python Spectroscopic Toolkit. Astrophysics Source Code Library, record ascl:1109.001, September 2011.

[103] Adam Ginsburg, Vlas Sokolov, Miguel de Val-Borro, Erik Rosolowsky, Jaime E. Pineda, Brigitta M. Sipőcz, and Jonathan D. Henshaw. Pyspeckit: A Spectroscopic Analysis and Plotting Package. Astronomical Journal, 163(6):291, June 2022.

[104] Ana Glidden, Marvin Rose, Martin Elvis, and Jonathan McDowell. A Model for Type 2 Coronal Line Forest (CLiF) AGNs. Astrophysical Journal, 824(1):34, June 2016.

[105] A. D. Goulding and D. M. Alexander. Towards a complete census of AGN in nearby Galaxies: a large population of optically unidentified AGN. Monthly Notices of the RAS, 398(3):1165–1193, September 2009.

[106] Alister W. Graham, Christopher A. Onken, E. Athanassoula, and F. Combes. An expanded M_{bh}-σ diagram, and a new calibration of active galactic nuclei masses. Monthly Notices of the RAS, 412(4):2211–2228, April 2011.

[107] G. L. Granato, C. G. Lacey, L. Silva, A. Bressan, C. M. Baugh, S. Cole, and C. S. Frenk. The Infrared Side of Galaxy Formation. I. The Local Universe in the Semianalytical Framework. Astrophysical Journal, 542(2):710–730, October 2000.

[108] Jenny E. Greene and Luis C. Ho. Estimating Black Hole Masses in Active Galaxies Using the Hα Emission Line. Astrophysical Journal, 630(1):122–129, September 2005.

[109] Jenny E. Greene and Luis C. Ho. A New Sample of Low-Mass Black Holes in Active Galaxies. Astrophysical Journal, 670(1):92–104, November 2007.

[110] Matthew A. Greenhouse, G. L. Grasdalen, C. E. Woodward, J. Benson, R. D. Gehrz, E. Rosenthal, and M. F. Skrutskie. The Infrared Coronal Lines of Recent Novae. Astrophysical Journal, 352:307, March 1990.

[111] James E. Gunn, Walter A. Siegmund, Edward J. Mannery, Russell E. Owen, Charles L. Hull, R. French Leger, Larry N. Carey, Gillian R. Knapp, Donald G. York, William N. Boroski, Stephen M. Kent, Robert H. Lupton, Constance M. Rockosi, Michael L. Evans, Patrick Waddell, John E. Anderson, James Annis, John C. Barentine, Larry M. Bartoszek, Steven Bastian, Stephen B. Bracker, Howard J. Brewington, Charles I. Briegel, Jon Brinkmann, Yorke J. Brown, Michael A. Carr, Paul C. Czarapata, Craig C. Drennan, Thomas Dombeck, Glenn R. Federwitz, Bruce A. Gillespie, Carlos Gonzales, Sten U. Hansen, Michael Harvanek, Jeffrey Hayes, Wendell Jordan, Ellyne Kinney,

Mark Klaene, S. J. Kleinman, Richard G. Kron, Jurek Kresinski, Glenn Lee, Siriluk Limmongkol, Carl W. Lindenmeyer, Daniel C. Long, Craig L. Loomis, Peregrine M. McGehee, Paul M. Mantsch, Jr. Neilsen, Eric H., Richard M. Neswold, Peter R. Newman, Atsuko Nitta, Jr. Peoples, John, Jeffrey R. Pier, Peter S. Prieto, Angela Prosapio, Claudio Rivetta, Donald P. Schneider, Stephanie Snedden, and Shu-i. Wang. The 2.5 m Telescope of the Sloan Digital Sky Survey. Astronomical Journal, 131(4):2332–2359, April 2006.

[112] F. Haardt and L. Maraschi. A Two-Phase Model for the X-Ray Emission from Seyfert Galaxies. Astrophysical Journal, Letters, 380:L51, October 1991.

[113] Martin G. Haehnelt, Piero Madau, Rolf Kudritzki, and Francesco Haardt. An Ionizing Ultraviolet Background Dominated by Massive Stars. Astrophysical Journal, Letters, 549(2):L151–L154, March 2001.

[114] L. M. Haffner, R. J. Dettmar, J. E. Beckman, K. Wood, J. D. Slavin, C. Giammanco, G. J. Madsen, A. Zurita, and R. J. Reynolds. The warm ionized medium in spiral galaxies. Reviews of Modern Physics, 81(3):969–997, July 2009.

[115] Lei Hao, Michael A. Strauss, Christy A. Tremonti, David J. Schlegel, Timothy M. Heckman, Guinevere Kauffmann, Michael R. Blanton, Xiaohui Fan, James E. Gunn, Patrick B. Hall, Željko Ivezić, Gillian R. Knapp, Julian H. Krolik, Robert H. Lupton, Gordon T. Richards, Donald P. Schneider, Iskra V. Strateva, Nadia L. Zakamska, J. Brinkmann, Robert J. Brunner, and Gyula P. Szokoly. Active Galactic Nuclei in the Sloan Digital Sky Survey. I. Sample Selection. Astronomical Journal, 129(4):1783–1794, April 2005.

[116] C. M. Harrison, D. M. Alexander, J. R. Mullaney, and A. M. Swinbank. Kiloparsec-scale outflows are prevalent among luminous AGN: outflows and feedback in the context of the overall AGN population. Monthly Notices of the RAS, 441(4):3306–3347, July 2014.

[117] G. Hasinger, T. Miyaji, and M. Schmidt. Luminosity-dependent evolution of soft X-ray selected AGN. New Chandra and XMM-Newton surveys. Astronomy and Astrophysics.

[118] T. M. Heckman, G. K. Miley, W. J. M. van Breugel, and H. R. Butcher. Emission-line profiles and kinematics of the narrow-line region in Seyfert and radio galaxies. Astrophysical Journal, 247:403–418, July 1981.

[119] T. M. Heckman, A. Ptak, A. Hornschemeier, and G. Kauffmann. The Relationship of Hard X-Ray and Optical Line Emission in Low-Redshift Active Galactic Nuclei. Astrophysical Journal, 634:161–168, November 2005.

[120] Timothy M. Heckman and Philip N. Best. The Coevolution of Galaxies and Supermassive Black Holes: Insights from Surveys of the Contemporary Universe. Annual Review of Astronomy and Astrophysics, 52:589–660, August 2014.

[121] Timothy M. Heckman, Guinevere Kauffmann, Jarle Brinchmann, Stéphane Charlot, Christy Tremonti, and Simon D. M. White. Present-Day Growth of Black Holes and Bulges: The Sloan Digital Sky Survey Perspective. Astrophysical Journal, 613(1):109–118, September 2004.

[122] L. Hernández-García, F. Panessa, L. Bassani, G. Bruni, F. Ursini, V. Chavushyan, O. González-Martín, S. Cazzoli, E. F. Jiménez-Andrade, P. Arévalo, Y. Díaz, A. Bazzano, and P. Ubertini. A young and obscured AGN embedded in the giant radio galaxy Mrk 1498. Monthly Notices of the RAS, 489(3):4049–4062, November 2019.

[123] Frank Herrmann, Ian Hinder, Deirdre Shoemaker, Pablo Laguna, and Richard A. Matzner. Gravitational Recoil from Spinning Binary Black Hole Mergers. Astrophysical Journal, 661(1):430–436, May 2007.

[124] Jason T. Hinkle and Richard Mushotzky. Fundamental X-ray corona parameters of Swift/BAT AGN. Monthly Notices of the RAS, 506(4):4960–4978, October 2021.

[125] L. C. Ho. Nuclear activity in nearby galaxies. Annual Review of Astronomy and Astrophysics, 46:475–539, September 2008.

[126] Philip F. Hopkins, Thomas J. Cox, Dušan Kereš, and Lars Hernquist. A Cosmological Framework for the Co-Evolution of Quasars, Supermassive Black Holes, and Elliptical Galaxies. II. Formation of Red Ellipticals. The Astrophysical Journal Supplement Series, 175(2):390–422, April 2008.

[127] Philip F. Hopkins, Lars Hernquist, Thomas J. Cox, Tiziana Di Matteo, Paul Martini, Brant Robertson, and Volker Springel. Black Holes in Galaxy Mergers: Evolution of Quasars. Astrophysical Journal, 630(2):705–715, September 2005.

[128] Philip F. Hopkins, Rachel S. Somerville, Lars Hernquist, Thomas J. Cox, Brant Robertson, and Yuexing Li. The Relation between Quasar and Merging Galaxy Luminosity Functions and the Merger-driven Star Formation History of the Universe. Astrophysical Journal, 652(2):864–888, December 2006.

[129] E. P. Hubble. A spiral nebula as a stellar system, Messier 31. Astrophysical Journal.

[130] E. P. Hubble. NGC 6822, a remote stellar system. Astrophysical Journal, 62:409–433, December 1925.

[131] E. P. Hubble. Extragalactic nebulae. Astrophysical Journal, 64:321–369, December 1926.

[132] Edwin. Hubble. No. 324. Extra-galactic nebulae. Contributions from the Mount Wilson Observatory / Carnegie Institution of Washington, 324:1–49, January 1926.

[133] Edwin Hubble. A Relation between Distance and Radial Velocity among Extra-Galactic Nebulae. Proceedings of the National Academy of Science, 15(3):168–173, March 1929.

[134] Sean D. Johnson, Hsiao-Wen Chen, and John S. Mulchaey. On the origin of excess cool gas in quasar host haloes. Monthly Notices of the RAS, 452(3):2553–2565, September 2015.

[135] E. Kalfountzou, J. A. Stevens, M. J. Jarvis, M. J. Hardcastle, D. Wilner, M. Elvis, M. J. Page, M. Trichas, and D. J. B. Smith. Observational evidence that positive and negative AGN feedback depends on galaxy mass and jet power. Monthly Notices of the RAS, 471(1):28–58, October 2017.

[136] Shai Kaspi, Dan Maoz, Hagai Netzer, Bradley M. Peterson, Marianne Vestergaard, and Buell T. Jannuzi. The Relationship between Luminosity and Broad-Line Region Size in Active Galactic Nuclei. Astrophysical Journal, 629(1):61–71, August 2005.

[137] Shai Kaspi, Paul S. Smith, Hagai Netzer, Dan Maoz, Buell T. Jannuzi, and Uriel Giveon. Reverberation Measurements for 17 Quasars and the Size-Mass-Luminosity Relations in Active Galactic Nuclei. Astrophysical Journal, 533(2):631–649, April 2000.

[138] Guinevere Kauffmann. The age of elliptical galaxies and bulges in a merger model. Monthly Notices of the RAS, 281(2):487–492, July 1996.

[139] Guinevere Kauffmann and Stephane Charlot. Constraints on Models of Galaxy Formation from the Evolution of Damped Lyman-Alpha Absorption Systems. Astrophysical Journal, 430:L97, August 1994.

[140] Guinevere Kauffmann and Martin Haehnelt. A unified model for the evolution of galaxies and quasars. Monthly Notices of the RAS, 311(3):576–588, January 2000.

[141] Guinevere Kauffmann, Timothy M. Heckman, Christy Tremonti, Jarle Brinchmann, Stéphane Charlot, Simon D. M. White, Susan E. Ridgway, Jon Brinkmann, Masataka Fukugita, Patrick B. Hall, Željko Ivezić, Gordon T. Richards, and Donald P. Schneider. The host galaxies of active galactic nuclei. Monthly Notices of the RAS, 346(4):1055–1077, December 2003.

[142] William C. Keel, S. Drew Chojnowski, Vardha N. Bennert, Kevin Schawinski, Chris J. Lintott, Stuart Lynn, Anna Pancoast, Chelsea Harris, A. M. Nierenberg, Alessandro Sonnenfeld, and Richard Proctor. The Galaxy Zoo survey for giant AGN-ionized clouds: past and present black hole accretion events. Monthly Notices of the RAS, 420(1):878–900, February 2012.

[143] L. J. Kewley, M. A. Dopita, R. S. Sutherland, C. A. Heisler, and J. Trevena. Theoretical Modeling of Starburst Galaxies. Astrophysical Journal, 556(1):121–140, July 2001.

[144] Lisa J. Kewley, Michael A. Dopita, Claus Leitherer, Romeel Davé, Tiantian Yuan, Mark Allen, Brent Groves, and Ralph Sutherland. Theoretical Evolution of Optical Strong Lines across Cosmic Time. Astrophysical Journal, 774(2):100, September 2013.

[145] Lisa J. Kewley, Brent Groves, Guinevere Kauffmann, and Tim Heckman. The host galaxies and classification of active galactic nuclei. Monthly Notices of the RAS, 372(3):961–976, November 2006.

[146] Lisa J. Kewley, David C. Nicholls, Ralph Sutherland, Jane R. Rigby, Ayan Acharya, Michael A. Dopita, and Matthew B. Bayliss. Theoretical ISM Pressure and Electron Density Diagnostics for Local and High-redshift Galaxies. Astrophysical Journal, 880(1):16, July 2019.

[147] W. Kollatschny. Accretion disk wind in the AGN broad-line region: Spectroscopically resolved line profile variations in Mrk 110. Astronomy and Astrophysics, 407:461–472, August 2003.

[148] W. Kollatschny and M. Zetzl. The shape of broad-line profiles in active galactic nuclei. Astronomy and Astrophysics, 549:A100, January 2013.

[149] W. Kollatschny and M. Zetzl. Vertical broad-line region structure in nearby active galactic nuclei. Astronomy and Astrophysics, 558:A26, October 2013.

[150] K. T. Korista and G. J. Ferland. The Origin of Coronal Lines in Seyfert Galaxies. Astrophysical Journal, 343:678, August 1989.

[151] John Kormendy and Luis C. Ho. Coevolution (Or Not) of Supermassive Black Holes and Host Galaxies. Annual Review of Astronomy and Astrophysics, 51(1):511–653, Aug 2013.

[152] A. T. Koski. Spectrophotometry of Seyfert 2 galaxies and narrow-line radio galaxies. Astrophysical Journal, 223:56–73, July 1978.

[153] Michael Koss, Richard Mushotzky, Sylvain Veilleux, and Lisa Winter. Merging and Clustering of the Swift BAT AGN Sample. Astrophysical Journal, Letters, 716(2):L125–L130, June 2010.

[154] S. B. Kraemer, M. L. Trippe, D. M. Crenshaw, M. Meléndez, H. R. Schmitt, and T. C. Fischer. Physical Conditions in the Inner Narrow-Line Region of the Seyfert 2 Galaxy Markarian 573. Astrophysical Journal, 698(1):106–114, June 2009.

[155] Andrey V. Kravtsov, Anatoly A. Klypin, and Alexei M. Khokhlov. Adaptive Refinement Tree: A New High-Resolution N-Body Code for Cosmological Simulations. Astrophysical Journal, Supplement, 111(1):73–94, July 1997.

[156] Claudia Del P. Lagos, Sofía A. Cora, and Nelson D. Padilla. Effects of AGN feedback on ΛCDM galaxies. Monthly Notices of the RAS, 388(2):587–602, August 2008.

[157] Hermine Landt, Martin Elvis, Martin J. Ward, Misty C. Bentz, Kirk T. Korista, and Margarita Karovska. The near-infrared broad emission line region of active galactic nuclei - II. The 1-μm continuum. Monthly Notices of the RAS, 414(1):218–240, June 2011.

[158] A. Laor. What is the Broad Line Region? In Gordon T. Richards and Patrick B. Hall, editors, AGN Physics with the Sloan Digital Sky Survey, volume 311 of Astronomical Society of the Pacific Conference Series, page 169, June 2004.

[159] David R. Law, Brian Cherinka, Renbin Yan, Brett H. Andrews, Matthew A. Bershady, Dmitry Bizyaev, Guillermo A. Blanc, Michael R. Blanton, Adam S. Bolton, Joel R. Brownstein, Kevin Bundy, Yanmei Chen, Niv Drory, Richard D'Souza, Hai Fu, Amy Jones, Guinevere Kauffmann, Nicholas MacDonald, Karen L. Masters, Jeffrey A. Newman, John K. Parejko, José R. Sánchez-Gallego, Sebastian F. Sánchez, David J. Schlegel, Daniel Thomas, David A. Wake, Anne-Marie Weijmans, Kyle B. Westfall, and Kai Zhang. The Data Reduction Pipeline for the SDSS-IV MaNGA IFU Galaxy Survey. Astronomical Journal, 152(4):83, October 2016.

[160] A. Lawrence. The relative frequency of broad-lined and narrow-lined active galactic nuclei : implications for unified schemes. Monthly Notices of the RAS, 252:586, October 1991.

[161] Michael J. Ledlow and Frazer N. Owen. 20 CM VLA Survey of Abell Clusters of Galaxies. VI. Radio/Optical Luminosity Functions. Astronomical Journal, 112:9, July 1996.

[162] Jong Hwan Lee and Myung Gyoon Lee. A New Optical Survey of Supernova Remnant Candidates in M31. Astrophysical Journal, 786(2):130, May 2014.

[163] Nancy A. Levenson, Robert P. Kirshner, William P. Blair, and P. Frank Winkler. On the Propinquity of Shock-Excited and Photoionized Plasma:The Supernova Remnant and the H II Region of N63A. Astronomical Journal, 110:739, August 1995.

[164] Guilin Liu, Nadia L. Zakamska, Jenny E. Greene, Nicole P. H. Nesvadba, and Xin Liu. Observations of feedback from radio-quiet quasars - I. Extents and morphologies of ionized gas nebulae. Monthly Notices of the RAS, 430(3):2327–2345, April 2013.

[165] He-Yang Liu, Wen-Juan Liu, Xiao-Bo Dong, Hongyan Zhou, Tinggui Wang, Honglin Lu, and Weimin Yuan. A Comprehensive and Uniform Sample of Broad-line Active Galactic Nuclei from the SDSS DR7. Astrophysical Journal, Supplement, 243(2):21, August 2019.

[166] He-Yang Liu, Weimin Yuan, Xiao-Bo Dong, Hongyan Zhou, and Wen-Juan Liu. A Uniformly Selected Sample of Low-mass Black Holes in Seyfert 1 Galaxies. II. The SDSS DR7 Sample. Astrophysical Journal, Supplement, 235(2):40, April 2018.

[167] Carlos O. Lousto and James Healy. Kicking gravitational wave detectors with recoiling black holes. Physical Review D, 100(10):104039, November 2019.

[168] V. Luridiana, C. Morisset, and R. A. Shaw. PyNeb: a new tool for analyzing emission lines. I. Code description and validation of results. Astronomy and Astrophysics, 573:A42, January 2015.

[169] D. Lutz, S. Veilleux, and R. Genzel. Mid-Infrared and Optical Spectroscopy of Ultraluminous Infrared Galaxies: A Comparison. Astrophysical Journal, Letters, 517(1):L13–L17, May 1999.

[170] D. Lutz, L. Yan, L. Armus, G. Helou, L. J. Tacconi, R. Genzel, and A. J. Baker. Millimeter Observations of Obscured Spitzer 24 μm Sources. Astrophysical Journal, Letters, 632(1):L13–L16, October 2005.

[171] Piero Madau, Henry C. Ferguson, Mark E. Dickinson, Mauro Giavalisco, Charles C. Steidel, and Andrew Fruchter. High-redshift galaxies in the Hubble Deep Field: colour selection and star formation history to z˜4. Monthly Notices of the RAS, 283(4):1388–1404, December 1996.

[172] Piero Madau, Lucia Pozzetti, and Mark Dickinson. The Star Formation History of Field Galaxies. Astrophysical Journal, 498(1):106–116, May 1998.

[173] Dan Maoz, Neil M. Nagar, Heino Falcke, and Andrew S. Wilson. The Murmur of the Sleeping Black Hole: Detection of Nuclear Ultraviolet Variability in LINER Galaxies. Astrophysical Journal, 625(2):699–715, June 2005.

[174] Alessandro Marconi and Leslie K. Hunt. The Relation between Black Hole Mass, Bulge Mass, and Near-Infrared Luminosity. Astrophysical Journal, Letters, 589(1):L21–L24, May 2003.

[175] F. Marin. Are there reliable methods to estimate the nuclear orientation of Seyfert galaxies? Monthly Notices of the RAS, 460(4):3679–3705, August 2016.

[176] Federico Marulli, Silvia Bonoli, Enzo Branchini, Lauro Moscardini, and Volker Springel. Modelling the cosmological co-evolution of supermassive black holes and galaxies - I. BH scaling relations and the AGN luminosity function. Monthly Notices of the RAS, 385(4):1846–1858, April 2008.

[177] D. S. Mathewson and J. N. Clarke. A Supernova Remnant in the Small Magellanic Cloud. Astrophysical Journal, Letters, 178:L105, December 1972.

[178] D. S. Mathewson and J. N. Clarke. Supernova remnants in the Large Magellanic Cloud. Astrophysical Journal, 180:725–738, March 1973.

[179] X. Mazzalay, A. Rodríguez-Ardila, S. Komossa, and Peter J. McGregor. Resolving the coronal line region of NGC 1068 with near-infrared integral field spectroscopy. Monthly Notices of the RAS, 430(3):2411–2426, April 2013.

[180] Ximena Mazzalay, Alberto Rodríguez-Ardila, and S. Komossa. Demystifying the coronal-line region of active galactic nuclei: spatially resolved spectroscopy with the Hubble Space Telescope. Monthly Notices of the RAS, 405(2):1315–1338, June 2010.

[181] Patrick J. McCarthy, Wil van Breugel, Hyron Spinrad, and S. Djorgovski. A Correlation between the Radio and Optical Morphologies of Distant 3 CR Radio Galaxies. Astrophysical Journal, Letters, 321:L29, October 1987.

[182] Anne M. Medling, Vivian U, Jeffrey A. Rich, Lisa J. Kewley, Lee Armus, Michael A. Dopita, Claire E. Max, David Sanders, and Ralph Sutherland. Shocked gas in IRAS F17207-0014: ISM collisions and outflows. Monthly Notices of the RAS, 448(3):2301–2311, April 2015.

[183] Andrea Merloni and Sebastian Heinz. Measuring the kinetic power of active galactic nuclei in the radio mode. Monthly Notices of the RAS, 381(2):589–601, October 2007.

[184] Mallory Molina, Amy E. Reines, Lilikoi J. Latimer, Vivienne Baldassare, and Sheyda Salehirad. A Sample of Massive Black Holes in Dwarf Galaxies Detected via [Fe X] Coronal Line Emission: Active Galactic Nuclei and/or Tidal Disruption Events. Astrophysical Journal, 922(2):155, December 2021.

[185] E. Moy and B. Rocca-Volmerange. The balance between shocks and AGN photoionization in radio sources and its relation to the radio size. Astronomy and Astrophysics, 383:46–55, January 2002.

[186] John S. Mulchaey, Andrew S. Wilson, and Zlatan Tsvetanov. An Emission-Line Imaging Survey of Early-Type Seyfert Galaxies. I. The Observations. The Astrophysical Journal Supplement Series, 102:309, February 1996.

[187] J. R. Mullaney, M. J. Ward, C. Done, G. J. Ferland, and N. Schurch. The location and kinematics of the coronal-line emitting regions in active galactic nuclei. Monthly Notices of the RAS, 394(1):L16–L20, March 2009.

[188] F. Müller-Sánchez, M. A. Prieto, E. K. S. Hicks, H. Vives-Arias, R. I. Davies, M. Malkan, L. J. Tacconi, and R. Genzel. Outflows from Active Galactic Nuclei: Kinematics of the Narrow-line and Coronal-line Regions in Seyfert Galaxies. Astrophysical Journal, 739(2):69, October 2011.

[189] Masahiro Nagashima, Hideki Yahagi, Motohiro Enoki, Yuzuru Yoshii, and Naoteru Gouda. Numerical Galaxy Catalog. I. A Semianalytic Model of Galaxy Formation with N-Body Simulations. Astrophysical Journal, 634(1):26–50, November 2005.

[190] Jayant V. Narlikar and T. Padmanabhan. Standard Cosmology and Alternatives: A Critical Appraisal. Annual Review of Astronomy and Astrophysics, 39:211–248, January 2001.

[191] James Negus, Julia M. Comerford, Francisco Müller Sánchez, Jorge K. Barrera-Ballesteros, Niv Drory, Sandro B. Rembold, and Rogemar A. Riffel. The Physics of the Coronal-line Region for Galaxies in Mapping Galaxies at Apache Point Observatory. Astrophysical Journal, 920(1):62, October 2021.

[192] James Negus, Julia M. Comerford, Francisco Müller Sánchez, Mitchell Revalski, Rogemar A. Riffel, Kevin Bundy, Rebecca Nevin, and Sandro B. Rembold. A Catalog of 71 Coronal Line Galaxies in MaNGA: [Ne V] Is an Effective AGN Tracer. Astrophysical Journal, 945(2):127, March 2023.

[193] Hagai Netzer and Ari Laor. Dust in the Narrow-Line Region of Active Galactic Nuclei. Astrophysical Journal, 404:L51, February 1993.

[194] R. Nevin, L. Blecha, J. Comerford, and J. Greene. Accurate Identification of Galaxy Mergers with Imaging. Astrophysical Journal, 872(1):76, February 2019.

[195] R. Nevin, L. Blecha, J. Comerford, J. Simon, B. A. Terrazas, R. S. Barrows, and J. A. Vázquez-Mata. A declining major merger fraction with redshift in the local Universe from the largest-yet catalogue of major and minor mergers in SDSS. Monthly Notices of the RAS, 522(1):1–28, June 2023.

[196] Jeffrey A. Newman, Michael C. Cooper, Marc Davis, S. M. Faber, Alison L. Coil, Puragra Guhathakurta, David C. Koo, Andrew C. Phillips, Charlie Conroy, Aaron A. Dutton, Douglas P. Finkbeiner, Brian F. Gerke, David J. Rosario, Benjamin J. Weiner, C. N. A. Willmer, Renbin Yan, Justin J. Harker, Susan A. Kassin, N. P. Konidaris, Kamson Lai, Darren S. Madgwick, K. G. Noeske, Gregory D. Wirth, A. J. Connolly, N. Kaiser, Evan N. Kirby, Brian C. Lemaux, Lihwai Lin, Jennifer M. Lotz, G. A. Luppino, C. Marinoni, Daniel J. Matthews, Anne Metevier, and Ricardo P. Schiavon. The DEEP2 Galaxy Redshift Survey: Design, Observations, Data Reduction, and Redshifts. Astrophysical Journal, Supplement, 208(1):5, September 2013.

[197] C. A. Norman and S. Ikeuchi. The disk-halo interaction - Superbubbles and the structure of the interstellar medium. Astrophysical Journal, 345:372–383, October 1989.

[198] James E. O'Donnell. R v-dependent Optical and Near-Ultraviolet Extinction. Astrophysical Journal, 422:158, February 1994.

[199] Kyuseok Oh, Michael Koss, Craig B. Markwardt, Kevin Schawinski, Wayne H. Baumgartner, Scott D. Barthelmy, S. Bradley Cenko, Neil Gehrels, Richard Mushotzky, Abigail Petulante, Claudio Ricci, Amy Lien, and Benny Trakhtenbrot. The 105-Month Swift-BAT All-sky Hard X-Ray Survey. The Astrophysical Journal Supplement Series, 235(1):4, March 2018.

[200] Kyuseok Oh, Sukyoung K. Yi, Kevin Schawinski, Michael Koss, Benny Trakhtenbrot, and Kurt Soto. A New Catalog of Type 1 AGNs and its Implications on the AGN Unified Model. The Astrophysical Journal Supplement Series, 219(1):1, July 2015.

[201] E. Oliva, M. Salvati, A. F. M. Moorwood, and A. Marconi. Size and physical conditions of the coronal line region in a nearby Seyfert 2: the Circinus galaxy. Astronomy and Astrophysics, 288:457–465, August 1994.

[202] Benjamin D. Oppenheimer and Romeel Davé. Mass, metal, and energy feedback in cosmological simulations. Monthly Notices of the RAS, 387(2):577–600, June 2008.

[203] D. E. Osterbrock. The spectrum of III ZW 77 : an unusual, high-ionization Seyfert 1 galaxy. Astrophysical Journal, 246:696–707, June 1981.

[204] D. E. Osterbrock. Active galactic nuclei. Quarterly Journal of the RAS, 25:1–18, March 1984.

[205] Donald E. Osterbrock and Gary J. Ferland. Astrophysics of gaseous nebulae and active galactic nucle 2006.

[206] Paolo Padovani. The faint radio sky: radio astronomy becomes mainstream. Astronomy and Astrophysics Reviews, 24(1):13, September 2016.

[207] Paolo Padovani. Active Galactic Nuclei at all wavelengths and from all angles. Frontiers in Astronomy and Space Sciences, 4:35, November 2017.

[208] Isabelle Pâris, Patrick Petitjean, Éric Aubourg, Adam D. Myers, Alina Streblyanska, Brad W. Lyke, Scott F. Anderson, Éric Armengaud, Julian Bautista, Michael R. Blanton, Michael Blomqvist, Jonathan Brinkmann, Joel R. Brownstein, William Nielsen Brandt, Étienne Burtin, Kyle Dawson, Sylvain de la Torre, Antonis Georgakakis, Héctor Gil-Marín, Paul J. Green, Patrick B. Hall, Jean-Paul Kneib, Stephanie M. LaMassa, Jean-Marc Le Goff, Chelsea MacLeod, Vivek Mariappan, Ian D. McGreer, Andrea Merloni, Pasquier Noterdaeme, Nathalie Palanque-Delabrouille, Will J. Percival, Ashley J. Ross, Graziano Rossi, Donald P. Schneider, Hee-Jong Seo, Rita Tojeiro, Benjamin A. Weaver, Anne-Marie Weijmans, Christophe Yèche, Pauline Zarrouk, and Gong-Bo Zhao. The Sloan Digital Sky Survey Quasar Catalog: Fourteenth data release. Astronomy and Astrophysics, 613:A51, May 2018.

[209] Alison Pennell, Jessie C. Runnoe, and M. S. Brotherton. Updating quasar bolometric luminosity corrections - III. [O III] bolometric corrections. Monthly Notices of the RAS, 468(2):1433–1441, June 2017.

[210] M. V. Penston, R. A. E. Fosbury, A. Boksenberg, M. J. Ward, and A. S. Wilson. The Fe 9+ region in active galactic nuclei. Monthly Notices of the RAS, 208:347–364, May 1984.

[211] Asher Peres. Classical Radiation Recoil. Physical Review, 128(5):2471–2475, December 1962.

[212] Bradley M. Peterson. An Introduction to Active Galactic Nuclei. 1997.

[213] Bradley M. Peterson. Measuring the Masses of Supermassive Black Holes. Space Science Reviews, 183(1-4):253–275, September 2014.

[214] Bradley M. Peterson and Amri Wandel. Keplerian Motion of Broad-Line Region Gas as Evidence for Supermassive Black Holes in Active Galactic Nuclei. Astrophysical Journal, Letters, 521(2):L95–L98, August 1999.

[215] M. Almudena Prieto, Olivier Marco, and Jack Gallimore. Morphology of the coronal-line region in active galactic nuclei*. Monthly Notices of the RAS, 364(1):L28–L32, November 2005.

[216] M. Almudena Prieto, A. M. Pérez García, and J. M. Rodríguez Espinosa. On the relation between the coronal line emission and the infrared/X-ray emission in Seyfert galaxies. Monthly Notices of the RAS, 329(2):309–314, January 2002.

[217] S. I. Raimundo and A. C. Fabian. Eddington ratio and accretion efficiency in active galactic nuclei evolution. Monthly Notices of the RAS, 396(3):1217–1221, July 2009.

[218] J. C. Raymond. Shock waves in the interstellar medium. The Astrophysical Journal Supplement Series, 39:1–27, January 1979.

[219] Michael Reefe, Shobita Satyapal, Remington O. Sexton, Sara M. Doan, Nathan J. Secrest, and Jenna M. Cann. CLASS: Coronal Line Activity Spectroscopic Survey. Astrophysical Journal, 936(2):140, September 2022.

[220] Sandro B. Rembold, Jáderson S. Shimoia, Thaisa Storchi-Bergmann, Rogério Riffel, Rogemar A. Riffel, Nícolas D. Mallmann, Janaína C. do Nascimento, Thales N. Moreira, Gabriele S. Ilha, Alice D. Machado, Rafael Cirolini, Luiz N. da Costa, Marcio A. G. Maia, Basílio X. Santiago, Donald P. Schneider, Dominika Wylezalek, Dmitry Bizyaev, Kaike Pan, and Francisco Müller-Sánchez. The first 62 AGNs observed with SDSS-IV MaNGA - I. Their characterization and definition of a control sample. Monthly Notices of the RAS, 472(4):4382–4403, December 2017.

[221] Mitchell Revalski, D. Michael Crenshaw, Marc Rafelski, Steven B. Kraemer, Garrett E. Polack, Anna Trindade Falcão, Travis C. Fischer, Beena Meena, Francisco Martinez, Henrique R. Schmitt, Nicholas R. Collins, and Julia Falcone. Quantifying Feedback from Narrow Line Region Outflows in Nearby Active Galaxies. IV. The Effects of Different Density Estimates on the Ionized Gas Masses and Outflow Rates. Astrophysical Journal, 930(1):14, May 2022.

[222] Mitchell Revalski, Beena Meena, Francisco Martinez, Garrett E. Polack, D. Michael Crenshaw, Steven B. Kraemer, Nicholas R. Collins, Travis C. Fischer, Henrique R. Schmitt, Judy Schmidt, W. Peter Maksym, and Marc Rafelski. Quantifying Feedback from Narrow Line Region Outflows in Nearby Active Galaxies. III. Results for the Seyfert 2 Galaxies Markarian 3, Markarian 78, and NGC 1068. Astrophysical Journal, 910(2):139, April 2021.

[223] J. A. Rich, M. A. Dopita, L. J. Kewley, and D. S. N. Rupke. NGC 839: Shocks in an M82-like Superwind. Astrophysical Journal, 721(1):505–517, September 2010.

[224] J. A. Rich, L. J. Kewley, and M. A. Dopita. Galaxy-wide Shocks in Late-merger Stage Luminous Infrared Galaxies. Astrophysical Journal, 734(2):87, June 2011.

[225] J. A. Rich, L. J. Kewley, and M. A. Dopita. Galaxy Mergers Drive Shocks: An Integral Field Study of GOALS Galaxies. The Astrophysical Journal Supplement Series, 221(2):28, December 2015.

[226] R. A. Riffel, O. L. Dors, M. Armah, T. Storchi-Bergmann, A. Feltre, G. F. Hägele, M. V. Cardaci, D. Ruschel-Dutra, A. C. Krabbe, E. Pérez-Montero, N. L. Zakamska, and I. C. Freitas. Chemical abundances in Seyfert galaxies - V. The discovery of shocked emission outside the AGN ionization axis. Monthly Notices of the RAS, 501(1):L54–L59, February 2021.

[227] R. A. Riffel, O. L. Dors, M. Armah, T. Storchi-Bergmann, A. Feltre, G. F. Hägele, M. V. Cardaci, D. Ruschel-Dutra, A. C. Krabbe, E. Pérez-Montero, N. L. Zakamska, and I. C. Freitas. Chemical abundances in Seyfert galaxies - V. The discovery of shocked emission outside the AGN ionization axis. Monthly Notices of the RAS, 501(1):L54–L59, February 2021.

[228] Rogemar A. Riffel, Marina Bianchin, Rogério Riffel, Thaisa Storchi-Bergmann, Astor J. Schönell, Luis Gabriel Dahmer-Hahn, Natacha Z. Dametto, and Marlon R. Diniz. Gemini NIFS survey of feeding and feedback in nearby active galaxies - IV. Excitation. Monthly Notices of the RAS, 503(4):5161–5178, May 2021.

[229] Thomas P. Robitaille and Barbara A. Whitney. The Present-Day Star Formation Rate of the Milky Way Determined from Spitzer-Detected Young Stellar Objects. Astrophysical Journal, Letters, 710(1):L11–L15, February 2010.

[230] Ian Robson. Active galactic nuclei. 1996.

[231] B. Rocca-Volmerange and B. Guiderdoni. Merging-driven evolution of high-redshift galaxies in a universe with omega 0 = 1. Monthly Notices of the RAS, 247:166, November 1990.

[232] A. Rodríguez-Ardila, M. A. Prieto, J. G. Portilla, and J. M. Tejeiro. The Near-infrared Coronal Line Spectrum of 54 nearby Active Galactic Nuclei. Astrophysical Journal, 743(2):100, December 2011.

[233] A. Rodríguez-Ardila, S. M. Viegas, M. G. Pastoriza, and L. Prato. Near-Infrared Coronal Lines in Narrow-Line Seyfert 1 Galaxies. Astrophysical Journal, 579(1):214–226, November 2002.

[234] Alberto Rodríguez-Ardila and Marcos A. Fonseca-Faria. A 700 pc Extended Coronal Gas Emission in the Circinus Galaxy. Astrophysical Journal, Letters, 895(1):L9, May 2020.

[235] Alberto Rodríguez-Ardila, M. Almudena Prieto, Sueli Viegas, and Ruth Gruenwald. Outflows of Very Ionized Gas in the Centers of Seyfert Galaxies: Kinematics and Physical Conditions. Astrophysical Journal, 653(2):1098–1114, December 2006.

[236] Marvin Rose, Martin Elvis, and Clive N. Tadhunter. Coronal-Line Forest AGN: the best view of the inner edge of the AGN torus? Monthly Notices of the RAS, 448(3):2900–2920, April 2015.

[237] Gwen C. Rudie, Andrew B. Newman, and Michael T. Murphy. A Unique View of AGN-driven Molecular Outflows: The Discovery of a Massive Galaxy Counterpart to a Z = 2.4 High-metallicity Damped Lyα Absorber. Astrophysical Journal, 843(2):98, July 2017.

[238] Anna Sajina, Mark Lacy, and Alexandra Pope. The Past and Future of Mid-Infrared Studies of AGN. Universe, 8(7):356, June 2022.

[239] S. F. Sánchez, V. Avila-Reese, H. Hernandez-Toledo, E. Cortes-Suárez, A. Rodríguez-Puebla, H. Ibarra-Medel, M. Cano-Díaz, J. K. Barrera-Ballesteros, C. A. Negrete, A. R. Calette, A. de Lorenzo-Cáceres, R. A. Ortega-Minakata, E. Aquino, O. Valenzuela, J. C. Clemente, T. Storchi-Bergmann, R. Riffel, J. Schimoia, R. A. Riffel, S. B. Rembold, J. R. Brownstein, K. Pan, R. Yates, N. Mallmann, and T. Bitsakis. SDSS IV MaNGA - Properties of AGN Host Galaxies. Revista Mexicana de Astronomia y Astrofisica, 54:217–260, April 2018.

[240] D. B. Sanders, E. S. Phinney, G. Neugebauer, B. T. Soifer, and K. Matthews. Continuum Energy Distributions of Quasars: Shapes and Origins. Astrophysical Journal, 347:29, December 1989.

[241] D. B. Sanders, B. T. Soifer, J. H. Elias, B. F. Madore, K. Matthews, G. Neugebauer, and N. Z. Scoville. Ultraluminous Infrared Galaxies and the Origin of Quasars. Astrophysical Journal, 325:74, February 1988.

[242] F. Santoro, J. B. R. Oonk, R. Morganti, T. A. Oosterloo, and C. Tadhunter. Embedded star formation in the extended narrow line region of Centaurus A: Extreme mixing observed by MUSE. Astronomy and Astrophysics, 590:A37, May 2016.

[243] S. Satyapal, D. Vega, R. P. Dudik, N. P. Abel, and T. Heckman. Spitzer Uncovers Active Galactic Nuclei Missed by Optical Surveys in Seven Late-Type Galaxies. Astrophysical Journal, 677(2):926–942, April 2008.

[244] Shobita Satyapal, Nicholas P. Abel, and Nathan J. Secrest. Star-forming Galaxies as AGN Imposters? A Theoretical Investigation of the Mid-infrared Colors of AGNs and Extreme Starbursts. Astrophysical Journal, 858(1):38, May 2018.

[245] Shobita Satyapal, Sara L. Ellison, William McAlpine, Ryan C. Hickox, David R. Patton, and J. Trevor Mendel. Galaxy pairs in the Sloan Digital Sky Survey - IX. Merger-induced AGN activity as traced by the Wide-field Infrared Survey Explorer. Monthly Notices of the RAS, 441(2):1297–1304, June 2014.

[246] Shobita Satyapal, Lara Kamal, Jenna M. Cann, Nathan J. Secrest, and Nicholas P. Abel. The Diagnostic Potential of JWST in Characterizing Elusive AGNs. Astrophysical Journal, 906(1):35, January 2021.

[247] P. Schechter. An analytic expression for the luminosity function for galaxies. Astrophysical Journal, 203:297–306, January 1976.

[248] David J. Schlegel, Douglas P. Finkbeiner, and Marc Davis. Maps of Dust Infrared Emission for Use in Estimation of Reddening and Cosmic Microwave Background Radiation Foregrounds. Astrophysical Journal, 500(2):525–553, June 1998.

[249] H. R. Schmitt, J. L. Donley, R. R. J. Antonucci, J. B. Hutchings, and A. L. Kinney. A Hubble Space Telescope Survey of Extended [O III] λ5007 Emission in a Far-Infrared Selected Sample of Seyfert Galaxies: Observations. The Astrophysical Journal Supplement Series, 148(2):327–352, October 2003.

[250] Donald P. Schneider, Gordon T. Richards, Patrick B. Hall, Michael A. Strauss, Scott F. Anderson, Todd A. Boroson, Nicholas P. Ross, Yue Shen, W. N. Brandt, Xiaohui Fan, Naohisa Inada, Sebastian Jester, G. R. Knapp, Coleman M. Krawczyk, Anirudda R. Thakar, Daniel E. Vanden Berk, Wolfgang Voges, Brian Yanny, Donald G. York, Neta A. Bahcall, Dmitry Bizyaev, Michael R. Blanton, Howard Brewington, J. Brinkmann, Daniel Eisenstein, Joshua A. Frieman, Masataka Fukugita, Jim Gray, James E. Gunn, Pascale Hibon, Željko Ivezić, Stephen M. Kent, Richard G. Kron, Myung Gyoon Lee, Robert H. Lupton, Elena Malanushenko, Viktor Malanushenko, Dan Oravetz, K. Pan, Jeffrey R. Pier, III Price, Ted N., David H. Saxe, David J. Schlegel, Audry Simmons, Stephanie A. Snedden, Mark U. SubbaRao, Alexander S. Szalay, and David H. Weinberg. The Sloan Digital Sky Survey Quasar Catalog. V. Seventh Data Release. Astrophysical Journal, 139(6):2360, June 2010.

[251] C. G. Seab and J. M. Shull. Shock processing of interstellar grains. Astrophysical Journal, 275:652–660, December 1983.

[252] Carl K. Seyfert. Nuclear Emission in Spiral Nebulae. Astrophysical Journal, 97:28, January 1943.

[253] Richard A. Shaw and Reginald J. Dufour. Software for the Analysis of Emission Line Nebulae. Publications of the ASP, 107:896, September 1995.

[254] J. M. Shuder. On the physical conditions and the velocity fields in Seyfert 1 galaxies and QSOs. Astrophysical Journal, 259:48–54, August 1982.

[255] J. M. Shuder. Emission-line profiles in low-redshift QSOs. Astrophysical Journal, 280:491–498, May 1984.

[256] Joseph Silk. Ultraluminous starbursts from supermassive black hole-induced outflows. Monthly Notices of the RAS, 364(4):1337–1342, December 2005.

[257] Joseph Silk and Martin J. Rees. Quasars and galaxy formation. Astronomy and Astrophysics, 331:L1–L4, March 1998.

[258] Chris Simpson. The luminosity dependence of the type 1 active galactic nucleus fraction. Monthly Notices of the RAS, 360(2):565–572, June 2005.

[259] Stephen A. Smee, James E. Gunn, Alan Uomoto, Natalie Roe, David Schlegel, Constance M. Rockosi, Michael A. Carr, French Leger, Kyle S. Dawson, Matthew D. Olmstead, Jon Brinkmann, Russell Owen, Robert H. Barkhouser, Klaus Honscheid, Paul Harding, Dan Long, Robert H. Lupton, Craig Loomis, Lauren Anderson, James Annis, Mariangela Bernardi, Vaishali Bhardwaj, Dmitry Bizyaev, Adam S. Bolton, Howard Brewington, John W. Briggs, Scott Burles, James G. Burns, Francisco Javier Castander, Andrew Connolly, James R. A. Davenport, Garrett Ebelke, Harland Epps, Paul D. Feldman, Scott D. Friedman, Joshua Frieman, Timothy Heckman, Charles L. Hull, Gillian R. Knapp, David M. Lawrence, Jon Loveday, Edward J. Mannery, Elena Malanushenko, Viktor Malanushenko, Aronne James Merrelli, Demitri Muna, Peter R. Newman, Robert C. Nichol, Daniel Oravetz, Kaike Pan, Adrian C. Pope, Paul G. Ricketts, Alaina Shelden, Dale Sandford, Walter Siegmund, Audrey Simmons, D. Shane Smith, Stephanie Snedden, Donald P. Schneider, Mark SubbaRao, Christy Tremonti, Patrick Waddell, and Donald G. York. The Multi-object, Fiber-fed Spectrographs for the Sloan Digital Sky Survey and the Baryon Oscillation Spectroscopic Survey. Astronomical Journal, 146(2):32, August 2013.

[260] Nathan Smith, Jeffrey M. Silverman, Ryan Chornock, Alexei V. Filippenko, Xiaofeng Wang, Weidong Li, Mohan Ganeshalingam, Ryan J. Foley, Jacob Rex, and Thea N. Steele. Coronal Lines and Dust Formation in SN 2005ip: Not the Brightest, but the Hottest Type IIn Supernova. Astrophysical Journal, 695(2):1334–1350, April 2009.

[261] Theodore P. Snow and Adolf N. Witt. Interstellar Depletions Updated: Where All the Atoms Went. Astrophysical Journal, Letters, 468:L65, September 1996.

[262] Rachel S. Somerville, James S. Bullock, and Mario Livio. The Epoch of Reionization in Models with Reduced Small-Scale Power. Astrophysical Journal, 593(2):616–621, August 2003.

[263] Rachel S. Somerville, Philip F. Hopkins, Thomas J. Cox, Brant E. Robertson, and Lars Hernquist. A semi-analytic model for the co-evolution of galaxies, black holes and active galactic nuclei. Monthly Notices of the RAS, 391(2):481–506, December 2008.

[264] V. Springel, S. D. M. White, A. Jenkins, C. S. Frenk, N. Yoshida, L. Gao, J. Navarro, R. Thacker, D. Croton, J. Helly, J. A. Peacock, S. Cole, P. Thomas, H. Couchman, A. Evrard, J. Colberg, and F. Pearce. Simulations of the formation, evolution and clustering of galaxies and quasars. Nature, 435:629–636, June 2005.

[265] Volker Springel. The cosmological simulation code GADGET-2. Monthly Notices of the RAS, 364(4):1105–1134, December 2005.

[266] Volker Springel, Tiziana Di Matteo, and Lars Hernquist. Modelling feedback from stars and black holes in galaxy mergers. Monthly Notices of the RAS, 361(3):776–794, August 2005.

[267] Charles C. Steidel, Kurt L. Adelberger, Mauro Giavalisco, Mark Dickinson, and Max Pettini. Lyman-Break Galaxies at z¿˜4 and the Evolution of the Ultraviolet Luminosity Density at High Redshift. Astrophysical Journal, 519(1):1–17, July 1999.

[268] Charles C. Steidel, Mauro Giavalisco, Max Pettini, Mark Dickinson, and Kurt L. Adelberger. Spectroscopic Confirmation of a Population of Normal Star-forming Galaxies at Redshifts Z ¿ 3. Astrophysical Journal, Letters, 462:L17, May 1996.

[269] Charles C. Steidel, Max Pettini, and Donald Hamilton. Lyman Imaging of High-Redshift Galaxies.III.New Observations of Four QSO Fields. Astronomical Journal, 110:2519, December 1995.

[270] Aaron Stemo, Julia M. Comerford, R. Scott Barrows, Daniel Stern, Roberto J. Assef, Roger L. Griffith, and Aimee Schechter. A Catalog of 204 Offset and Dual Active Galactic Nuclei (AGNs): Increased AGN Activation in Major Mergers and Separations under 4 kpc. Astrophysical Journal, 923(1):36, December 2021.

[271] Aaron Stemo, Adi Foord, Julia Comerford, Robert Barrows, Daniel Stern, Roberto Assef, Aimee Schechter, and Jessie Runnoe. Examining AGN Activation in Mergers in the 1 to 20 kpc Separation Range. In American Astronomical Society Meeting Abstracts, volume 55 of American Astronomical Society Meeting Abstracts, page 360.30, January 2023.

[272] E. Sturm, D. Lutz, A. Verma, H. Netzer, A. Sternberg, A. F. M. Moorwood, E. Oliva, and R. Genzel. Mid-Infrared line diagnostics of active galaxies. A spectroscopic AGN survey with ISO-SWS. Astronomy and Astrophysics, 393:821–841, October 2002.

[273] Ai-Lei Sun, Jenny E. Greene, and Nadia L. Zakamska. Sizes and Kinematics of Extended Narrow-line Regions in Luminous Obscured AGN Selected by Broadband Images. Astrophysical Journal, 835(2):222, February 2017.

[274] C. N. Tadhunter. The Ionization of the Emission Line Gas in Nearby Powerful Radio Galaxies. In William J. Henney, Wolfgang Steffen, Luc Binette, and Alejandro Raga, editors, Revista Mexicana de Astronomia y Astrofisica Conference Series, volume 13 of Revista Mexicana de Astronomia y Astrofisica Conference Series, pages 213–221, June 2002.

[275] C. N. Tadhunter, R. A. E. Fosbury, S. di Serego Alighieri, J. Bland, I. J. Danziger, W. M. Goss, W. B. McAdam, and M. A. J. Snijders. Very extended ionized gas in radio galaxies - IV. PKS 2152-69. Monthly Notices of the RAS, 235:403–423, November 1988.

[276] Robert J. Thacker, Evan Scannapieco, and H. M. P. Couchman. Quasars: What Turns Them Off? Astrophysical Journal, 653(1):86–100, December 2006.

[277] L. Trouille and A. J. Barger. The OPTX Project. IV. How Reliable is [O III] as a Measure of AGN Activity? Astrophysical Journal, 722(1):212–221, October 2010.

[278] L. Trouille, A. J. Barger, and C. Tremonti. The OPTX Project. V. Identifying Distant Active Galactic Nuclei. Astrophysical Journal.

[279] Yoshihiro Ueda, Masayuki Akiyama, Kouji Ohta, and Takamitsu Miyaji. Cosmological Evolution of the Hard X-Ray Active Galactic Nucleus Luminosity Function and the Origin of the Hard X-Ray Background. Astrophysical Journal.

[280] C. Megan Urry and Paolo Padovani. Unified Schemes for Radio-Loud Active Galactic Nuclei. Publications of the ASP, 107:803, September 1995.

[281] Pieter G. van Dokkum, Katherine E. Whitaker, Gabriel Brammer, Marijn Franx, Mariska Kriek, Ivo Labbé, Danilo Marchesini, Ryan Quadri, Rachel Bezanson, Garth D. Illingworth, Adam Muzzin, Gregory Rudnick, Tomer Tal, and David Wake. The Growth of Massive Galaxies Since z = 2. Astrophysical Journal, 709(2):1018–1041, February 2010.

[282] E. van Groningen and A. G. de Bruyn. Broad emission line profiles in Seyfert-1 galaxies : O III -wings from a transition zone. Astronomy and Astrophysics, 211:293–309, March 1989.

[283] Daniel E. Vanden Berk, Gordon T. Richards, Amanda Bauer, Michael A. Strauss, Donald P. Schneider, Timothy M. Heckman, Donald G. York, Patrick B. Hall, Xiaohui Fan, G. R. Knapp, Scott F. Anderson, James Annis, Neta A. Bahcall, Mariangela Bernardi, John W. Briggs, J. Brinkmann, Robert Brunner, Scott Burles, Larry Carey, Francisco J. Castander, A. J. Connolly, J. H. Crocker, István Csabai, Mamoru Doi, Douglas Finkbeiner, Scott Friedman, Joshua A. Frieman, Masataka Fukugita, James E. Gunn, G. S. Hennessy, Željko Ivezić, Stephen Kent, Peter Z. Kunszt, D. Q. Lamb, R. French Leger, Daniel C. Long, Jon Loveday, Robert H. Lupton, Avery Meiksin, Aronne Merelli, Jeffrey A. Munn, Heidi Jo Newberg, Matt Newcomb, R. C. Nichol, Russell Owen, Jeffrey R. Pier, Adrian Pope, Constance M. Rockosi, David J. Schlegel, Walter A. Siegmund, Stephen Smee, Yehuda Snir, Chris Stoughton, Christopher Stubbs, Mark SubbaRao, Alexander S. Szalay, Gyula P. Szokoly, Christy Tremonti, Alan Uomoto, Patrick Waddell, Brian Yanny, and Wei Zheng. Composite Quasar Spectra from the Sloan Digital Sky Survey. Astronomical Journal, 122(2):549–564, August 2001.

[284] Ludovica Varisco, Tullia Sbarrato, Giorgio Calderone, and Massimo Dotti. AGN mass estimates in large spectroscopic surveys: the effect of host galaxy light. Astronomy and Astrophysics, 618:A127, October 2018.

[285] S. Veilleux, D. S. N. Rupke, D. C. Kim, R. Genzel, E. Sturm, D. Lutz, A. Contursi, M. Schweitzer, L. J. Tacconi, H. Netzer, A. Sternberg, J. C. Mihos, A. J. Baker, J. M. Mazzarella, S. Lord, D. B. Sanders, A. Stockton, R. D. Joseph, and J. E. Barnes. Spitzer Quasar and Ulirg Evolution Study (QUEST). IV. Comparison of 1 Jy Ultraluminous Infrared Galaxies with Palomar-Green Quasars. Astrophysical Journal, Supplement, 182(2):628–666, June 2009.

[286] Sylvain Veilleux and Donald E. Osterbrock. Spectral Classification of Emission-Line Galaxies. Astrophysical Journal, Supplement.

[287] W. Voges, B. Aschenbach, T. Boller, H. Brauninger, U. Briel, W. Burkert, K. Dennerl, J. Englhauser, R. Gruber, F. Haberl, G. Hartner, G. Hasinger, E. Pfeffermann, W. Pietsch, P. Predehl, J. Schmitt, J. Trumper, and U. Zimmermann. Rosat All-Sky Survey Faint Source Catalogue. IAU Cirulars, 7432:3, May 2000.

[288] W. Voges, B. Aschenbach, Th. Boller, H. Bräuninger, U. Briel, W. Burkert, K. Dennerl, J. Englhauser, R. Gruber, F. Haberl, G. Hartner, G. Hasinger, M. Kürster, E. Pfeffermann, W. Pietsch, P. Predehl, C. Rosso, J. H. M. M. Schmitt, J. Trümper, and H. U. Zimmermann. The ROSAT all-sky survey bright source catalogue. Astronomy and Astrophysics, 349:389–405, September 1999.

[289] Marta Volonteri, Francesco Haardt, and Piero Madau. The Assembly and Merging History of Supermassive Black Holes in Hierarchical Models of Galaxy Formation. Astrophysical Journal, 582(2):559–573, January 2003.

[290] David A. Wake, Kevin Bundy, Aleksandar M. Diamond-Stanic, Renbin Yan, Michael R. Blanton, Matthew A. Bershady, José R. Sánchez-Gallego, Niv Drory, Amy Jones, Guinevere Kauffmann, David R. Law, Cheng Li, Nicholas MacDonald, Karen Masters, Daniel Thomas, Jeremy Tinker, Anne-Marie Weijmans, and Joel R. Brownstein. The SDSS-IV MaNGA Sample: Design, Optimization, and Usage Considerations. Astronomical Journal, 154(3):86, September 2017.

[291] S. Walg, A. Achterberg, S. Markoff, R. Keppens, and O. Porth. Relativistic AGN jets - III. Synthesis of synchrotron emission from double-double radio galaxies. Monthly Notices of the RAS, 497(3):3638–3657, September 2020.

[292] Tim Waters, Amit Kashi, Daniel Proga, Michael Eracleous, Aaron J. Barth, and Jenny Greene. Reverberation Mapping of the Broad Line Region: Application to a Hydrodynamical Line-driven Disk Wind Solution. Astrophysical Journal, 827(1):53, August 2016.

[293] D. W. Weedman, B. T. Soifer, Lei Hao, J. L. Higdon, S. J. U. Higdon, J. R. Houck, E. Le Floc'h, M. J. I. Brown, A. Dey, B. T. Jannuzi, M. Rieke, V. Desai, C. Bian, D. Thompson, L. Armus, H. Teplitz, P. Eisenhardt, and S. P. Willner. Spitzer IRS Spectra of Optically Faint Infrared Sources with Weak Spectral Features. Astrophysical Journal, 651(1):101–112, November 2006.

[294] Kyle B. Westfall, Michele Cappellari, Matthew A. Bershady, Kevin Bundy, Francesco Belfiore, Xihan Ji, David R. Law, Adam Schaefer, Shravan Shetty, Christy A. Tremonti, Renbin Yan, Brett H. Andrews, Joel R. Brownstein, Brian Cherinka, Lodovico Coccato, Niv Drory, Claudia Maraston, Taniya Parikh, José R. Sánchez-Gallego, Daniel Thomas, Anne-Marie Weijmans, Jorge Barrera-Ballesteros, Cheng Du, Daniel Goddard, Niu Li, Karen Masters, Héctor Javier Ibarra Medel, Sebastián F. Sánchez, Meng Yang, Zheng Zheng, and Shuang Zhou. The Data Analysis Pipeline

for the SDSS-IV MaNGA IFU Galaxy Survey: Overview. Astronomical Journal, 158(6):231, December 2019.

[295] Simon D. M. White and Carlos S. Frenk. Galaxy Formation through Hierarchical Clustering. Astrophysical Journal, 379:52, September 1991.

[296] D. Whysong and R. Antonucci. Thermal Emission as a Test for Hidden Nuclei in Nearby Radio Galaxies. Astrophysical Journal, 602(1):116–122, February 2004.

[297] Kyle W. Willett, Chris J. Lintott, Steven P. Bamford, Karen L. Masters, Brooke D. Simmons, Kevin R. V. Casteels, Edward M. Edmondson, Lucy F. Fortson, Sugata Kaviraj, William C. Keel, Thomas Melvin, Robert C. Nichol, M. Jordan Raddick, Kevin Schawinski, Robert J. Simpson, Ramin A. Skibba, Arfon M. Smith, and Daniel Thomas. Galaxy Zoo 2: detailed morphological classifications for 304 122 galaxies from the Sloan Digital Sky Survey. Monthly Notices of the RAS, 435(4):2835–2860, November 2013.

[298] Hartmut Winkler. The unusually strong coronal emission lines of SDSS J1055+5637. arXiv e-prints, page arXiv:1604.04515, April 2016.

[299] Edward L. Wright, Peter R. M. Eisenhardt, Amy K. Mainzer, Michael E. Ressler, Roc M. Cutri, Thomas Jarrett, J. Davy Kirkpatrick, Deborah Padgett, Robert S. McMillan, Michael Skrutskie, S. A. Stanford, Martin Cohen, Russell G. Walker, John C. Mather, David Leisawitz, III Gautier, Thomas N., Ian McLean, Dominic Benford, Carol J. Lonsdale, Andrew Blain, Bryan Mendez, William R. Irace, Valerie Duval, Fengchuan Liu, Don Royer, Ingolf Heinrichsen, Joan Howard, Mark Shannon, Martha Kendall, Amy L. Walsh, Mark Larsen, Joel G. Cardon, Scott Schick, Mark Schwalm, Mohamed Abid, Beth Fabinsky, Larry Naes, and Chao-Wei Tsai. The Wide-field Infrared Survey Explorer (WISE): Mission Description and Initial On-orbit Performance. Astronomical Journal, 140(6):1868–1881, December 2010.

[300] X. B. Wu, R. Wang, M. Z. Kong, F. K. Liu, and J. L. Han. Black hole mass estimation using a relation between the BLR size and emission line luminosity of AGN. Astronomy and Astrophysics, 424:793–798, September 2004.

[301] Dominika Wylezalek, Nadia L. Zakamska, Jenny E. Greene, Rogemar A. Riffel, Niv Drory, Brett H. Andrews, Andrea Merloni, and Daniel Thomas. SDSS-IV MaNGA: identification of active galactic nuclei in optical integral field unit surveys. Monthly Notices of the RAS, 474(2):1499–1514, February 2018.

[302] Renbin Yan and Michael R. Blanton. The Nature of LINER-like Emission in Red Galaxies. Astrophysical Journal, 747(1):61, March 2012.

[303] Renbin Yan, Kevin Bundy, David R. Law, Matthew A. Bershady, Brett Andrews, Brian Cherinka, Aleksandar M. Diamond-Stanic, Niv Drory, Nicholas MacDonald, José R. Sánchez-Gallego, Daniel Thomas, David A. Wake, Anne-Marie Weijmans, Kyle B. Westfall, Kai Zhang, Alfonso Aragón-Salamanca, Francesco Belfiore, Dmitry

Bizyaev, Guillermo A. Blanc, Michael R. Blanton, Joel Brownstein, Michele Cappellari, Richard D'Souza, Eric Emsellem, Hai Fu, Patrick Gaulme, Mark T. Graham, Daniel Goddard, James E. Gunn, Paul Harding, Amy Jones, Karen Kinemuchi, Cheng Li, Hongyu Li, Roberto Maiolino, Shude Mao, Claudia Maraston, Karen Masters, Michael R. Merrifield, Daniel Oravetz, Kaike Pan, John K. Parejko, Sebastian F. Sanchez, David Schlegel, Audrey Simmons, Karun Thanjavur, Jeremy Tinker, Christy Tremonti, Remco van den Bosch, and Zheng Zheng. SDSS-IV MaNGA IFS Galaxy Survey—Survey Design, Execution, and Initial Data Quality. Astronomical Journal, 152(6):197, December 2016.

[304] Donald G. York, J. Adelman, Jr. Anderson, John E., Scott F. Anderson, James Annis, Neta A. Bahcall, J. A. Bakken, Robert Barkhouser, Steven Bastian, Eileen Berman, William N. Boroski, Steve Bracker, Charlie Briegel, John W. Briggs, J. Brinkmann, Robert Brunner, Scott Burles, Larry Carey, Michael A. Carr, Francisco J. Castander, Bing Chen, Patrick L. Colestock, A. J. Connolly, J. H. Crocker, István Csabai, Paul C. Czarapata, John Eric Davis, Mamoru Doi, Tom Dombeck, Daniel Eisenstein, Nancy Ellman, Brian R. Elms, Michael L. Evans, Xiaohui Fan, Glenn R. Federwitz, Larry Fiscelli, Scott Friedman, Joshua A. Frieman, Masataka Fukugita, Bruce Gillespie, James E. Gunn, Vijay K. Gurbani, Ernst de Haas, Merle Haldeman, Frederick H. Harris, J. Hayes, Timothy M. Heckman, G. S. Hennessy, Robert B. Hindsley, Scott Holm, Donald J. Holmgren, Chi-hao Huang, Charles Hull, Don Husby, Shin-Ichi Ichikawa, Takashi Ichikawa, Željko Ivezić, Stephen Kent, Rita S. J. Kim, E. Kinney, Mark Klaene, A. N. Kleinman, S. Kleinman, G. R. Knapp, John Korienek, Richard G. Kron, Peter Z. Kunszt, D. Q. Lamb, B. Lee, R. French Leger, Siriluk Limmongkol, Carl Lindenmeyer, Daniel C. Long, Craig Loomis, Jon Loveday, Rich Lucinio, Robert H. Lupton, Bryan MacKinnon, Edward J. Mannery, P. M. Mantsch, Bruce Margon, Peregrine McGehee, Timothy A. McKay, Avery Meiksin, Aronne Merelli, David G. Monet, Jeffrey A. Munn, Vijay K. Narayanan, Thomas Nash, Eric Neilsen, Rich Neswold, Heidi Jo Newberg, R. C. Nichol, Tom Nicinski, Mario Nonino, Norio Okada, Sadanori Okamura, Jeremiah P. Ostriker, Russell Owen, A. George Pauls, John Peoples, R. L. Peterson, Donald Petravick, Jeffrey R. Pier, Adrian Pope, Ruth Pordes, Angela Prosapio, Ron Rechenmacher, Thomas R. Quinn, Gordon T. Richards, Michael W. Richmond, Claudio H. Rivetta, Constance M. Rockosi, Kurt Ruthmansdorfer, Dale Sandford, David J. Schlegel, Donald P. Schneider, Maki Sekiguchi, Gary Sergey, Kazuhiro Shimasaku, Walter A. Siegmund, Stephen Smee, J. Allyn Smith, S. Snedden, R. Stone, Chris Stoughton, Michael A. Strauss, Christopher Stubbs, Mark SubbaRao, Alexander S. Szalay, Istvan Szapudi, Gyula P. Szokoly, Anirudda R. Thakar, Christy Tremonti, Douglas L. Tucker, Alan Uomoto, Dan Vanden Berk, Michael S. Vogeley, Patrick Waddell, Shu-i. Wang, Masaru Watanabe, David H. Weinberg, Brian Yanny, Naoki Yasuda, and SDSS Collaboration. The Sloan Digital Sky Survey: Technical Summary. Astronomical Journal, 120(3):1579–1587, September 2000.

[305] Y. Y. Zhou, K. N. Yu, E. C. M. Young, J. M. Wang, and E. Ma. Statistical Properties of the Big Blue Bump in Active Galactic Nuclei. Astrophysical Journal, Letters, 475(1):L9–L12, January 1997.

Appendix A

Double Gaussian Fit For Hγ and [OIII] λ4363

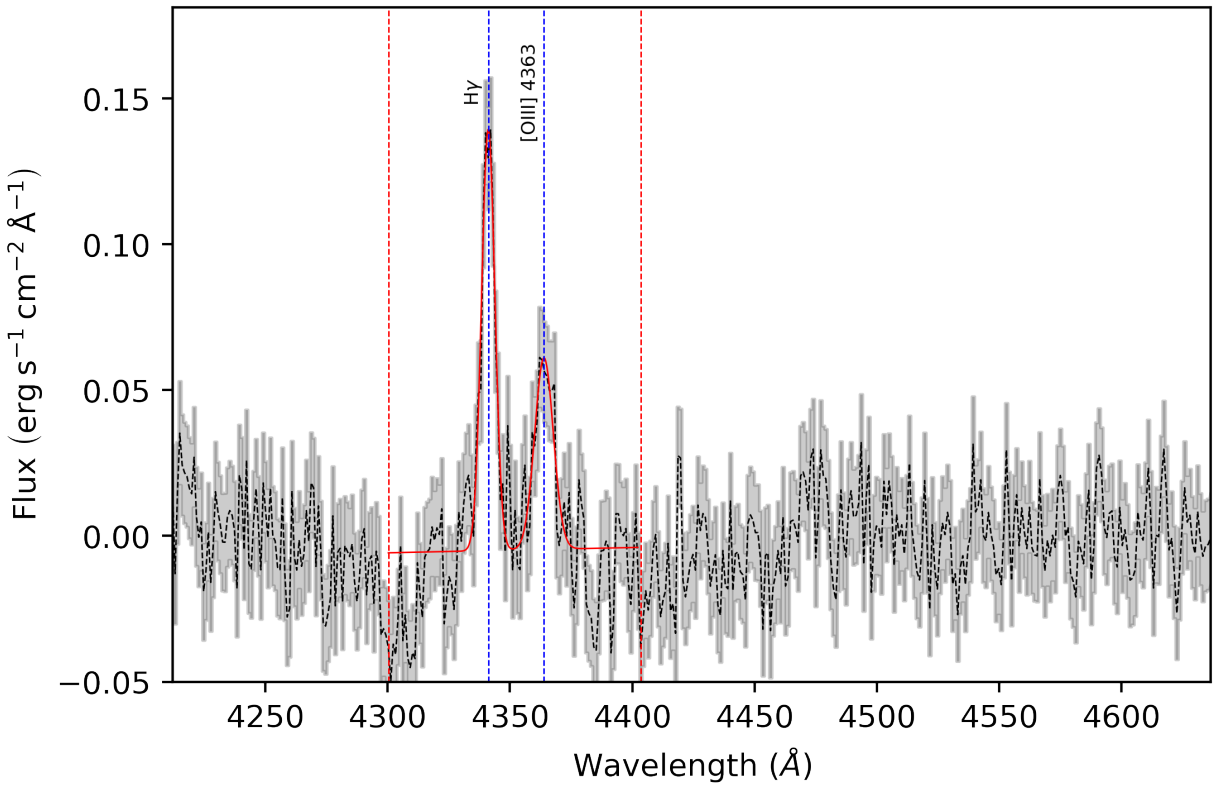

Figure A.1: A sample spectrum showing a double Gaussian fit on the Hγ and the [OIII] λ4363 lines (detected at $\geq 5\sigma$ above the continuum) in a single spaxel for J2116. The dashed black line is the continuum subtracted spectrum, the shaded gray region is the uncertainty, the solid red line represents the best fit, the red dotted vertical lines mark the fitting window, and the blue dotted lines show the rest wavelengths of Hγ and [OIII] λ4363.

Appendix B

[OIII] λ5007 Flux Maps for the CL galaxies

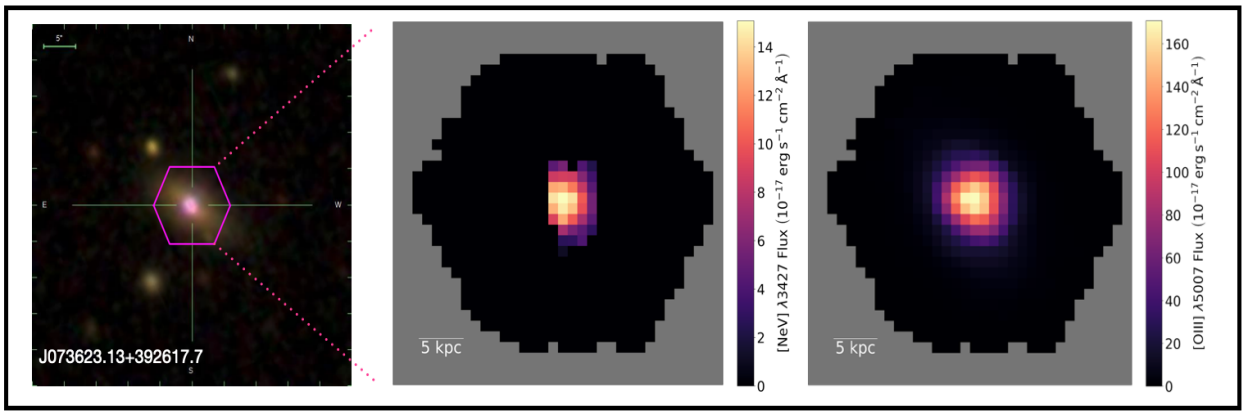

Figure B.1: From left to right: SDSS optical image, [NeV] λ3427 flux map, and [OIII] λ5007 flux map for J0736.

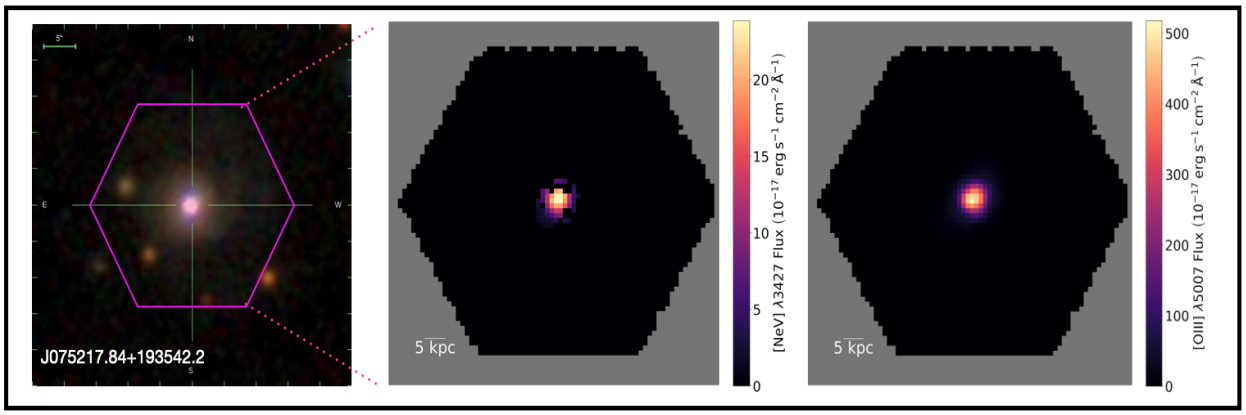

Figure B.2: From left to right: SDSS optical image, [NeV] λ3427 flux map, and [OIII] λ5007 flux map for J0752.

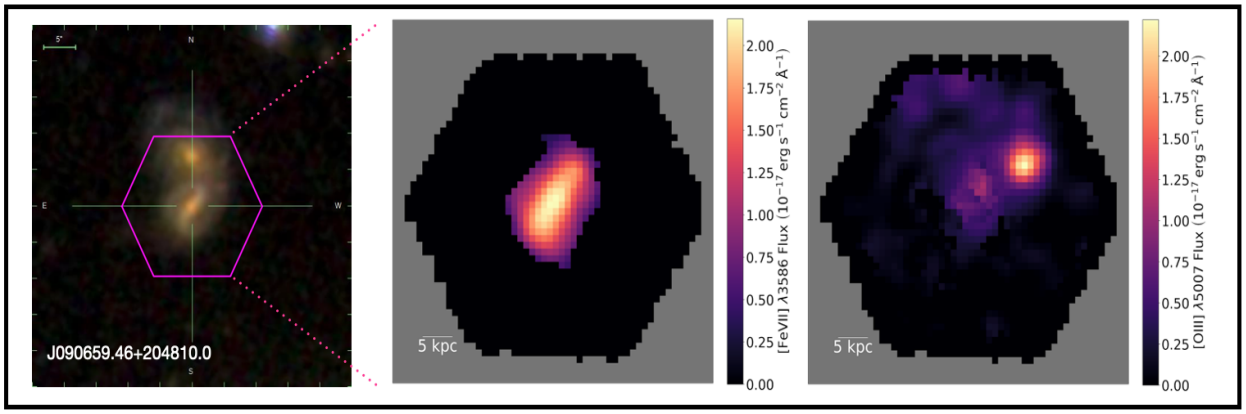

Figure B.3: From left to right: SDSS optical image, [FeVII] λ3586 flux map, and [OIII] λ5007 flux map for J0906.

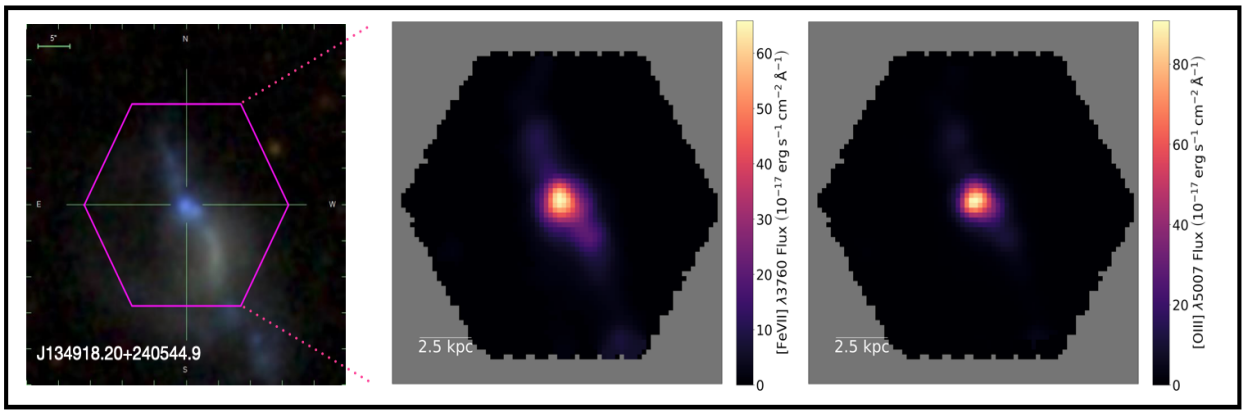

Figure B.4: From left to right: SDSS optical image, [FeVII] λ3760 flux map, and [OIII] λ5007 flux map for J1349

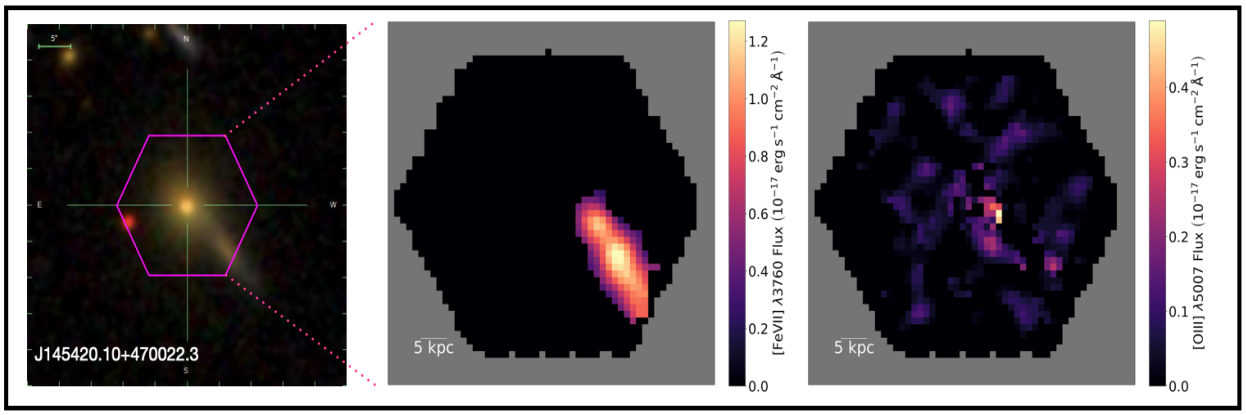

Figure B.5: From left to right: SDSS optical image, [FeVII] λ3760 flux map, and [OIII] λ5007 flux map for J1454

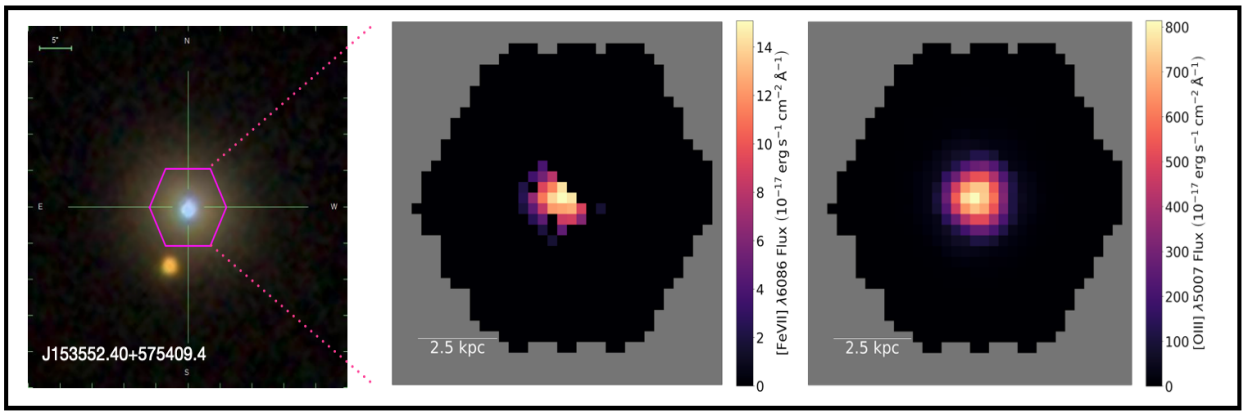

Figure B.6: From left to right: SDSS optical image, [FeVII] λ6086 flux map, and [OIII] λ5007 flux map for J1535

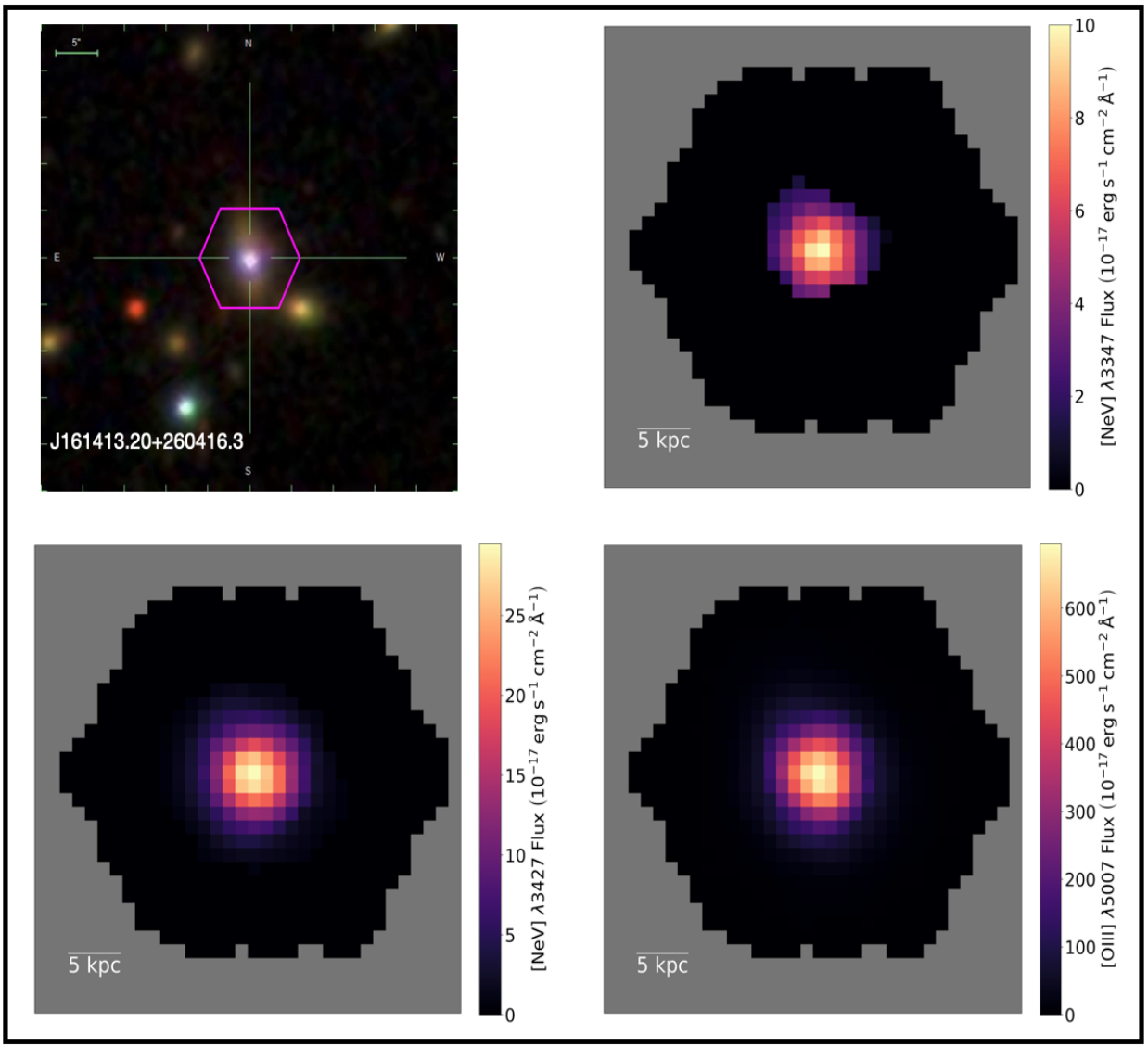

Figure B.7: Top row (left to right): SDSS optical image and [NeV] λ3347 flux map for J1614. Bottom row (left to right): [NeV] λ3427 flux map and [OIII] λ5007 flux map for J1614.

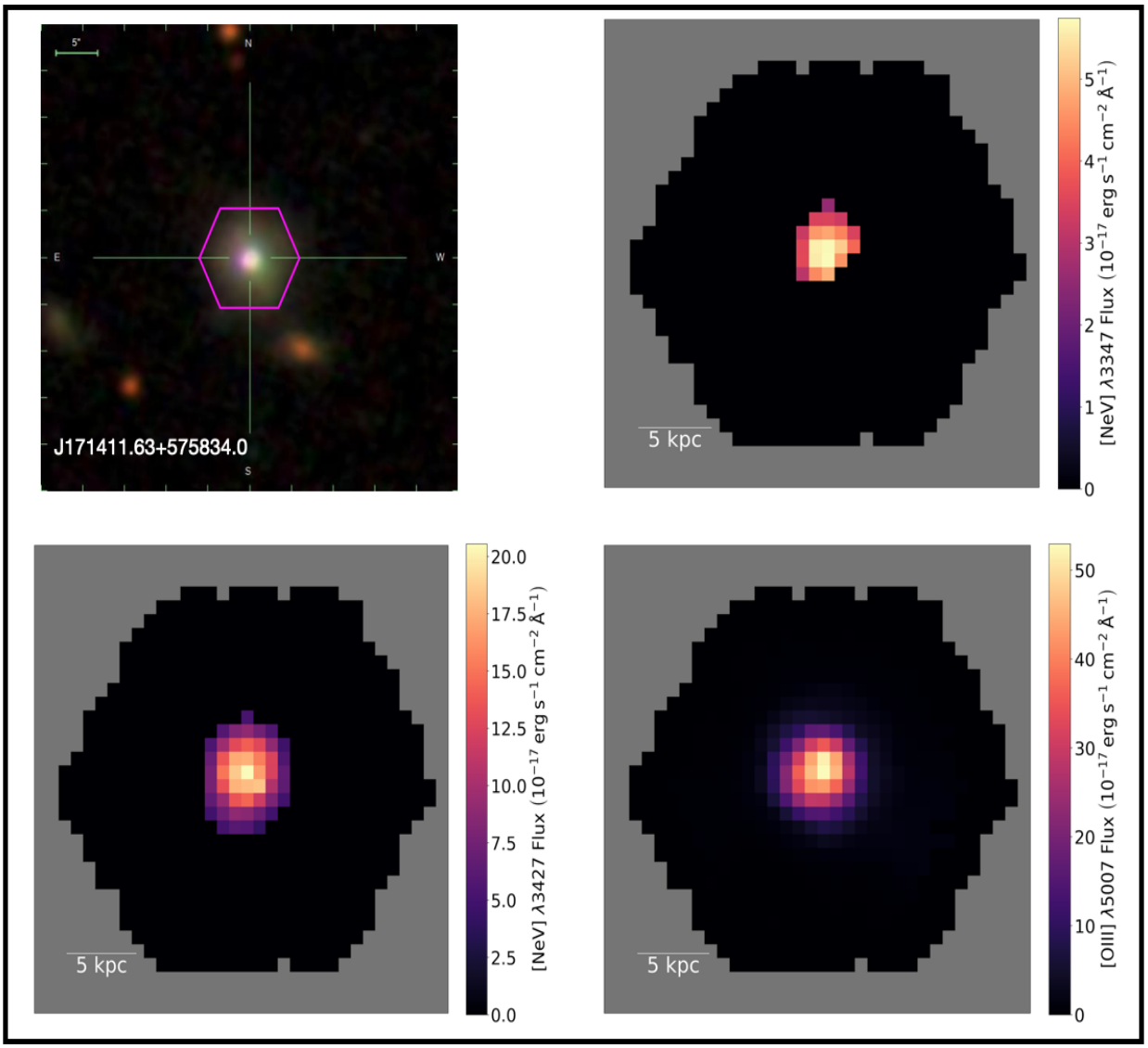

Figure B.8: Top row (left to right): SDSS optical image and [NeV] λ3347 flux map for J1714. Bottom row (left to right): [NeV] λ3427 flux map and [OIII] λ5007 flux map for J1714.

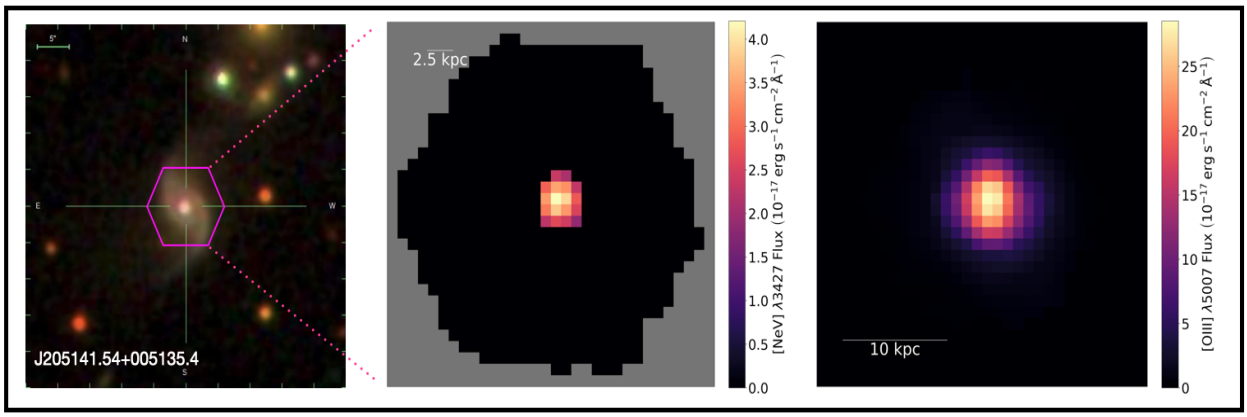

Figure B.9: From left to right: SDSS optical image, [NeV] λ3427 flux map, and [OIII] λ5007 flux map for J2051.

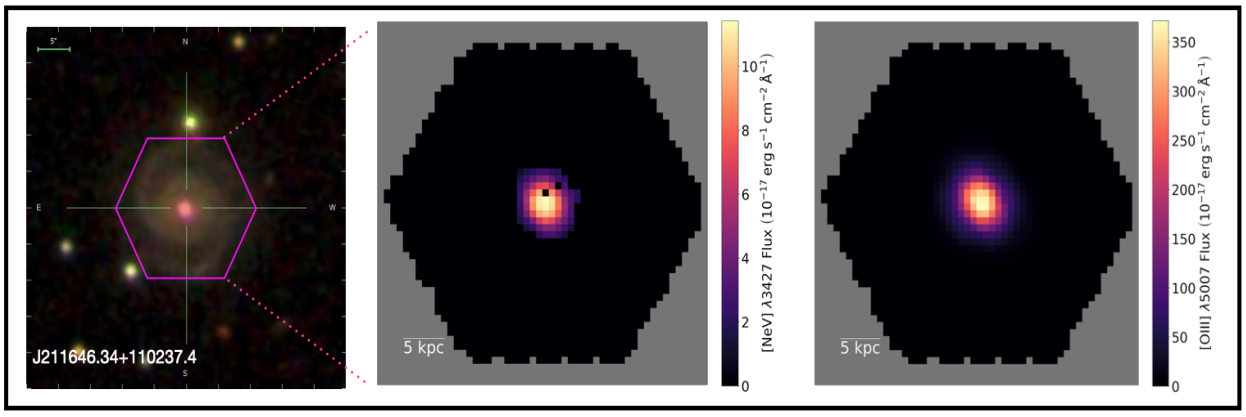

Figure B.10: From left to right: SDSS optical image, [NeV] λ3427 flux map, and [OIII] λ5007 flux map for J2116.

Appendix C

Example Broad Hβ Maps

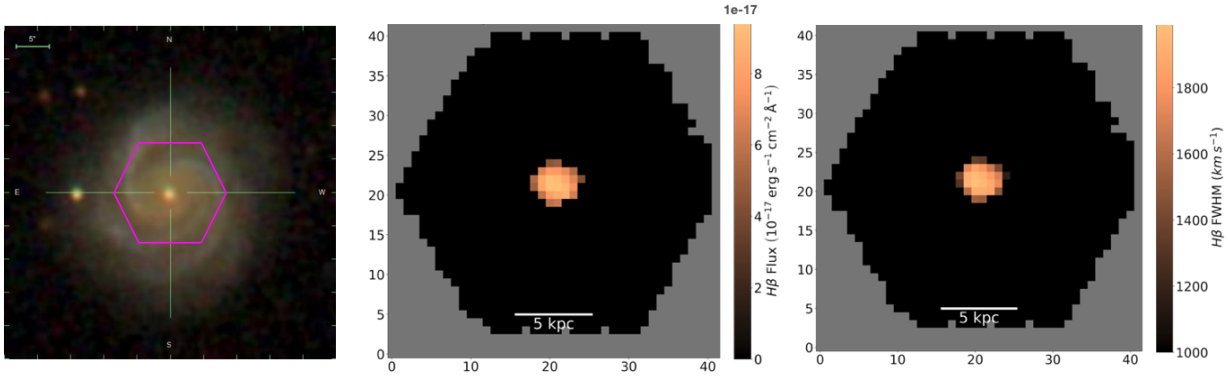

Figure C.1: From left to right, an example SDSS optical image from MaNGA, a custom generated broad Hβ flux map, and a custom generated broad Hβ FWHM map for J212851.19-010412.4. The gray region is outside of the MaNGA FoV and the black region are spaxels with no BL emission. North is up and east is to the left.

Appendix D

Broad Hα and Hβ Companion Galaxies

Table D.1: Broad Hα Companion Galaxies

SDSS Name	z	BH Mass (10^6 $M_\odot$)	Broad Hα FWHM (km s^{-1})	Broad Hα Luminosity (erg s^{-1})
J021035.31+125505.6	0.1	50	2247	2.63e+39
J073905.83+442410.3	0.134	148	2257	1.82e+40
J074746.00+513856.1	0.101	3449	4283	5.03e+41
J075931.82+375252.1	0.042	34	1180	1.44e+40
J075956.13+262258.6	0.074	37	1771	3.71e+39
J082150.35+415235.8	0.038	5	1249	4.65e+38
J082218.77+381559.4	0.052	13	2196	2.42e+38
J083823.79+254517.0	0.018	3	1843	4.71e+37
J084002.36+294902.6	0.065	221	2173	4.32e+40
J085206.99+285013.0	0.097	52	1782	6.54e+39
J091014.95+444102.7	0.035	1	1145	4.77e+37
J091954.10+325558.9	0.05	6	1392	4.05e+38
J095851.32+320422.9	0.027	9	1743	3.02e+38
J103723.62+021845.5	0.04	20	1890	9.86e+38
J110158.99+451340.9	0.02	8	1601	3.34e+38
J111803.22+450646.8	0.107	2958	4964	2.19e+41
J122737.49+400938.9	0.037	16	1372	2.12e+39
J132023.06+302641.0	0.048	15	1850	6.35e+38
J132651.27+263528.5	0.023	5	1156	4.74e+38
J133008.03+485335.7	0.071	22	1976	9.68e+38
J135638.55+433508.7	0.103	10	1353	1.07e+39
J142937.38+491944.1	0.125	10	1379	9.96e+38
J151600.58+342119.1	0.125	75	1576	2.06e+40
J151806.10+424438.0	0.04	3	1245	1.57e+38
J155850.44+272323.9	0.094	68	2006	6.99e+39
J160806.49+252906.7	0.042	9	1405	7.13e+38
J161413.20+260416.3	0.131	7008	3444	4.13e+42
J162002.93+260315.2	0.132	177	2660	1.36e+40
J162332.74+390715.9	0.035	4	1837	6.32e+37
J162952.88+242638.4	0.038	174	2523	1.61e+40
J165547.13+391837.8	0.063	8	1822	2.07e+38
J165550.29+272629.6	0.037	4	1771	7.97e+37
J165714.97+265010.8	0.036	7	2073	1.03e+38
J170450.70+344858.9	0.056	8	1785	2.52e+38
J211326.02+005828.0	0.137	497	2370	1.37e+41

Note: Columns are (1) SDSS Name, (2) host galaxy stellar continuum redshift, (3) BH mass, (4) median Broad Hα FWHM, with a systematic uncertainty of $\sigma = 72$ km s^{-1}, and (4) Broad Hα luminosity.

Table D.2: Broad Hβ Companion Galaxies

SDSS Name	z	BH Mass (10^6 $M_\odot$)	Broad Hβ FWHM (km s^{-1})	Broad Hβ Luminosity (erg s^{-1})
J005554.23-005521.1	0.045	1	1140	3.31e+37
J005620.79+135143.6	0.04	16	1222	1.45e+39
J005846.77-004506.5	0.044	87	2391	2.75e+39
J024416.39+002029.7	0.022	9	1584	2.44e+38
J031510.78-072956.0	0.032	14	1621	4.23e+38
J031945.63-000437.9	0.037	5	1084	3.82e+38
J072952.25+395329.3	0.05	170	2801	5.08e+39
J074806.96+500648.5	0.021	9	2603	3.9e+37
J074910.04+200815.5	0.073	13	1215	1.09e+39
J074921.08+522104.0	0.066	2	1107	6.6e+37
J075236.26+243403.3	0.05	5	1153	2.32e+38
J075353.88+204657.9	0.141	163	2477	7.3e+39
J075438.20+391038.6	0.096	18	1059	3.16e+39
J075526.32+185831.9	0.043	95	2801	1.83e+39
J080452.51+293454.7	0.08	25	1163	3.84e+39
J080614.67+373825.7	0.041	1020	2244	2.75e+41
J080648.17+531158.6	0.05	19	2333	2.07e+38
J080815.71+451705.8	0.04	5	1124	3.13e+38
J081705.39+481843.4	0.055	87	2307	3.11e+39
J082800.89+281548.9	0.094	3	1060	1.54e+38
J082834.42+501739.1	0.078	7	1181	4.48e+38
J083431.92+270312.9	0.08	8	1095	7.03e+38
J084411.66+233204.9	0.077	111	2539	3.37e+39
J085216.34+503738.0	0.112	378	2715	2.37e+40
J085404.53+290312.7	0.084	2	1029	1.16e+38
J085509.01+522813.6	0.058	5	1120	2.66e+38
J091204.30+002518.4	0.055	4	1068	2.39e+38
J091327.76+463644.9	0.08	62	1326	1.23e+40
J093657.37+481737.8	0.025	17	2140	2.2e+38
J094554.76+430248.1	0.073	2	1031	9.08e+37
J100546.90+021435.9	0.046	1	1149	3.55e+37
J101003.53+470715.3	0.065	39	1581	2.94e+39
J101601.37+441034.3	0.045	40	1223	7.58e+39
J102209.85+383109.3	0.053	5	1362	1.54e+38
J102433.13+464952.2	0.042	2	1048	9.75e+37
J103029.79+431431.9	0.099	23	1220	2.88e+39
J111000.74+464211.8	0.053	24	1460	1.64e+39
J121053.16+363244.8	0.022	17	2115	2.27e+38
J125817.89+290743.9	0.026	58	1687	4.62e+39

Note: Columns are (1) SDSS Name, (2) host galaxy stellar continuum redshift, (3) BH mass, (4) median Broad Hβ FWHM, with a systematic uncertainty of $\sigma = 72$ km s^{-1}, and (4) Broad Hβ luminosity.

Table D.3: Broad Hβ Companion Galaxies (Continued)

SDSS Name	z	SMBH Mass (10^6 $M_\odot$)	Broad Hβ FWHM (km s^{-1})	Broad Hβ Luminosity (erg s^{-1})
J133952.76+292247.2	0.044	60	2431	1.31e+39
J134458.27+310016.8	0.043	71	2939	9.1e+38
J134552.96+264630.6	0.03	6	1093	4.48e+38
J140800.78+554345.7	0.075	84	2256	3.18e+39
J144808.37+314237.2	0.033	1	1024	3.64e+37
J145359.23+004956.0	0.043	40	2136	1.02e+39
J145804.60+340720.4	0.088	12	1073	1.55e+39
J151235.36+084146.4	0.08	66	1274	1.58e+40
J152856.43+281722.4	0.073	5	1060	3.21e+38
J154255.49+091342.6	0.035	5	1645	7.69e+37
J154517.07+275449.5	0.077	2046	5227	4.65e+40
J155440.99+281129.8	0.08	53	2607	8.24e+38
J155540.99+285802.9	0.077	6	1060	5.03e+38
J155852.66+262619.0	0.087	5	1132	2.58e+38
J155929.59+094901.9	0.073	14	1304	1.01e+39
J155941.68+262958.3	0.09	12	1090	1.43e+39
J160436.23+435247.2	0.06	29	1391	2.68e+39
J162145.09+282549.0	0.116	6	1178	3.17e+38
J162332.74+390715.9	0.035	8	1054	8.18e+38
J162356.48+361339.3	0.033	4	1254	1.32e+38
J163454.41+261629.1	0.044	6	1445	1.65e+38
J163735.67+251823.8	0.056	4	1054	2.97e+38
J163917.51+202853.7	0.062	10	1149	8.15e+38
J164107.75+273045.1	0.054	314	5849	1.1e+39
J165714.97+265010.8	0.036	7	1131	4.53e+38
J171327.09+580436.6	0.093	147	2100	1.1e+40
J173541.00+552816.5	0.086	59	3140	5.24e+38
J203701.02-055949.4	0.036	11	1241	7.06e+38
J205250.49-004631.7	0.054	3	1027	1.4e+38
J210319.51+105638.9	0.043	151	3747	1.46e+39
J210431.56+095423.4	0.108	68	2202	2.36e+39
J210518.11-071525.9	0.053	123	2946	2.41e+39
J211326.02+005828.0	0.137	682	3015	4.67e+40
J211748.43+113938.1	0.038	23	3109	9.93e+37
J213351.93+100418.6	0.088	13	1595	4.09e+38
J213702.36+002541.7	0.051	10	1305	4.94e+38
J220201.62+000747.3	0.063	3	1177	1.01e+38
J220943.19+133802.9	0.027	6	1080	4.93e+38

Note: Columns are (1) SDSS Name, (2) host galaxy stellar continuum redshift, (3) SMBH mass, (4) median Broad Hβ FWHM, with a systematic uncertainty of σ = 72 km s^{-1}, and (4) Broad Hβ luminosity.

Appendix E

Recoiling BH Candidates

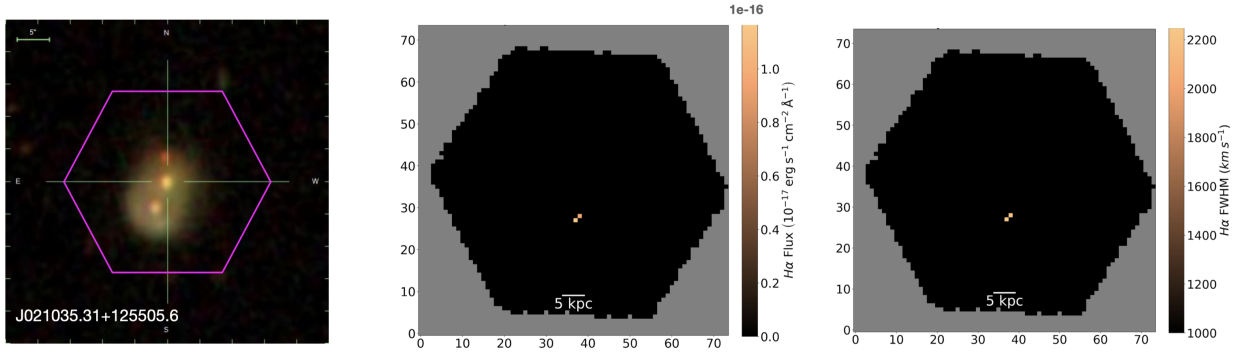

Figure E.1: From left to right: optical SDSS image, broad Hα flux map, and broad Hα FWHM map for recoiling BH candidate J021035.31+125505.6.

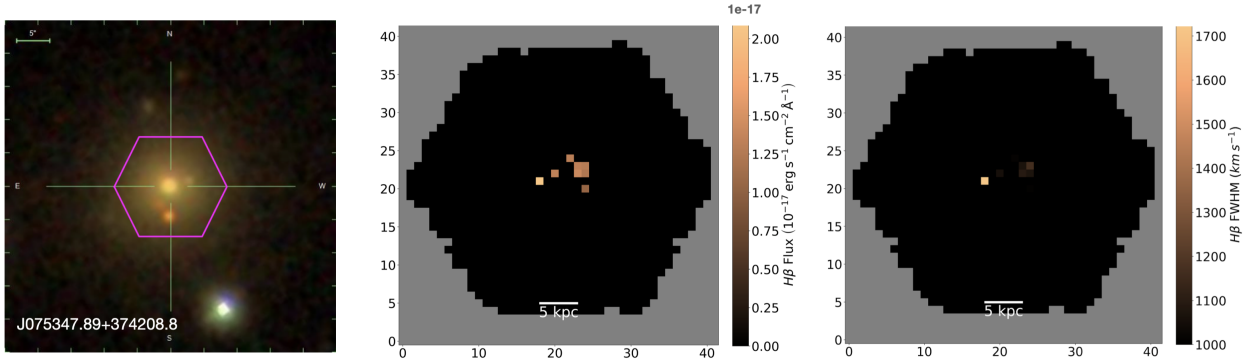

Figure E.2: From left to right: optical SDSS image, broad Hβ flux map, and broad Hβ FWHM map for recoiling BH candidate J075347.89+374208.8.

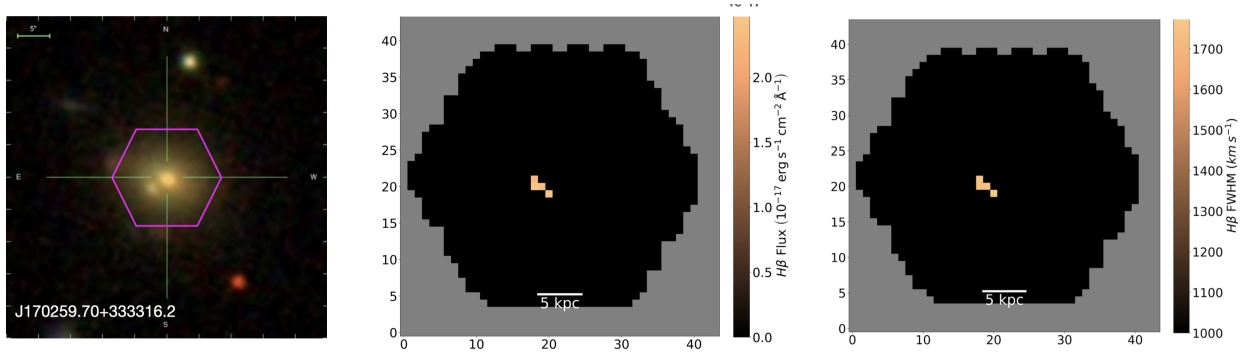

Figure E.3: From left to right: optical SDSS image, broad Hβ flux map, and broad Hβ FWHM map for recoiling BH candidate J170259.70+333316.2.

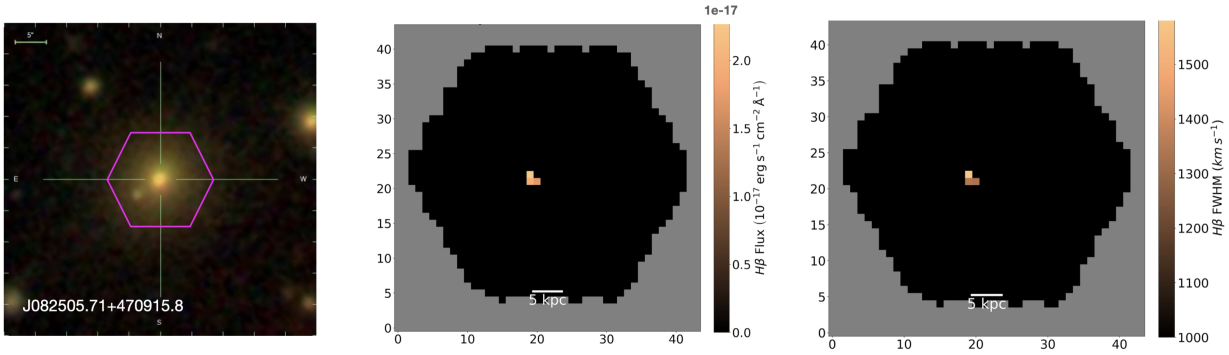

Figure E.4: From left to right: optical SDSS image, broad Hβ flux map, and broad Hβ FWHM map for recoiling BH candidate J082505.71+470915.8.

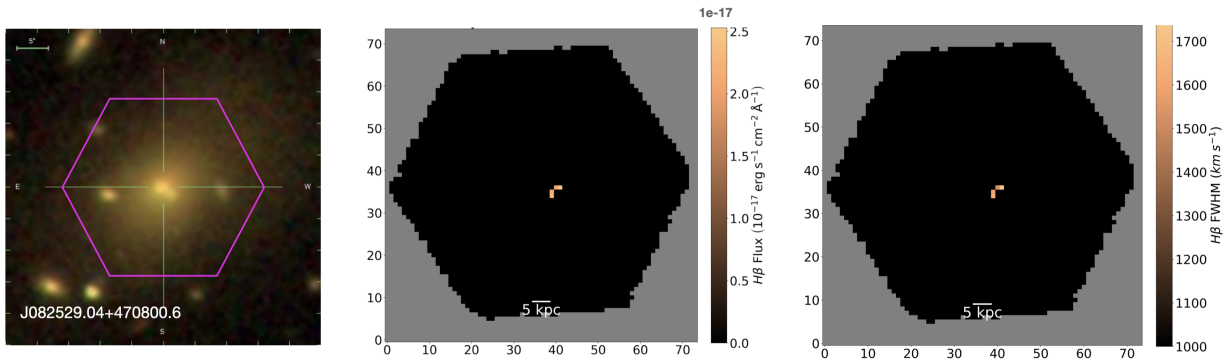

Figure E.5: From left to right: optical SDSS image, broad Hβ flux map, and broad Hβ FWHM map for recoiling BH candidate J082529.04+470800.6.